Model Complexes of Cytochrome P450 Nitric Oxide Reductase

by

Lauren E. Goodrich

A dissertation submitted in partial fulfillment
of the requirements for the degree of
Doctor of Philosophy
(Chemistry)
in The University of Michigan
2012

Doctoral Committee:

Associate Professor Nicolai Lehnert, Chair
Professor Mark M. Banaszak Holl
Assistant Professor Mi Hee Lim
Professor Yoichi Osawa

To my grandparents:

Vern and Thelma Meyer

Jack and Audrey Goodrich

Claire VanZant

Acknowledgements

The Lehnert Group, thanks for all the laughs over the years. Don't forget: 6pm on Friday is quitting time! Nicolai, your mentorship has been invaluable. I think you are teaching us to be the right kind of scientists. Thanks for always pushing us and expecting our best. Your patience is something I still aspire to.

Mom and Dad, thank you for all the encouragement over the years. I love you! You taught me to believe in myself. Because of your support I have always thought that I can accomplish anything I put my mind to—that is priceless. To all five of my grandparents, I could not ask for a more extraordinary family. Your enthusiasm for life is beyond inspiring.

Tim, I love you and could not have made it through this process without your unwavering support and friendship. Here's to new adventures and many more years of laughter!

Table of Contents

Dedication ii

Acknowledgements iii

List of Tables vi

List of Figures ix

List of Schemes xix

Abstract xxi

Chapter 1 1

Introduction 1

1.1. Nitric Oxide Biosynthesis and Sensing 1

1.2. Detoxification of NO in Biological Systems 2

1.3. Fungal NO Reductase (P450nor) 4

1.4. Scope of Thesis 23

Chapter 2 32

Six-Coordinate Ferric Porphyrin Nitrosyl Complexes 32

2.1. Ferric Heme-Nitrosyls with Thiolate Coordination 34

2.2. The Phenolate Ligand: A More Stable Alternative to Thiolate Ligation in Ferric Heme-Nitrosyls? 60

2.3. The Effect of Axial Ligand Strength in Ferric Heme-Nitrosyls 69

Chapter 3 98

One-Electron Reduction of Five- and Six-Coordinate {FeNO}^{7} Porphyrin Complexes: Exploring the Reactivity of Low-Spin {FeNO}^{8} Complexes and the *trans* Effect of NO$^-$ 98

Chapter 4 145

Investigations into the Active Species of P450nor: Towards High-Valent Iron Porphyrin Complexes with N-Based Ligands 145

4.1. Ferric Porphyrin O-Benzylhydroxylamide Complexes 146

4.2. Towards High-Valent Iron Porphyrin Nitride Complexes 153

a. Is Formation of a Fe(VI) Porphyrin Nitride Complex Energetically Feasible? A DFT Analysis 153

b. Photochemistry of Ferric Bis-Picket Fence Porphyrin Azide Complexes 157

Chapter 5 176

The *trans* Effect of Nitroxyl (HNO) in Ferrous Heme Systems: Implications for Soluble Guanylate Cyclase Activation by HNO 176

Chapter 6 204

Conclusions 204

List of Tables

Table 1.1. Crystal structures of cytochrome P450nor. 6

Table 1.2. Geometric and vibrational properties of ferric [Fe^{III}(Porphyrin)(L)(NO)] complexes (L = thiolate). 11

Table 1.3. Geometric and vibrational properties of $[Fe(P)(L)(NO)]^{-/2-}$ complexes and corresponding protonated intermediates (L = MI or MeS^{-}) from experiment in comparison to DFT results. 22

Table 2.1. Crystal data and structure refinement for [Fe(OETPP)(SPh_{F4})]. 40

Table 2.2. Fe(III)/Fe(II) reduction potential of [Fe(porph)(SR)] complexes vs. Fc/Fc^{+}, measured in CH_2Cl_2 with 0.1 M TBAP. The reduction wave is reported as the process is irreversible, see Figure 2.6. 45

Table 2.3. BP86/TZVP calculated geometric and vibrational parameters for [Fe(P)(SR)(NO)] complexes. 57

Table 2.4. BP86/TZVP calculated geometric and vibrational parameters of selected ferric heme-nitrosyl complexes with axial phenolate coordination. 68

Table 2.5. Geometric and vibrational parameters of selected $[Fe^{III}(P)(X)(NO)]^{0/1+}$ complexes. All data are experimental unless otherwise indicated. 71

Table 2.6. Charge contributions of important molecular orbitals of $[Fe^{III}(P)(AcF_3)(NO)]$ calculated with BP86/TZVP. 72

Table 2.7. BP86/TZVP calculated force constants and stretching frequencies of $[Fe^{III}(P)(X)(NO)]^{0/1+}$ complexes. 74

Table 2.8. Charge contributions of important molecular orbital of $[Fe^{III}(P)(X)(NO)]^{0/1+}$ calculated with BP86/TZVP. 75

Table 3.1. Crystallographic data for compound [Fe(3,5-Me-BAFP)(NO)] (**1-NO**). . 103

Table 3.2. Crystallographic parameters ([Å] and [^{o}]) of selected five-coordinate ferrous porphyrin nitrosyls. 103

Table 3.3. Fe-NO and N-O stretching frequencies of selected five- and six-coordinate $\{FeNO\}^7$ and $\{FeNO\}^8$ iron porphyrin nitrosyls. 106

Table 3.4. Half wave potentials (in V vs. Fc/Fc^+) for the first reduction of ferrous porphyrin nitrosyls. 109

Table 3.5. Equilibrium constants, K_{eq} [M^{-1}], and free reaction energies, ΔG (kcal/mol), for the reaction of [Fe(TPP*)(NO)] + MI $\rightleftarrows$ [Fe(TPP*)(MI)(NO). 118

Table 3.6. BP86/TZVP calculated geometric and vibrational parameters of five- and six-coordinate $\{FeNO\}^7$ and $\{FeNO\}^8$ heme complexes. 119

Table 3.7. Charge contributions of key σ bonding orbitals for $[Fe(P)(MI)(NO)]^{0/1-}$. Calculated with B3LTP/TZVP from BP86/TZVP optimized structures. 126

Table 4.1. Potentials [V vs. Fc/Fc^+] of various ferric bis-picket fence porphyrin complexes. Measured in THF with 0.1 M TBAP at 100 mV/sec. 152

Table 4.2. BP86/TZVP calculated geometric parameters of various Fe(II)-NHO and Fe(VI)-nitride porphyrin complexes. 155

Table 4.3. B3LYP/TZVP calculated free energies (ΔG) for reaction of five- (without $SR\text{-}H_1^-$) and six-coordinate $[Fe(P)(SR\text{-}H_1)(NHO)]^- + H^+ \rightarrow [Fe(P)(SR\text{-}H_1)(N)] + H_2O$ at 298.15 K in toluene. 156

Table 4.4. Asymmetric azide N-N stretch in five-coordinate $[Fe(porphyrin)(N_3)]$ and six-coordinate $[Fe(porphyrin)(MI)(N_3)]$ complexes measured in a KBr matrix. . 160

Table 5.1. Experimental and calculated geometric parameters of [Fe(P)(X)] and [Fe(P)(MI)(X)], where X = NO, HNO, CO, and MI. 181

Table 5.2. Reaction Energies (kcal/mol) for [Fe(P)(X)] +MI ⇄ [Fe(P)(X)(MI)] at 298.15K. 184

Table 5.3. Binding constants (M^{-1}) for [Fe(P)(X)] + MI ⇄ [Fe(P)(X)(MI)] at 298.15 K. K_{eq} is calculated using the listed method on BP86/TZVP geometries. 186

Table 5.4. Relative binding constants (M^{-1}) for [Fe(P)(X)] + MI ⇄ [Fe(P)(X)(MI)] at 298.15 K. K_{eq} values are taken from Table 5.3. 192

Table 5.5. Charge contributions of the key Fe-X σ-bonding orbitals for [Fe(P)(MI)(X)] calculated with B3LYP/TZVP. 195

List of Figures

Figure 1.1. Overlay of B', F, G, and I helices and the Cys ligand loop in cytochromes P450nor (blue) and P450cam (green). The B', F, and G helices are flipped up in cytochrome P450nor, resulting in a more open distal pocket than observed in P450cam. The image was generated using PyMOL from PDB code 1ROM (blue) and 1PHC (green). 7

Figure 1.2. Crystal structure of the NO complex of ferric cytochrome P450nor. The image was generated using PyMOL from PDB code 1CL6. 10

Figure 1.3. Structure of the ferric NO complex of the cytochrome P450nor active site. The image was generated using PyMOL from PDB code 1CL6. 13

Figure 1.4. Ferric heme-thiolate NO complexes as models of P450nor. (a) Crystal structure of [Fe(OEP)(SR-H_2)(NO)] (SR-H_2 = S-2,6-$(CF_3CONH)_2C_6H_3$), the only structurally characterized ferric heme-nitrosyl with thiolate coordination; (b) schematic representation of a ferric porphyrin benzylthiolate model complex with bound NO, [Fe^{III}(SPorph)(NO)]. 15

Figure 2.1. EPR spectra of [Fe(TPP)(SPh_{F4})(THF)] (top, red) and [Fe(T*o*-F_2PP)(SPh_{F4})] (bottom, black) measured at 10 K. 36

Figure 2.2. EPR spectrum of [Fe(OETPP)(SPh_{F4})] (black) in toluene, recorded at 10 K, and simulation (red) generated using the program Spin Count. Fit parameters are g_x = 1.95, g_y = 2.02, g_z = 2.02, D > 10 cm^{-1}, E/D = 0.0234, E/D-strain = -0.12. 38

Figure 2.3. Molecular structure of [Fe(OETPP)(SPh_{F4})] in two different orientations. Hydrogen atoms and solvent molecule (hexane) are omitted for clarity. Thermal ellipsoids are shown at 30% probability. Crystal data and structure refinement are shown in Table 2.1. 39

Figure 2.4. UV-Vis spectral changes for the reaction of [Fe(TPP)(SPh_{F4})] with ~1 equivalent nitric oxide at -40 °C in toluene. The desired six-coordinate ferric complex [Fe(TPP)(SPh_{F4})(NO)] is formed intermediately (left) before decomposition to ferrous [Fe(TPP)(NO)] (right). 42

Figure 2.5. UV-Vis spectral changes for the reaction of [Fe(OEP)(SPh_{F4})] with ~1 equivalent nitric oxide at -40 °C in toluene, forming the desired six-coordinate ferric complex [Fe(OEP)(SPh_{F4})(NO)]. 43

Figure 2.6. Cyclic voltammogram of [Fe(OEP)(SPh_{F4})] in toluene at room temperature recorded at various scan rates. 46

Figure 2.7. UV-Vis spectral changes for the reaction of [Fe(T*o*-$(Am)_2$PP)(SPh_{F4})] with ~1 equivalent of nitric oxide at -40 °C in toluene, forming the five-coordinate ferrous decomposition product [Fe(T*o*-$(Am)_2$PP)(NO)]. 47

Figure 2.8. EPR spectrum of [Fe(OETPP)(NO)] (black) obtained from the reaction of [Fe(OETPP)(SPh_{F4})] with NO at -40^{o}C. The three-line hyperfine pattern on all g-values originates from the nuclear spin of the ^{14}N-atom (I = 1) of NO. The simulated spectrum was generated using the program SpinCount. Fit parameters are g_x = 2.064, g_y = 2.041, g_z = 2.005, A_x = 49 MHz, A_y = 46 MHz, A_z = 47 MHz, sg_x (g-strain) = 0.0035, sg_y = 0.0031, and sg_z = 0.0001. 48

Figure 2.9. Molecular structure of a 77:23 co-crystal of [Fe(OETPP)(NO)] and [Fe(OETPP)(Cl)] obtained from the reductive nitrosylation of [Fe(OETPP)(Cl)] in

CH_2Cl_2 and 10% MeOH. Hydrogen atoms and solvent are omitted for clarity. Thermal ellipsoids shown at 30% probability. 49

Figure 2.10. UV-Vis spectral changes for the reaction of [Fe(OEP)(SR-H_2)] with ~1 equivalent of nitric oxide at -40 °C in toluene, forming the stable six-coordinate ferric complex [Fe(OEP)(SR-H_2)(NO)]. 52

Figure 2.11. BP86/TZVP calculated N-O and Fe-NO stretching frequencies of various [Fe(P)(SR-H_2)(NO)] complexes with different thiophenolate type ligands in closed-shell ferric heme-nitrosyls. SR_{pX}-H_2 denotes variation in the 4-position of SR-H_2 whereas SR_{oX}-H_2 indicates a substitution of the -CF_3 groups on the amide substituents of SR-H_2 for X (see Figure 2.12). 58

Figure 2.12. BP86/TZVP optimized structure of [Fe(P)(SR-H_2)(NO)]. Here, *p* and *o* denote a systematic variation of the 4-position and the -CF_3 groups in SR-H_2, respectively. 59

Figure 2.13. EPR spectra of [Fe(TPP)(X)] where X = OPh, OPh_{F4}, and OR-H_2 in toluene recorded at 10 K. Simulation of the spectrum of [Fe(TPP)(OR-H_2)] (bottom) generated using Spin Count with the following parameters: $g_x = g_y = g_z$ = 2.02; D > 5 cm^{-1}; E/D = 0.033; E/D-strain = -0.21. 62

Figure 2.14. UV-visible spectra for the reaction of [Fe(TPP)(OPh)] (left) and [Fe(TPP)(OPh_{F4})] (right) with NO at -40^{o}C in toluene. The resulting UV-visible spectra (blue) correspond to the formation of [Fe(TPP)(NO_2)(NO)]. 63

Figure 2.15. UV-visible spectra for the reaction of [Fe(TPP)(OR-H_2)] (red) with NO at -40^{o}C in toluene. The resulting UV-visible spectrum (blue) corresponds to the formation of [Fe(TPP)(NO)]. 65

Figure 2.16. DFT optimized structures of (a) [Fe(P)(OPh)(NO)], (b) [Fe(P)(OR-H_1)(NO)], and (c) [Fe(P)(OR-H_2)(NO)] calclulated with BP86/TZVP. Bond lengths and angles are provided in Table 2.4. 67

Figure 2.17. Molecular structure of [Fe(TPP)(AcF_3)(NO)] with thermal ellipsoids drawn at 35%. Hydrogen atoms have been omitted for clarity. The compound was prepared by Nan Xu and the structure was solved by Douglas R. Powell from the University of Oklahoma. 70

Figure 2.18. Important molecular orbitals of [Fe^{III}(P)(AcF_3)(NO)] calculated with BP86/TZVP. (a) and (b) correspond to the strong π backbonding interactions, (c) to the weak sigma interaction, and (d) to the anitbonding σ*_d_{z2} type interaction involved in the bending of the Fe-N-O unit. 72

Figure 2.19. Optimized geometric parameters of [Fe(P)(X)(NO)]$^{0/1+}$ calculated with BP86/TZVP. 74

Figure 2.20. ^{1}H NMR spectrum of 4-methyl-2,6-dinitro-1-S-trityl-benzene (**11**) in DMSO-d_6. 88

Figure 2.21. ^{1}H NMR spectrum of 4-methyl-2,6-dinitro-thiophenol (**12**) in $CDCl_3$. .. 88

Figure 2.22. ^{1}H NMR spectrum of bis(2,6-dinitro-4-methylphenyl) disulfide (**13**) in $CDCl_3$. 90

Figure 2.23. ^{1}H NMR spectrum of bis(2,6-di(trifluoracetylamino)-4-methylphenyl) disulfide (**15**) in DMSO-d_6. 90

Figure 3.1. Crystal structure of [Fe(3,5-Me-BAFP)(NO)] (**1-NO**), hydrogen atoms are omitted for clarity. Selected bond lengths and angles are summarized in Table 3.2. Thermal ellipsoids are shown at 30% probability. 102

Figure 3.2. EPR spectrum of [Fe(3,5-Me-BAFP)(NO)] (**1-NO**) recorded at 77 K in frozen toluene. The spectrum shows typical g-values indicative of ferrous heme-nitrosyls with S = 1/2 ground state. The three-line hyperfine pattern on the smallest g-value, g_z, originates from the nuclear spin of the ^{14}N-atom (I = 1) of NO. The hyperfine coupling constant, A_z, is 50 MHz in toluene. 104

Figure 3.3. Vibrational density of states (VDOS) for [^{57}Fe(3,5-Me-BAFP)(NO)] (**1-NO**, red) and [^{57}Fe(3,5-Me-BAFP)(^{15}N^{18}O)] (**1-^{15}N^{18}O**, black) calculated from raw nuclear resonance vibrational spectroscopy (NRVS) data. 105

Figure 3.4. EPR spectrum of [Fe(T*o*-F_2PP)(NO)] (**2-NO**) recorded at 77 K in frozen toluene. The three-line hyperfine pattern on all g-values originates from the nuclear spin of the ^{14}N-atom (I = 1) of NO. The simulated spectrum was generated using the program SpinCount. Fit parameters are g_x = 2.109, g_y = 2.0375, g_z = 2.003, A_x = 39 MHz, A_y = 46 MHz, A_z = 47 MHz, sg_x (g-strain) = 0.0025, sg_y = 0.0035, and sg_z = 0.002. 107

Figure 3.5. EPR spectra of [Fe(T*per*-F_5PP)(NO)] (**3-NO**) and [Fe(T*o*-$(NO_2)_2$-*p*-*t*BuP)(NO)] (**4-NO**) recorded at 77K in frozen toluene. The spectra show typical g-values indicative of ferrous heme-nitrosyls with S=1/2 ground state. The hyperfine coupling constant, A_z, for **3-NO** and **4-NO** is 47 MHz. 108

Figure 3.6. Cyclic voltammograms for [Fe(3,5-Me-BAFP)(NO)] (**1-NO**) in THF at various scan rates. 108

Figure 3.7. Infrared spectra from the spectroelectrochemical reduction of [Fe(3,5-Me-BAFP)(NO)] (top, **1-NO**) and [Fe(3,5-Me-BAFP)(^{15}N^{18}O)] (middle, **1-^{15}N^{18}O**) in 1,2-DCE-d_4. The asterisk (*) indicates poor subtraction of a porphyrin band at 1450 cm^{-1}. The estimated isotope shift (by DFT) of the N-O stretch in the NO^- complex is 61

cm^{-1}, indicating that the 1450 cm^{-1} feature in the reduced compound is too high in energy to be the $\nu(^{15}N\text{-}^{18}O)$ stretch. 110

Figure 3.8. UV-visible absorption spectra from the spectroelectrochemical reduction of [Fe(3,5-Me-BAFP)(NO)] (**1-NO**, red to green), obtained by sweeping from -0.4 V to -1.8 V vs. Ag wire at a rate of 10 mV/s in a 0.1 M TBAP solution in dry (top) 1,2-DCE and (bottom) THF. The reaction is completely reversible upon sweeping from -1.8 V to -0.4 V vs. Ag wire (inset). 112

Figure 3.9. Reversible electrochemical reduction of [Fe(3,5-Me-BAFP)] to [Fe(3,5-Me-BAFP)]$^-$ in an OTTLE UV-vis cell, taken in 0.1 M TBAP solution in dry THF. The working electrode is Pt mesh. 113

Figure 3.10. UV-visible absorption spectra from the spectroelectrochemical reduction of [Fe(T*o*-F_2PP)(NO)] (red to green), obtained by sweeping from 0 V to -1 V at a rate of 10 mV/s in a 0.1 M TBAP solution in dry 1,2-DCE. The reaction is completely reversible upon sweeping from -1 V to 0 V. Asterisk indicates a small amount of [Fe(T*o*-F_2PP)] impurity that reduces at ~ 200 mV vs. Ag wire. 114

Figure 3.11. Infrared spectra from the spectroelectrochemical reduction of [Fe(T*o*-F_2PP)(NO)] (top, **2-NO**) and [Fe(T*o*-F_2PP)($^{15}N^{18}O$)] (bottom, **2-^{15}N^{18}O**) in 1,2-DCE-d_4. Difference spectra are provided in Figure 3.14. 115

Figure 3.12. Comparison of N-O stretching frequencies in $\{FeNO\}^7$ and $\{FeNO\}^8$ porphyrin complexes. 115

Figure 3.13. Solution IR spectra of [Fe(3,5-Me-BAFP)(NO)] (red, top) and [Fe(3,5-Me-BAFP)(NO)] with the addition of 15 µL MI (green, bottom). Incomplete conversion is observed from the five-coordinate species to the six-coordinate

complex [Fe(3,5-Me-BAFP)(MI)(NO)] which has a N-O stretching frequency of 1630 cm^{-1}. 116

Figure 3.14. NO – $^{15}N^{18}O$ IR difference spectra from the spectroelectrochemical reduction of [Fe(T*o*-F_2PP)(NO)] in the absence (A: {FeNO} in , C: $\{FeNO\}^8$) and presence (B: $\{FeNO\}^7$, D: $\{FeNO\}^8$) of MI. 119

Figure 3.15. The model system $[Fe(P)(MI)(NO)]^{-}$, where P = $porphine^{2-}$ and MI = 1=methylimidazole, and applied coordinate system. The structure shown is calculated using BP86/TZVP. 120

Figure 3.16. Key $\pi^*_h\_d_{z2}/d_{xz}$ molecular orbitals of (left) [Fe(P)(MI)(NO)] and (right) $[Fe(P)(MI)(NO)]^{-}$ which defines the thermodynamic σ-*trans* effect in ferrous porphyrin systems. Calculated with B3LYP/TZVP on BP86/TZVP optimized structures. 126

Figure 3.17. UV-vis spectra from the one-electron reduction of [Fe(T*o*-F_2PP)] (**2**, blue) to $[Fe(T\textit{o}\text{-}F_2PP)]^-$ (**2**$^-$, purple), shown left, and subsequent reaction with 10 µL NO (g) (right, orange) in THF at room temperature. 129

Figure 3.18. UV-visible spectra for the reaction of $[Fe(T\textit{o}\text{-}F_2PP)]^-$ (**2**$^-$, purple) with NO to generate $[Fe(T\textit{o}\text{-}F_2PP)(NO)]^-$ (**2-NO**$^-$, green) in THF at room temperature. 130

Figure 3.19. UV-visible spectra for the reaction of $[Fe(T\textit{o}\text{-}F_2PP)(NO)]^-$ (**2-NO**$^-$, green) with 5 equivalents of acetic acid in THF at room temperature. The resulting spectrum (red) is in agreement with formation of [Fe(T*o*-F_2PP)(NO)] (**2-NO**). 131

Figure 3.20. UV-vis spectra from the one-electron reduction of [Fe(3,5-Me-BAFP)] (**1**, blue) to $[Fe(3,5\text{-}Me\text{-}BAFP)]^-$ (**2**$^-$, red), shown at left, and subsequent reaction

with 100 µL NO (g) in THF at room temperature resulting in formation of [Fe(3,5-Me-BAFP)(NO)]⁻ (right, green). 132

Figure 3.21. UV-visible spectra for the reaction of [Fe(3,5-Me-BAFP)(NO)]⁻ (**1-NO**⁻, green) with 5 equivalents of acetic acid in THF at room temperature. The resulting spectrum is shown in purple. 133

Figure 3.22. ^{1}H NMR of 3,5-methyl-Bis(Aryloxy)-FencePorphyrin, H_2[3,5-Me-BAFP] in $CDCl_3$. 136

Figure 4.1. UV-visible spectra of [Fe(3,5-Me-BAFP)(ClO_4)] (black) and of the product of the reaction of this complex with excess NH_2OBn (blue) in toluene at room temperature. 148

Figure 4.2. EPR spectra of [Fe(3,5-Me-BAFP)(ClO_4)] (black) and of the product of the reaction of this complex with excess NH_2OBn (blue) in toluene. Spectra measure at 10 K. 149

Figure 4.3. Crystal structure of [Fe(3,5-Me-BAFP)(NH_3)$_2$]. Hydrogen atoms and a solvent molecule (toluene) are omitted for clarity. Thermal ellipsoids are shown at 30%. The structure was obtained by Ashley McQuarters. 150

Figure 4.4. UV-visible spectra of [Fe(3,5-Me-BAFP)(ClO_4)] (black) and of the product of the reaction of this complex with excess K[NHOBn] (red) in toluene at room temperature. 151

Figure 4.5. EPR spectra of [Fe(3,5-Me-BAFP)(ClO_4)] (black) and of the product of the reaction of this complex with excess K[NHOBn] (red) in toluene. Measure at 77 K. 151

Figure 4.6. Cyclic volatmmogram of a solution of [Fe(3,5-Me-BAFP)(ClO_4)] and K[NHOBn]. Measured at 100 mV/sec in THF with 0.1 M TBAP. 153

Figure 4.7. BP86/TZVP optimized structures of $[Fe(P)(SR\text{-}H_1)(NHO)]^-$ (S = 0) and $[Fe(P)(SR\text{-}H_1)(N)]$ (S = 0) used to calculate ΔG for the reaction above. 154

Figure 4.8. UV-visible spectra of [Fe(3,5-Me-BAFP)(Cl)] and $[Fe(3,5\text{-}Me\text{-}BAFP)(N_3)]$ in CH_2Cl_2. 158

Figure 4.9. Preliminary crystal structure of $[Fe(3,5\text{-}ME\text{-}BAFP)(N_3)]$. Thermal ellipsoids are shown at 30% probability and hydrogen atoms are omitted for clarity. 159

Figure 4.10. IR spectra (KBr pellets) of $[Fe(3,5\text{-}Me\text{-}BAFP)(N_3)]$ before (blue) and after (red) UV irradiation for 25 minutes. 162

Figure 4.11. UV-visible spectral changes after UV irradiation of $[Fe(3,5\text{-}Me\text{-}BAFP)(N_3)]$ in 2-MeTHF for 3.5 minutes at room temperature. 162

Figure 4.12. EPR spectra of 2 mM $[Fe(Im\text{-}BAFP)(N_3)]$ (blue), indicative of a high-spin ferric complex (S = 5/2), and of the EPR silent photolysis product (red) after 25 minutes of UV irradiation in 2-MeTHF at room temperature. EPR spectra were recorded at 10 K. 163

Figure 4.13. UV-visible spectrum of [Fe(3,5-Me-BAFP)] in 2-MeTHF prepared through the reduction of $[Fe(3,5\text{-}Me\text{-}BAFP)(ClO_4)]$ with 1 equivalent of KC_8. .. 163

Figure 4.14. UV-visible spectra of $[Fe(Im\text{-}BAFP)(N_3)]$ (blue) and of the photolysis product (red) after 1.5 minutes of UV irradiation in 2-MeTHF at room temperature. 165

Figure 4.15. EPR spectra of 2 mM $[Fe(Im\text{-}BAFP)(N_3)]$ (blue), indicative of a low-spin ferric complex (S = 1/2), and of the EPR silent photolysis product (red) after 25 minutes of UV irradiation in 2-MeTHF at room temperature. EPR spectra were recorded at 77 K. 165

Figure 4.16. ^{1}H NMR spectrum of NO_2-BAFP in $CDCl_3$. Top portion of spectrum is intensified x 3. 169

Figure 4.17. ^{1}H NMR spectrum of Im-BAFP in $CDCl_3$. Top portion of spectrum is intensified x 3. 171

Figure 5.1. The model system [Fe(P)(MI)(X)], where P = porphine2-, MI = 1=methylimidazole, and X = NHO, and applied coordinate system. The structure shown is calculated with BP86/TZVP. 180

Figure 5.2. Experimental and DFT free energies (kcal/mol) for the reaction: [Fe(P)(X)] + MI ⇄ [Fe(P)(MI)(X)] where X = NO and MI at 298.15 K. All calculations were performed on BP86/TZVP structures. 188

Figure 5.3. Relevant molecular orbitals of (a) [Fe^{II}(P)(NO)(MI)], (b) [Fe^{II}(P)(NHO)(MI)], and (c) [Fe^{II}(P)(CO)(MI)] which define the thermodynamic σ-*trans* effect in these ferrous porphyrin systems. Calculated with B3LYP/TZVP on the BP86/TZVP optimized structures. 194

List of Schemes

Scheme 1.1. Proposed reaction cycle for the reduction of two molecules of NO to N_2O by cytochrome P450nor. 14

Scheme 1.2. Calculated mechanism of P450nor. Free energies, ΔG, are given relative to complex **3a** (set to 0.0 kcal/mol). 21

Scheme 2.1. Porphyrin and thiolate ligands. 37

Scheme 2.2. Saddling versus ruffling distortions in heme systems. (Reprinted with permission from reference 69. Copyright 1998 American Chemical Society). ... 41

Scheme 2.3. Proposed reaction mechanisms of [Fe(porph)(SR)] complexes with NO. 44

Scheme 2.4. Original synthesis of the hydrogen-bond stabilized thiolate ligand, SR-H_2^-. 55

Scheme 2.5. Alternate synthesis of the hydrogen-bond stabilized thiolate ligand, SR-H_2^-. 55

Scheme 3.1. Molecular orbitals proposed to be involved in the σ-*trans* effect of NO in six-coordinate ferrous heme-nitrosyls complexes. 122

Scheme 3.2. Electronic structures of low-spin $\{FeNO\}^7$ and $\{FeNO\}^8$ complexes. 127

Scheme 4.1. Two possible mechanistic pathways for N_2O production by P450nor. 145

Scheme 4.2. Target complex, [Fe(3,5-Me-BAFP)(NHOBn)], for modeling the proposed Fe(IV)-NHOH intermediate in the catalytic cycle of P450nor. 147

Scheme 4.3. [Fe(3,5-Me-BAFP)(N_3)] (left) and [Fe(Im-BAFP)(N_3)] (right). 158

Scheme 5.1. The key Fe-NO σ-bonding orbital of six-coordinate ferrous heme-nitrosyls. 178

Scheme 5.2. Possible route for sGC activation by HNO through deprotonation strong hydrogen bonding to HNO. 196

Abstract

It came as quite a surprise when it was discovered in the 1980s that the toxic molecule nitric oxide (NO) is a signaling molecule in mammals responsible for nerve signal transduction, blood pressure control, and immune response. Unfortunately, overproduction of NO in the blood stream due to a bacterial infection can lead to septic shock and organ degradation, both of which can be fatal. Thus, the need to develop a method by which to detoxify NO from biological systems is of critical importance. Cytochrome P450nor, a NO reductase, represents one way to achieve this detoxification. The active site of this fungal cytochrome P450-type enzyme contains a ferric heme with proximal cysteinate ligation. P450nor plays a vital role in the fungal denitrification by catalyzing the reduction of NO to N_2O through a two electron reduction of the initially formed ferric heme-nitrosyl by NADH. In order to fully elucidate the mechanism of this enzyme, stable model complexes are necessary. In this dissertation, small molecule synthetic models of intermediates in the catalytic cycle of P450nor have been prepared. First, a series of ferric heme-nitrosyl complexes with thiolate coordination have been synthesized employing substituted porphyrins and a series of thiolate ligands. This has allowed us to determine the key characteristics required to form these highly unstable ferric nitrosyls. In conjunction with density functional theory (DFT) calculations, we have now been able to gain detailed insight into the electronic structures and spectroscopic properties of these species as a function of the axial ligand donor strength. The second intermediate in the catalytic cycle of P450nor, a ferrous heme-

nitroxyl complex, has been prepared and its fundamental properties and reactivity explored. Then, using a bis-picket fence porphyrin we work towards synthesis of high-valent iron complexes with N-based ligands as models for the key intermediate in the catalytic cycle of P450nor responsible for the critical N-N bond formation in the reduction of NO to N_2O. Finally, the *trans* effect of HNO in ferrous heme complexes and the implications for soluble guanylate cyclase activity has been investigated using DFT calculations.

Chapter 1

Introduction

For decades, the free radical nitric oxide (NO) was viewed exclusively as a toxin and environmental pollutant. As a byproduct of fossil fuel combustion in air, NO and its homologue nitrogen dioxide (NO_2) are key contributors smog. Interestingly, NO is also naturally produced by lightning during electrical storms. Since the gaseous diatomic is poisonous to humans in concentrations as low as ~100 ppm in air (μM in blood), it came as quite a surprise when it was discovered in the 1980s that NO is a signaling molecule in biological systems at low (sub-nanomolar) concentrations. NO is produced in mammals for the purpose of blood pressure control, nerve signal transduction, and (less surprisingly) immune defense.[1-4] This remarkable contradiction resulted in NO being named "Molecule of the Year" in 1992 by Science Magazine.[5] Six years later, Furchgott, Ignarro, and Murad received the 1998 Nobel Prize in Medicine for the discovery of NO as a signaling molecule in the cardiovascular system.[6-8]

1.1. Nitric Oxide Biosynthesis and Sensing

The biosynthesis of NO in mammals is performed by the nitric oxide synthase (NOS) family, a class of enzymes similar in active site structure to cytochrome P450 proteins. All NOS isozymes catalyze the generation of NO through the oxidation of L-arginine to L-citrulline by O_2 at the heme thiolate active site.[9-13] There are three

classes of NOS proteins found throughout the human body. The first type, inducible NOS (*i*-NOS) is located in macrophages and is involved in immune defense against various pathogens.[14-16] Unfortunately, overproduction of NO by *i*-NOS, as in the case of a severe bacterial infection, results in nitrosative stress. Nitrosative stress, like oxidative stress, can be detrimental to health resulting in septic shock, organ degradation, and initiation of cancer. Endothelial NOS (*e*-NOS) and neuronal NOS (*n*-NOS) are involved in signaling in the endothelial cells lining the arteries and in neuronal cells, respectively, for blood pressure control and nerve signal transduction.[17]

The produced NO diffuses from the endothelium (in the case of *e*-NOS) to smooth muscle tissue, and is detected by the ferrous heme enzyme soluble guanylate cyclase (sGC) which catalyzes the conversion of guanosine triphosphate (GTP) to the secondary messenger molecule cyclic guanosine monophosphate (cGMP).[18] Through the strong thermodynamic σ-*trans* effect (also called *trans* "interaction") of NO, binding of nitric oxide at the distal side of the ferrous heme center with proximal hisitdine ligation induces cleavage of the Fe-N_{His} bond, forming a five-coordinate ferrous nitrosyl complex in the NO sensing domain of the protein.[19-21] This induces a conformation change in the enzyme which activates the catalytic domain of the enzyme for production of cGMP. Once produced, cGMP activates a cascade of biological events inculding vasodilation, prevention of blood coagulation, and inhibition of smooth muscle contraction.

1.2. Detoxification of NO in Biological Systems

Due to the fact that NO is toxic at high (micromolar) concentrations, it is crucial that mechanisms are in place to detoxify NO in biological systems. In

mammals, the elimination of NO is accomplished predominantly through the oxidation of NO to nitrate, NO_3^-, by oxyhemoglobin (and to a small extent oxymyoglobin).[22-24] However, this oxidation is easily overwhelmed leading to undesired side effects including septic shock and organ degradation as a result of excess NO accumulation. For this reason, there is a great need to explore the catalytic degradation of noxious NO to less harmful compounds. Interestingly, both bacteria and fungi reduce NO to nitrous oxide (N_2O) as a part of the denitrification process where NO_3^- is reduced in a stepwise fashion to either N_2 (bacteria) or N_2O (fungi), as shown below.[25]

$$NO_3^- \rightarrow NO_2^- \rightarrow NO \rightarrow N_2O \rightarrow N_2$$

While denitrification is a means of anaerobic respiration in fungi and bacteria, the reduction of NO, interestingly, does not contribute to the proton gradient and instead serves to eliminate toxic NO from the system. Here, NO is catalytically reduced to N_2O by a class of enzymes called nitric oxide reductases (NOR), which catalyze the following reaction:

$$2\ NO + 2\ e^- + 2\ H^+ \rightarrow N_2O + H_2O$$

There are two main types of bacterial NORs—FNOR, a flavodiiron protein, and NorBC, a dinuclear heme/non-heme enzyme.[26] In contrast to the bi-metallic active sites found in bacterial NORs, fungal NOR (P450nor), a cytochrome P450-type enzyme, contains a single heme thiolate active site.[27-28] Fungal P450nor is discussed in great detail in Section 1.3,[29] and modeling intermediates of NO reduction by this enzyme is the focus of this thesis.

1.3. Fungal NO Reductase (P450nor)

Fungal NOR is a member of the cytochrome P450 superfamily and is therefore designated as P450nor.[28] A unique P450, fungal NOR is incapable of performing monooxygenation chemistry and instead facilitates the reduction of nitric oxide (NO) to nitrous oxide (N_2O).[27, 30] Interestingly, P450nor is one of the few reductases in the P450 family.[31-32] Found in soil dwelling fungi and yeasts, this enzyme operates from a single heme *b* center with bound proximal cysteinate,[33-35] unlike bacterial NOR counterparts which utilize a dinuclear heme/non-heme active site.[26] In contrast to bacterial denitrification, which reduces nitrate (NO_3^-) to dinitrogen (N_2) in four steps, fungal denitrification evolves nitrous oxide (N_2O) as the final product.[36-37] Further, the final step of denitrification in fungi, reduction of NO to N_2O, is not wholly associated with the respiratory chain.[35, 38-40] Instead, this step is believed to prevent the build-up of toxic NO in the denitrifying organisms (as discussed above).[41]

P450nor is incredibly proficient at reducing NO with a maximum turnover rate (against NO) estimated to be as high as 30,000 min^{-1},[34] much higher than those measured for respiratory bacterial NO reductases.[42] Nitric oxide is reduced to N_2O by P450nor following the equation:[34]

$$2\ NO + NAD(P)H + H^+ \rightarrow N_2O + NAD(P)^+ + H_2O$$

As the equation above indicates, the NO reduction occurs without the aid of a separate electron transfer protein (i.e., flavoprotein, iron-sulfur protein).[37] Instead, the reaction proceeds through a direct two electron reduction of the initially formed ferric heme-nitrosyl by direct hydride transfer from NAD(P)H.[43]

Protein Sequences and Gene Structure of Fungal NOR

P450nor has been isolated and purified from several fungi including *Fusarium oxysporum*,[35, 44] *Cylindrocarpon tonkinense*,[45-46] and *Trichosporon cutaneum*.[47-48] However, genome analysis shows the presence of P450nor enzymes in many fungi.[49-50] Isozymes of P450nor show 65-83% sequence identity with each other and an average of 25% (up to 40%) sequence identity with the cytochrome P450 monooxygenases.[28] Interestingly, all known genes of the fungal NOR family exhibit higher sequence homologies with bacterial than eukaryotic P450s, suggesting that lateral gene transfer from bacteria to fungi occurred very early during evolution.[51]

P450nor enzymes can be found in either the mitochondria, $P450nor_A$, or cytosol, $P450nor_B$, of the cell.[52] The mitochondrial form, $P450nor_A$, contains 26 additional amino acids at the N-terminus not found in $P450nor_B$. In P450nor from *F. oxysporum*, the two forms are both encoded by a single gene, *CYP 55*. Examination of the amino acid sequence of this gene revealed the presence of two separate initiation codons for translation.[48, 52-53] Of the two resulting genetic codes, one ($P450nor_A$) contains an extension sequence at the N-terminus characteristic of a targeting sequence for transportation to the mitochondria. Likewise, the N-terminus in $P450nor_B$ contains an acetylated alanine which indicates post- or co-translational elimination of a methionine residue.[53] Cytosolic and mitochondrial forms of P450nor were also isolated from *C. tonkinense*, but in this case, two separate genes (*CPY 55A2* and *CYP 55A3*) were found to code for the two differing forms.[46] Interestingly, $P450nor_B$ shows increased selectivity for NADPH over NADH, suggesting P450nor could act as an electron sink to allow $NADP^+$ formation as a substrate for the pentose-phosphate cycle.[54]

Table 1.1. Crystal structures of cytochrome P450nor.

Molecule	Organism	PDB Code	Resolution (Å)	Ref.
P450nor(III)	*Fusarium oxysporum*	1ROM	2.0	[33]
		1EHE	1.7	[55]
		1JFB	1.00	[56]
S286V P450nor(III)	*Fusarium oxysporum*	1EHG	1.7	[33]
S286T P450nor(III)	*Fusarium oxysporum*	1EHF	1.7	[33]
S73/75G P450nor(III)	*Fusarium oxysporum*	1ULW	2.0	[57]
P450nor(III)-NO	*Fusarium oxysporum*	1CL6	1.7	[58]
S286V P450nor(III)-NO	*Fusarium oxysporum*	1CMN	1.7	[58]
S286T P450nor(III)-NO	*Fusarium oxysporum*	1CMJ	1.7	[58]
T243A P450nor(III)-NO	*Fusarium oxysporum*	1F24	1.4	[59]
T243N P450nor(III)-NO	*Fusarium oxysporum*	1F25	1.4	[59]
T243V P450nor(III)-NO	*Fusarium oxysporum*	1F26	1.4	[59]
P450nor(III)-CN(*n*-C_4H_9)	*Fusarium oxysporum*	1GEJ	1.5	[60]
S73/75G P450nor(III)-NAD* [a]	*Fusarium oxysporum*	1XQD	1.8	[57]
P450nor(III)-Br^-	*Fusarium oxysporum*	1GED	2.0	[61]
P450nor(II)-CO	*Fusarium oxysporum*	2ROM	2.0	[33]
		1JFC	1.05	[56]
P450nor(II)-CN(*n*-C_4H_9)	*Fusarium oxysporum*	1GEI	1.6	[60]
P450cam(III)	*Pseudomanas putida*	1PHC	1.6	[62]
P450cam(III)-CN(*n*-C_4H_9)	*Pseudomanas putida*	1GEM	2.0	[60]
P450cam(II)-CN(*n*-C_4H_9)	*Pseudomanas putida*	1GEK	1.7	[60]

[a] NAD* = 3-pyridinealdehyde adenine dinucleotide

Structure of P450nor

Several crystal structures of fungal NOR from *Fusarium oxysporum* have been determined cf. Table 1.1).[33, 56, 58-61] This protein, $P450nor_A$, is comprised of 403 amino acids with a molecular weight of 46 kDa.[33] Interestingly, the overall fold and protein topography for P450nor is extremely similar to that of cytochrome P450 monoxygenases (including P450cam). As seen in Figure 1.1 (P450nor/cam overlay), the main differences lie in the position of the F,G, and B' helices. In comparison to P450cam, the F and G helices are 'flipped up' in P450nor resulting in a larger cavity at the distal heme pocket. The upswing of the F and G helix is a result of repulsion between hydrophilic regions on both the I and G helix, leading to the G helix being positioned farther away from the heme site.[33]

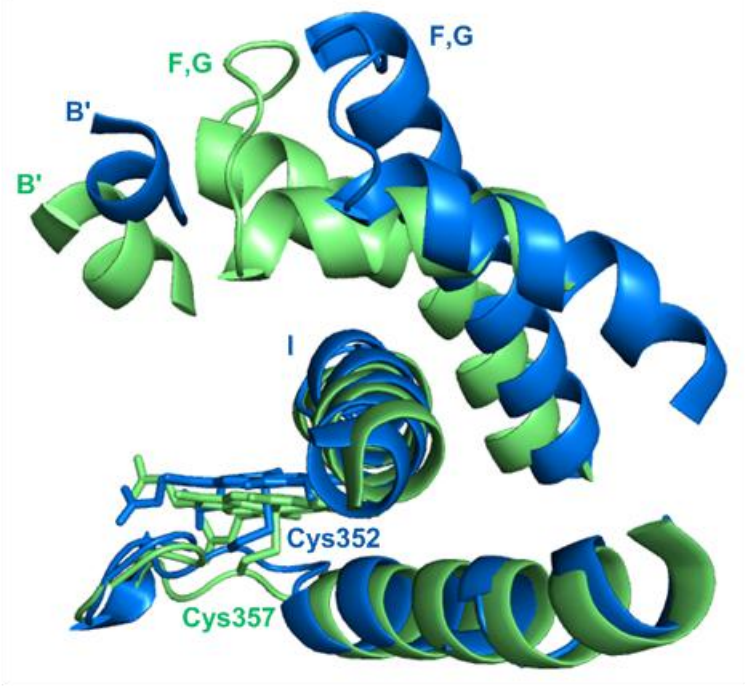

Figure 1.1. Overlay of B', F, G, and I helices and the Cys ligand loop in cytochromes P450nor (blue) and P450cam (green). The B', F, and G helices are flipped up in cytochrome P450nor, resulting in a more open distal pocket than observed in P450cam. The image was generated using PyMOL from PDB code 1ROM (blue) and 1PHC (green). (Adapted from reference [33].)

The B' helix, proposed to act as a substrate access and binding channel in cytochrome P450 monooxygenases,[63-65] has also shifted substantially in P450nor compared to the structure of P450cam. Unlike P450cam, P450nor does not require the binding of an organic substrate during the course of its catalytic cycle, but does require direct interaction of the heme with NAD(P)H. Consequently, the B' helix has been proposed to be the site of NAD(P)H binding.[61, 66] While no direct evidence for this hypothesis has been provided, crystal structures of P450nor show a cluster of positively charged amino acids (Lys62, Arg64, Lys291, and Arg392) at the bottom (distal side) of the B' helix.[55, 61] These positively charged groups could potentially interact with the negatively charged NAD(P)H molecule through ionic interactions, binding NAD(P)H to the distal side of helix B', and enabling the delivery of the two

electrons required for NO reduction directly from the distal site to the heme. As expected, site directed mutagenesis of this region indicates that NAD(P)H binding depends directly on the steric bulk and charge distribution of the B' helix.[66] Although lack of a NAD(P)H-bound crystal structure makes it very difficult to definitively determine the role of the B' helix, a crystal structure has been solved with bound bromide ions.[61] This structure shows Br^- bound to the proposed NAD(P)H binding site, providing evidence that the negatively charged NAD(P)H molecule could in fact interact directly with the B' helix.

Additionally, the B' helix has been shown to provide cofactor specificity between NADH and NADPH.[66] *F. oxysporum* utilizes only NADH,[34] whereas *T. cutaneum* and *C. tonkinense* P450nor can employ either NADH or NADPH as electron donors.[45-46, 48] To date, there are no P450nor enzymes that reduce NO only in the presence of NADPH. Examination of the B' helix shows that the amino acid residues at the distal side of the helix provide more steric bulk in P450nor from *F. oxysporum* than the corresponding residues in *T. cutaneum* or *C. tonkinense*.[66] Further studies have shown that NADPH is able to bind to the B' helix of P450nor from *F. oxysporum*, but electron transfer is blocked by Ser75, resulting in a lack of N_2O formation.[66] As expected, mutation of Ser75 to the smaller Gly residue significantly improves the overall NADPH dependent activity of P450nor from *F. oxysporum*. Therefore, the B' helix also seems crucial for determining NAD(P)H specificity.

Equally important as the electron transfer for the reduction of NO by P450nor is the proton delivery pathway. Crystal structures of P450nor at cryogenic temperatures have located the precise position of water molecules in the protein structure.[58-59] One of these water molecules adjacent to the iron, Wat99, forms a

hydrogen bonding network with Ser286, Thr243, and Asp393, which has been proposed to be essential for proton delivery. Mutation of Ser286 to Val or Thr has been shown to disrupt the hydrogen bonding network and, thus, no reduction of NO occurs.[58] This mutation does not, however, decrease the rate constant for formation of the Fe(III)-NO species, as will be discussed later. Additionally, site directed mutagenesis studies that replace Thr243 show significantly reduced rates of NADH consumption, the formation of a 444 nm intermediate, and N_2O release.[59, 67-68] The levels of NO reduction by T243N, T243V, and T243A are 2%, 0.01%, and 3%, respectively (wt = 100%).[59] These mutation studies suggest that both Ser286 and Thr243 are crucial for the delivery of protons to the active site. The fact that neither the hydrogen bonding network nor the accumulation of positively charged residues on the B' helix is observed in cytochrome P450 monooxygenases suggests their importance in the unique function of P450nor.[30]

Moving closer to the active site, the I helix is situated directly next to the heme center in the distal pocket and spans the length of the enzyme, defining the heme pocket (see Figure 1.2).[33] While this helix is conserved among all cytochrome P450s, its usual function is to stabilize O_2 in the binding pocket.[69] As P450nor does not show monooxygenase activity, it is surprising that this region is conserved. Importantly, the I helix contains the previously mentioned Thr243 necessary for proton delivery to the active site and this is assumed to be its main function.[59] Additionally, the I helix in P450nor is more stretched than that of P450cam. The stretched helix is stabilized by Wat63 and Wat72, which provides a strong structural hydrogen bonding network from Thr243 to Ala239.[33] However, these water molecules are believed to be purely structural and not part of the proton delivery pathway.

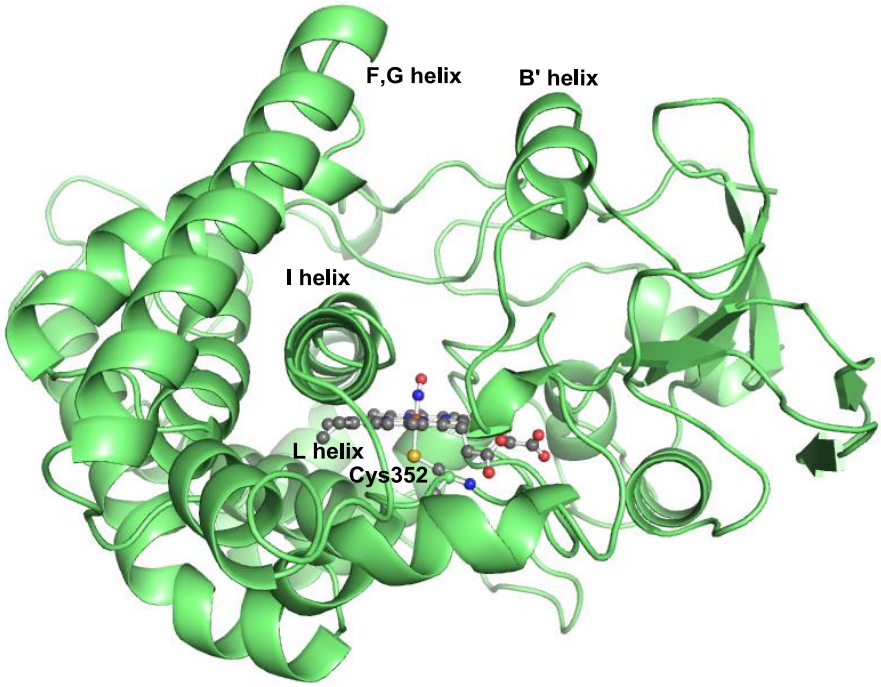

Figure 1.2. Crystal structure of the NO complex of ferric cytochrome P450nor. The image was generated using PyMOL from PDB code 1CL6.

Upon examination of the gene sequence of fungal NORs, a highly conserved region around Cys352 has been identified as the heme binding site.[28] Crystal structures of P450nor from *F. oxysporum* confirm this result.[33] These structures show a heme *b* with axial cysteinate coordination from Cys352 as illustrated in Figure 1.2, where the Fe-S bond distance is 2.17 Å in the 5C high-spin ferric resting state of the enzyme. The heme group is embedded between the distal I and proximal L helices with the proximal face of the heme around 8 Å away from the surface of the protein.

Characterization of the Fe(III)-NO Complex

In addition to the previously mentioned crystal structures of the ferric resting state, structures of P450nor have been solved for the following 6C wild-type forms at

Table 1.2. Geometric and vibrational properties of ferric [Fe^{III}(Porphyrin)(L)(NO)] complexes (L = thiolate). See references [70-73] for additional examples.

Molecule [a]	Geometric Parameters [Å]						Vibrational Frequencies [cm^{-1}]			
	ΔFe-N	ΔN-O	<Fe-N-O	ΔFe-L_{tr}	ΔFe-N_P	Ref.	*v*(N-O)	*v*(Fe-NO)	δ(Fe-N-O)	Ref.
[Fe^{III}(SPorph)(NO)]							1828	510		[74]
[Fe^{III}(SPorph-HB)(NO)]							1837	515		[74]
[Fe^{III}(OEP)(SR-H_2)(NO)]	1.671	1.187	160	2.356	2.01	[75]	1850	549		[75, 76]
P450nor(III)-NO	1.63	1.16	161	2.31	1.993	[58]	1851	530		[77]
S286V P450nor(III)-NO	1.62	1.13	162	2.37	1.990	[58]	1851	529		[58]
S286T P450nor(III)-NO	1.65	1.13	165	2.33	1.983	[58]	1851	529		[58]
T243N P450nor(III)-NO	1.94	1.15	131	2.36	1.985	[59]		530		[59]
T243A P450nor(III)-NO	2.10	1.42	120	2.33	2.008	[59]		530		[59]
T243V P450nor(III)-NO	2.01	1.37	119	2.34	1.970	[59]		530		[59]
P450cam(III)-NO	1.76			2.26	2.00	[77]	1806	528		[77-78]
P450cam(III)-NO + camphor							1806	522	546	[77, 79]
P450cam (III)-NO + norcamphor							1818	524		[77, 79]
P450cam(III)-NO + adamantanone							1818	520	542	[77, 79]
[Fe^{III}(P)(SR-H_2)(NO)] BP86/TZVP	1.668	1.158	167	2.434	2.024	[80]	1859	604	552/539	[80]
[Fe^{III}(P)(SPh)(NO)] BP86/TZVP	1.685	1.162	164	2.343	2.027	[80]	1829	584	560/535	[80]

[a] SPorph = *meso-a,a,a,a*-[*o*-[[o-[(acetylthio)methyl]phenoxy]acetamido]phenyl] tris(o-pivalamidophenyl)porphyrin^{2-}; SPorph-HB = SPorph with proposed hydrogen bonding; SR-H_2 = [S-2,6-$(CF_3CONH)_2C_6H_3$}]$^-$; P = Porphyrin^{2-} (formerly Porphine^{2-}) ligand used for calculations; values for ΔFe-N_P (iron-N_{Pyr} distance; Pyr = pyrrole) are averaged; ΔFe-L_{tr} = bond distance between iron and the axial (proximal) ligand *trans* to NO.

room and cryogenic temperatures: wt Fe(III)-NO,[58] wt Fe(II)-CO,[33, 56] and wt Fe(III)/Fe(II) *n*-butyl-isocyanide complexes.[60] Additionally, several mutants have been crystallized including the Fe(III)-NO complexes of S286V and S286T,[58] as well as T243N, T243A, and T243V.[59] The structural and spectroscopic information determined for these protein forms is collected in Table 1.2. While the aforementioned structures are valuable for the complete characterization of this enzyme, the structures of the ferric heme-nitrosyl species have strong implications for the mechanism of NO reduction by P450nor. Through comparison of wt Fe(III)-NO structures of P450nor with those of the cytochrome P450 monooxygenases, namely P450cam, inherent differences can be identified. These differences in coordination geometry may provide a chemical basis for the unique function of P450nor. EXAFS data estimate that the Fe-NO bond lengths in the ferric nitrosyl

complexes of P450nor and P450cam are 1.66 ± 0.02 Å and 1.76 ± 0.02 Å, respectively.[77] This is in good agreement with the wt Fe(III)-NO crystal structure of P450nor which reports an Fe-NO bond length of 1.63 Å (as shown in Table 1.2).[58] These data suggest a stronger Fe-NO bond in P450nor than in P450cam, and this trend is reproduced by the Fe-NO and N-O vibrational data listed in Table 1.2. The N-O and Fe-NO stretching frequencies are found at 1851 and 530 cm^{-1}, respectively, for P450nor.[77, 81] The corresponding values for P450cam are 1806 and 522 cm^{-1}, respectively.[77-78] As the authors claim,[77] the shorter Fe-NO distance in P450nor facilitates the electron transfer from the singly-occupied π* orbital of NO to the Fe center, formally creating an Fe(II)-NO^+ complex. This species would be more susceptible to reduction by direct hydride donation from NAD(P)H. Another key observation from the Fe(III)-NO crystal structure of P450nor is the Fe-N-O bond angle as illustrated in Figure 1.3. Most known Fe(III)-NO complexes show a linear Fe-NO unit.[82-85] While the Fe-N-O bond angle of 161° observed in P450nor is still considered "linear" in terms of Fe-N-O unit classification, there is a significant bend from linearity in this case.[58] Additionally, the Fe-NO bond vector is displaced by 9° from the heme normal towards the β-meso direction. The central question with respect to these findings is whether these are due to a structural effect of the protein active site (via steric interactions) or an electronic effect. Examination of the distal binding pocket shows a fairly open environment, making structural crowding unlikely. Therefore, the effect must be purely electronic. This hypothesis is confirmed by the crystal structure of a ferric heme-thiolate model complex, [Fe(OEP)(SR-H_2)(NO)] (SR-H_2 = S-2,6-$(CF_3CONH)_2C_6H_3$).[75] This model system shows an Fe-N-O bond

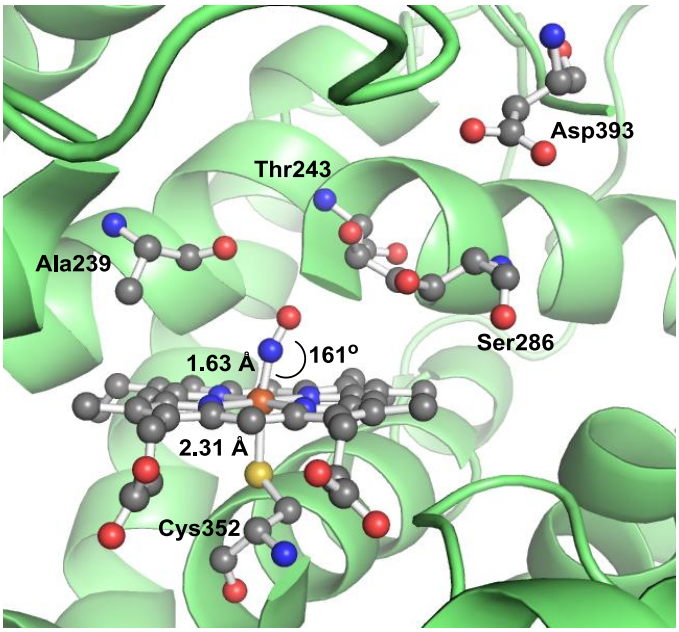

Figure 1.3. Structure of the ferric NO complex of the cytochrome P450nor active site. The image was generated using PyMOL from PDB code 1CL6.

angle of 159.6° and a tilt of 9.1° of the Fe-NO axis, confirming that this must be caused by an electronic effect.

Mechanism NO Reduction by Cytochrome P450nor

The catalytic cycle of P450nor starts from the ferric heme-thiolate resting state as illustrated in Scheme 1.1. From EPR studies, it is known that this species contains a high- and low-spin fraction where the latter is caused by coordination of water.[86] The g values for the high-spin complex are 7.97, 4.12, and 1.75. The low-spin component shows g values of 2.442, 2.260, and 1.911. This is further confirmed by single crystal EPR results at 10 K.[87] UV-Visible absorption spectroscopy also shows a mixture of high- and low-spin states for resting P450nor.[34, 88] The g values are typical for cytochrome P450s, and are in good agreement, for example, with the high- and low-spin components of P450cam.[89] The ratio of high- to low-spin complex

Scheme 1.1. Proposed reaction cycle for the reduction of two molecules of NO to N_2O by cytochrome P450nor.[43]

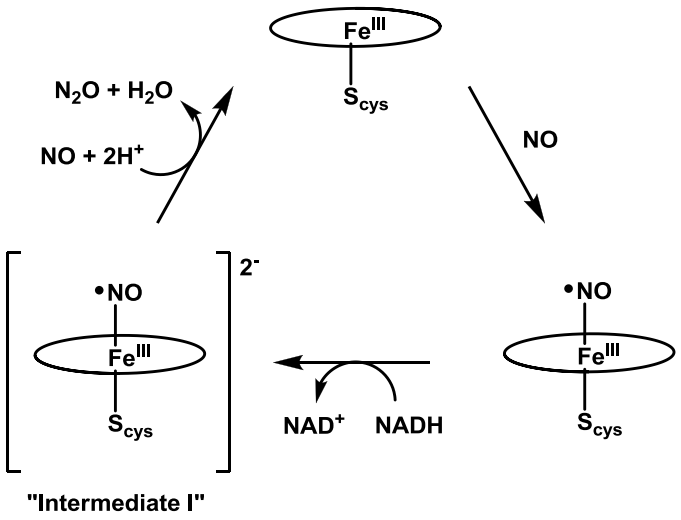

has been proposed to be of critical importance for the high catalytic activity of NO reduction by P450nor. Substitution of the native protoheme with a 2,4-diacetyldeuteroheme gives rise to a completely 6C low-spin ferric heme center, as evidenced by UV-Visible and resonance Raman spectroscopy.[90] Accordingly, the k_{on} rate for the formation of the ferric nitrosyl complex is significantly decreased to 0.24 x 10^7 $M^{-1}s^{-1}$ in this case, and the turnover rate dropped to 5,052 min^{-1}, as compared to 1.90 x 10^7 $M^{-1}s^{-1}$ and 12,650 min^{-1} for the reconstituted native form, respectively.

While the resting state shows a mixture of high- and low-spin species, the 5C high spin form (S = 5/2) is catalytically active, i.e. the water molecule must dissociate before NO can bind to the ferric 5C form of the enzyme. Studies on the association of NO with P450cam and corresponding model complexes by van Eldik and coworkers illustrate this point.[91-94] The model complex [Fe^{III}(SPorph)(NO)] shown in Figure 1.4, right, when solvated in methanol, displays large positive values of $\Delta H^{\ddagger}$ and $\Delta S^{\ddagger}$, accompanied by a positive activation volume. This suggests that the rate-

determining step in the binding of NO to the corresponding ferric precursor is dominated by the dissociation of a solvent (methanol) molecule.[92] Additionally, rates of NO binding to $P450_{cam}$ are highly dependent on the presence of camphor. The camphor-free (6C, water bound) and camphor-bound (5C) k_{on} rates are 3.2×10^5 and 3.45×10^7, respectively, indicating a much slower association when a water molecule is bound to the sixth coordination site of the heme.[91] The Fe(III)/Fe(II)

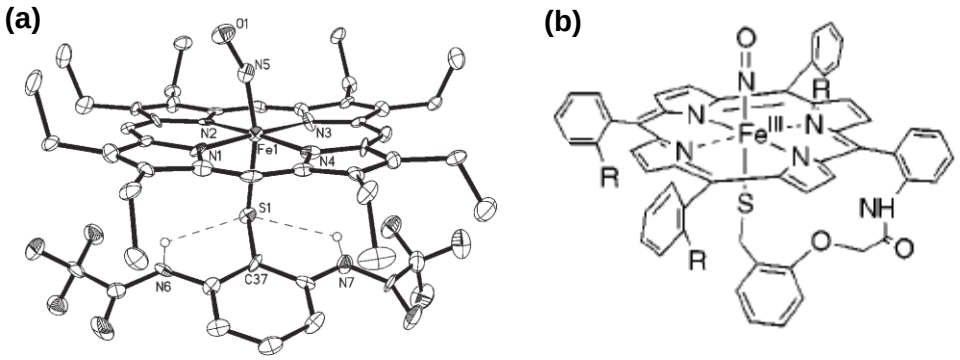

Figure 1.4. Ferric heme-thiolate NO complexes as models of P450nor. (a) Crystal structure of [Fe(OEP)(SR-H_2)(NO)] (SR-H_2 = S-2,6-$(CF_3CONH)_2C_6H_3$), the only structurally characterized ferric heme-nitrosyl with thiolate coordination[75] (Reprinted with permission from reference [75]. Copyright 2006 Royal Society of Chemistry); (b) schematic representation of a ferric porphyrin benzylthiolate model complex with bound NO, [Fe^{III}(SPorph)(NO)].[74] (Reprinted with permission from reference [74]. Copyright 2000 American Chemical Society).

redox potential for P450nor is quite different than that of the cytochrome P450 monooxygenases.[86, 95-96] The redox potential of fungal NOR is extremely negative at -307 mV, suggesting the possibility of reductive activation of the nitrosyl ligand. It is known that the Fe(II) form is not involved in the catalytic cycle of P450nor, as the reaction is not inhibited by CO.[34] Binding of one molecule of NO to the catalytically active, ferric form of P450nor then leads to a six-coordinate low-spin ferric heme-nitrosyl complex as the first intermediate (cf. Scheme 1.1).[34, 43, 77, 86, 90] The Soret band shifts from 414 nm to 431 nm upon NO binding,[43] and the Fe-NO and N-O

stretching frequencies of the resulting species are 530 cm^{-1} and 1851 cm^{-1}, respectively.[77] Flash photolysis determined the k_{on} rate for Fe(III)-NO formation to be 2.6 x 10^7 $M^{-1}s^{-1}$ at 10°C.[43] Binding of NO activates P450nor for reaction with NAD(P)H, which does not react with the 5C ferric ligand-free form of this enzyme.

Stopped-flow kinetic investigations have demonstrated that the 6C Fe(III)-NO species undergoes a two-electron reduction with NADH forming the so-called 'intermediate I', as identified by a shift of the Soret band to 444 nm.[43] The second order rate constant for this reduction has been estimated to be 0.9 x 10^6 $M^{-1}s^{-1}$ at 10°C. This result was reproduced using a chemical hydride donor, sodium borohydride ($NaBH_4$), indicating that the most likely mechanism is a direct hydride donation from NADH to the ferric heme-nitrosyl.[97] Using a synthetic analogue of NADH, 4,4-^{2}H,^{2}H-NADH, a kinetic isotope effect of 3.8 ± 0.2 has been determined for NADH oxidation,[97] indicating that the rate limiting step in the reduction of NO by P450nor is the hydride transfer from NADH to the ferric heme-nitrosyl complex. With a lifetime of around 100 ms, intermediate I is challenging to study and thus, its exact nature is unknown. Resonance Raman indicates an Fe-N stretching frequency of 596 cm^{-1}, which likely corresponds to an iron(II)-nitroxyl or iron(I)-NO complex.[81] This is in agreement with the fact that NADH generally performs two electron reductions. As such, formation of an Fe(II)-NO complex as intermediate I is unlikely, since this would correspond to a one-electron reduction. In addition, the Fe(II)-NO complex of P450nor prepared independently shows a Soret band at 434 nm rather than at 444 nm like intermediate I,[43] and the (potential) Fe-NO stretching frequency of this species is observed at 543 cm^{-1} by resonance Raman.[81] This vibrational frequency is also not in agreement with *v*(Fe-N) of intermediate I as mentioned above. Therefore,

the Fe(III)-NO complex of P450nor undergoes direct hydride donation from NADH to form an unknown intermediate I, which is not an Fe(II)-NO complex. The nature of this species is discussed in greater detail below.

As shown in Scheme 1.1, reaction of intermediate I with a second molecule of NO then closes the catalytic cycle.[43] The unimolecular rate constant for the spontaneous decay of intermediate I in the absence of NO back to the ferric resting state has been estimated to be 0.027 s^{-1} at 10°C. This rate constant, however, is too small to account for the large turnover number of this enzyme. Therefore, it is important to note that the formation of N_2O from intermediate I must be highly accelerated by excess NO. Finally, the following kinetic parameters have been determined for the total reaction: K_M = 113 nM and $V_{max} \geq 1200\ s^{-1}$.[34, 43]

The most important question with respect to the mechanism of P450nor concerns the exact nature of intermediate I.[27] Recently, strong evidence has been presented that this species is actually protonated.[97-98] Pulse radiolysis of H_2NOH has been shown to generate •NHOH and water at a rate of $9.5 \times 10^9\ M^{-1}s^{-1}$.[99] Upon irradiation of H_2NOH and ferric P450nor, a single Soret band was generated around 444 nm, exactly the wavelength of intermediate I.[97] Based on this result, the species at 444 nm should correspond to an $[Fe\text{-}NHOH]^{3+}$ complex; more specifically, either a ferryl heme with bound hydroxylamine anion or a ferric heme with a bound hydroxylamine radical. In addition, the molecular mechanism of P450nor has been elucidated using density functional theory (DFT) computations as discussed in greater detail below.[98, 100-103] Recent DFT results support these experimental findings.[98]

To truly understand the exact nature of intermediate I, model complexes will need to be employed. Unfortunately, model complex studies on P450nor suffer

greatly from the instability of the Fe-S bond in corresponding ferric heme-nitrosyls (*vide infra*).[92] Only two moderately stable ferric heme-thiolate NO model complexes have been synthesized so far, both of which are incapable of catalyzing the reduction of NO (Figure 1.4).[74-75] In fact, reduction of the ferric heme-nitrosyl model complex [Fe^{III}(SPorph)(NO)] prepared by Suzuki et al. with $NaBH_4$ led to the formation of the corresponding six-coordinate ferrous heme-nitrosyl, as evident from EPR. Interestingly, the formation of the initial Fe(III)-NO complex with thiolate coordination is a completely reversible process.[74]

Proposed Intermediates in the Catalytic Mechanism of Cytochrome P450nor

Using DFT calculations, a number of mechanisms have been postulated for cytochrome P450nor,[100-101, 103] based on the experimentally derived, kinetic scheme shown in Scheme 1.1. Tsukamoto et al. postulated an unusual mechanism where the initial Fe(III)-NO complex is one-electron reduced by NADH, generating the corresponding ferrous heme-nitrosyl and an $NADH^{\bullet+}$ radical.[101] NO then dissociates from the ferrous heme, and reacts with the $NADH^{\bullet+}$ radical to generate free nitroxyl, NO^-. Finally, the nitroxyl anion combines with the previously generated NAD^+ to form (NAD)(NOH) in close proximity to the heme site. The second molecule of NO then enters the active site to form N_2O. However, considering the stability of ferrous heme-nitrosyls, this is not a very likely scenario as fast NO dissociation from the ferrous heme is unlikely.[104] In fact, it could be envisioned that the sole reason for the use of the two-electron reductant (hydride donor) NADH (compared to two individual one-electron reductions) in P450nor catalysis is to avoid formation of a stable ferrous heme-nitrosyl complex. Additionally, this mechanism fails to address the experimentally observed properties of intermediate I, which does not correspond to a

Fe(II)-NO complex. In conclusion, the mechanism proposed by Tsukamoto et al. is highly unrealistic.

Cytochrome P450nor has also been proposed to reduce NO via the formation of an Fe(VI)-nitride complex[100] in analogy to compound I in classic cytochrome P450 dioxygen activation chemistry. A mechanism for the formation of an Fe(VI)-nitride intermediate could be imagined as follows: after nitrosylation to form the Fe(III)-NO species, a two-electron reduction results in an Fe(II)-NO^{-} complex, which could then be doubly protonated. After heterolytic N-O bond cleavage, a formally Fe(VI)-nitride intermediate is generated along with a water molecule. Reaction of the Fe(VI)-nitride species with a second molecule of NO would then generate N_2O. Finally, loss of N_2O from the heme completes the catalytic cycle. However, there is no experimental evidence to support the formation of an Fe(VI)-nitride complex in the catalytic cycle of cytochrome P450nor. In particular, the Fe-N stretching frequency of intermediate I has been observed at 596 cm^{-1}, which is incompatible with an Fe(VI)-nitride complex.[105]

DFT calculations have also been used to evaluate the relative free energies of potential intermediates of P450nor catalysis, leading to the postulated mechanism shown in Scheme 1.2.[98] After initial formation of the ferric heme-nitrosyl complex, a two-electron reduction by NADH occurs, leading to a formal Fe(II)-nitroxyl complex, **2**, which is very basic and immediately picks up a proton. This means that *the reaction of the Fe(III)-nitrosyl with NADH has to be considered as a hydride transfer* (see also reference [97]). The resulting protonated species can exist in the form of two tautomers; however, the DFT calculations show that the N-protonated complex (**3a**) is 26.2 kcal/mol more favorable than the O-protonated form (**3b**), indicating that this species is most likely N-protonated.[98] This is in agreement with results from Farmer

and coworkers, who studied the ferrous nitroxyl complex of Mb.[106-107] In this case, spectroscopic studies clearly indicate N-protonation of the Fe(II)-NHO species. Vibrational data show *v*(N-O) at 1385 and *v*(Fe-NO) at 651 cm^{-1}, respectively, for Mb(II)-NHO as listed in Table 1.3.[108] In the case of P450nor, the DFT calculations predict that the generated Fe(II)-NHO complex is still basic enough to pick up an additional proton from aqueous solution. This finding offers an attractive explanation for the function of the cysteinate in the active site of P450nor: the presence of the proximal thiolate ligand increases the basicity of the Fe(II)-NHO complex, and in this way, enables the second protonation.[98] This leads to the generation of a formally Fe(IV)-NHOH intermediate (**4**), which is energetically favored by 8.6 kcal/mol over the Fe(II)-NHO species. The Fe(IV)-NHOH complex is ideally set up for the following reaction with the second molecule of NO, which can be interpreted as a two-step process. First, outer sphere electron transfer takes place from the incoming NO to reduce the formally Fe(IV) center.[98] This generates NO^+ that then attacks the bound $NHOH^-$ ligand, leading to N-N bond formation (species **7a** in Scheme 1.2). This species rearranges subsequently, forming the hyponitrous acid complex Fe(III)-$N_2H_2O_2$ (**7b**). Interestingly, this species is predicted to be quite stable by the DFT calculations. Decomposition of **7b** then produces N_2O and water, closing the catalytic cycle. Importantly, this process is exergonic by 53 kcal/mol and, therefore, has a strong thermodynamic driving force.[98]

One of the most important questions with respect to the mechanism of P450nor is the exact nature of intermediate I. Lehnert and coworkers believe that intermediate I as defined in the original mechanism in Scheme 1.1 corresponds to the doubly-protonated NHOH complex,[686] in agreement with additional experimental evidence.[27, 97] Experimentally, vibrational spectroscopy could be used to determine

Scheme 1.2. Calculated mechanism of P450nor.[98, 109] Free energies, ΔG, are given relative to complex **3a** (set to 0.0 kcal/mol).

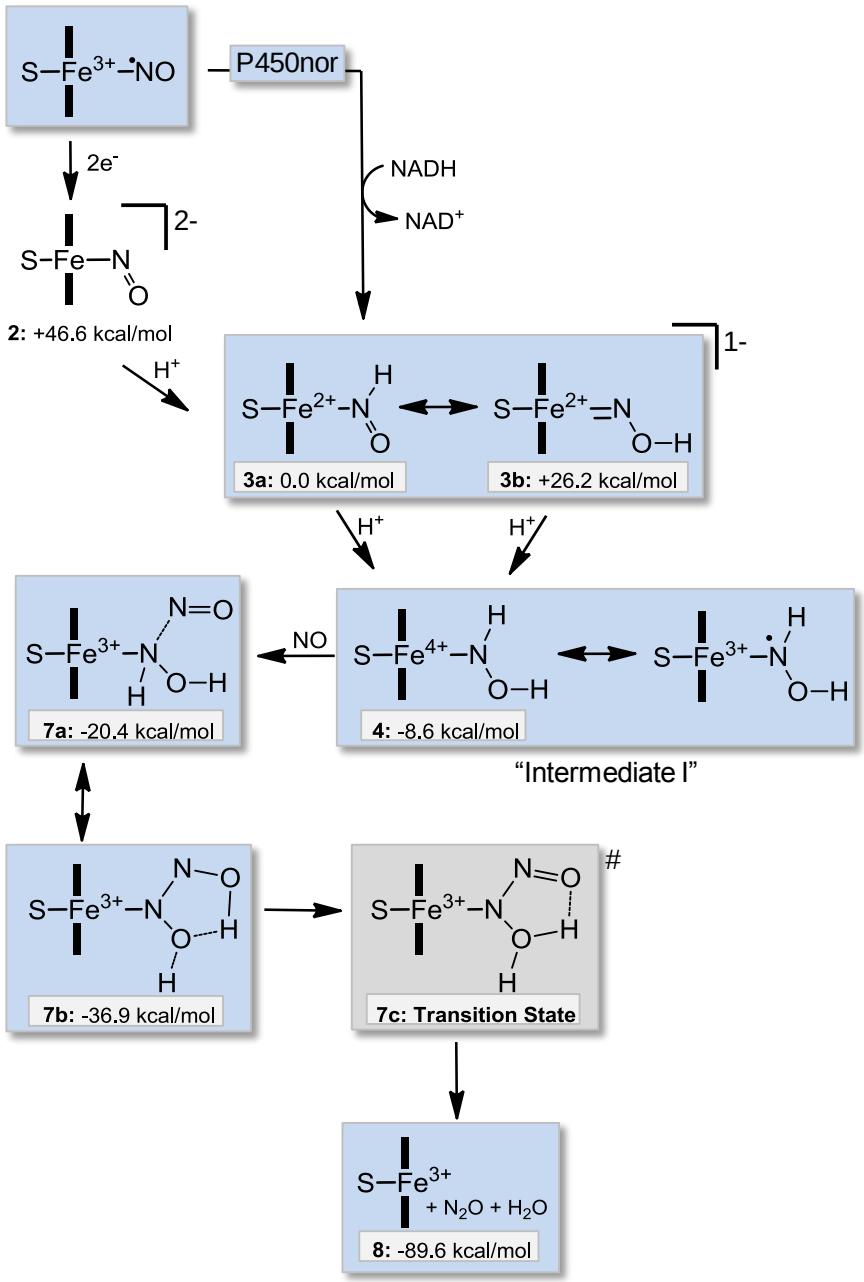

Table 1.3. Geometric and vibrational properties of $[Fe(P)(L)(NO)]^{-/2-}$ complexes and corresponding protonated intermediates (L = MI or MeS^-) from experiment in comparison to DFT results.

Molecule [a]	Geometric Parameters [Å]				Vibrational Frequencies [cm^{-1}]		Ref.
	ΔFe-N	ΔN-O	<Fe-N-O	ΔFe-L_{tr}	*v*(N-O)	*v*(Fe-NO)	
$[Fe(TPP)(NO)]^-$					1496	549	110
$[Fe(T\textit{per}\text{-}F_5PPBr_8)(NO)]^-$					1550		111
[Mb-HNO]	1.82	1.24	131	2.09	1385	651	108
P450nor: intermediate *I*						596	81
$[Fe(CN)_5(HNO)]^{3-}$					1380/1304	662	112
[Fe(Cyclam-Ac)(NO)]					1271		113
$[Fe(P)(SMe)(NO)]^{2-}$ (**2**, S=0)	1.776	1.215	131	2.587	1500	502	98
$[Fe(P)(SMe)(NHO)]^-$ (**3a**, S=0)	1.824	1.252	133	2.354	1386	601/430	98
$[Fe(P)(SMe)(NOH)]^-$ (**3b**, S=0)	1.746	1.401	117	2.411	833	649	98
[Fe(P)(SMe)(NHOH)] (**4**, S=0)	1.810	1.397	125	2.230	952	609/544 [b]	98
[Fe(P)(MI)(NHO)] (S=0)	1.789	1.236	132	2.082	1459	651/464	76

[a] MI = 1-methylimidazole; P = $Porphyrin^{2-}$ (formerly $Porphine^{2-}$).
[b] Both modes at 609 and 544 cm^{-1} are strongly mixed with in-plane and out-of-plane Fe-N-H bends.

the protonation state of intermediate I as shown in Table 1.3.[98] DFT calculations predict that the singly-protonated NHO and NOH tautomers, and the doubly-protonated NHOH complex have significantly different Fe-N and N-O stretching frequencies. Here, the Fe(II)-NHO complex shows *v*(N-O) at 1386 cm^{-1} and *v*(Fe-N) as a split feature at 601 and 430 cm^{-1}. The O-protonated tautomer has a stronger Fe-N bond, evidenced by an increase of *v*(Fe-N) to 649 cm^{-1}, whereas *v*(N-O) drops to 833 cm^{-1}. Finally, the doubly-protonated complex shows an intermediate *v*(N-O) at 952 cm^{-1}, and *v*(Fe-N) is predicted as a split feature at 609 and 544 cm^{-1} from the DFT calculations. Hence, the N-O stretch is particularly diagnostic for the protonation state of intermediate I.[98] Unfortunately, *v*(N-O) has not been determined experimentally for this species, but the Fe-N stretch has been identified at 596 cm^{-1}.[81] This rules out the NOH tautomer, but based on this result, both the NHO and the NHOH complex would still be feasible. In contrast, note that the unprotonated ferrous heme-nitroxyl complex shows the N-O stretch around 1500 cm^{-1} as predicted by DFT,[98] and observed experimentally for $[Fe(TPP)(NO)]^-$.[110, 114-115]

Similar to the molecular mechanism of P450nor discussed above, Hillier and coworkers concluded that intermediate I corresponds to the doubly protonated complex, Fe(IV)-NHOH, using DFT calculations.[102] Intermediate I then reacts with another molecule of NO to form a species that is similar to **7a** in Scheme 1.2. At this point the two mechanisms divert, as Hillier and coworkers predict that $N_2O_2H_2$ dissociates from the iron center, and subsequently decomposes. While this mechanism is plausible, it has been shown that the tautomerization of **7a** to **7b** is energetically more favorable than loss of $N_2O_2H_2$ from heme as discussed above.

Finally, computational studies on NO binding to ferric P450cam,[116] and on the properties of the reduced and protonated species shown in Scheme 1.2 with different axial ligands to heme[103, 117] have also been published.

1.4. Scope of Thesis

This thesis focuses on the generation of small molecule models of intermediates in the catalytic cycle of P450nor. Chapter 2 focuses on modeling the first intermediate, a six-coordinate ferric heme-nitrosyl with axial thiolate ligation. In Section 2.1, porphyrins (including bis-picket fence porphyrins) and axial thiolate ligands have been screened to determine the key factors for the formation of *stable* ferric porphyrin nitrosyl complexes with thiolate coordination. Additionally, due to the reactivity of the Fe-S bond towards NO, the formation and properties of six-coordinate Fe(III) porphyrin nitrosyl complexes with alternative anionic phenolate and acetate (O-donor) ligands are reported in Section 2.2 and Section 2.3, respectively. The complexes [Fe(OEP)(SR-H_2)], [Fe(OEP)(SR-H_1)], and [Fe(TPP)(AcF_3)(NO)] were provided by our collaborator, Geroge B. Richter-Addo, at the University of Oklahoma. Section 2.2 was completed with undergraduate student

Breana Siljander. Section 2.1 is reported, in part, in Inorganic Chemistry: Goodrich, L.E.; Paulat, F.; Praneeth, V.K.K.; Lehnert, N. *Inorg. Chem.* **2010**, *49*, 6293-6316. Section 2.3 has been submitted for publication: Xu, N.; Goodrich, L.E.; Lehnert, N.; Powell, D.; Richter-Addo, G.B. **2012**.

In Chapter 3, ferrous heme-nitroxyl complexes are studied. In P450nor, a Fe(II)-NHO complex is formed through direct hydride transfer from NAD(P)H to a ferric heme-nitrosyl. An alternate synthetic pathway can be envisioned where a Fe(II)-NO complex is reduced by one electron to the corresponding Fe(II)-NO^- species followed by protonation to form the desired Fe(II)-NHO complex. Here, the one-electron reduction of Fe(II)-NO complexes has been studied using spectroelectrochemistry and density functional theory (DFT) calculations. Additionally, the reactivity of heme Fe(II)-NO^- complexes with NO and acid have been explored. Dr. Saikat Roy (Matzger Laboratory) performed X-ray crystallography on [Fe(3,5-Me-BAFP)(NO)]. A manuscript is in preparation: Goodrich, L.E.; Saikat, Roy; Matzger, A.J.; Lehnert, N. **2012**, *to be submitted*.

Chapter 4 describes initial attempts at modeling the active species (Intermediate I) in P450nor. From enzymatic studies, this key complex is proposed for form the important N-N bond by reaction with a second NO molecule. Proposals for the structure of this species include a (formally) Fe(IV)-NHOH complex or, upon loss of H_2O, a Fe(VI)-N species. Section 4.1 focuses on synthesis of Fe(III)-NHOR bis-picket fence porphyrin complexes with the eventual goal of one-electron oxidation to the desired ferryl complex. Section 4.2 is focused on high-valent heme-nitride complexes. Here, the likelihood of formation of a Fe(VI)-nitride complex in the catalytic cycle of P450nor is investigated. Irradiation of high- and low-spin ferric azide complexes in an attempt to generate Fe(V)-nitride complexes has been

performed. Section 4.1 was completed with Claire Goodrich and [Fe(3,5-Me-BAFP)(NH_3)$_2$] was crystallized by Ashley McQuarters. The starting five-coordinate ferric azide complexes, [Fe(T*o*-(OBn)$_2$PP)(N_3)] and [Fe(3,5-Me-BAFP)(N_3)], in Section 4.2.b were prepared by Cathy Mocny and Ashley McQuarters, respectively. Dr. Saikat Roy (Matzger Laboratory) performed X-ray crystallography on [Fe(3,5-Me-BAFP)(N_3)].

Finally, activation of the primary mammalian nitric oxide (NO) sensor, soluble guanylate cyclase (sGC), is discussed in Chapter 5. Through the strong thermodynamic σ-*trans* effect of NO, binding of NO at the distal side of the ferrous heme induces cleavage of the proximal Fe-N_{His} bond, activating the catalytic domain of the enzyme.[19-20] It has been proposed that nitroxyl (HNO) is also capable of activating sGC, but the key question remains as to whether HNO can induce cleavage of the Fe-N_{His} bond. Here, we report calculated binding constants for 1-methylimidazole (MI) to [Fe(P)(X)] (P = porphine^{2-}) where X = NO, HNO, CO, and MI to evaluate the *trans* interaction of these molecules, X, with the proximal imidazole (histidine) in sGC. Additionally, calculated Fe-N_{MI} bond lengths and key molecular orbitals in [Fe(P)(MI)(X)] are analyzed. This work is reprinted with permission from the Journal of Inorganic Biochemistry: Goodrich, L.E.; Lehnert, N. *J. Inorg. Biochem.* **2012**, *in press*.

References

1. Moncada, S.; Palmer, R. M.; Higgs, E. A., *Pharmacol. Rev.* **1991,** *43*, 109-142.
2. Snyder, S. H., *Science* **1992,** *257*, 494-496.
3. Bredt, D. S.; Snyder, S. H., *Annu. Rev. Biochem.* **1994,** *63*, 175-195.

4. Ignarro, L., *Nitric Oxide: Biology and Pathobiology*. Academic Press: San Diego, 2000.

5. Culotta, E.; Koshland, D. E., Jr., *Science* **1992,** *258*, 1862-1865.

6. Furchgott, R. F., *Angew. Chem. Int. Ed.* **1999,** *38*, 1870-1880.

7. Ignarro, L., *Angew. Chem. Int. Ed.* **1999,** *38*, 1882-1892.

8. Murad, F., *Angew. Chem. Int. Ed.* **1999,** *38*, 1856-1868.

9. Stuehr, D. J., *Annu. Rev. Pharmacol. Toxicol.* **1997,** *37*, 339-359.

10. Fischmann, T. O.; Hruza, A.; Niu, X. D.; Fossetta, J. D.; Lunn, C. A.; Dolphin, E.; Prongay, A. J.; Reichert, P.; Lundell, D. J.; Narula, S. K.; Weber, P. C., *Nat. Struct. Biol.* **1999,** *6*, 233-242.

11. Li, H.; Poulos, T., *J. Inorg. Biochem.* **2005,** *99*, 293-305.

12. Rousseau, D. L.; Li, D.; Couture, M.; Yeh, S.-R., *J. Inorg. Biochem.* **2005,** *99*, 306-323.

13. Martin, N. I.; Woodward, J. J.; Winter, M. B.; Beeson, W. T.; Marletta, M. A., *J. Am. Chem. Soc.* **2007,** *129*, 12563-12570.

14. Stuehr, D. J.; Gross, S. S.; Sakuma, I.; Levi, R.; Nathan, C. F., *J. Exp. Med.* **1989,** *169*, 1011-1020.

15. MacMicking, J.; Xie, Q.-W.; Nathan, C., *Annu. Rev. Immunol.* **1997,** *15*, 323-350.

16. Terenzi, F.; Diaz-Guerra, J. M.; Casado, M.; Hortelano, S.; Leoni, S.; Boscá, L., *J. Biol. Chem.* **1995,** *270*, 6017-6021.

17. Montague, P. R.; Gancayco, C. D.; Winn, M. J.; Marchase, R. B.; Friedlander, M. J., *Science* **1994,** *263*, 973-977.

18. Ignarro, L. J., *J. Biochem. Soc. Trans.* **1992,** *20*, 465-469.

19. Traylor, T. G.; Sharma, V. S., *Biochemistry* **1992,** *31*, 2847-2849.

20. Zhao, Y.; Brandish, P. E.; Ballou, D. P.; Marletta, M. A., *Proc. Natl. Acad. Sci. USA* **1999,** *96*, 14753-14758.

21. Goodrich, L. E.; Paulat, F.; Praneeth, V. K. K.; Lehnert, N., *Inorg. Chem.* **2010,** *49*, 6293-6316.

22. Olson, J. S.; Foley, E. W.; Rogge, C.; Tsai, A.-L.; Doyle, M. P.; Lemon, D. D., *Free Rad. Biol. Med.* **2004,** *36*, 685-697.

23. Gardner, P. R.; Gardner, A. M.; Martin, L. A.; Salzman, A. L., *Proc. Natl. Acad. Sci. USA* **1998,** *95*, 10378-10383.

24. Eich, R. F.; Li, T.; Lemon, D. D.; Doherty, D. H.; Curry, S. R.; Aitken, J. F.; Mathews, A. J.; Johnson, K. A.; Smith, R. D.; Phillips, G. N., Jr.; Olson, J. S., *Biochemistry* **1996,** *35*, 6976-6983.

25. Zumft, W. G., *J. Inorg. Biochem.* **2005,** *99*, 194-215.

26. Wasser, I. M.; deVries, S.; Moënne-Loccoz, P.; Schröder, I.; Karlin, K. D., *Chem. Rev.* **2002,** *102*, 1201-1234.

27. Daiber, A.; Shoun, H.; Ullrich, V., *J. Inorg. Biochem.* **2005,** *99*, 185-193

28. Kizawa, H.; Tomura, D.; Oda, M.; Fukamizu, A.; Hoshino, T.; Gotoh, O.; Yasui, T.; Shoun, H., *J. Biol. Chem.* **1991,** *266*, 10632-10637.

29. Lehnert, N.; Berto, T. C.; Galinato, M. G. I.; Goodrich, L. E., The Role of Heme-Nitrosyls in the Biosynthesis, Transport, Sensing, and Detoxification of Nitric Oxide (NO) in Biological Systems: Enzymes and Model Complexes. In *The Handbook of Porphyrin Science*, Kadish, K.; Smith, K.; Guilard, R., Eds. World Scientific: 2011; Vol. 15, pp 1-247.

30. Zhang, L.; Kudo, T.; Takaya, N.; Shoun, H. In *Distribution, structure and function of fungal nitric oxide reductase P450nor—recent advances*, Int. Cong. Ser., Elsevier: 2002; pp 197-202.

31. Denisov, I. G.; Makris, T. M.; Sligar, S. G.; Schlichting, I., *Chem. Rev.* **2005,** *105*, 2253-77.

32. Peterson, J. A.; Graham, S. E., *Structure* **1998,** *6*, 1079-1085.

33. Park, S.-Y.; Shimizu, H.; Adachi, S.; Nagagawa, A.; Tanaka, I.; Nakahara, K.; Shoun, H.; Obayashi, E.; Nakamura, H.; Iizuka, T.; Shiro, Y., *Nat. Struct. Biol.* **1997,** *4*, 827-832.

34. Nakahara, K.; Tanimoto, T.; Hatano, K.; Usuda, K.; Shoun, H., *J. Biol. Chem.* **1993,** *268*, 8350-8355.

35. Shoun, H.; Tanimoto, T., *J. Biol. Chem.* **1991,** *266*, 11078-11082.

36. Takaya, N.; Shoun, H., *Mol. Gen. Gent.* **2000,** *263*, 342-348.

37. Zumft, W., *Microbiol. Mol. Biol. Rev.* **1997,** *61*, 533-616.

38. Takaya, N.; Kuwazaki, S.; Adachi, Y.; Suzuki, S.; Kikuchi, T.; Nakamura, H.; Shiro, Y.; Shoun, H., *J. Biochem.* **2003,** *133*, 461-465.

39. Zhou, Z.; Takaya, N.; Sakairi, M. A. C.; Shoun, H., *Arch. Microbiol.* **2001,** *175*, 19-25.

40. Kobayashi, M.; Matsuo, Y.; Takimoto, A.; Suzuki, S.; Maruo, F.; Shoun, H., *J. Biol. Chem.* **1996,** *271*, 16263-16267.

41. Tanimoto, T.; Nakahara, K.; Shoun, H., *Biosci. Biotech. Biochem.* **1992,** *56*, 2058-2059.

42. Heiss, B.; Frunzke, K.; Zumft, W. G., *J. Bacteriol.* **1989,** *171*, 3288-3297.

43. Shiro, Y.; Fujii, M.; Iizuka, T.; Adachi, S.; Tsukamoto, K.; Nakahara, K.; Shoun, H., *J. Biol. Chem.* **1995,** *270*, 1617-1623.

44. Shoun, H.; Suyama, W.; Yasui, T., *FEBS Lett.* **1989,** *244*, 11-14.

45. Usuda, K.; Toritsuka, N.; Matsuo, Y.; Kim, D. H.; Shoun, H., *Appl. Environ. Microbiol.* **1995,** *61*, 883-889.

46. Kudo, T.; Tomura, D.; Liu, D. L.; Dai, X. Q.; Shoun, H., *Biochimie* **1996,** *78*, 792-799.

47. Tsuruta, S.; Takaya, N.; Zhang, L.; Shoun, H.; Kimura, K.; Hamamoto, M.; Nakase, T., *FEMS Microbiol. Lett.* **1998,** *168*, 105-110.

48. Zhang, L.; Takaya, N.; Kitazume, T.; Kondo, T.; Shoun, H., *Eur. J. Biochem.* **2001,** *268*, 3198-3204.

49. Shoun, H.; Kano, M.; Baba, I.; Takaya, N.; Matsuo, M., *J. Bacteriol.* **1998,** *180*, 4413-4415.

50. Shoun, H.; Kim, D. H.; Uchiyama, H.; Sugiyama, J., *FEMS Microbiol. Lett.* **1992,** *94*, 277-282.

51. Tomura, D.; Obika, K.; Fukamizu, A.; Shoun, H., *J. Biochem.* **1994,** *116*, 88-94.

52. Takaya, N.; Suzuki, S.; Kuwazaki, S.; Shoun, H.; Maruo, F.; Yamaguchi, M.; Takeo, K., *Arch. Biochem. Biophys.* **1999,** *372*, 340-346.

53. Nakahara, K.; Shoun, H., *J. Biochem.* **1996,** *120*, 1082-1087.

54. Watsuji, T. O.; Takaya, N.; Nakamura, A.; Shoun, H., *Biosci. Biotech. Biochem.* **2003,** *67*, 1109-1114.

55. Shimizu, H.; Park, S. Y.; Lee, D. S.; Shoun, H.; Shiro, Y., *J. Inorg. Biochem.* **2000,** *81*, 191-205.

56. Shimizu, H.; Park, S.-Y.; Shiro, Y.; Adachi, S.-I., *Acta Crystallogr. D* **2002,** *58*, 81.

57. Oshima, R.; Fushinobu, S.; Su, F.; Zhang, L.; Takaya, N.; Shoun, H., *J. Mol. Biol.* **2004,** *342*, 207-217.

58. Shimizu, H.; Park, S.-Y.; Gomi, Y.; Arakawa, H.; Nakamura, H.; Adachi, S.-I.; Obayashi, E.; Iizuka, T.; Shoun, H.; Shiro, Y., *J. Biol. Chem.* **2000,** *275*, 4816-4826.

59. Obayashi, E.; Shimizu, H.; Park, S. Y.; Shoun, H.; Shiro, Y., *J. Inorg. Biochem.* **2000,** *82*, 103-111.

60. Lee, D. S.; Park, S. Y.; Yamane, K.; Obayashi, E.; Hori, H.; Shiro, Y., *Biochemistry* **2001,** *40*, 2669-2677.

61. Kudo, T.; Takaya, N.; Park, S. Y.; Shiro, Y.; Shoun, H., *J. Biol. Chem.* **2001,** *276*, 5020-5026.

62. Poulos, T. L.; Finzel, B. C.; Howard, A. J., *Biochemistry* **1986,** *25*, 5314-5322.

63. Gotoh, O., *J. Biol. Chem.* **1992,** *267*, 83-90.

64. Hasemann, C. A.; Ravichandran, K. G.; Peterson, J. A.; Deisenhofer, J., *J. Mol. Biol.* **1994,** *236*, 1169-1185.

65. Cupp-Vickery, J. R.; Poulos, T. L., *Nat. Struct. Mol. Biol.* **1995,** *2*, 144-153.

66. Zhang, L.; Kudo, T.; Takaya, N.; Shoun, H., *J. Biol. Chem.* **2002,** *277*, 33842-33847.

67. Okamoto, N.; Imai, Y.; Shoun, H.; Shiro, Y., *Biochemistry* **1998,** *37*, 8839-8847.

68. Okamoto, N.; Tsuruta, K.; Imai, Y.; Tomura, D.; Shoun, H., *Arch. Biochem. Biophys.* **1997,** *337*, 338-344.

69. Poulos, T. L.; Finzel, B. C.; Howard, A. J., *J. Mol. Biol.* **1987,** *195*, 687-700.

70. Ding, X. D.; Weichsel, A.; Andersen, J. F.; Shokhireva, T. K.; Balfour, C.; Pierik, A. J.; Averill, B. A.; Montfort, W. R.; Walker, F. A., *J. Am. Chem. Soc.* **1999,** *121*, 128-138.

71. Praneeth, V. K. K.; Paulat, F.; Berto, T. C.; DeBeer George, S.; Näther, C.; Sulok, C. D.; Lehnert, N., *J. Am. Chem. Soc.* **2008,** *130*, 15288-15303.

72. Cheng, L.; Richter-Addo, G. B., Binding and Activation of Nitric Oxide by Metalloporphyrins and Heme. In *The Porphyrin Handbook*, Kadish, K. M.; Smith, K. M.; Guilard, R., Eds. Academic Press: New York, 2000; Vol. 4, Chapter 33, pp 219-291.

73. Wyllie, G. R. A.; Scheidt, W. R., *Chem. Rev.* **2002,** *102*, 1067-1090.

74. Suzuki, N.; Higuchi, T.; Urano, Y.; Kikuchi, K.; Uchida, T.; Mukai, M.; Kitagawa, T.; Nagano, T., *J. Am. Chem. Soc.* **2000,** *122*, 12059-12060.

75. Xu, N.; Powell, D. R.; Cheng, L.; Richter-Addo, G. B., *Chem. Commun.* **2006**, 2030-2032.

76. Goodrich, L. E.; Paulat, F.; Praneeth, V. K. K.; Lehnert, N., *Inorg. Chem.* **2010,** *49*, 6293-6316.

77. Obayashi, E.; Tsukamoto, K.; Adachi, S.; Takahashi, S.; Nomura, M.; Iizuka, T.; Shoun, H.; Shiro, Y., *J. Am. Chem. Soc.* **1997,** *119*, 7807-7816.

78. Hu, S.; Kincaid, J. R., *J. Am. Chem. Soc.* **1991,** *113*, 2843-2850.

79. Hu, S.; Kincaid, J. R., *J. Am. Chem. Soc.* **1991,** *113*, 9760-9766.

80. Paulat, F.; Lehnert, N., *Inorg. Chem.* **2007,** *46*, 1547-1549.

81. Obayashi, E.; Takahashi, S.; Shiro, Y., *J. Am. Chem. Soc.* **1998,** *120*, 12964-12965.

82. Scheidt, W. R.; Lee, Y. J.; Hatano, K., *J. Am. Chem. Soc.* **1984,** *106*, 3191-3198.

83. Ellison, M. K.; Scheidt, W. R., *J. Am. Chem. Soc.* **1999,** *121*, 5210-5219.

84. Ellison, M. K.; Schulz, C. E.; Scheidt, W. R., *J. Am. Chem. Soc.* **2002,** *124*, 13833-13841.

85. Yi, G.-B.; Chen, L.; Khan, M. A.; Richter-Addo, G. B., *Inorg. Chem.* **1997,** *36*, 3876-3885.

86. Shiro, Y.; Fujii, M.; Isogai, Y.; Adachi, S.; Iizuka, T.; Obayashi, E.; Makino, R.; Nakahara, K.; Shoun, H., *Biochemistry* **1995,** *34*, 9052-9058.

87. Park, S. Y.; Shimizu, H.; Adachi, S.; Shiro, Y.; Iizuka, T.; Nakagawa, A.; Tanaka, I.; Shoun, H.; Hori, H., *FEBS Lett.* **1997,** *412*, 346-350.

88. Shoun, H.; Sudo, Y.; Seto, Y.; Beppu, T., *J. Biochem.* **1983,** *94*, 1219-1229.

89. Lipscomb, J. D., *Biochemistry* **1980,** *19*, 3590-3599.

90. Singh, U. P.; Obayashi, E.; Takahashi, S.; Iizuka, T.; Shoun, H.; Shiro, Y., *Biochim. Biophys. Acta* **1998,** *1384*, 103-111.

91. Franke, A.; Stochel, G.; Jung, C.; Van Eldik, R., *J. Am. Chem. Soc.* **2004,** *126*, 4181-4191.

92. Franke, A.; Stochel, G.; Suzuki, N.; Higuchi, T.; Okuzono, K.; van Eldik, R., *J. Am. Chem. Soc.* **2005,** *127*, 5360-5375.

93. Franke, A.; Hessenauer-Ilicheva, N.; Meyer, D.; Stochel, G.; Woggon, W.-D.; van Eldik, R., *J. Am. Chem. Soc.* **2006,** *128*, 13611-13624.

94. Ivanovic-Burmazovic, I.; van Eldik, R., *J. Chem. Soc. Dalton Trans.* **2008**, 5259-5275.

95. Makino, T.; Iizuka, T.; Sakaguchi, K.; Ishimura, Y., *Oxygenase and Oxygen Metabolism*. Academic Press: New York, 1982; p 466-477.

96. Gunsalus, I. C.; Meeks, J. R.; Lipscomb, J. D.; Debrunner, P.; Munck, E., *Molecular mechanisms of oxygen activation*. Academic Press: New York, 1974; p 599-613.

97. Daiber, A.; Nauser, T.; Takaya, N.; Kudo, T.; Weber, P.; Hultschig, C.; Shoun, H.; Ullrich, V., *J. Inorg. Biochem.* **2002,** *88*, 343-352.

98. Lehnert, N.; Praneeth, V. K. K.; Paulat, F., *J. Comp. Chem.* **2006,** *27*, 1338-1351.

99. Buxton, G. V.; Greenstock, C. L.; Helman, W. P.; Ross, A. B., *J. Phys. Chem. Ref. Data* **1988,** *17*, 513-886.

100. Harris, D. L., *Int. J. Quantum Chem.* **2002,** *88*, 183-200.

101. Tsukamoto, K.; Watanabe, T.; Nagashima, U.; Akiyama, Y., *J. Mol. Struct. THEOCHEM* **2005,** *732*, 87-98.

102. Vincent, M. A.; Hillier, I. H.; Ge, J., *Chem. Phys. Lett.* **2005,** *407*, 333-336.

103. Silaghi-Dumitrescu, R., *Eur. J. Inorg. Chem.* **2003,** *2003*, 1048-1052.

104. Cooper, C. E., *Biochim. Biophys. Acta* **1999,** *1411*, 290-309.

105. Petrenko, T.; DeBeer George, S.; Aliaga-Alcalde, N.; Bill, E.; Mienert, B.; Xiao, Y.; Guo, Y.; Sturhahn, W.; Cramer, S. P.; Wieghardt, K.; Neese, F., *J. Am. Chem. Soc.* **2007,** *129*, 11053–11060.

106. Sulc, F.; Immoos, C. E.; Pervitsky, D.; Farmer, P. J., *J. Am. Chem. Soc.* **2004,** *126*, 1096.

107. Farmer, P. J.; Sulc, F., *J. Inorg. Biochem.* **2005,** *99*, 166-184.

108. Immoos, C. E.; Sulc, F.; Farmer, P. J.; Czarnecki, K.; Bocian, D. F.; Levina, A.; Aitken, J. B.; Armstrong, R. S.; Lay, P. A., *J. Am. Chem. Soc.* **2005,** *127*, 814-815.

109. Riplinger, C.; Neese, F., *Chem. Phys. Chem.* **2011,** *12*, 3192-3203.

110. Choi, I.-K.; Liu, Y.; Feng, D.; Paeng, K.-J.; Ryan, M. D., *Inorg. Chem.* **1991,** *30*, 1832-1839.

111. Pellegrino, J.; Bari, S. E.; Bikiel, D. E.; Doctorovich, F., *J. Am. Chem. Soc.* **2010,** *132*, 989-995.

112. Montenegro, A. C.; Amorebieta, V. T.; Slep, L. D.; Martin, D. F.; Roncaroli, F.; Murgida, D. H.; Bari, S. E.; Olabe, J. A., *Angew. Chem. Int. Ed.* **2009,** *48*, 4213-4216.

113. Serres, R. G.; Grapperhaus, C. A.; Bothe, E.; Bill, E.; Weyhermüller, T.; Neese, F.; Wieghardt, K., *J. Am. Chem. Soc.* **2004,** *126*, 5138-5153.

114. Liu, Y.; Ryan, M. D., *J. Electroanal. Chem.* **1994,** *368*, 209-219.

115. Liu, Y.; DeSilva, C.; Ryan, M. D., *Inorg. Chim. Acta* **1997,** *258*, 247-255.

116. Scherlis, D. A.; Cymeryng, C. B.; Estrin, D. A., *Inorg. Chem.* **2000,** *39*, 2352-2359.

117. Linder, D. P.; Rodgers, K. R., *Inorg. Chem.* **2005,** *44*, 8259-8264.

Chapter 2

Six-Coordinate Ferric Heme-Nitrosyl Complexes

The first step in reduction of nitric oxide (NO) to nitrous oxide (N_2O) by cytochrome P450 nitric oxide reductase (P450nor) is formation of a ferric heme-nitrosyl intermediate with bound cysteinate, as discussed in detail in Chapter 1. Therefore, in order to model the reaction cycle of P450nor, stable ferric heme-nitrosyl complexes are necessary. However, synthesis of these model complexes is not a trivial task as ferric heme-nitrosyls are intrinsically labile with respect to loss of NO. This is in contrast to the very stable and generally unreactive *ferrous* heme-nitrosyls. The binding constant for NO to ferrous heme complexes is in the range of 10^{11} – 10^{12} M^{-1} which equates to a free energy (ΔG) of NO binding of -15 to -16 kcal/mol,[1-4] highly favorable with respect to association of NO. The binding constant of NO to *ferric* heme-nitrosyls is significantly lower and generally ranges from 10^3 to 10^5 M^{-1}, translating to a ΔG of only -4 to -7 kcal/mol.[5-8] This difference in intrinsic binding constants is nicely illustrated by water-soluble model complexes with H_2TPPS ($TPPS^{2-}$ = tetra(4-sulfonatophenyl)porphyrin) investigated by Laverman et al.:[2] in the ferrous case, K_{eq} equals 2.3 x 10^{12} M^{-1}, which drops to 1.0 x 10^3 M^{-1} in the analogous ferric complex. Additionally, ferric heme-nitrosyl complexes are prone to a process called “reductive nitrosylation.” Due to the Fe(II)–NO^+ electronic structure of these species, the coordinated NO is actually electrophilic, and reacts with various bases including alcohols, water, amines, and thiols. This leads to the generation of

the corresponding ferrous heme-nitrosyl in the presence of excess NO.[9-11] In terms of model complex synthesis, the reactivity and instability of the coordinated NO in ferric hemes constitutes a significant challenge for the preparation and characterization of model compounds for structural and spectroscopic analysis.

The first crystal structure of a ferric heme-nitrosyl complex, [Fe(TPP)(H_2O)(NO)](ClO_4), with bound water in axial position was not published until 1984 by Scheidt and co-workers.[12] While this was a significant step towards modeling ferric heme-nitrosyls in biological systems, ideal model complexes would be six-coordinate with N- or S-donor ligands to accurately model enzyme active site structure. It was not until 15 years later that the structures of a series of six-coordinate octaethylporphyrin (OEP) complexes with axial N-donor coordination (1-methylimidazole, pyrazole, indazole, pyrazine) were reported.[13] Since that time, significant spectroscopic characterization of ferric-nitrosyl complexes with neutral N-donor ligands has been performed.[13-17] Surprisingly, however, this is not the case for ferric heme-nitrosyl model complexes with anionic S-donors, as is found in P450nor. In this case, there is an added complication in the synthesis of these systems—the axial thiolate ligand is susceptible to S-nitrosylation by NO, leading to decomposition of the complex. This is unfortunate as the presence of the axial S-donor ligand is predicted to be responsible for new, interesting ferric heme-nitrosyl properties. To this end, Chapter 2 describes the preparation and characterization of six-coordinate ferric heme-nitrosyl model complexes with thiolate (S-donor) coordination. Additionally, due to the non-innocence of the Fe-S bond with respect to nitric oxide (discussed below), the formation and properties of six-coordinate iron(III) porphyrin nitrosyl complexes with anionic phenolate and acetate (O-donor) ligands are reported.

2.1. Ferric Heme-Nitrosyls with Thiolate Coordination

The first indication that the presence of an axial (proximal) thiolate ligand leads to new, interesting properties came from the crystal structure of ferric P450nor with bound NO, shown in Figure 1.3.[18] This structure exhibits a bent Fe-N-O unit with an Fe-N-O angle of ~160^{o} as described in Chapter 1. In contrast, ferric heme-nitrosyls with axial coordination of neutral N-donor ligands show linear Fe-N-O units. There are several possible explanations for this finding, including (a) a cryo-reduction of the single crystal generating a mixture of ferrous and ferric heme-nitrosyls, which would lead to a superposition of these structures with an intermediate Fe-N-O angle, (b) a steric effect of the active site pocket of the protein that would force the Fe-N-O unit to bend (as has been proposed for the Fe-C-O unit in CO-bound ferrous globins), or (c) an electronic effect. However, the crystal structure of P450nor(III)-NO is not indicative of strong steric interactions of protein side chains with the bound NO in disagreement with (b).

To date, only one ferric heme-nitrosyl model complex with thiolate coordination has been structurally characterized. This complex, [Fe(OEP)(SR-H_2)(NO)] (SR-H_2^- = S-2,6-$(CF_3CONH)_2C_6H_3$), shown in Figure 1.4, left, exhibits a bent Fe-N-O unit with an Fe-N-O angle of 160^{o}, very similar to the structure of P450nor(III)-NO.[19] This result provides direct evidence that this bending of the Fe-N-O unit in ferric heme-nitrosyls with axial thiolate coordination is caused by an electronic effect, which indicates that this is an intrinsic feature of this class of complexes. The vibrational data collected in Table 1.2 highlight another consequence of thiolate coordination to ferric heme-nitrosyls: in this case, N-O and Fe-NO stretching frequencies are typically observed at about 1820 – 1850 and 510 –

530 cm^{-1}, respectively, in different proteins. These vibrational energies are distinctively lower compared to the imidazole ligated proteins, where v(N-O) and v(Fe-NO) are found at ~1900 and ~590 cm^{-1}, respectively.[15]

Although interesting structural and vibrational differences have been highlighted between ferric heme-nitrosyls with N- versus S-donor ligands, only one model complex has been successfully characterized in solution, [Fe^{III}(SPorph)(NO)] where SPorph is a porphyrin with a tethered thiolate ligand (Figure 1.4, right).[20] This system, however, fails to act as a model for P450nor reactivity. Upon addition of a hydride source to [Fe^{III}(SPorph)(NO)], the resulting product quickly decomposes to [Fe^{II}(SPorph)(NO)], rather than the desired two-electron reduced species [Fe^{II}(SPorph)(NHO)].[20] This decomposition is hypothesized to be a result of disproportionation of two intermediately formed Fe(II)-NHO complexes into two Fe(II)-NO species and H_2. As a result, model complexes are necessary that prevent interaction of the formed ferrous-NHO species. To accomplish this task, we propose the use of bis-picket fence porphyrins to create a sterically hindered binding pocket for NO intermediates in the mechanistic cycle of P450nor. In this section, we screen porphyrins (including bis-picket fence porphyrins) and axial thiolate ligands to determine the *key factors for the formation of stable ferric porphyrin nitrosyl complexes* with thiolate coordination. Such stable complexes are a necessity for future reactivity studies.

Synthesis and Characterization of Ferric Porphyrin Thiolate Precursors

The synthesis of ferric heme-thiolate complexes has been published previously;[21-25] however, the methodology has proven difficult to apply across a series of porphyrin and thiolate ligands. As a result, we have explored alternate

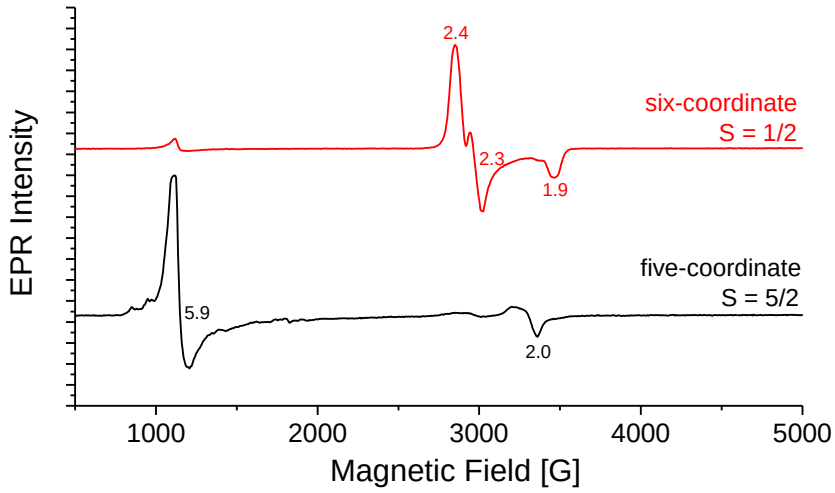

Figure 2.1. EPR spectra of [Fe(TPP)(SPh_{F4})(THF)] (top, red) and [Fe(T*o*-F_2PP)(SPh_{F4})] (bottom, black) measured at 10 K.

syntheses of [Fe(porph)(SR)] complexes where the SR^- is a thiolate derivative. Initial attempts were focused on the reaction of ferric porphyrins with the potassium salt of the thiolate ligand in the presence of 18-crown-6 as shown below.

$$[Fe(porph)(ClO_4)] + [K(18\text{-}Cr\text{-}6)]SR \rightarrow \quad (1)$$

$$[Fe(porph)(SR)] + [K(18\text{-}Cr\text{-}6)]ClO_4$$

The product complexes, [Fe(porph)(SR)], where SR^- is a simple thiophenolate ligand, were characterized by UV-visible and electron paramagnetic resonance spectroscopy. In non-coordinating solvents, the ferric product, for example [Fe(TPP)(SPh_{F4})], is five-coordinate and exhibits a high-spin (S = 5/2) axial EPR spectrum with $g_x = g_y = 5.9$ and $g_z = 2.0$ as shown in Figure 2.1, bottom. In coordinating solvents, however, the resulting six-coordinate complex [Fe(TPP)(SPh_{F4})(THF)], for example, is low-spin (S = 1/2) with $g_x = 2.36$, $g_y = 2.26$, and $g_z = 1.94$ (Figure 2.1, top). While this reaction is favorable in the sense that the iron complex remains in the air-stable ferric state, drastic differences in solubility

Scheme 2.1. Porphyrin and thiolate ligands.

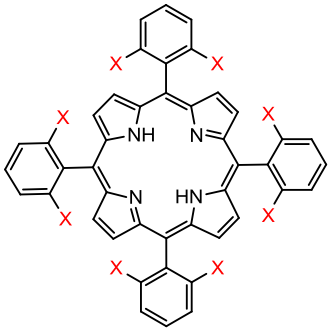

X = H (**TPP**)
= F (**To-F_2PP**)
= OCH_3 (**To-$(OCH_3)_2$PP**)

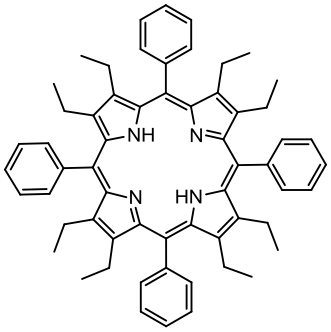

OETPP

= 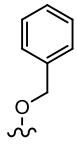 (**To-$(OBn)_2$PP**)

= 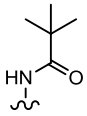 (**To-$(Am)_2$PP**)

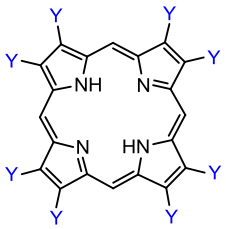

Y = Et (**OEP**)
= OCH_3 (**OOMeP**)

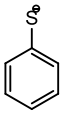

SPh^-

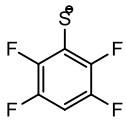

SPh_{F4}^-

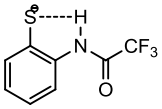

$SR\text{-}H_1^-$

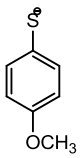

SPh_{OCH3}^-

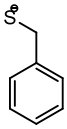

SBn^-

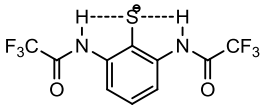

$SR\text{-}H_2^-$

between [Fe(porph)(ClO_4)] and [Fe(porph)(SR)] made this reaction difficult to apply across a wide range of porphyrin ligands. For this reason, a new synthetic procedure was developed in which the ferrous porphyrin is heated to 70°C with the corresponding disulfide in toluene to generate the desired five-coordinate ferric porphyrin complex.

$$2\ [Fe(porph)] + RS\text{-}SR \rightarrow 2\ [Fe(porph)(SR)] \qquad (2)$$

This procedure is universal over a range of porphyrins (see Scheme 2.1) and has been applied to tetraphenylporphyrin derivates (TPP), octaethylporphyrin (OEP), octamethoxyporphyrin (OOMeP), and octaethyltetraphenylporphyrin (OETPP) utilizing the simple thiolate (SR^-) ligands SPh^- SPh_{F4}^-, SPh_{OCH3}^-, and SBn^-. EPR spectroscopy at 10 K of the ferric heme thiolate complexes shows spectra typical of axial Fe(III) high-spin (S = 5/2) complexes with $g_x = g_y \sim 6$ and $g_z = 2$.

Of the complexes studied here, the only exception to the axial high-spin EPR spectra is the octaethyltetraphenylporphyrin complex [Fe(OETPP)(SPh_{F4})]. The EPR spectrum, shown in Figure 2.2, shows a rhombic S = 5/2 signal with $g_x = 6.5$, $g_y =$

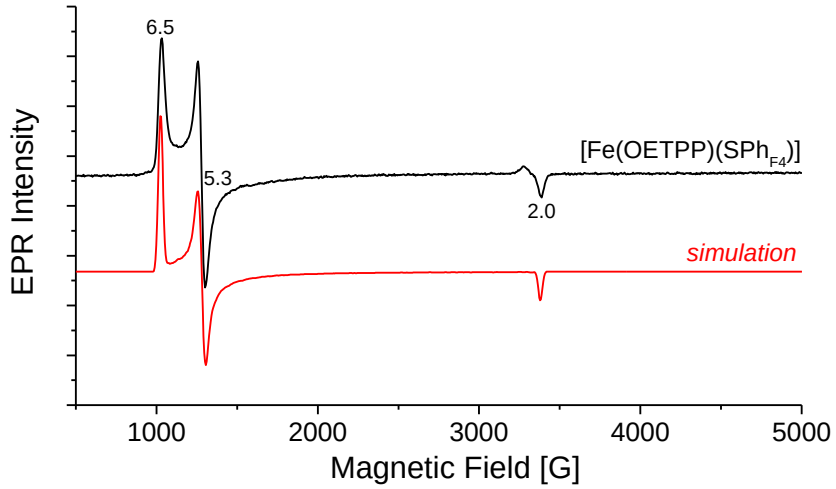

Figure 2.2. EPR spectrum of [Fe(OETPP)(SPh_{F4})] (black) in toluene, recorded at 10 K, and simulation (red) generated using the program Spin Count. Fit parameters are $g_x = 1.95$, $g_y = 2.02$, $g_z = 2.02$, D > 10 cm^{-1}, E/D = 0.0234, E/D-strain = -0.12.

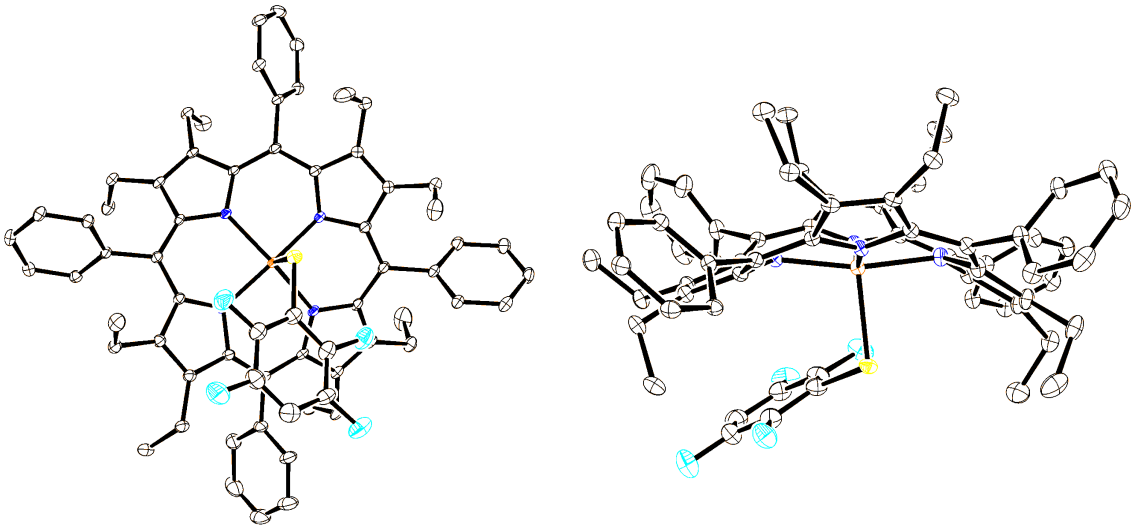

Figure 2.3. Molecular structure of [Fe(OETPP)(SPh_{F4})] in two different orientations. Hydrogen atoms and solvent molecule (hexane) are omitted for clarity. Thermal ellipsoids are shown at 30% probability. Crystal data and structure refinement are shown in Table 2.1.

5.3, and g_z = 2.0. Using the program Spin Count an E/D value of 0.023 is determined, where D > 10 cm^{-1}. To understand the inherent rhombicity in the EPR spectrum of this complex versus other [Fe(porph)(SR)] compounds, the crystal structure of [Fe(OETPP)(SPh_{F4})] was solved as shown in Figure 2.3. Interestingly, the porphyrin in this structure displays an extreme out-of-plane distortion, typical for porphyrins with both *meso*-cabon and β-pyrrole substitution. Using a normal-coordinate structural decomposition (NSD) method developed by Shelnutt and co-workers,[26-27] the type of heme distortion (saddling, ruffling, doming, waving, or propellering) can be determined. For [Fe(OETPP)($SPhF_4$)], the heme distortion is classified predominantly as saddling (B_{2u}, Scheme 2.2, left), where one pair of opposite pyrrole rings is tipped up and the other pair is tipped down. Additionally, a small contribution to the overall heme distortion comes from ruffling (B_{1u}, Scheme 2.2, right), which is characterized by a rotation of the *trans* pyrrole rings in the same direction around the Fe–$N_{pyrrole}$ bonds. The out-of-plane displacement is quantified

Table 2.1. Crystal data and structure refinement for [Fe(OETPP)(SPh_{F4})].

Empirical formula	$C_{69}H_{68}F_4FeN_4S$
Formula weight	1117.18
Temperature	85(2) K
Wavelength	1.54187 Å
Crystal system, space group	Monoclinic, P2(1)/n
Unit cell dimensions	a = 13.7738(3) Å b = 12.8877(2) Å c = 32.715(2) Å α = 90° β = 96.649(7)° γ = 90°
Volume	5768.2(4) $Å^3$
Z, Calculated density	4, 1.286 Mg/m^3
Absorption coefficient	2.906 mm^{-1}
F(000)	2352
Crystal size	0.18 x 0.13 x 0.06 mm
θ range for data collection	3.36 to 68.24°
Limiting indices	-16<=h<=16, -15<=k<=15, -39<=l<=38
Reflections collected / unique	94942 / 10516 [R(int) = 0.0487]
Completeness to θ = 68.24	99.3%
Absorption correction	Semi-empirical from equivalents
Max. and min. transmission	0.841 and 0.616
Refinement method	Full-matrix least-squares on F^2
Data / restraints / parameters	10516 / 0 / 721
Goodness-of-fit on F^2	1.067
Final R indices [I>2σ(I)]	R1 = 0.0553, ωR2 = 0.1569
R indices (all data)	R1 = 0.0600, ωR2 = 0.1620
Largest diff. peak and hole	0.581 and -0.835 $e.Å^{-3}$

by a “minimum basis” which corresponds to the total distortion simulated using displacements along the lowest frequency modes. The calculated minimum basis for [Fe(OETPP)(SPh_{F4})] is 3.3311 Å for the saddling distortion and -0.5324 Å for the ruffling distortion.

As an additional measure of out-of-plane distortion, the root mean square deviation (RMSD) from the heme plane can be determined. The RMSD is calculated from the following equation:[28]

$$RMSD = \sqrt{\frac{1}{N}\sum (dist)^2}$$

Scheme 2.2. Saddling versus ruffling distortions in heme systems. [29] (Reprinted with permission from reference [29]. Copyright 1998 American Chemical Society).

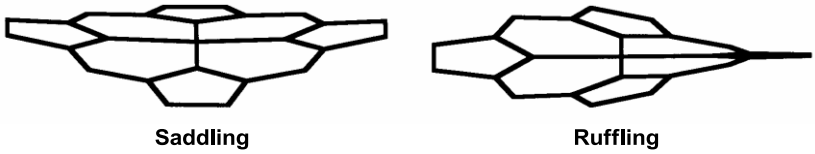

where *N* corresponds to the number of atoms that constitute the mean heme plane and *dist* is the distance (in Å) of a specific atom to the mean heme plane. The RMSD can be calculated as a 25-atom core displacement or a 4-atom *meso* carbon displacement. The 25-atom core displacement is 0.68 Å in [Fe(OETPP)(SPh_{F4})], where *planar* hemes are defined by a 25-atom core displacement of less than 0.10 Å.[28] For example, the essentially planar complex [Fe(TMP)$(MI)_2$](ClO_4) (TMP^{2-} = tetramesitylporphyrin, MI = 1-methylimidazole) has a RMSD from the 25-atom mean plane of 0.02 Å,[30] 34 times smaller than that of [Fe(OETPP)(SPh_{F4})]. The RMSD for the 4-atom *meso* carbon displacement is 0.19 Å. Finally, the Fe-S bond in [Fe(OETPP)(SPh_{F4})] is 2.364 Å and the average Fe-$N_{pyrrole}$ bond length is 1.997 Å, similar to other ferric heme complexes with thiophenolate coordination.[21]

Reaction of Nitric Oxide with Ferric Heme Thiolate Complexes

Initial attempts at formation of six-coordinate ferric heme-nitrosyls with thiolate coordination focused on tetraphenylporphyrin complexes. With the phenyl rings rotated 90^o from the heme plane, the *ortho*-phenyl position is ideally positioned to build steric bulk around the iron center. As discussed previously, this steric bulk may be crucial to preventing disproportionation of key P450nor reaction intermediates. Upon addition of ~1 equivalent nitric oxide (NO) to the high-spin five-coordinate starting material [Fe(TPP)(SPh_{F4})] at -40^{o}C in toluene, ~40% conversion

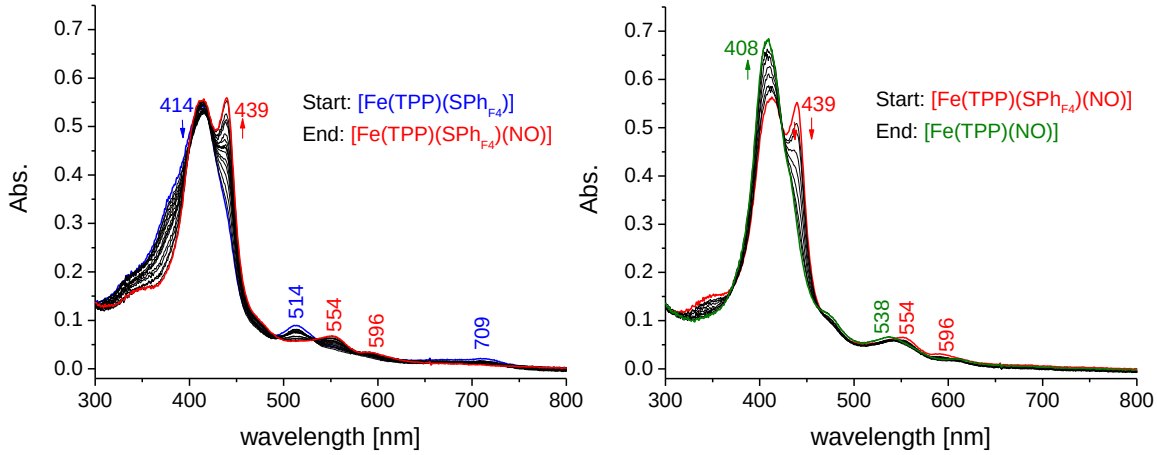

Figure 2.4. UV-Vis spectral changes for the reaction of [Fe(TPP)(SPh$_{F4}$)] with ~1 equivalent nitric oxide at -40 °C in toluene. The desired six-coordinate ferric complex [Fe(TPP)(SPh$_{F4}$)(NO)] is formed intermediately (left) before decomposition to ferrous [Fe(TPP)(NO)] (right).

to the desired product [Fe(TPP)(SPh$_{F4}$)(NO)] is observed by *in situ* UV-visible spectroscopy, see Figure 2.4. The intermediately formed ferric nitrosyl [Fe(TPP)(SPh$_{F4}$)(NO)] is characterized by an absorbance maximum at 439 nm (Soret band) and features in the Q-region at 554 and 596 nm. *In situ* IR measurements show a band at 1840 cm^{-1} corresponding to the N-O stretch of [Fe(TPP)(SPh$_{F4}$)(NO)]. The ferric nitrosyl complex, however, is highly unstable and quickly decomposes to the ferrous nitrosyl [Fe(TPP)(NO)], see Figure 2.4. Importantly, if the reaction is not performed under extremely oxygen-free conditions (O_2 < 0.1 ppm) with highly purified NO the observed decomposition product is [Fe(TPP)(NO$_2$)(NO)]. This is due, in part, to the low porphyrin concentrations (1 μM) necessary for UV-visible spectroscopy. We, and others, have shown this product to be a result of trace impurities of O_2 rather than a "legitimate" reaction product.[20]

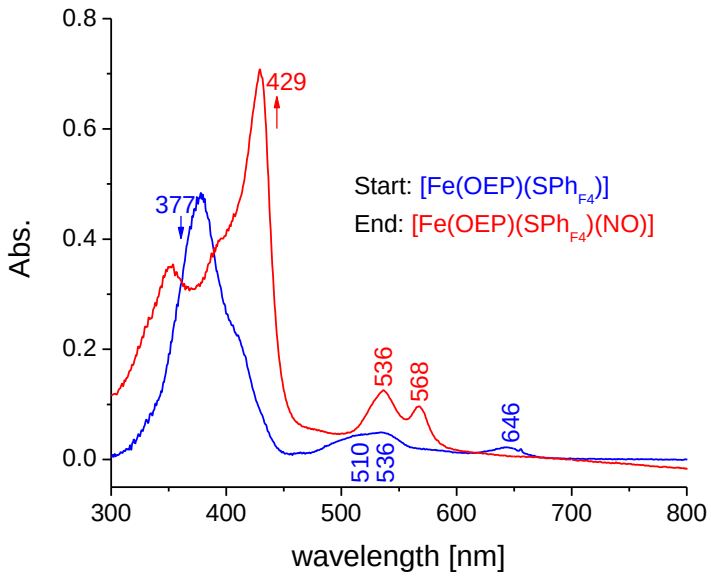

Figure 2.5. UV-Vis spectral changes for the reaction of [Fe(OEP)(SPh$_{F4}$)] with ~1 equivalent nitric oxide at -40 °C in toluene, forming the desired six-coordinate ferric complex [Fe(OEP)(SPh$_{F4}$)(NO)].

As reaction of [Fe(TPP)(SPh$_{F4}$)] with NO did not lead to a stable ferric nitrosyl complex, a slightly more electron-rich porphyrin, OEP^{2-}, was employed in an attempt to stabilize the ferric oxidation state of the product complex. The reaction of [Fe(OEP)(SPh$_{F4}$)] with NO at -40^{o}C in toluene was monitored by *in situ* UV-visible spectroscopy. As shown in Figure 2.5, upon addition of NO, the six-coordinate ferric complex [Fe(OEP)(SPh$_{F4}$)(NO)] can be observed with absorbance bands at 429, 536, and 568 nm. The desired ferric nitrosyl with thiolate coordination was formed in quantitative yield and the reaction is reversible upon bubbling the solution with inert gas. However, [Fe(OEP)(SPh$_{F4}$)(NO)] is still highly unstable with respect to free NO and quickly decomposes to [Fe(OEP)(NO)]. Five-coordinate ferric octaethylporphyrin complexes with SPh^{-}, SPh$_{OCH3}^{-}$, and SBn^{-} as ligands were also prepared. Their reactivity with NO was similar to that of the corresponding SPh$_{F4}^{-}$ complex discussed here. Several attempts were made at preparing resonance Raman samples,

however, the intrinsic instability of these compounds did not allow for a successful preparation of the samples.

The general reactivity difference between [Fe(TPP)(SPh_{F4})] and [Fe(OEP)(SPh_{F4})] is quite interesting as it represents the rare case where the porphyrin ligand, rather than the axial ligand, controls the observed reactivity. Scheme 2.3 summarizes our results where k_1 corresponds to the rate of NO reaction with iron and k_2 is the rate of NO reaction with the bound thiolate ligand. As shown in Scheme 2.3, top, the reaction of [Fe(OEP)(SPh_{F4})] with ~1 equivalent of NO is reversible at low temperature, generating the six-coordinate adduct [Fe(OEP)(SR)(NO)], which only in the presence of excess NO (presumably due to attack of free NO on the thiolate ligand) leads to decomposition and generation of [Fe(OEP)(NO)]. This corresponds to the case where k_1 >> k_2. In contrast, the reaction of [Fe(TPP)(SR)] with ~1 equivalent of NO presumably also generates the adduct [Fe(TPP)(SR)(NO)], which, however, is *intrinsically* unstable and decomposes in a NO-independent pathway as shown in Scheme 2.3. We believe

Scheme 2.3. Proposed reaction mechanisms of [Fe(porph)(SR)] complexes with NO.

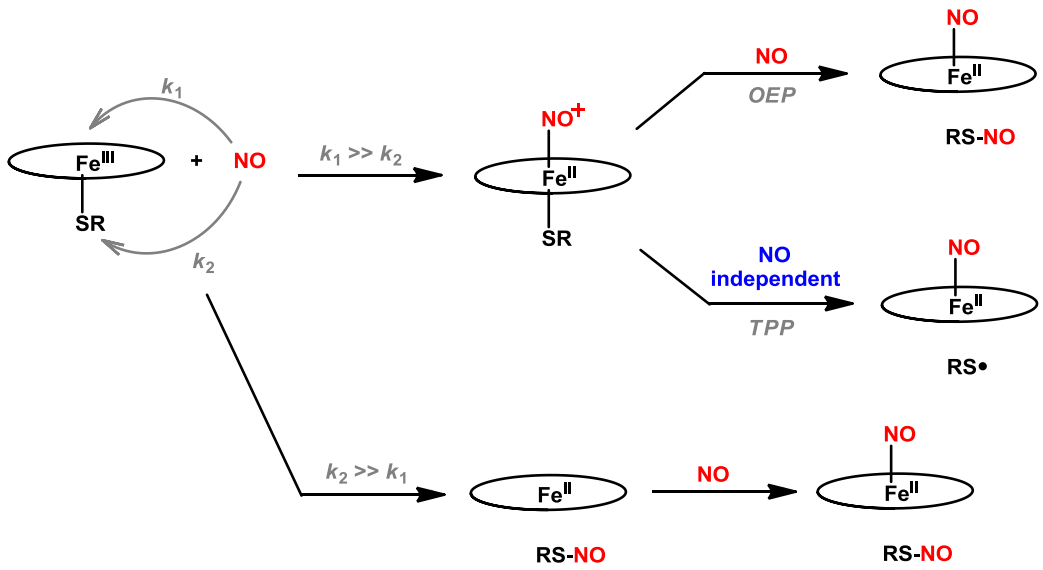

Table 2.2. Fe(III)/Fe(II) reduction potential of [Fe(porph)(SR)] complexes vs. Fc/Fc^+, measured in CH_2Cl_2 with 0.1 M TBAP. The reduction wave is reported as the process is irreversible, see Figure 2.6.

complex	E_{red} vs. Fc/Fc^+ [V]
[Fe(OETPP)(SPh_{F4})]	-1.28
[Fe(OEP)(SPh_{F4})]	-1.18
[Fe(OEP)(SPh_{OCH3})]	-1.18
[Fe(T*o*-$(Am)_2$PP)(SPh_{F4})]	-1.08
[Fe(TPP)(SPh_{F4})]	-1.06
[Fe(OOMeP)(SPh_{F4})]	-1.01
[Fe(OEP)(SR-H_2)]	-1.01

that this is due to homolytic cleavage of the Fe(III)-SR bond—in this case, generating a sulfur radical and the ferrous [Fe(TPP)(NO)] species. Alternatively, in the case of TPP, it is also possible that there is an initial competition between the iron center and the thiolate ligand for NO (where $k_1 \approx k_2$). As shown in Scheme 2.3, if $k_2 >> k_1$, NO could react first with the thiolate ligand, generating an S-nitrosothiol and a ferrous heme. The resulting ferrous complex will quickly bind NO, generating the observed ferrous nitrosyl. Whereas the coordination chemistry of Fe(OEP) and Fe(TPP) complexes and corresponding derivatives with NO has always been very similar, this is the first case where such a pronounced porphyrin *cis*-effect is observed.

We hypothesize that this difference is due to the fact that OEP^{2-} is a somewhat stronger donor to iron(III) than TPP^{2-}. This is demonstrated by the reduction potential of the corresponding ferric chloride complexes: the reduction potential of [Fe(OEP)(Cl)] is -660 mV vs. SCE, 240 mV more negative than that of [Fe(TPP)(Cl)].[31] The cyclic voltammograms of [Fe(OEP)(SPh_{F4})] and [Fe(TPP)(SPh_{F4})] were recorded and the reduction potentials are reported in Table 2.2. Only the reduction wave is reported as the CV is essentially irreversible, see

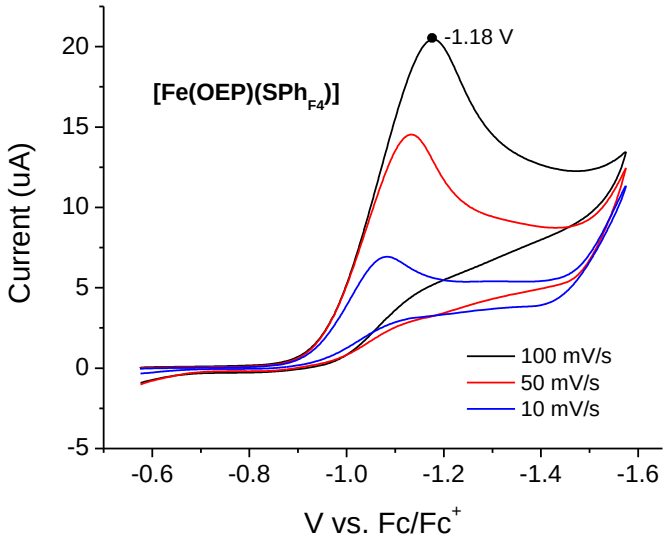

Figure 2.6. Cyclic voltammogram of [Fe(OEP)(SPh$_{F4}$)] in toluene at room temperature recorded at various scan rates.

Figure 2.6—indicating decomposition of the complex upon reduction to iron(II). As expected, the reduction of [Fe(OEP)(SPh$_{F4}$)] occurs at a lower potential than that of [Fe(TPP)(SPh$_{F4}$)] with E_{red} of -1.18 and -1.06 V vs. Fc/Fc$^+$ in CH_2Cl_2, respectively. Hence, OEP^{2-} stabilizes iron(III), and in this way, prevents the intrinsic Fe(III)-SR bond cleavage observed for TPP^{2-}.

Since OEP^{2-} complexes did show further long term stability than TPP^{2-} complexes, the eight β-pyrrole ethyl groups of OEP^{2-} were replaced with methoxy groups to further increase the electron donating ability of the porphyrin macrocycle. The corresponding ferric thiolate complex was generated, [Fe(OOMeP)(SPh$_{F4}$)] where OOMeP = octamethoxyporphyrin, and reacted with NO at -40^{o}C in toluene. Unfortunately, the OOMeP^{2-} ligand did not serve to stabilize the ferric nitrosyl species; only ~30% conversion was observed by *in-situ* UV-visible spectroscopy before decomposition occured through the usual pathway to [Fe(OOMeP)(NO)]. The

observed reactivity is supported by the reduction potential of [Fe(OOMeP)(SPh_{F4})] which is -1.01 V vs. Fc/Fc^+ (Table 2.2). The E_{red} is, surprisingly, more positive than that of [Fe(OEP)(SPh_{F4})]—indicating that eight $–OCH_3$ groups do not translate to a more electron rich iron center.

Direct Decomposition of Ferric Heme Thiolate Complexes by Nitric Oxide

Next, the reactions of *ortho*-phenyl substituted tetraphenylporphyrin model complexes [Fe(T*o*-X_2PP)(SPh_{F4})] (X = OCH_3, F), in particular of the desired bis-picket fence porphyrins (X = OBn, Am), with NO at low temperature were investigated. The reactions were, again, followed by *in-situ* UV-visible and IR spectroscopy. To our surprise, the formation of the six-coordinate NO adduct was worse in this case compared to the TPP^{2-} complex described above, and in most cases the corresponding complex [Fe(T*o*-X_2PP)($SPhF_4$)(NO)] was not even observed as an intermediate. Instead the reaction led directly to formation of ferrous

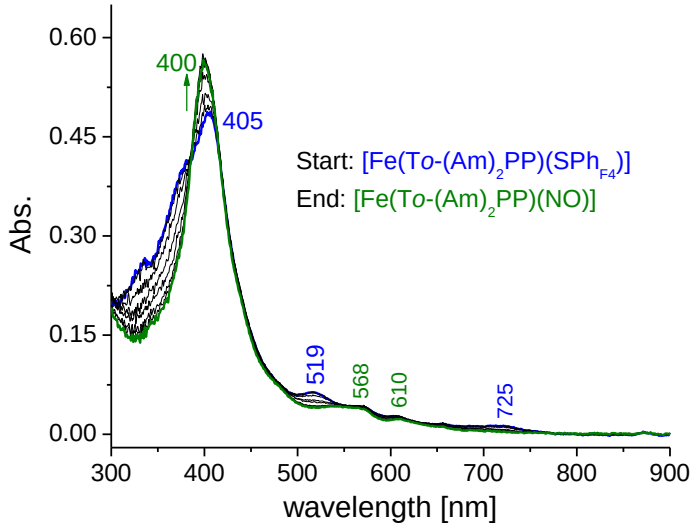

Figure 2.7. UV-Vis spectral changes for the reaction of [Fe(T*o*-$(Am)_2$PP)(SPh_{F4})] with ~1 equivalent of nitric oxide at -40 °C in toluene, forming the five-coordinate ferrous decomposition product [Fe(T*o*-$(Am)_2$PP)(NO)].

[Fe(T*o*-X_2PP)(NO)]. UV-visible spectra for the reaction of ~1 equivalent NO at -40^{o}C with [Fe(To-$(Am)_2$PP)(SPh_{F4})] are provided in Figure 2.7. This complex quickly decomposes to form the corresponding ferrous nitrosyl [Fe(T*o*-$(Am)_2$PP)(NO)] in the presence of ~1 equivalent of NO. Based on these observations, we believe that for [Fe(T*o*-X_2PP)(SPh_{F4})], a direct competition between NO binding and NO attack on the thiolate ligand occurs with $k_2 > k_1$.

Similar reactivity is observed for [Fe(OETPP)(SPh_{F4})] where $OETPP^{2-}$ corresponds to octaethyltetraphenylporphyrin, see Scheme 2.1. The product of the reaction with NO was also confirmed by EPR spectroscopy. The resulting spectrum, shown in Figure 2.8, shows g-values of 2.06, 2.04, and 2.01 with resolved three line

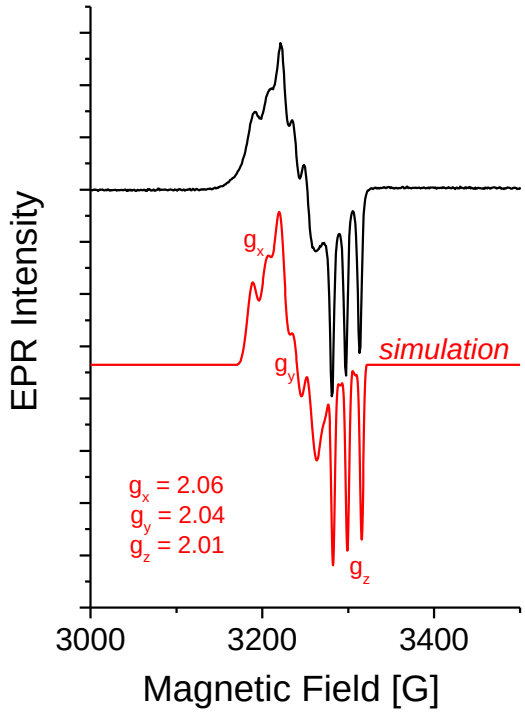

Figure 2.8. EPR spectrum of [Fe(OETPP)(NO)] (black) obtained from the reaction of [Fe(OETPP)(SPh_{F4})] with NO at -40^{o}C. The three-line hyperfine pattern on all g-values originates from the nuclear spin of the ^{14}N-atom (I = 1) of NO. The simulated spectrum was generated using the program SpinCount. Fit parameters are g_x = 2.064, g_y = 2.041, g_z = 2.005, A_x = 49 MHz, A_y = 46 MHz, A_z = 47 MHz, sg_x (g-strain) = 0.0035, sg_y = 0.0031, and sg_z = 0.0001.

hyperfine couplings of 49, 46, and 47 MHz, respectively, on each g-value. The observed hyperfine splittings originate from the nuclear spin of the ^{14}N (I = 1) atom of NO. This spectrum is characteristic of the S = 1/2 ferrous heme-nitrosyl and further confirms the product as [Fe(OETPP)(NO)]. Interestingly, resolved hyperfine interactions on all three g-values is rare for ferrous heme-nitrosyls. To further confirm the nature of the product, [Fe(OETPP)(NO)] was prepared through autoreduction of [Fe(OETPP)(Cl)] in the presence of excess NO. The EPR spectrum of the resulting complex is identical to the spectrum provided in Figure 2.8. Interestingly, upon crystallization of the product from the reaction mixture, a co-crystal that corresponds to a 77:23 mixture of the ferrous nitrosyl and the ferric chloride complex was isolated. The resulting crystal structure is shown in Figure 2.9. Typical Fe-NO and N-O bond lengths of 1.67 and 1.25 Å are observed, respectively, with a measured Fe-N-O angle of 143^{o}. Reductive nitrosylation of ferric chloride complexes is generally a reliable method for the preparation of the corresponding ferrous nitrosyls, so a

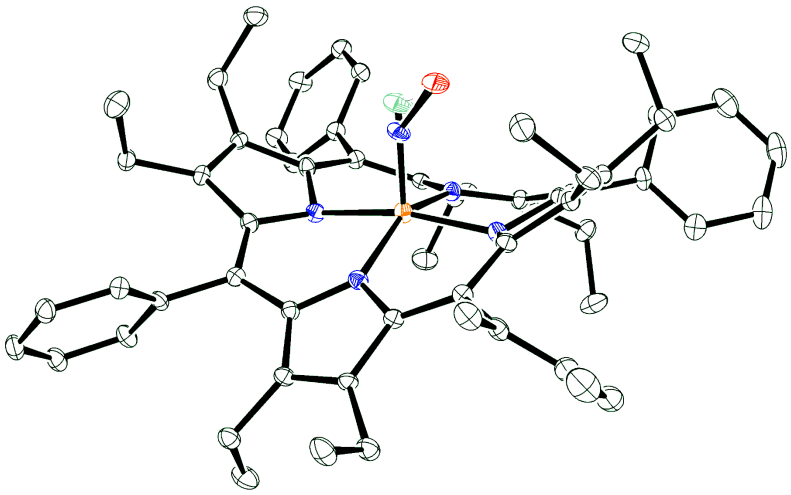

Figure 2.9. Molecular structure of a 77:23 co-crystal of [Fe(OETPP)(NO)] and [Fe(OETPP)(Cl)] obtained from the reductive nitrosylation of [Fe(OETPP)(Cl)] in CH_2Cl_2 and 10% MeOH. Hydrogen atoms and solvent are omitted for clarity. Thermal ellipsoids shown at 30% probability.

mixture of [Fe(OETPP)(Cl)] and [Fe(OETPP)(NO)] in this crystal is surprising. However, it has been shown previously that distorted hemes stabilize the ferric oxidation state.[28] Here, the highly distorted porphyrin $OETPP^{2-}$ could act to inhibit reduction of the initial $[Fe(OETPP)(NO)]^{+}$ complex. As a side note, preliminary studies on [Fe(OETPP)(NO)] indicate that this complex is unusually unstable and easily loses NO. This result is significant, as this indicates that the stability of ferrous heme-nitrosyls in biological systems could be fine tuned by the conformation (saddled, ruffled) of the heme. Normally, ferrous heme-nitrosyls are very stable and unreactive, but it might be possible to overcome this limitation through the use of distorted hemes. This point requires further study.

Decomposition of $OETPP^{2-}$ and *ortho*-phenyl substituted TPP^{2-} ferric thiolate complexes in the presence of NO is presumably occurring through NO independent homolytic cleavage of the Fe-S bond as shown in Scheme 2.3. Alternatively, in the presence of a second equivalent of NO, direct S-nitrosylation of the bound thiophenolate ligand could occur followed by fast coordination of NO to the resulting ferrous heme (Scheme 2.3, $k_2 >> k_1$). Interestingly, in contrast to TPP^{2-} where ~40% formation of the desired ferric heme-nitrosyl with thiolate coordination is observed, the complexes in this section undergo direct decomposition to the resulting ferrous species. Interestingly, the reduction potential of $[Fe(To\text{-}(Am)_2PP)(SPh_{F4})]$ is -1.08 V vs. Fc/Fc^{+}, which is nearly identical to that of the corresponding TPP^{2-} complex, see Table 2.2, while $[Fe(OETPP)(SPh_{F4})]$ has a more negative reduction potential of -1.28 V vs. Fc/Fc^{+}. So based on reduction potential we would expect a similar reactivity of NO with $[Fe(TPP)(SPh_{F4})]$ and $[Fe(To\text{-}(Am)_2PP)(SPh_{F4})]$, and significantly higher formation of the ferric nitrosyl complex with thiolate coordination for the electron-rich $OETPP^{2-}$ ligand. Thus, it is surprising that no formation of

[Fe(porph)(SPh_{F4})(NO)] was observed for $OETPP^{2-}$ and T*o*-$(Am)_2PP^{2-}$. Heme distortion and steric bulk around the iron center may have a significant effect on NO reactivity and/or Fe-S bond stability in these complexes. Whether steric or electronic effects are responsible for the observed reactivity has not been determined, but the *ortho*-phenyl substituted TPP^{2-} derivatives and the $OETPP^{2-}$ complex are extremely susceptible to cleavage of the Fe-S bond in the presence of NO.

The First STABLE Ferric Heme-Nitrosyl with Thiolate Coordination

As none of the ferric heme thiolate complexes prepared thus far are stable with respect to > 1 equivalent of NO, we decided to turn towards the only structurally characterized ferric heme-nitrosyl with thiolate ligation. [Fe(OEP)(SR-H_2)(NO)] was initially prepared by the solid state reaction of single crystals of the corresponding five-coordinate thiolate complex with NO gas.[19] While previous work in our laboratory (Dr. Florian Paulat) indicated that formation of the desired six-coordinate ferric heme-nitrosyl was possible, stability of this species was not known. Here, the solution stability of [Fe(OEP)(SR-H_2)] towards NO is explored. [Fe(OEP)(SR-H_2)] was provided by Dr. George B. Richter-Addo from the University of Oklahoma.

The reaction of ferric octaethylporphyrin (OEP) complexed to a hydrogen-bond stabilized thiolate (SR-H_2^-, see Scheme 2.1) with nitric oxide was monitored using *in situ* UV-visible absorbtion spectroscopy. [Fe(OEP)(SR-H_2)] was reacted with ~1 equivalent of nitric oxide at -40°C to form the desired [Fe(OEP)(SR-H_2)(NO)] complex in a completely reversible reaction (Figure 2.10). Excitingly, in the presence of an additional equivalent of NO, the six-coordinate ferric heme-nitrosyl <u>*does not decompose*</u> to form [Fe(OEP)(NO)]. Using resonance Raman spectroscopy (measured by Dr. Florian Paulat, data not shown), a strong band at 550 cm^{-1} is

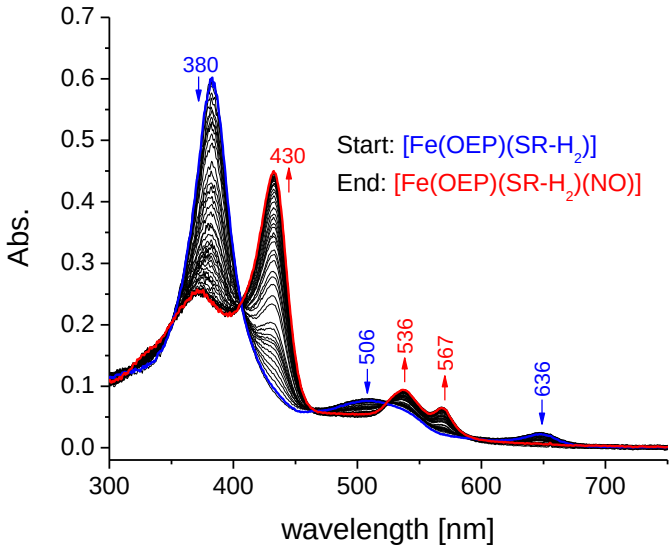

Figure 2.10. UV-Vis spectral changes for the reaction of [Fe(OEP)(SR-H_2)] with ~1 equivalent of nitric oxide at -40 °C in toluene, forming the stable six-coordinate ferric complex [Fe(OEP)(SR-H_2)(NO)].

observed for [Fe(OEP)(SR-H_2)(NO)], which shifts to 535 cm^{-1} in [Fe(OEP)(SR-H_2)($^{15}N^{18}O$)]. This band is therefore assigned to the Fe-NO stretching vibration *v*(Fe-NO) of the nitrosyl complex. The observed isotopic shift of 15 cm^{-1} is in excellent agreement with the calculated shift of 17 cm^{-1}. Interestingly, the corresponding ferric OEP^{2-} complex with a thiolate ligand stabilized by a *single* hydrogen-bond, [Fe(OEP)(SR-H_1)] (see Scheme 2.1), does not show the same stability of the Fe-S bond (data not shown) and quickly decomposes to the ferrous nitrosyl complex upon exposure to NO.

In summary, [Fe(OEP)(SR-H_2)(NO)] is the only ferric heme-nitrosyl with thiolate coordination prepared thus far that is stable with respect to excess NO. From decomposition of [Fe(OEP)(SR-H_1)] and [Fe(OEP)(SPh_{F4})] in the presence of more than one equivalent of NO (discussed above), it is clear that the *two* hydrogen-bond

stabilized thiolate ligand is crucial to this observed stability of [Fe(OEP)(SR-H_2)(NO)]. Thus, we hypothesize that SR-H_2^- is able to effectively stabilize the Fe(III)-SR^- state over an Fe(II)-SR(radical) configuration. This is critical as it is the sulfur radical that promotes degradation of the desired ferric nitrosyl either through S-nitrosylation or through homolytic cleavage of the Fe-S bond as illustrated in Scheme 2.3. Interestingly, the reduction potential of [Fe(TPP)(SR-H_2)] is 220 mV more positive than that of [Fe(TPP)(SR-H_1)].[31] This indicates that the ligand SR-H_2^- donates less electron density to the iron center than SR-H_1^- (and SPh^- derivatives). As a result, [Fe(OEP)(SR-H_2)(NO)] is less likely to form the Fe(II)-SR(radical) state responsible for homolytic cleavage of the Fe-S bond (Scheme 2.3, middle). This finding also supports the hypothesis that OEP^{2-} ferric thiolate complexes, unlike the corresponding TPP^{2-} derivatives, do not undergo homolytic Fe-S bond cleavage. Importantly, due to the stabilization of the negative charge on the sulfur atom of SR-H_2^- by the two hydrogen bonds, [Fe(OEP)(SR-H_2)(NO)] resists S-nitrosylation in the formed ferric nitrosyl complex (Scheme 2.3, top), in contrast to simple thiophenolate ligands. In conclusion, the porphyrin ligand appears to contribute to fine tuning the stability of ferric nitrosyls with thiolate coordination, but the key factor to successful preparation of stable ferric heme-nitrosyls is the presence of SR-H_2^-, a *two* hydrogen-bond stabilized thiolate ligand.

Alternate Synthesis of the Hydrogen-Bond Stabilized Thiolate Ligand

From the reaction of a variety of ferric porphyrin thiolate complexes with NO we have shown that the porphyrin ligand can be responsible for fine tuning the stability of ferric nitrosyls with thiolate coordination, but the most dramatic effects result from the nature of the thiolate ligand. All complexes synthesized thus far with

simple thiophenolate ligands decompose rapidly under slight excess of NO. The only complex that resists decomposition to the corresponding ferrous nitrosyl is [Fe(OEP)(SR-H_2)], where SR-H_2 is a thiophenolate ligand stabilized by two hydrogen bonds. Considering this, one could argue that the *key* factor in successful formation of these complexes is the nature of the thiolate ligand. Specifically, hydrogen-bond stabilized thiolate ligands are critical to the stability of these complexes. Historically these ligands have been prepared through the nitration of benzothiazole followed by ring-opening of the thiazole.[32-34] Although these ligands have been prepared for decades by Okamura et al.[35] the exact experimental protocol for the complete synthesis was actually not reported. As a result, we have developed a working procedure for the synthesis of SR-H_2 in accordance with the original method. Here, synthesis of the corresponding disulfide is ideal as reaction with ferrous hemes results in the desired ferric thiolate complexes.

Nitration of benzothiazole in the 7-position to 7-nitrobenzothiazole (**5**), as shown in Scheme 2.4, is the first step of this synthesis. The yield of this reaction is only 10% as the major product is 6-nitrobenzothioazole. Separation of 7- and 6-nitrobenzothiazole is extremely tedious and, although possible, requires around one week of column chromatography. **5** is then reduced with tin(II) chloride to 7-aminobenzothiazole (**6**) in quantitative yield followed by ring opening of the thiazole to form 2,6-diaminothiophenol (**7**) in low yield. **7** is quickly oxidized with hydrogen peroxide to the corresponding disulfide, **8**. At this point, **8** can be reacted with a variety of carbonyls (carboxylic acid, acyl chloride, etc.) to form the disulfide of SR-H_2, **9**. We have found the most reliable method for the formation of amide bonds in this system to be reaction of **9** with trifluoroacetic anhydride in the presence of triethylamine. Unfortunately, the synthesis of these sophisticated hydrogen-bond

Scheme 2.4. Original synthesis of the hydrogen-bond stabilized thiolate ligand, SR-H_2–.

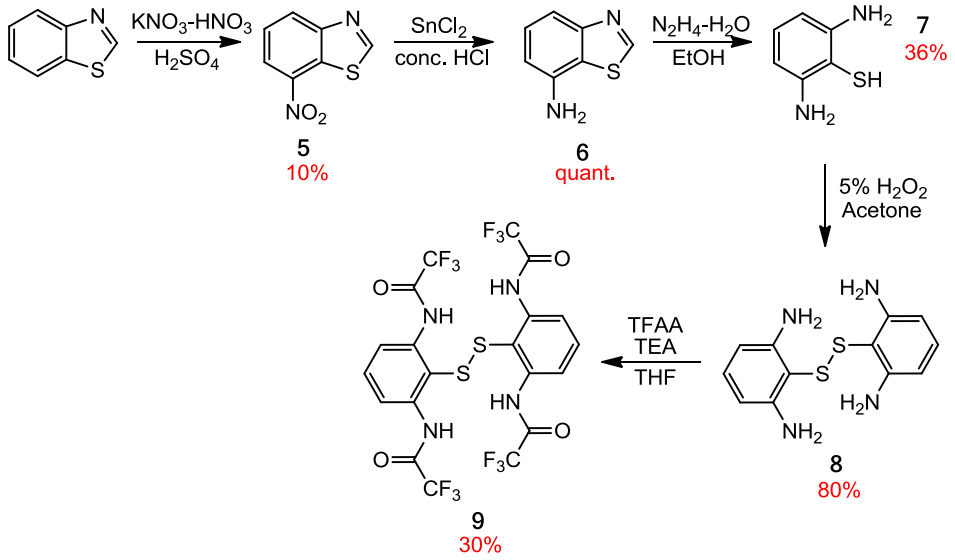

Scheme 2.5. Alternate synthesis of the hydrogen-bond stabilized thiolate ligand, SR-H_2–.

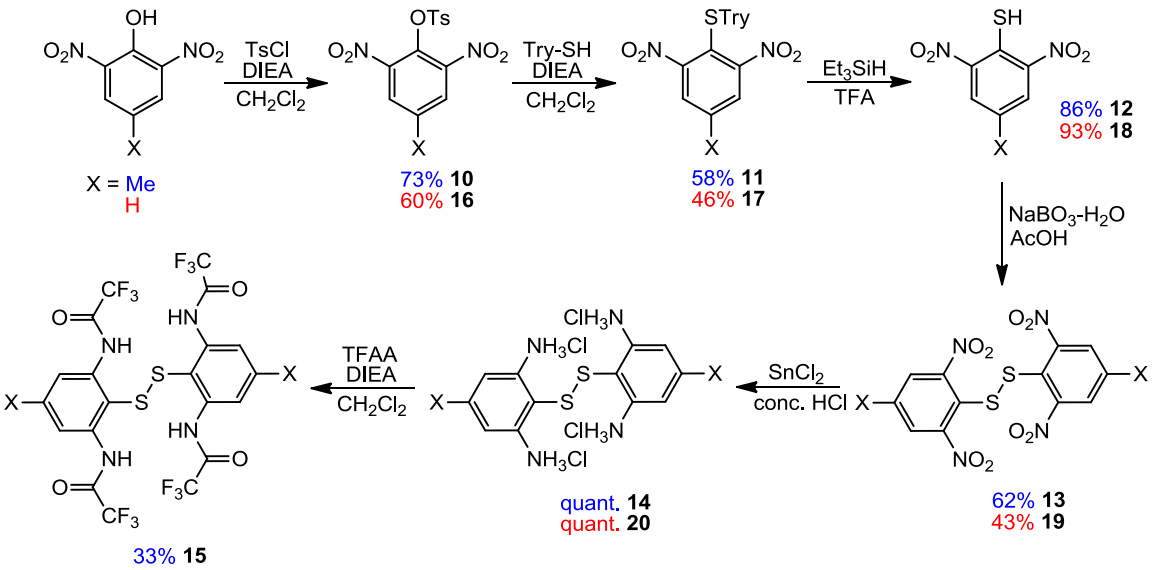

stabilized ligands is extremely tedious and low yielding. In our hands this method is five steps, four of which are purified by column chromatography, with an overall yield anywhere from 1-3% (~20 mg per two week synthesis). This is a quite poor result and to make use of this important ligand, a more efficient synthesis is necessary.

As a result, we have developed a new synthesis of this important hydrogen-bond stabilized thiolate ligand, SR-H_2^-. Our new synthesis is shown in Scheme 2.5 and yields 1 gram of ligand with column chromatography only in the final step. In this method we utilize a tosylate group to easily introduce a protected thiol to 4-methyl-2,6-dinitrophenol (X = Me) or 2,6-dinitrophenol (X = H). 4-methyl-2,6-dinitrophenol (X = Me) is reacted with tosyl chloride to give **10** in 73% yield.[36] Nucleophilic attack by triphenylmethyl mercaptan results in loss of the tosyl group and formation of **11**. When experimenting with sulfur protecting groups, triphenylmethyl (rather than benzyl, ethyl, or methyl) mercaptan was most successful due to the ease of removal by triethylsilane in TFA to form 4-methyl-2,6-dinitrothiophenol (**12**). Simple oxidation by sodium perborate monohydrate to **13** is followed by reduction of the nitro-groups to the corresponding amine hydrochloride salt, **14**, in quantitative yield. Amide bonds are then formed by reaction with trifluoroacetic anhydride to generate the desired hydrogen-bond stabilized disulfide (**15**).

The overall yield of this reaction is around 7%—nearly nine times higher than the original method (shown in Scheme 2.4). Additionally, with column chromatography only in the final step (purification of the disulfide), this method allows for considerably faster production of this important ligand.

Table 2.3. BP86/TZVP calculated geometric and vibrational parameters for [Fe(P)(SR)(NO)] complexes.

Complex	Geometric Parameters [Å] [°]				Frequencies [cm^{-1}]	
	ΔFe-NO	ΔN-O	< Fe-X-O	ΔFe-X	*ν*(N-O)	*ν*(Fe-NO)
[Fe(P)(SBn)(NO)]	1.691	1.163	165.1	2.306	1827	574
[Fe(P)(SPh_{F4})(NO)]	1.675	1.160	167.9	2.360	1849	592
[Fe(P)(SPh)(NO)]	1.685	1.162	164.4	2.343	1829	584
[Fe(P)(SPh_{OCH3})(NO)]	1.687	1.163	163.7	2.345	1825	581
[Fe(P)(SR-H_2)(NO)]	1.668	1.158	167	2.434	1859	604
[Fe(P)(SR_{pCH3}-H_2)(NO)]	1.671	1.158	165.4	2.434	1850	600
[Fe(P)(SR_{oPh}-H_2)(NO)]	1.680	1.161	161.7	2.428	1831	588
[Fe(P)(SR_{oCH3}-H_2)(NO)]	1.685	1.162	160.2	2.422	1822	585
[Fe(P)(SR_{oNMe2}-H_2)(NO)]	1.689	1.164	158.1	2.435	1809	578

Prediction of Fe-NO and N-O Stretching Frequencies in a Series of Ferric Heme-nitrosyls with Thiolate Coordination by DFT

With the hydrogen-bond stabilized thiolate ligand in hand, we are ideally suited to form the first series of stable ferric porphyrin nitrosyl complexes in future studies. This will allow us to experimentally probe the effects of thiolate ligand strength in ferric heme-nitrosyls for the first time. In the mean time, however, DFT can be used to predict how modifications of the thiolate ligand will affect the properties of the Fe-NO unit. This is important as synthetically accessible modification sites in SR-$H_2$$^-$ are several atoms removed from the coordinating sulfur atom (see below). So the question is whether such substitutions would have any measureable effect of the Fe-NO bond. DFT is ideally suited to investigate this further. The model complex [Fe(P)(SR)(NO)] was used for the calculations where P^{2-} is porphine and SR^- corresponds to a series of thiolate ligands. In this way, effects from variation of the thiolate ligand can be modeled computationally. All structures were optimized and frequencies calculated with BP86/TZVP and structural and vibrational parameters are listed in Table 2.3. Initial calculations were performed on the "simple" thiolate ligands SPh^-, SPh_{F4}^-, SPh_{OCH3}^-, and SBn^-. As expected, the Fe-

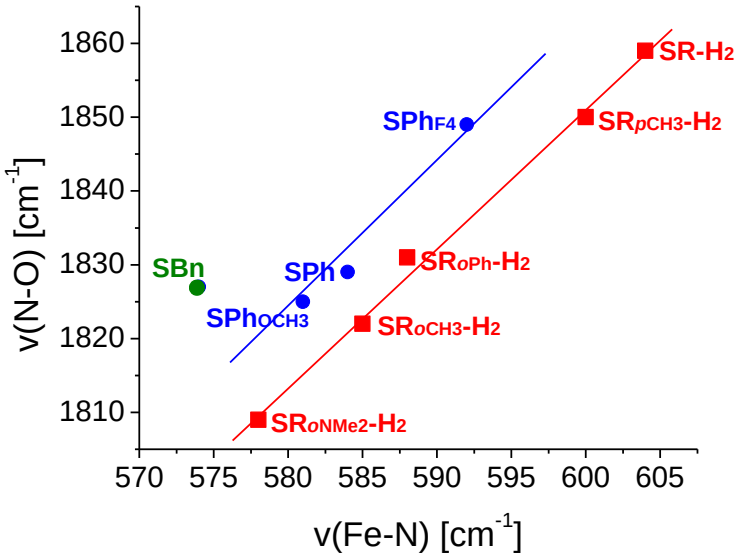

Figure 2.11. BP86/TZVP calculated N-O and Fe-NO stretching frequencies of various [Fe(P)(SR-H_2)(NO)] complexes with different thiophenolate type ligands in closed-shell ferric heme-nitrosyls. SR_{pX}-H_2 denotes variation in the 4-position of SR-H_2 whereas SR_{oX}-H_2 indicates a substitution of the -CF_3 groups on the amide substituents of SR-H_2 for X (see Figure 2.12).

NO and N-O stretching frequencies of the three corresponding thiophenolate complexes show a linear correlation as the strength of thiolate donation is varied, see Figure 2.11 (blue). The N-O stretching frequency is actually quite dependent on the nature of the thiolate and varies by 25 cm^{-1} between [Fe(P)(SPh_{F4})(NO)] and [Fe(P)(SPh_{OCH3})(NO)]! Perhaps not surprisingly, the calculated Fe-NO and N-O frequencies of [Fe(P)(SBn)(NO)] do not fall on the same line as the corresponding thiophenolate complexes (Figure 2.11, green) and instead shows a lower v(Fe-NO) stretch than is calculated for the thiophenolate derivatives.

As we have shown that ferric heme-nitrosyl complexes with “simple” thiolate coordination are quite unstable, the more interesting question is if we can build this variation of thiolate donor strength into a series of hydrogen-bond stabilized thiolate complexes. The structure of [Fe(P)(SR-H_2)(NO)] is provided in Figure 2.12 and

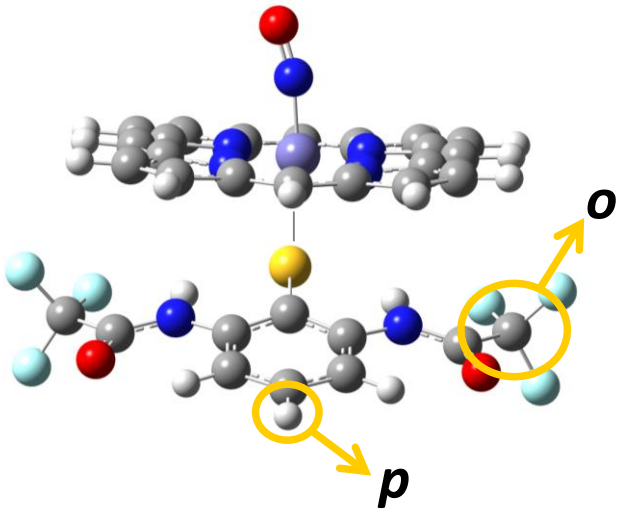

Figure 2.12. BP86/TZVP optimized structure of [Fe(P)(SR-H_2)(NO)]. Here, *p* and *o* denote a systematic variation of the 4-position and the -CF_3 groups in SR-H_2, respectively.

illustrates where synthetic modifications to the hydrogen-bond stabilized thiolate ligand are possible. Substitutions can be made at either the *para* position of the thiophenolate ring (denoted as SR_{pX}-H_2) or at the R-group of the amide bond (denoted as SR_{oX}-H_2). Only ligands that are synthetically accessible are calculated here. Excitingly, these results indicate that through the addition of electron-donating groups to the amide bonds, the N-O and Fe-NO stretching frequencies can be dramatically decreased by over 50 and 25 cm^{-1}, respectively, compared to SR-H_2^-. Here, the simple substitution of the amide bond is enough to cause drastic changes in the strength of the Fe-NO and N-O bonds. This result indicates that we can, *in theory*, successfully modulate the properties of the Fe-NO unit in our model complexes through thiolate donor strength, which may be crucial in generating key P450nor intermediates in our model systems.

2.2. The Phenolate Ligand: A More Stable Alternative to Thiolate Ligation in Ferric Heme-Nitrosyls?

Through the work discussed in Section 2.1, we propose that ferric heme thiolate complexes in the presence of nitric oxide degrade through attack of NO on the thiolate ligand to form S-nitrosothiols (SNOs) or via homolytic cleavage of the Fe-S bond. Therefore, to form stable ferric heme-nitrosyl model complexes with axial, anionic ligands to study intermediates in the catalytic cycle P450nor, it is necessary to find a way to prevent degradation or replace the anionic sulfur ligand with a more stable alternative. While we have shown that the hydrogen-bond stabilized thiolate ligand can be used successfully to prevent S-nitrosylation, the synthesis of these compounds is tedious. As such, an attractive substitute for the thiolate ligand (SR^-) used in our model complexes is the phenolate (OPh^-) ligand. Ferric heme phenolate complexes provide the anionic axial ligand found in P450nor and should, in theory, be resistant to attack of NO on the axial ligand. In addition, these complexes are easy to prepare. It is therefore surprising that the synthesis and characterization of ferric heme-nitrosyl model complexes with axial phenolate coordination has not been reported.

Additionally, ferric heme-nitrosyl complexes with axial phenolate ligation serve as model complexes for heme proteins with a proximally bound tyrosinate such as catalase.[37] Catalase is found in nearly all plants and animals and many bacteria.[38] Of crucial importance to aerobically respiring organisms, catalase performs the vital degradation of the toxic reactive oxygen species (ROS) hydrogen peroxide through the following equation:[39]

$$2\ H_2O_2 \rightarrow 2\ H_2O + O_2 \qquad (3)$$

Catalase is also responsible for ethanol oxidation to acetaldehyde in the liver.

Interestingly, NO has been shown to be a competitive inhibitor of catalase.[40] Whether this reaction is physiologically relevant has yet to be determined, but it has been proposed that pathogens could exploit this inhibition to cause increased concentrations of H_2O_2 in mammalian systems. Unfortunately, remarkably little is known about the interaction of nitric oxide with heme-tyrosinate species. The ferric nitrosyl form of catalase was recently crystallized, and the Fe-N-O angle was reported to be 165°.[41] The nitrosyl appears to be stabilized in the distal pocket through hydrogen bonding to a nearby water molecule—1.85 Å to the nitrogen and 2.50 Å to the oxygen of NO. Without model complexes, however, it is unknown if this bending of the Fe-NO unit is a result of steric crowding in the distal pocket of catalase, hydrogen bonding from the distal pocket water molecule, or an inherent property of ferric heme-nitrosyls with axial tyrosinate coordination.

To further understand the inhibition of catalase by NO and at the same time model the ferric nitrosyl intermediate of P450nor, we report the characterization of three ferric porphyrin complexes with axial phenolate coordination and their reaction with nitric oxide. This work was performed in part by the undergraduate student Breana Siljander.

EPR Spectra of Five-Coordinate Ferric Tetraphenylporphyrin Complexes with Axial Phenolate Ligation

The iron(III) tetraphenylporphyrin phenolate complexes [Fe(TPP)(OPh)], [Fe(TPP)(OPh_{F4})], and [Fe(TPP)(OR-H_2)] were synthesized by reaction of [(Fe(TPP))$_2$O] with the corresponding phenol in toluene.[31] Here, OPh^- corresponds to the simple phenolate ligand, OPh_{F4}^- is 2,3,5,6-tetraflurophenolate, and OR-H_2^- is the hydrogen-bond stabilized phenolate ligand 2,6-di(trifluoracetylamino)phenolate

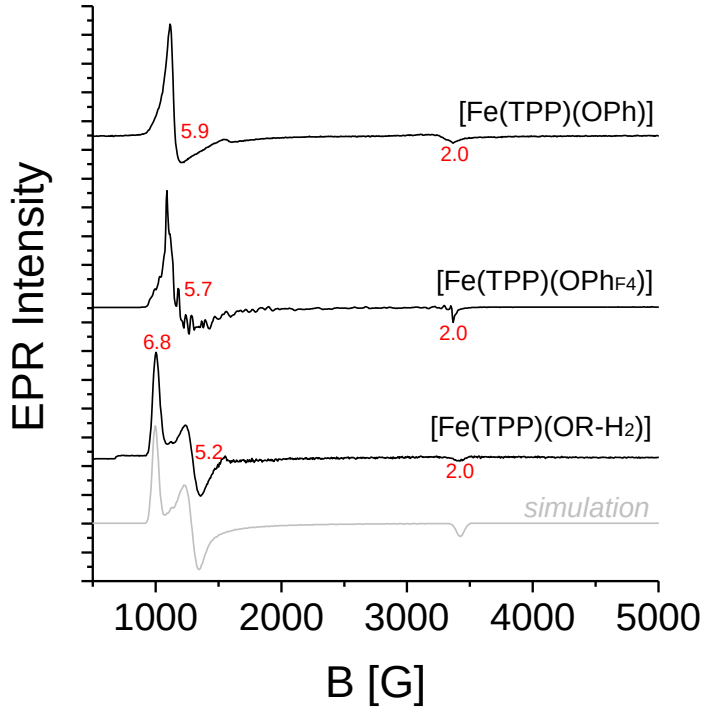

Figure 2.13. EPR spectra of [Fe(TPP)(X)] where X = OPh, OPh_{F4}, and OR-H_2 in toluene recorded at 10 K. Simulation of the spectrum of [Fe(TPP)(OR-H_2)] (bottom) generated using Spin Count with the following parameters: $g_x = g_y = g_z = 2.02$; D > 5 cm^{-1}; E/D = 0.033; E/D-strain = -0.21.

(the phenolate analog of SR-H_2–; see Scheme 2.1). A significant amount of spectroscopy has been reported in the literature for these ferric heme phenolate complexes including UV-visible, IR, and ^{1}H NMR spectroscopy.[31, 42] The electrochemistry and crystal structures of several derivatives have also been published,[31, 42] but electron paramagnetic resonance spectroscopy (EPR) has not yet been explored. To this end, we have measured the EPR spectra of [Fe(TPP)(OPh)], [Fe(TPP)(OPh_{F4})], and [Fe(TPP)(OR-H_2)] in toluene at 10 K. All three complexes show g_x and g_y values around 6, indicative of high-spin (S = 5/2) ferric heme complexes, see Figure 2.13. [Fe(TPP)(OPh)] and [Fe(TPP)(OPh_{F4})] display an axial spectrum with $g_x = g_y = 6$ and $g_z = 2$. Interestingly, for the complex [Fe(TPP)(OR-

H_2)], g_x and g_y undergo rhombic splitting. The E/D value for the spectrum is 0.033 where D > 5 cm^{-1}, obtained from simulation of the experimental EPR spectrum using the program Spin Count. This indicates a loss of symmetry in the case of [Fe(TPP)(OR-H_2)] compared to [Fe(TPP)(OPh)] and [Fe(TPP)(OPh_{F4})]. Likely, the free rotation of the phenolate ligand is highly hindered in the case of the bulky OR-H_2^- ligand.

Reaction of Five-Coordinate Ferric Porphyrin Phenolate Complexes with NO

The reaction of the five-coordinate precursors [Fe(TPP)(OPh)], [Fe(TPP)(OPh_{F4})], and [Fe(TPP)(OR-H_2)] with NO (g) has been studied at -40°C in toluene. The reactions were performed under inert atmosphere and monitored by *in situ* UV-visible spectroscopy. As shown in Figure 2.14, left, reaction of [Fe(TPP)(OPh)] with NO (g) results in a loss of the Soret band at 414 nm and the Q band at 494 nm. A new Soret band appears at 433 nm, while a prominent new band in the Q-region occurs at 544 nm. Interestingly, this new species with a Soret band

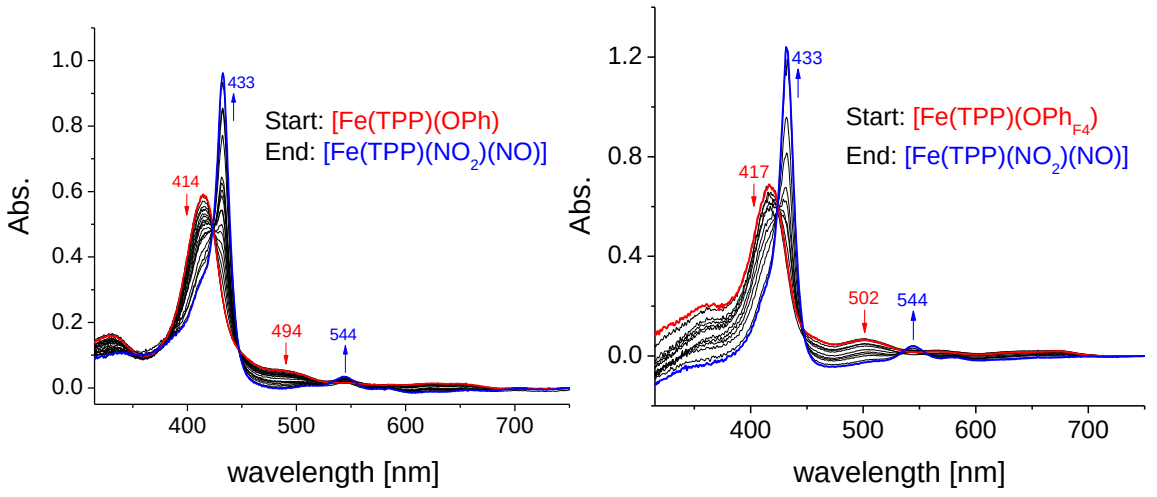

Figure 2.14. UV-visible spectra for the reaction of [Fe(TPP)(OPh)] (left) and [Fe(TPP)(OPh_{F4})] (right) with NO at -40°C in toluene. The resulting UV-visible spectra (blue) correspond to the formation of [Fe(TPP)(NO_2)(NO)].

at 433 nm corresponds to the complex [Fe(TPP)(NO_2)(NO)] as opposed to the desired product [Fe(TPP)(OPh)(NO)]. This was confirmed by separate synthesis of [Fe(TPP)(NO_2)(NO)].[15] Additionally, the N-O stretching frequency of the isolated reaction product (in a KBr pellet) is 1875 cm^{-1}—identical to the v(N-O) band of [Fe(TPP)(NO_2)(NO)] prepared separately. Interestingly, reaction of [Fe(TPP)(OPh_{F4})] with NO gave a similar result as shown in Figure 2.14, right. Decrease of starting material bands at 417 and 502 nm gave rise to absorption bands at 433 and 544 nm upon addition of NO—indicating, again, formation of [Fe(TPP)(NO_2)(NO)].

There are two feasible explanations for the formation of [Fe(TPP)(NO_2)(NO)] from the reaction of NO with [Fe(TPP)(OPh)] and [Fe(TPP)(OPh_{F4})]. First, we have shown previously that trace amounts of O_2 in the system or impure NO (g) can both lead to formation of ferric porphyrin nitro-nitrosyl complexes. Here, however, this is highly unlikely as great care was taken to keep the reaction systems free of O_2 and freshly purified NO was used for each reaction. Additionally, each reaction was repeated three times. The second possibility is that NO is able to react with the bound phenolate ligand in the same way that S-nitrosothiol formation occurs from a bound thiolate and NO, as outlined below.

$$[Fe(TPP)(OPh)] + NO \rightarrow [Fe(TPP)] + ONOPh \quad (4)$$

$$[Fe(TPP)] + NO \rightarrow [Fe(TPP)(NO)] \quad (5)$$

$$2\ ONOPh \rightarrow 2\ NO_2\cdot + Ph\text{-}Ph \quad (6)$$

$$[Fe(TPP)(NO)] + NO_2\cdot \rightarrow [Fe(TPP)(NO_2)(NO)] \quad (7)$$

In this scenario, NO attacks the five-coordinate ferric heme precursor with phenolate coordination resulting in a ferrous tetraphenylporphyrin complex and O-nitrobenzene (ONOPh). The formed ferrous complex then quickly binds free NO, and the unusual

molecule O-nitrobenzene decomposes to NO_2· and a benzene radical. Two benzene radicals will quickly combine to form biphenyl and NO_2· could then react with [Fe(TPP)(NO)] resulting in formation of the observed ferric complex [Fe(TPP)(NO_2)(NO)]. While reaction of NO_2· with five-coordinate ferrous nitrosyls has been published previously,[43] the reaction of NO with bound phenolate has not been reported. As such, the viability of this mechanism is unknown. Finally, [Fe(TPP)(OPh)(NO)] could be formed initially followed by a fast reaction with NO at the phenolate oxygen, analogous to Scheme 2.3, top.

In an attempt to prevent attack of NO on the bound phenolate ligand, we then employed the use of a hydrogen-bond stabilized phenolate ligand, OR-H_2^-. We hypothesized that this ligand would, as in the case of the thiolate complexes (see Section 2.1), provide the much needed stability to the Fe-$O_{phenolate}$ bond in the presence of NO. Interestingly, upon reaction of NO with [Fe(TPP)(OR-H_2)] at -40°C, formation of the ferrous complex [Fe(TPP)(NO)] was observed by *in situ* UV-visible

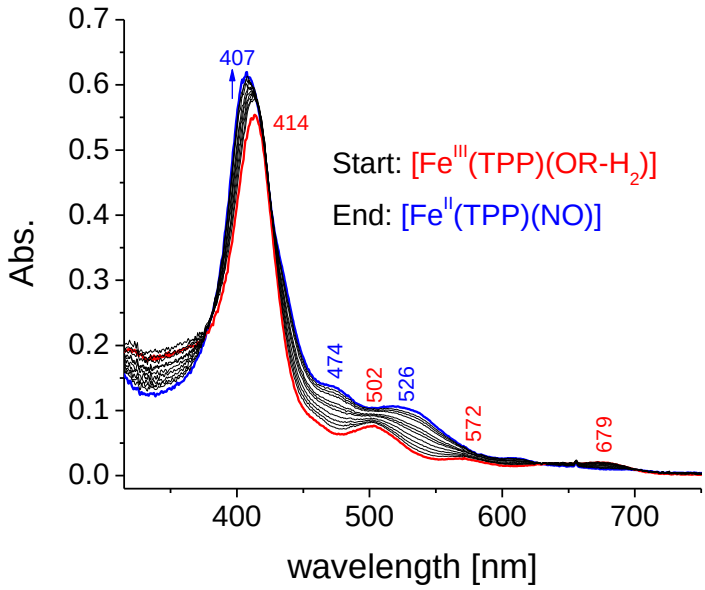

Figure 2.15. UV-visible spectra for the reaction of [Fe(TPP)(OR-H_2)] (red) with NO at -40°C in toluene. The resulting UV-visible spectrum (blue) corresponds to the formation of [Fe(TPP)(NO)].

spectroscopy as shown in Figure 2.15. The ferrous tetraphenylporphyrin nitrosyl complex is characterized by a Soret band at 407 nm with bands in the Q-region of the spectrum at 474, 526, and 612 nm in toluene. Here, key differences in reactivity between the hydrogen-bond stabilized phenolate ligand and the simple phenolate ligands are, again, observed.

The first possible explanation for formation of [Fe(TPP)(NO)] would be that NO does, in fact, attack the Fe-$O_{phenolate}$ bond in [Fe(TPP)(OR-H_2)] as implicated above. Instead of the formed O-nitrobenzene decomposing to release NO_2· (equation 4, above), however, the resulting benzene-derivative must then decompose through an alternate pathway in the presence of hydrogen bonds, stalling the reaction at the [Fe(TPP)(NO)] level (equation 5, above). An alternative mechanism can also be proposed from a reaction previously observed in myoglobin. Here, the formed ferric nitrosyl, Fe(II)-NO^+ in the ground state, has been shown to nitrosylate the *para* position of free phenol to form 4-nitrosophenol and ferrous Mb.[44] In our system we could envision that the formed Fe(II)-NO^+ complex could actually nitrosylate the *para* position of a phenolate ligand bound to another [Fe(TPP)(OR-H_2)] complex. In this way the formed [Fe(TPP)] can then bind free NO(g), resulting in [Fe(TPP)(NO)] as outlined below.

$$[Fe(TPP)(OR\text{-}H_2)] + NO \rightarrow [Fe^{II}(TPP)(OR\text{-}H_2)(NO^+)] \quad (8)$$

$$[Fe^{II}(TPP)(OR\text{-}H_2)(NO^+)] + [Fe(TPP)(OR\text{-}H_2)] \rightarrow \quad (9)$$

$$2\,[Fe(TPP)] + OR_{NO}\text{-}H_2^-$$

$$2\,[Fe(TPP)] + 2\,NO \rightarrow 2\,[Fe(TPP)(NO)] \quad (10)$$

Finally, ferric heme-nitrosyls undergo autoreduction to ferrous heme-nitrosyls in the presence of base. Here, excess phenol ligand from formation of the ferric precursor could act as the required base to perform this reduction. This is highly unlikely, however, as ^{1}H NMR of the starting complex [Fe(TPP)(OR-H_2)] does not show any free phenol.

While further studies are necessary to determine the reactivity of five-coordinate ferric heme phenolate complexes with NO, the difference in reactivity between simple phenolate ligands (OPh^-, OPH_{F4}^-) and their hydrogen-bond stabilized counterpart ($OR\text{-}H_2^-$) is interesting. This finding demonstrates the effectiveness of proximal pocket hydrogen bonds in tuning the properties and reactivites of heme active sites in proteins.

DFT Analysis of Ferric Porphyrin Nitrosyl Complexes with Axial Phenolate Ligation

Although we have been unsuccessful in isolating ferric heme-nitrosyl complexes with axial phenolate coordination, we are able to probe their properties and the effect of the hydrogen-bond stabilized phenolate ligand using DFT calculations. To this end, we have performed geometry optimizations and vibrational analysis of three [Fe(P)(X)(NO)] complexes where X is OPh^-, $OR\text{-}H_1^-$, and $OR\text{-}H_2^-$.

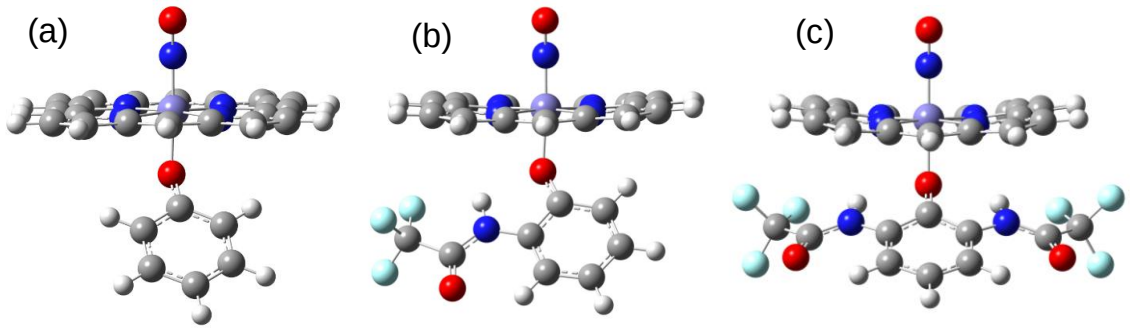

Figure 2.16. DFT optimized structures of (a) [Fe(P)(OPh)(NO)], (b) [Fe(P)(OR-H_1)(NO)], and (c) [Fe(P)(OR-H_2)(NO)] calclulated with BP86/TZVP. Bond lengths and angles are provided in Table 2.4.

Table 2.4. BP86/TZVP calculated geometric and vibrational parameters of selected ferric heme-nitrosyl complexes with axial phenolate coordination.

Complex	Geometric Parameters [Å] [°]					*v*(N-O) [cm^{-1}]
	ΔFe-NO	ΔN-O	< Fe-X-O	ΔFe-X	ΔFe-Np	
[Fe(P)(OPh)(NO)]	1.668	1.163	164.2	1.901	2.030	1838
[Fe(P)(OR-H_1)(NO)]	1.662	1.161	164.9	1.942	2.026	1848
[Fe(P)(OR-H_2)(NO)]	1.655	1.159	165.8	2.019	2.019	1858

In this way, we can systematically assess the effect of hydrogen bonds to the phenolate ligand in ferric heme-nitrosyl complexes, and compare the results to the analogous thiolate complexes (where X is SPh^-, $SR\text{-}H_1^-$, and $SR\text{-}H_2^-$) which was published previously.[45]

The BP86/TZVP optimized structures of [Fe(P)(OPh)(NO)], [Fe(P)(OR-H_1)(NO)], and [Fe(P)(OR-H_2)(NO)] are shown in Figure 2.16 with geometric parameters listed in Table 2.4. As hydrogen bonds are successively added, the Fe-$O_{phenolate}$ bond becomes longer in accordance with a decrease in the phenolate donor strength. In [Fe(P)(OPh)(NO)], the Fe-$O_{phenolate}$ bond is 1.90 Å, whereas it is 2.02 Å in [Fe(P)(OR-H_2)(NO)]. The donor strength of the phenolate also trends well with the calculated Fe-NO and N-O bond lengths. As the donor strength of the phenolate is reduced through the addition of hydrogen bonds, the Fe-NO and N-O bonds become shorter and the Fe-N-O angle becomes more linear (listed in Table 2.4). Additionally, the N-O stretching frequencies follow this trend: for X = OPh^-, the calculated N-O stretching frequency is 1938 cm^{-1} which increases systematically to 1948 and 1958 cm^{-1} for X = $OR\text{-}H_1^-$ and $OR\text{-}H_2^-$, respectively. Unfortunately, the Fe-NO stretching frequencies in these complexes are spread over several vibrational bands and as a result are difficult to assign from the BP68/TZVP frequency calculations. In summary, the stronger the donation of the axial phenolate ligand in ferric heme-nitrosyl complexes, the weaker the Fe-NO and N-O bonds become and the more the

Fe-N-O angle bends. This trend is observed for both S-[45] and O-donor anionic axial ligands.

Interestingly, the effect of added hydrogen bonds is slightly more dramatic in the case of thiolate coordination to ferric heme-nitrosyls. In the case of thiolate ligation, addition of two hydrogen bonds straightens the Fe-N-O unit by 3^{o} whereas in the corresponding phenolate complex, addition of two hydrogen bonds straightens the Fe-N-O unit by 1.6^{o}. Additionally, the calculated N-O stretching frequency increases by 30 cm^{-1} with the addition of hydrogen bonds: v(N-O) is 1829 and 1859 cm^{-1} for [Fe(P)(SPh)(NO)] and [Fe(P)(SR-H_2)(NO)], respectively. For the corresponding phenolate complexes, the increase in v(N-O) is only 20 cm^{-1}. In conclusion, the strength of the Fe-NO and N-O bonds and the geometry of the Fe-NO unit are directly related to the strength of the axial anionic donor in ferric heme-nitrosyls. This emphasizes that the bending of the Fe-NO unit in ferric catalase and P450nor is due to an electronic effect of the proximal tyrosinate/cysteinate ligand rather than steric crowding in the distal pockets of these enzymes.

2.3. The Effect of Axial Ligand Strength in Ferric Heme-Nitrosyls

While synthesis of ferric heme-nitrosyls with axial phenolate ligation has been surprisingly difficult, recently our collaborator Dr. George B. Richter-Addo from the University of Oklahoma has successfully synthesized an analogous ferric heme-nitrosyl with acetate ligation. The complex, [Fe(TPP)(AcF_3)(NO)] where AcF_3^- = trifluroracetate, was synthesized by solid state reaction of NO (g) with the five-coordinate precursor, [Fe(TPP)(AcF_3)]. The resulting complex was characterized by X-ray crystallography as shown in Figure 2.17. This complex is a model for the

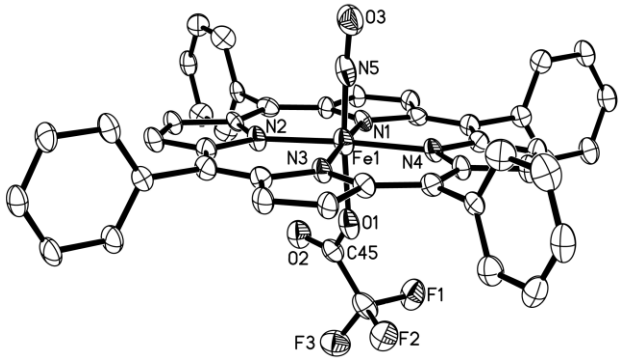

Figure 2.17. Molecular structure of [Fe(TPP)(AcF_3)(NO)] with thermal ellipsoids drawn at 35%. Hydrogen atoms have been omitted for clarity. The compound was prepared by Nan Xu and the structure was solved by Douglas R. Powell from the University of Oklahoma.[46]

ferric nitrosyl formed in catalase, as discussed in Section 2.2, and the first ferric heme-nitrosyl model complex with anionic oxygen ligation. Interestingly, the Fe-N-O unit displays an angle of 175.8^o, in contrast to the linear Fe-N-O unit observed for $[Fe(OEP)(Iz)(NO)]^+$ where Iz is the N-donor indazole.[13] This bending of the Fe-NO unit has been observed previously for [Fe(OEP)(SR-H_2)(NO)] as discussed above, and was determined to be an electronic effect of the axial thiolate ligand. The question is whether the slight bending of the Fe-N-O unit in [Fe(TPP)(AcF_3)(NO) is also an effect of the axial ligand (trifluoroacetate) or instead an effect of steric crowding imposed by the solid state crystal lattice. To this end, DFT calculations were performed on [Fe(P)(AcF_3)(NO)] and [Fe(P)(Ac)(NO)], P^{2-} = porphine and Ac^- = acetate, to determine the effect of axial ligand strength on the properties of ferric heme-nitrosyls.

The BP86/TZVP optimized structure of [Fe(P)(AcF_3)(NO)] compares well in terms of overall geometry with the crystal structure of [Fe(TPP)(AcF_3)(NO)] solved by Richter-Addo and co-workers,[46] as listed in Table 2.5. Excitingly, the calculated Fe-N-O angle of [Fe(P)(AcF_3)(NO)] is 175.8^o, identical to the experimentally determined

Table 2.5. Geometric and vibrational parameters of selected $[Fe^{III}(P)(X)(NO)]^{0/1+}$ complexes. All data are experimental unless otherwise indicated.

Complex	Geometric Parameters [Å] [°]					Frequencies [cm^{-1}]	
	ΔFe-NO	ΔN-O	< Fe-X-O	ΔFe-X	ΔFe-Np	*v*(N-O)	*v*(Fe-NO)
calc. $[Fe(P)(MI)(NO)]^+$	1.644	1.147	180	2.018	2.022	1933	639
$[Fe(OEP)(MI)(NO)](ClO_4)$	1.646	1.135	177	1.988	2.003	1921	-
$[Fe(TPP)(MI)(NO)](BF_4)$	-	-	-	-	-	1896	580
calc. $[Fe(P)(AcF_3)(NO)]$	1.637	1.155	175.8	1.936	2.025	1898	649
calc. $[Fe(P)(Ac)(NO)]$	1.656	1.158	170.6	1.905	2.027	1871	644
$[Fe(TPP)(AcF_3)(NO)]$	1.618	1.151	175.8	1.899	2.011	1907	-
calc. $[Fe(P)(NO_2)(NO)]$	1.676	1.158	165.4	2.067	2.025	1854	596
$[Fe(TPP)(NO_2)(NO)]$	1.671	1.144	169	1.998	1.996	1874	-
calc. $[Fe(P)(SPh)(NO)]$	1.685	1.162	164.4	2.343	2.027	1829	584
$[Fe(OEP)(SR\text{-}H_2)(NO)]$	1.671	1.187	160	2.356	2.01	1850	549

angle. This indicates that the bending of the Fe-NO unit is an inherent electronic property of the complex and not a result of steric restraints imposed by packing of the crystal lattice, as first proposed for $[Fe(OEP)(SR\text{-}H_2)(NO)]$ where the Fe-N-O angle is 160^o.[19] Molecular orbital analysis was performed for $[Fe(P)(AcF_3)(NO)]$ and key molecular orbitals are shown in Figure 2.18 with charge contributions listed in Table 2.6. The electronic ground state of ferric heme-nitrosyls corresponds to a Fe(II)-NO^+ electronic structure where NO is oxidized by one electron upon binding to Fe(III).[15] As a result, the main bonding interaction between the resulting Fe(II) and NO^+ species corresponds to two strong π-backbonds from the d_{xz} and d_{yz} orbitals of Fe(II) into the empty π^*_x and π^*_y orbitals of NO^+, respectively. The strength of the π-backbond is best estimated from the charge contributions of the corresponding antibonding combinations, where MO <129>, for example, has 29% d orbital and 65% π^*_y character. Additionally, a weak sigma bond is observed at lower energy between the d_{z2} (5%) orbital of Fe and the σ_{nb} (64%) orbital of NO.

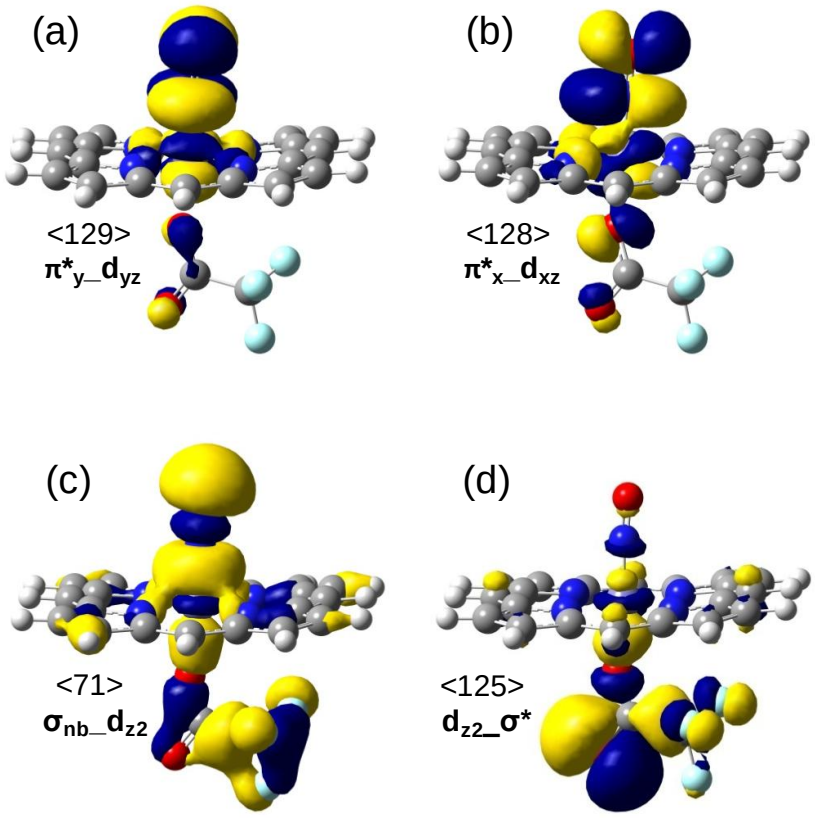

Figure 2.18. Important molecular orbitals of [Fe^{III}(P)(AcF_3)(NO)] calculated with BP86/TZVP. (a) and (b) correspond to the strong π backbonding interactions, (c) to the weak sigma interaction, and (d) to the anitbonding $\sigma^*\_d_{z2}$ type interaction involved in the bending of the Fe-N-O unit.

Table 2.6. Charge contributions of important molecular orbitals of [Fe^{III}(P)(AcF_3)(NO)] calculated with BP86/TZVP.

			Fe	N		O		O(AcF_3)
MO #	label	energy	d	s	p	s	p	s+p
<129>	$\pi^*_y\_d_{yz}$	-0.15192	28.3	0	40.8	0	24.3	0.8
<128>	$\pi^*_x\_d_{xz}$ (LUMO)	-0.15303	31.8	0.5	36.1	0.1	21.9	3.0
<127>	A_{2u} (HOMO)	-0.19883	0.7	0.2	0.1	0	0	1.5
<125>	$AcF_3^-(\sigma) + d_{z2}\_\sigma^*$	-0.2196	3.1	0.3	0.1	0	0.1	4.0
<115>	$d_{yz}\_\pi^*_y$	-0.2998	46.9	0	3.6	0	10.6	3.0
<114>	$d_{xz}\_\pi^*_x$	-0.30115	48.2	0	4.0	0	12.2	6.0
<71>	$\sigma_{nb}\_d_{z2}$	-0.53473	4.8	2.6	18.2	11.4	32.3	1.9

To understand the electronic effect of the trifluoroacetate ligand further, the structure of the corresponding acetate (Ac^-) complex, [Fe(P)(Ac)(NO)], was calculated, where Ac is expected to be a stronger donor than AcF_3^-. Interestingly, the Fe-N-O angle in this case is 170.6°, 5° more bent than for the AcF_3^- analogue, providing further evidence for a *trans* effect of the axial anionic ligand on the bound NO. This σ-*trans* effect has been reported previously, but only for a series of ferric heme-nitrosyls with strong thiolate donors as axial ligands. In this case, it was observed that an increase in donation from the axial thiolate ligand leads to a simultaneous weakening of the Fe-NO and N-O bond strengths, and an increase in bending on the Fe-N-O unit (with a minimum angle of ~160°).[45, 47] This effect was traced back to a backbond into the σ* orbital of the Fe-N-O unit (see below).

Excitingly, our new results show that this σ-*trans* effect applies to other anionic ligands as well. We have now a complete series of $[Fe(P)(X)(NO)]^{0/1+}$ complexes available with X = methylimidazole (MI), AcF_3^-, Ac^-, NO_2^-, thiophenolate (SPh^-), and phenolate (OPh^-) as shown in Figure 2.19 (geometric parameters are given in Table 2.5). The trends are striking: the stronger the donation from the axial ligand, the weaker the Fe-NO and N-O bonds become, and the more the Fe-N-O unit bends. For example, for [Fe(P)(MI)(NO)] the Fe-N-O unit is linear with Fe-NO and N-O bond lengths of 1.644 and 1.147 Å, respectively. Upon an increase in the axial ligand strength, for example NO_2^- in $[Fe(P)(NO_2)(NO)]$, the Fe-N-O unit bends to 165.4° and the Fe-NO and N-O bonds lengthen to 1.676 and 1.158 Å, respectively. The calculated N-O force constants and frequencies and Fe-N-O angles trend nicely with the strength of the axial ligand—the weaker the axial donor,

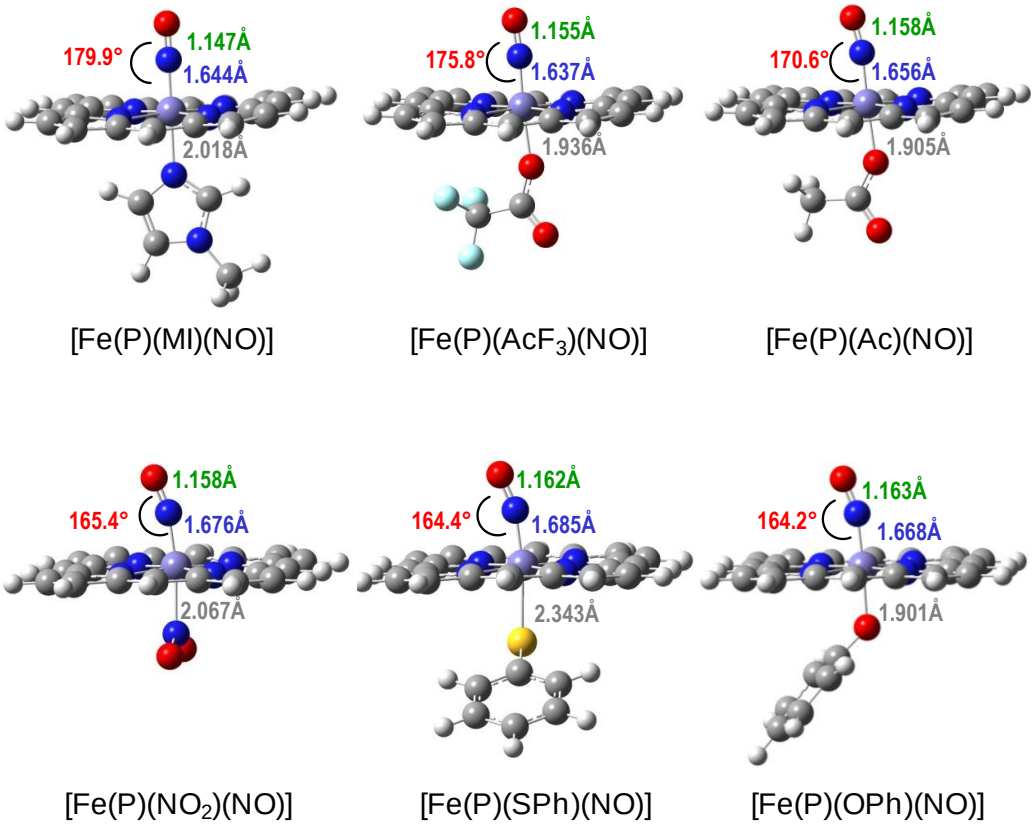

Figure 2.19. Optimized geometric parameters of $[Fe(P)(X)(NO)]^{0/1+}$ calculated with BP86/TZVP.

Table 2.7. BP86/TZVP calculated force constants and stretching frequencies of $[Fe^{III}(P)(X)(NO)]^{0/1+}$ complexes.

	Calculated Force Constants (mdyn/Å)			Calculated Frequencies [cm^{-1}]	
Complex	N-O	Fe-NO	Fe-X[a]	*v*(N-O)	*v*(Fe-NO)
$[Fe(P)(MI)(NO)]^{+}$	15.62	4.82	1.48	1933	639
$[Fe(P)(AcF_3)(NO)]$	14.87	5.14	1.62	1898	649
[Fe(P)(Ac)(NO)]	14.54	4.67	1.90	1871	644
$[Fe(P)(NO_2)(NO)]$	14.43	4.24	1.29	1854	596
[Fe(P)(SPh)(NO)]	14.03	3.99	1.16	1829	584

[a]axial ligand trans to NO

Table 2.8. Charge contributions of important molecular orbital of $[Fe^{III}(P)(X)(NO)]^{0/1+}$ calculated with BP86/TZVP.

		Fe	N		O		X	
Complex	MO	d	s	p	s	p	s+p	ref
				π-backbond				
$[Fe(P)(MI)(NO)]^+$	<124>π*_d_{yz}	27	0	42	0	26	0	[15]
	<123> π*_d_{xz}	27	0	42	0	26	0	
$[Fe(P)(AcF_3)(NO)]$	<129> π*_d_{yz}	28	0	41	0	24	1	*t.w.*
	<128> π*_d_{xz}	32	1	36	0	22	3	
$[Fe(P)(NO_2)(NO)]$	<113> π*_d_{xz}	28	0	42	0	25	0	*t.w.*
	<112> π*_d_{yz}/d_{z2}	28	1	33	0	21	4	
$[Fe(P)(SPh)(NO)]$	<130> π*_d_{z2}/d_{xz}	25	0	42	0	25	0	[45]
	<129> π*_d_{yz}_p_z(S)	32	1	28	0	17	11	
				d_{z2}/d_{xz}_σ*				
$[Fe(P)(MI)(NO)]^+$	<122>	1	0	0	0	0	2	[15]
$[Fe(P)(AcF_3)(NO)]$	<125>	3	0	0	0	0	4	*t.w.*
$[Fe(P)(NO_2)(NO)]$	<108> + <109>	15**	1	1	0	1	8	*t.w.*
$[Fe(P)(SPh)(NO)]$	<124> + <127>	15	2	1	0	1	27	[45]

the more linear the Fe-N-O angle becomes (Table 2.7).

Analysis of the molecular orbitals of [Fe(P)(SPh)(NO)] shows a weak *antibonding* σ interaction between the Fe(d_{z2}/d_{xz}) orbital and a σ*-type orbital of NO. The resulting d_{z2}/d_{xz}_σ* orbital is unoccupied. However, anionic donor ligands have a σ-donor orbital at relatively high energy (close to the d orbitals of iron) that mediates the Fe-[anionic ligand] σ bond. Importantly, this MO shows an admixture of the unoccupied σ* orbital of the Fe-N-O unit, where the degree of this admixture depends on the donor strength of the anionic ligand. This backbonding interaction into the σ* orbital of the Fe-N-O unit is responsible for the weakening of the Fe-O and N-O bonds, and the bending of the Fe-NO unit.[45] It is proposed that the Fe-N-O unit bends to decrease the unfavorable antibonding interaction between the Fe(II)

and NO^+ orbitals. The charge contributions for this d_{z2}/d_{xz}_σ* orbital for X = MI, AcF_3^-, NO_2^-, and SPh^- are listed in Table 2.8. As expected, for the strong donor X = SPh^- where the Fe-N-O bond is highly bent and the lowest N-O stretching frequency is predicted, the largest admixture of the d_{z2}/d_{xz}_σ* orbital is observed: 15% Fe(d) character and 4% NO(σ*) character as previously reported.[45] As the Fe-N-O unit straightens and the N-O stretching frequency increases, the charge contribution of this key orbital decreases accordingly. When X corresponds to the weak donor AcF_3^- the orbital contains only 3% Fe(d) character and less than 1% NO(σ*) character. For the completely linear complex [Fe(P)(MI)(NO)] with a neutral N-donor ligand this backbond into d_{z2}/d_{xz}_σ* disappears.

In summary, the nature of the axial ligand in six-coordinate ferric heme-nitrosyls controls the properties of the Fe-NO unit. Here we provide the first series of compounds to illustrate this point. The stronger the donation of the axial ligand, the weaker the Fe-NO and N-O bonds become. A weakening of the Fe-NO and N-O bonds is accompanied by a distinct bending of the Fe-N-O unit. In addition, the calculated force constants and Fe-NO and N-O stretching frequencies decrease accordingly. In this way, proteins can utilize the nature of the axial ligand in ferric heme-nitrosyls to fine tune the properties and reactivity of these species in biological systems.

Experimental

The following porphyrin ligands were synthesized as previously reported: tetraphenylporphyrin (H_2[TPP]),[48] tetrakis-5,10,15,20-(*o*-difluorophenyl)porphyrin (H_2[T*o*-F_2PP]),[49] tetrakis-5,10,15,20-(*o*-dimethoxyphenyl)porphyrin (H_2[T*o*-

$(OCH_3)_2PP]$),[50] tetrakis-5,10,15,20-(*o*-dihydroxyphenyl)porphyrin (H_2[T*o*-$(OH)_2PP]$),[50] and octaethyltetraphenylporphyrin (H_2[OETPP]).[51] Tetrakis-5,10,15,20-(2,6-dinitro-4-tert-butylphenyl)porphyrin, H_2[T*o*-$(NO_2)_2$-*p*-*t*BuPP], was prepared by BF_3-OEt catalyzed condensation of 2,6-dinitro-4-*tert*-butylbenzaldehyde[52] and pyrrole in CH_2Cl_2 as reported previously.[53] Octaethylporphyrin (H_2[OEP]) was purchased from Frontier Scientific. [Fe(OEP)(SR-H_2)] and [Fe(OEP)(SR-H_1)] were provided by Dr. George B. Richter-Addo at the University of Oklahoma. The ferric phenolate complexes [Fe(TPP)(OPh)], [Fe(TPP)(OPh_{F4})], and [Fe(TPP)(OR-H_2)] were prepared through the synthesis developed by Ueyama and co-workers.[54] Diphenyl disulfide derivatives were prepared as previously reported.[55]

Porphyrin Synthesis

3,4-dihydroxy-2,5-dimethoxytetrahydrofuran (**1**).[56] Under inert atmosphere, 12.2 g $KMnO_4$ (77 mmol) in 450 mL water was added dropwise to a stirring solution of 10 g 2,5-dihyrdo-2,5-dimethoxyfuran (77 mmol) in 100 mL THF at -10^{o}C. The $KMnO_4$ solution was added slowly enough that the temperature did not rise above 5^{o}C. After addition, the reaction was allowed to stir at room temperature for 12 hours. After 12 hours, the reaction mixture is filtered and the filtrate evaporated to an oil. The resulting oil is dissolved in ethyl acetate, dried with magnesium sulfate, rotovaped to a yellow oil, and used without further purification. Yield: 5.53 g (44%). ^{1}H NMR ($CDCl_3$): 4.92 (s, 2H); 4.16 (s, 2H); 3.41 (s, 6H).

2,3,4,5-tetramethoxytetrahydrofuran (**2**).[57] A stirring mixture of 2.6 g 3,4-dihydroxy-2,5-dimethoxytetrahydrofuran (**1**, 15.8 mmol), 5.7 g KOH, and 32 mL THF were heated at reflux for 1 hour. Then, over a 3 hour period, 4.6 mL dimethylsulfate (48

mmol) in 19 mL THF was added via disposable needle. The solution was refluxed for 16 hours. Next, 100 mL of water was added and solution was stirred for and additional hour. Water (600 mL) was added to the reaction mixture and the resulting solution was extracted with an equal portion of ether. The aqueous layer was then washed with CH_2Cl_2 four times. The organic layers were combined and evaporated to yellow oil. Yield: 2.8 g (92%). ^{1}H NMR ($CDCl_3$): 4.97 (s, 2H); 3.81 (s, 2H); 3.44 (s, 6H); 3.41 (s, 6H). LCT-MS: m/z 192.1

1-benzyl-3,4-dimethoxypyrrole (**3**). 2.8 g 2,3,4,5-tetramethoxytetrahydrofuran (**2**, 15 mmol) was added to 2.0 M HCl (2.5 mL, 5 mmol) and heated to 70°C for 30 minutes. Once the solution cooled to room temperature, a solution of 8 mL benzylamine (73 mmol) and 14.1 g sodium acetate trihydrate (104 mmol) in 220 mL $CHCl_3$ was added to the reaction mixture and stirred for 24 hours. After 24 hours, the reaction mixture was washed with saturated sodium bicarbonate, dried with magnesium sulfate, and solvent removed via reduced pressure. The resulting residue was purified via silica column with 100% CH_2Cl_2. The second fraction (emits a light green fluorescence) was collected. Yield: 1.58 g (50%). ^{1}H NMR ($CDCl_3$): 7.28 (m, 3H); 7.07 (d, 2H); 6.09 (s, 2H); 4.82 (s, 2H); 3.69 (s, 6H). LCT-MS: m/z 218.1 (M+1).

3,4-dimethoxypyrrole (**4**). While stirring, ~73 mL NH_3 was condensed into 336 mg Na(s) (14.6 mmol) in a dry ice-acetone bath. Then, 1.58 g 1-benzyl-3,4-dimethoxypyrrole (**3**, 7.3 mmol) in 7.15 mL dry THF was added dropwise to the Na(s)/NH_3 solution. As the reaction progressed, the solution turned from navy blue to orange. After stirring for 20 minutes, the reaction was warmed to room

temperature and 0.78 g ammonium chloride in 44mL H_2O was added to quench excess Na (s). The NH_3 was allowed to evaporate and the solution was extracted with CH_2Cl_2. The organic layer was evaporated to dryness and the yellow-brown oil was purified via column chromatography on silica with 100% CH_2Cl_2. The product, 3,4-dimethoxypyrrole, was in the 2nd band. Yield: 0.26 g (27%). ^{1}H NMR ($CDCl_3$): 6.93 (s, 1H); 6.20 (d, 2H); 3.74 (s, 6H).

2,3,7,8,12,13,17,18-octamethoxyporphyrin (H_2[OOMeP]). Synthesized through the condensation of 3,4-dimethoxylpyrrole (**4**) and formaldehyde as reported by Merz et al.[58] ^{1}H NMR ($CDCl_3$): 10.04 (s, 4H); 4.77 (s, 24H). UV-vis (CH_2Cl_2): 373, 477, 535, 597 nm. LCT-MS: m/z 551 (M + 1).

Tetrakis-5,10,15,20-(2,6-di-O-benzylphenyl)porphyrin (*H_2[To-(OBn)$_2$PP],* **6**). Under inert atmosphere, 100 mg H_2[T*o*-(OH)$_2$PP] (0.13 mmol), 0.67 g potassium carbonate (4.8 mmol), and 0.28 g 18-crown-6 (1 mmol) were brought to reflux in 8 mL dry DMF. Once at reflux, 0.25 mL benzyl bromide (2 mmol) was added and the reaction refluxed for 5 days. The DMF was removed via Schlenk line and the crude product column chromatographed on silica with 2:1 CH_2Cl_2:acetone. The red product band was recrystallized at -30^{o}C by dissolving in a minimum amount of CH_2Cl_2 and layering with hexanes. Yield: 111 mg (56%). ^{1}H NMR ($CDCl_3$): 8.86 (s, 8H); 7.66 (t, 4H); 6.98 (d, 8H); 6.65 (m, 40H); 4.89 (s, 16H); -2.21 (s, 2H). UV-vis (CH_2Cl_2): 421, 514, 548, 589, 646 nm. LCT-MS: m/z 1464.8.

Tetrakis-5,10,15,20-(2,6-diamino-4-tert-butylphenyl)porphyrin (*H_2[To-(NH$_2$)$_2$-p-tBuPP]*). Under inert atmosphere, 25 mg H_2[T*o*-(NO$_2$)$_2$-*p*-*t*BuPP] (0.025 mmol), 25

mg 10% palladium on carbon, and 3 mL absolute ethanol were brought to reflux. Then, 0.22 mL hydrazine hydrate in 0.75 mL absolute ethanol was added dropwise to the refluxing solution. The mixture was refluxed overnight before being poured through a pad of Celite. The Celite was rinsed with boiling ethanol and CH_2Cl_2. The filtrate was collected and rotovaped to dryness. Yield: 19 mg (77%). ^{1}H NMR ($CDCl_3$): 8.93 (s, 8H); 6.75 (s, 8H); 3.75 (s, 16 H); 1.62 (s, 36H); -2.85 (s, 2H). UV-vis (CH_2Cl_2): 424, 521, 559, 595, 656 nm. LCT-MS: m/z 959.5.

H_2[To-(Am)$_2$-p-tBuPP]. 100 mg H_2[To-(NH_2)$_2$-p-tBuPP] (0.1 mmol), 0.8 mL pyridine (0.8 mmol), and 0.8 mL pivolyl chloride (0.8 mmol) were stirred in 10 mL CH_2Cl_2 under inert atmosphere for 12 hours. After 12 hours, the reaction mixture was washed with ammonium hydroxide, twice with water, and then evaporated to dryness. The resulting purple residue was column chromatgraphed on silica with 1:1 hexanes:CH_2Cl_2. The red product band was recrystallized at -30^{o}C by dissolving in a minimum amount of CH_2Cl_2 and layering with hexanes. Yield: 119 mg (73%). ^{1}H NMR (acetone-d_6): 9.21 (s, 8H); 8.68 (s, 8H); 7.92 (s, 8H); 1.34 (s, 72H); 0.14 (s, 36H); -2.85 (s, 2H). UV-vis (CH_2Cl_2): 423, 518, 554, 596, 654 nm. LCT-MS: m/z 1632.6.

Iron Insertion and Ligand Exchange

General procedures for iron insertion and formation of the corresponding five-coordinate ferric porphyrin complexes with thiolate coordination follow:

[Fe(P)(Cl)].[49] Under inert atmosphere, porphyrin (0.1 mmol) is brought to reflux in 20 mL DMF. Once at reflux, anhydrous iron(II) chloride (1 mmol) is added and the

reaction refluxed for 3 hours. The reaction is cooled to room temperature and the DMF partioned between ethyl acetate and water. The organic layer is evaporated to dryness and chromatographed on a silica column eluted with (1) 100% CH_2Cl_2 to remove free-base porphyrin and (2) 97:3 CH_2Cl_2:methanol to removed desired product. The product band is evaporated to dryness, redissolved in CH_2Cl_2 and washed twice with 1 M HCl. The organic layer is dried with sodium sulfate and evaporated to dryness to yield a dark purple solid.

[Fe(P)(OH)] or [(Fe(P))$_2$O]. [Fe(P)(Cl)] (0.1 mmol) was dissolved in 25 mL CH_2Cl_2 and stirred with 4 M NaOH (aq). Reaction progress was monitored by UV-visible spectroscopy. Once full conversion to the product is observed (~1 hour), the organic layer is washed three times with H_2O, dried with sodium sulfate, and evaporated to dryness to yield a brown solid.

[Fe(P)]. Ethanethiol (40 mmol) and [Fe(P)(OH)] or [(Fe(P))$_2$O] (0.1 mmol) were dissolved in 10 mL toluene under inert atmosphere. The reaction is heated to 70^{o}C for 4 hours at which point the solvent and excess ethanethiol are removed via reduced pressure. The residue is redissolved in a minimum volume of toluene and layered with hexanes for recrystallization at -30^{o}C overnight. The resulting solid is filtered under inert atmosphere yielding bright purple solid.

[Fe(P)(SR)]. Under inert atmosphere, [Fe(P)] (0.1 mmol) and diphenyl disulfide (0.2 mmol) were heated to 70^{o}C in 12 mL toluene. Reaction progress was monitored by UV-visible spectroscopy. Typical reaction time at 70^{o}C is 4 hours. Alternatively, the reaction can be stirred at room temperature overnight with 10 equivalents diphenyl

disulfide. Once full formation of the ferric porphyrin thiolate complex is observed, the reaction mixture is cooled to room temperature, layered with hexanes, and stored at -30^{o}C overnight to crystallize.

[Fe(TPP)(Cl)]. UV-vis (CH_2Cl_2): 379, 416, 509, 588, 659, 692 nm.

[(Fe(TPP))$_2$O]. UV-vis (CH_2Cl_2): 407, 569, 613 nm.

[Fe(TPP)]. UV-vis (toluene): 418, 442, 542 nm.

[Fe(TPP)(SPh$_{F4}$)]. UV-vis (toluene): 417, 512, 577, 671, 715 nm.

[Fe(TPP)(NO)]. UV-vis (toluene): 408, 475, 538, 613 nm.

[Fe(OEP)(Cl)]. UV-vis (CH_2Cl_2): 379, 507, 537, 636 nm.

[(Fe(OEP))$_2$O]. UV-vis (CH_2Cl_2): 385, 558, 595 nm.

[Fe(OEP)]: UV-vis (toluene): 386, 411, 528, 562 nm.

[Fe(OEP)(SPh$_{F4}$)]. UV-vis (toluene): 376, 513, 537, 645 nm.

[Fe(OEP)(SPh$_{OMe}$)]. UV-vis (toluene):383, 521, 638 nm.

[Fe(OEP)(SBn)]. UV-vis (toluene):388, 541, 558, 637 nm.

[Fe(OEP)(NO)]. UV-vis (toluene): 392, 480, 534, 559 nm.

[Fe(OOMeP)(Cl)]. UV-vis (CH_2Cl_2): 318, 370, 467, 651 nm.

[Fe(OOMeP)(OH)]. UV-vis (CH_2Cl_2): 370, 455, 562, 590 nm.

[Fe(OOMeP)]. UV-vis (toluene): 384, 527, 564 nm.

[Fe(OOMeP)(SPh$_{F4}$)]. UV-vis (toluene): 381, 513, 653 nm.

[Fe(OOMeP)(NO)]. UV-vis (toluene): 385, 484, 528, 561 nm.

[Fe(OETPP)(Cl)]. UV-vis (CH_2Cl_2): 399, 445, 540, 580, 694 nm.

[Fe(OETPP)(OH)]. UV-vis (CH_2Cl_2): 436, 492, 697 nm.

[Fe(OETPP)]. UV-vis (toluene): 436, 467, 574 nm.

[Fe(OETPP)(SPh_{F4})]. UV-vis (toluene): 415, 577 nm.

[Fe(OETPP)(NO)]. UV-vis (toluene): 431, 577 nm.

[Fe(To-$(OBn)_2$PP)(Cl)]. UV-vis (CH_2Cl_2): 376, 423, 511, 586, 655, 690 nm.

[Fe(To-$(OBn)_2$PP)(OH)]. UV-vis (toluene): 420, 500 (broad), 581, 631 nm.

[Fe(To-$(OBn)_2$PP)]. UV-vis (toluene): 420, 444, 541 nm.

[Fe(To-$(OBn)_2$PP)(SPh_{F4})]. UV-vis (toluene): 424, 509, 583, 654, 687 nm.

[Fe(To-$(OBn)_2$PP)(NO)]. UV-vis (toluene): 409, 476, 545 nm.

[Fe(To-$(Am)_2$-p-tBuPP)(Cl)]. UV-vis (CH_2Cl_2): 381, 422, 515, 595, 654, 692 nm.

[Fe(To-$(Am)_2$-p-tBuPP)(OH)]. UV-vis (toluene): 413, 573, 612 nm.

[Fe(To-$(Am)_2$-p-tBuPP)]. UV-vis (toluene): 409, 551 nm.

[Fe(To-$(Am)_2$-p-tBuPP)(SPh_{F4})]. UV-vis (toluene): 406, 523, 569, 612, 723 nm.

[Fe(To-$(Am)_2$-p-tBuPP)(NO)]. UV-vis (toluene): 399, 486, 547, 619 nm.

[Fe(To-F_2PP)(Cl)]. UV-vis (CH_2Cl_2): 368, 412, 506, 580, 640 nm.

[Fe(To-F_2PP)(OH)]. UV-vis (CH_2Cl_2): 410, 569 nm.

[Fe(To-F_2PP)]. UV-vis (THF): 422, 542 nm.

[Fe(To-F_2PP)(SPh_{F4})]. UV-vis (toluene): 411, 510, 573 nm.

[Fe(To-F_2PP)(NO)]. UV-vis (THF): 410, 472, 548 nm.

[Fe(To-$(OCH_3)_2$PP)(Cl)]. UV-vis (CH_2Cl_2): 380, 416, 508, 591, 656, 689 nm.

[Fe(To-$(OCH_3)_2$PP)(OH)]. UV-vis (CH_2Cl_2): 416, 506, 584, 642 nm.

[Fe(To-$(OCH_3)_2$PP)]. UV-vis (toluene): 418, 437, 537 nm.

[Fe(To-$(OCH_3)_2$PP)(SPh_{F4})]. UV-vis (CH_2Cl_2): 417, 508, 583 nm.

Crystallization of [Fe(OETPP)(SPh_{F4})]. 25 mg [Fe(OETPP)] and 283 mg bis(2,4,5,6-tetrafluorophenyl) disulfide were stirred at room temperature in 2 mL toluene for 16 hours. The flask was layered with 4mL hexane and allowed to stand for 3 days. After 3 days, crystals suitable for X-ray analysis were obtained.

Thiolate Ligand, SR-H_2^-, Synthesis

7-Nitrobenzothiazole (**5**)*.* 200 mL conc. H_2SO_4 was cooled to 10^{o}C in a 500 mL RBF. 16 mL benzothiazole was added dropwise to the H_2SO_4 via addition funnel. The solution became a cloudy light brown. In a separate flask, 1.55 g KNO_3 ws added to 100 mL HNO_3 and stirred until all KNO_3 was dissolved. The KNO_3-HNO_3 solution was then added dropwise via addition funnel to the benzothiazole-H_2SO_4 mixture. The reaction was allowed to stir at 10^{o}C for 1.5 hours and then at room temperature overnight. After stirring overnight, the reaction mixture was poured over ice and a yellow precipitate formed. The yellow precipitate was filtered and dissolved in ethyl acetate. The organic layer was washed with NaCl (aq) and dried with Na_2SO_4. The organic layer was rotovaped to dryness and recrystallized with ethanol (heat on a stir plate until all solid dissolved, let cool overnight). Brown crystals of 6-nitrobenzothiazole were filtered and recrystallized in ethanol a second time. The orange filtrate from both recrystallizations was retained and rotovaped to dryness. The resulting solid was purified on neutral alumina with 1:2 CH_2Cl_2:hexane. Product was dry loaded on an alumina column in silica (residue dissolved in acetone/silica slurry and carefully rotovaped to a dry powder). The product, 7-nitrobenzothiazole,

elutes in the first band and 6-nitrobenzothiazole elutes in the second. The yield of this reaction is very low as the major product of this reaction is 6-nitrobenzothiazole rather than the desired 7-nitrobenzothiazole. Yield: 2.624 g (10%). ^{1}H-NMR ($CDCl_3$): 9.20 (s, 1H); 8.50-8.48 (dd, 2H); 7.73 (t, 1H).

6-nitrobenzothiazole: ^{1}H-NMR ($CDCl_3$): 9.27 (s, 1H); 8.93 (s, 1H); 8.41 (d, 1H); 8.26 (d, 1H)

7-Aminobenzothiazole (**6**). 5.65 g $SnCl_2$ and 20 mL conc. HCl were placed in a 50 mL RBF and heated to 40^{o}C while stirring. The solution was heated to 55^{o}C and 0.91 g of 7-nitrobenzothiazole (**5**) was added slowly. Once all 7-nitrobezothiazole was added, the reaction was heated to 65^{o}C for 1 hour and then put on ice and left overnight to stir. Reaction progress was monitored by mini-extraction with water/$CHCl_3$ and then TLC on silica in 100% $CHCl_3$. After stirring overnight, 50 mL DI H_2O was added and the pH adjusted to 12 with ~4 M NaOH. The product was extracted from the aqueous layer with 100 mL ether and 2 x 100 mL $CHCl_3$. The organic layer was rotovaped to dryness. A yellow oil resulted that dried over time to a light yellow solid. Yield: quantitative (100%). ^{1}H-NMR ($CDCl_3$): 8.95 (s, 1H); 7.63 (d, 1H); 7.36 (t, 1H); 6.76 (d, 1H); 3.95 (br s, 2H). LCT MS (E+): m/z 151.1 (M+1)

2,6-Diaminobenzenethiol (**7**). 0.76 g 7-aminobenzothiazole (**6**) was dissolved in 43 mL of ethanol was placed in a 250 mL Schlenk flask fitted with condenser. The system was flushed with Ar(g) and 22 mL hydrazine hydrate was added via syringe. The reaction was brought to reflux under Ar(g) and refluxed overnight. After refluxing overnight, solvent was pulled off via Schlenk line. Care was taken not to raise temperature over 40^{o}C. The brown crude material was column

chromatographed on silica with 80:2:1 $CHCl_3$:MeOH:NH_4OH. The product band was identified by MS and solvent evaporated via Schlenk line. The obtained thiol was oxidized immediately to the disulfide. Yield: 0.26 g (36%). LCT MS (E+): m/z 139.1

Bis(2,6-diaminophenyl) Disulfide (**8**). Under an Ar(g) atmosphere, 100 mg 2,6-diaminobenzenethiol (**7**) and 2 mL acetone was cooled to 0^oC. Then 3 mL of 5% H_2O_2 in acetone was added dropwise to the cooled solution. The reaction was allowed to stir for 3.5 hours. Solvent was evaporated to dryness. Purification was performed on silica with 1:2 acetone:hexane. Product was stored under inert atmosphere. Yield: 80%. ^1H NMR ($CDCl_3$): 6.88 (t, 1H); 6.04 (d, 2H); 4.30 (br s, 4H). LCT MS(E+): m/z 279.1 (M+1)

Bis(2,6-di(trifluoracetylamino)phenyl) Disulfide (**9**).[35] LCT MS(E+): m/z 685.0 ($M+Na^+$). ^1H NMR ($CDCl_3$): 8.56 (s, 2H); 8.12(d, 2H); 7.56 (t, 1H). ^{19}F NMR ($CDCl_3$): -75.66 (s). ^{13}C NMR ($CDCl_3$): 154.69; 138.68; 134.66; 118.86; 116.90; 112.12

4-Methyl-2,6-dinitrotosylbenzene (**10**).[36] 2,6-dinitro-*p*-cresol (4.0 g, 18.2 mmol) and p-toluenesulfonyl chloride (3.8 g, 20 mmol) were dissolved in 15 mL dry CH_2Cl_2. While stirring, diisopropylethylamine 6.3 mL, 36.4 mmol) was added dropwise over the course of 10 minutes. Upon addition of diisopropylethyamine (DIEA), the solution became warm and turned from orange to red. The reaction mixture was allowed to stir at room temperature for 18 hours. After 18 hours, the solution was filtered and the precipitate was washed with cold CH_2Cl_2. The light orange solid was redissolved in ethyl acetate and washed with 10% citric acid, saturated $NaHCO_3$(aq), and brine. The organic layer was dried with sodium sulfate and evaporated to dryness. The

solid can be further purified by recrystallization from a small amount of ethyl acetate to yield 3.0 g (47%) of light yellow crystals. An additional 1.7 g of product can be obtained by evaporating all CH_2Cl_2 from the original reaction mixture filtrate under reduced pressure and redissolving in ethyl acetate. After work-up and recrystallization (as described above), the resulting overall yield is 4.7 g (73%). ^{1}H NMR (DMSO-d_6, 400 MHz): 8.27 (s, 2H), 7.65 (d, 2H), 7.50 (d, 2H), 2.48 (s, 3H), 2.45 (s, 3H). ^{1}H NMR ($CDCl_3$, 400 MHz): 7.93 (s, 2H), 7.76 (d, 2H), 7.37 (d, 2H), 2.53 (s, 3H), 2.49 (s, 3H). ^{13}C NMR (DMSO-d_6, 100 MHz): 147.44, 143.67, 140.43, 130.66, 130.52, 130.44, 129.01, 128.32, 21.14, 20.00. IR (KBr): 1548 (NO_2), 1344 cm^{-1} (NO_2).

4-Methyl-2,6-dinitro-1-S-trityl-benzene (**11**). 4-methyl-2,6-dinitro-p-tosylbenzene (**10**, 4.0 g, 11 mmol) and triphenylmethanethiol (4.7 g, 17 mmol) were dissolved in 30 mL dry CH_2Cl_2 under N_2 (g). Diisopropylethylamine (4 mL, 23 mmol) was added via syringe to the stirring solution and the reaction allowed to stir under inert atmosphere for 18 hours. After 18 hours, a yellow precipitate formed. The reaction mixture was filtered and the solid redissoved in CH_2Cl_2. The CH_2Cl_2 solution was washed with 5% NaOH (aq.), 10% citric acid, saturated $NaHCO_3$ (aq.), and brine. The organic layer was dried with sodium sulfate and evaporated to a tan solid. Yield: 2.9 g (58%). ^{1}H NMR (DMSO-d_6, 400 MHz): 7.80 (s, 2H), 7.24 (m, 9H), 7.04 (d, 6H), 2.38 (s, 3H); see Figure 2.20. ^{13}C NMR (DMSO-d_6, 100 MHz): 156.45, 142.99, 142.67, 130.00, 127.43, 127.22, 126.10, 118.16, 75.87, 20.83. IR (KBr): 1538 (NO_2), 1350 cm^{-1} (NO_2).

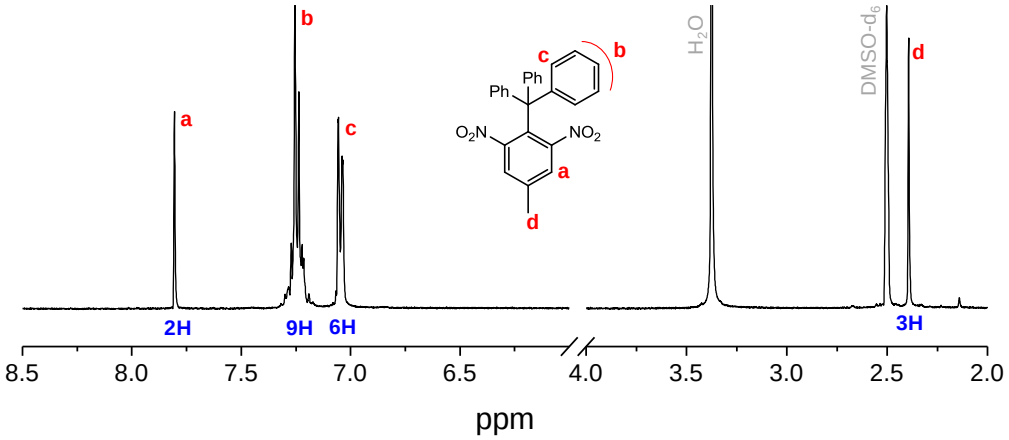

Figure 2.20. ^{1}H NMR spectrum of 4-methyl-2,6-dinitro-1-S-trityl-benzene (**11**) in DMSO-d_6.

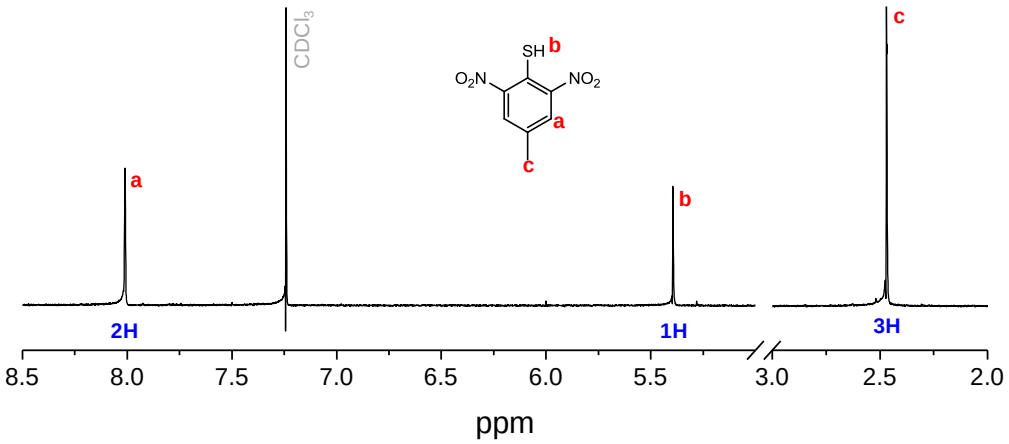

Figure 2.21. ^{1}H NMR spectrum of 4-methyl-2,6-dinitro-thiophenol (**12**) in $CDCl_3$.

4-Methyl-2,6-dinitrothiophenol (**12**). Under N_2 (g), 4-methyl-2,6-dinitro-1-S-trityl-benzene (**11**, 2.0 g) was added to 2.3 mL CH_2Cl_2. To this was added 10 mL trifluoroacetic acid and triethylsilane (2.7 mL) via syringe. The solution was stirred for 15 minutes at room temperature. All volatiles were blown off using a gentle stream of N_2 (g). The resulting yellow solid was stirred vigorously with hexanes for 1 hour (to remove triphenylmethane) and the yellow solid filtered. Yield: 0.81 g (86%). ^{1}H NMR ($CDCl_3$, 400 MHz): 8.02 (s, 2H), 5.40 (s, 1H), 2.48 (s, 3H); see Figure 2.21. ^{13}C NMR ($CDCl_3$, 100 MHz): 148.48, 136.10, 130.09, 124.16, 20.24. IR (KBr): 2581 (S-H), 1523 (NO_2), 1342 cm^{-1} (NO_2).

Bis(2,6-dinitro-4-methylphenyl) Disulfide (**13**). 4-methyl-2,6-dinitrothiophenol (**12**, 2.14 g) was dissolved in 29 mL CH_2Cl_2. To this was added sodium perborate monohydrate (1.95 g) in a mixture of glacial acetic acid (26 mL) and water (10 mL). The reaction mixture was stirred for 3 hours. Solvent was removed via reduced pressure and residue was redissolved in ethyl acetate and brine. The organic layer was separated, washed with saturated $NaHCO_3$ (aq) and brine, and dried with sodium sulfate. The solution was evaporated to dryness and the yellow product was recrystallized by dissolving in a minimum volume of CH_2Cl_2 and layering with hexanes. Yield: 1.31 g (62%). ^{1}H NMR ($CDCl_3$, 400 MHz): 7.77 (s, 4H), 2.55 (s, 6H); see Figure 2.22. ^{13}C NMR ($CDCl_3$, 100 MHz): 152.61, 143.41, 128.04, 121.41, 21.04. IR (KBr): 1540 (NO_2), 1348 cm^{-1} (NO_2).

Bis(2,6-diamino-4-methylphenyl) Disulfide·4HCl (**14**). Tin (II) chloride dihydrate (24 g) was added slowly to a mixture of bis(2,6-dinitro-4-methylphenyl) disulfide (**13**, 1.31

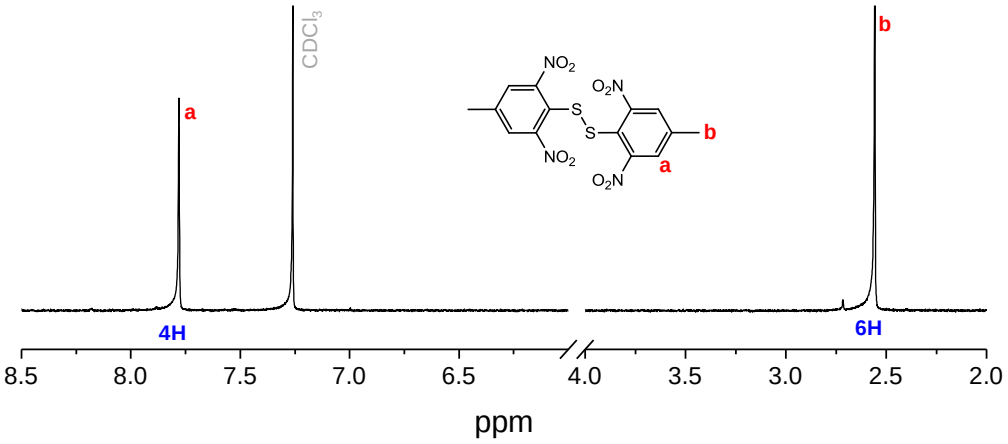

Figure 2.22. ^{1}H NMR spectrum of bis(2,6-dinitro-4-methylphenyl) disulfide (**13**) in $CDCl_3$.

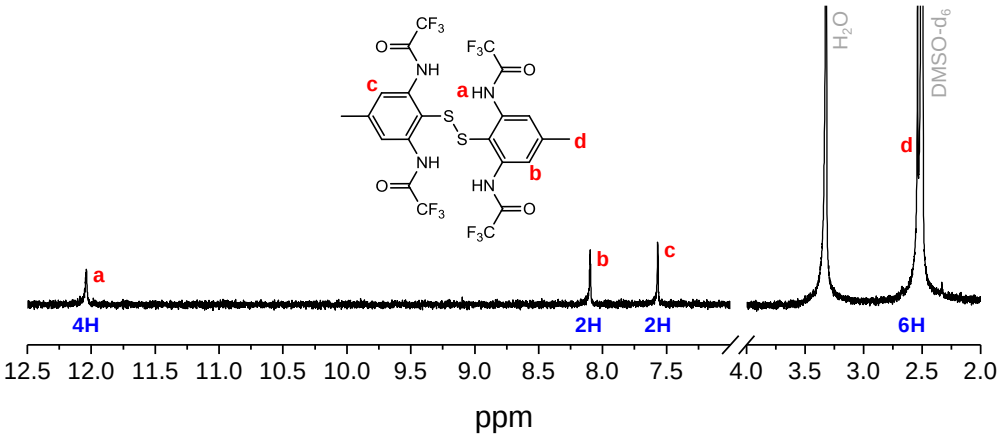

Figure 2.23. ^{1}H NMR spectrum of bis(2,6-di(trifluoracetylamino)-4-methylphenyl) disulfide (**15**) in DMSO-d_6.

g) in 40 mL concentrated hydrochloric acid. The reaction was allowed to stir 12 hours at which point and additional 5 g of tin(II) chloride dihydrate was added and the reaction stirred and additional 12 hours. The white solid was filtered and dried under reduced pressure for 12 hours, resulting in a quantitative yield. ^{1}H NMR (DMSO-d_6, 400 MHz): 6.73 (s, 4H), 4.03 (br s, 12H), 2.16 (s, 6H). IR (KBr): 2914 cm^{-1} (N-H).

Bis(2,6-di(trifluoracetylamino)-4-methylphenyl) Disulfide (**15**). Under inert atmosphere, bis(2,6-diamino-4-methylphenyl) disulfide·4HCl (**14**, 1.45 g) was dissolved in 50 mL dry CH_2Cl_2. Diisoprophylethylamine was added via syrine and the reaction cooled to 0^{o}C. Trifluoroacteic anhydride was added dropwise and the reaction stirred at 0^{o}C for 1 hour at which point the ice bath was removed and the reaction stirred an additional 12 hours. After 12 hours, 50 mL H_2O was added to quench the reaction, CH_2Cl_2 removed via evaporation under reduced pressure, and the residue was redissolved in ethyl acetate. The ethyl acetate was washed twice with H_2O, dried with sodium sulfate, and evaporated to dryness. Crude product was chromatographed on silica with 100% ethyl acetate resulting in 0.68 g (33%) of white solid. ^{1}H NMR (DMSO-d_6, 400 MHz): 12.02 (s, 4H), 8.08 (s, 2H), 7.55 (s, 2H), 2.49 (s, 6H); see Figure 2.23. ^{1}H NMR ($CDCl_3$, 400 MHz): 8.02 (s, 4H), 7.97 (s, 2H), 7.55 (s, 2H), 2.67 (s, 6H). ^{19}F NMR (CDCl3, 400MHz): -61.86 (s, 6H), -75.27 (s, 6H). IR (KBr): 3261 (N-H), 1710 cm^{-1} (C=O).

The alternate hydrogen-bonded thiolate ligand where X = H was prepared using the same synthetic procedure as X = CH_3. Characterization of compounds **16**-**19** follows:

2,6-dinitrotosylbenzene (**16**). ^{1}H NMR ($CDCl_3$, 400 MHz): 8.16 (d, 2H), 7.77 (d, 2H), 7.61 (t, 1H), 7.40 (d, 2H), 2.50 (s, 3H).

2,6-dinitro-S-tritylbenzene (**17**). ^{1}H NMR (DMSO-d_6, 400 MHz): 7.92 (d, 2H), 7.80 (t, 1H), 7.24 (m, 9H), 7.07 (d, 6H).

2,6-dinitrothiophenol (**18**). ^{1}H NMR ($CDCl_3$, 400 MHz): 8.22 (d, 2H), 7.43 (t, 1H), 5.57 (s, 1H).

Bis(2,6-dinitrophenyl) Disulfide (**19**). ^{1}H NMR ($CDCl_3$, 400 MHz): 7.98 (d, 4H), 7.69 (t, 2H).

Physical Methods

FTIR spectra were obtained from KBr pellets on a Perkin-Elmer BX spectrometer at room temperature. Resolution was set to 2 cm^{-1}. *In situ* IR measurement were recorded using a Mettler Toledo ReactIR ic10. Proton magnetic resonance spectra were recorded on a Varian Innova 400 MHz instrument. Electronic absorbance spectra were measured using an Analytical Jena Specord 600 instrument at room temperature. *In situ* UV-visible measurements were taken with a Hellma all-quartz immersion probe with 10 mm pathlength. Electron paramagnetic resonance (EPR) spectra were recorded on a Bruker X-band EMX spectrometer equipped with an Oxford Instruments liquid helium cryostat. EPR spectra were typically obtained on frozen solutions using 20 mW microwave power and 100 kHz field modulation with the amplitude set to 1 G. Sample concentrations employed were ~2 mM. Cyclic voltammograms were recorded with a CH instruments CHI660C electrochemical workstation using a three component system consisting of a platinum working electrode, a platinum auxiliary electrode, and an Ag wire pseudo-

reference electrode. CVs were measured in 0.1 M tetrabutylammonium perchlorate (TBAP) solutions in CH_2Cl_2. Potentials are reported against the measured Fc/Fc^+ couple.

Crystal structure determination was carried out using a Bruker SMART APEX CCD-based X-ray diffractometer equipped with a low temperature device and a fine focus Mo-target X-ray tube (wavelength) 0.71073 Å) operated at 1500 W power (50 kV, 30 mA). Measurements were taken at 85 K and the detector was placed 5.055 cm from the crystal. See Table 2.1 for crystallographic data and measurement parameters. The data were processed with SADABS and corrected for absorption.[59] The structure was solved and refined with the Bruker SHELXTL (vs. 2008/3) software package.[60-61]

DFT Calculations

All geometry optimizations and frequency calculations were performed with the program package Gaussian 03[62] using the BP68[63-64] functional and TZVP[65-66] basis set. Molecular orbitals were obtained from BP86/TZVP single point calculations using ORCA.[67] In Gaussian calculations, convergence was reached when the relative change in the density matrix between subsequent iterations was less that 1×10^{-8}. Molecular orbitals were plotted with the program orca_plot included in the ORCA package and visualized using GaussView. Force constants in internal coordinates were extracted from the Gaussian output using a modified version of the program Redong (QCPE 628).[68-69]

References

1. Moore, E. G.; Gibson, Q. H., *J. Biol. Chem.* **1976,** *251*, 2788-2794.

2. Laverman, L. E.; Ford, P. C., *J. Am. Chem. Soc.* **2001,** *123*, 11614-11622.

3. Scheele, J. S.; Bruner, E.; Kharitonov, V. G.; Martasek, P.; Roman, L. J.; Masters, B. S. S.; Sharma, V. S.; Magde, D., *J. Biol. Chem.* **1999,** *274*, 13105-13110.

4. Rose, E. J.; Hoffman, B. M., *J. Am. Chem. Soc.* **1983,** *105*, 2866-2873.

5. Abu-Soud, H. M.; Gachhui, R.; Raushel, F. M.; Stuehr, D. J., *J. Biol. Chem.* **1997,** *272*, 17349-17353.

6. Sharma, V. S.; Traylor, T. G.; Gardiner, R.; Mizukami, H., *Biochemistry* **1987,** *26*, 3837-3843.

7. Franke, A.; Stochel, G.; Jung, C.; Van Eldik, R., *J. Am. Chem. Soc.* **2004,** *126*, 4181-4191.

8. Hoshino, M.; Ozawa, K.; Seki, H.; Ford, P. C., *J. Am. Chem. Soc.* **1993,** *115*, 9568-9575.

9. Addison, A. W.; Stephanos, J. J., *Biochemistry* **1986,** *25*, 4104-4113.

10. Roncaroli, F.; Videla, M.; Slep, L. D.; Olabe, J. A., *Coord. Chem. Rev.* **2007,** *251*, 1903-1930.

11. Hoshino, M.; Maeda, M.; Konishi, R.; Seki, H.; Ford, P. C., *J. Am. Chem. Soc.* **1996,** *118*, 5702-5707.

12. Scheidt, W. R.; Lee, Y. J.; Hatano, K., *J. Am. Chem. Soc.* **1984,** *106*, 3191-3198.

13. Ellison, M. K.; Scheidt, W. R., *J. Am. Chem. Soc.* **1999,** *121*, 5210-5219.

14. Ellison, M. K.; Schulz, C. E.; Scheidt, W. R., *J. Am. Chem. Soc.* **2002,** *124*, 13833-13841.

15. Praneeth, V. K. K.; Paulat, F.; Berto, T. C.; DeBeer George, S.; Näther, C.; Sulok, C. D.; Lehnert, N., *J. Am. Chem. Soc.* **2008,** *130*, 15288-15303.

16. Yi, G.-B.; Chen, L.; Khan, M. A.; Richter-Addo, G. B., *Inorg. Chem.* **1997,** *36*, 3876-3885.

17. Lipscomb, L. A.; Lee, B.-S.; Yu, N.-T., *Inorg. Chem.* **1993,** *32*, 281-286.

18. Shimizu, H.; Park, S.-Y.; Gomi, Y.; Arakawa, H.; Nakamura, H.; Adachi, S.-I.; Obayashi, E.; Iizuka, T.; Shoun, H.; Shiro, Y., *J. Biol. Chem.* **2000,** *275*, 4816-4826.

19. Xu, N.; Powell, D. R.; Cheng, L.; Richter-Addo, G. B., *Chem. Commun.* **2006**, 2030-2032.

20. Suzuki, N.; Higuchi, T.; Urano, Y.; Kikuchi, K.; Uchida, T.; Mukai, M.; Kitagawa, T.; Nagano, T., *J. Am. Chem. Soc.* **2000,** *122*, 12059-12060.

21. Koch, S.; Tang, S. C.; Holm, R. H.; Frankel, R. B.; Ibers, J. A., *J. Am. Chem. Soc.* **1975,** *97*, 916-918.

22. Schappacher, M.; Ricard, L.; Fischer, J.; Weiss, R.; Bill, E.; Montiel-Montoya, R.; Winkler, H.; Trautwein, A. X., *Eur. J. Biochem.* **1987,** *168*, 419-429.

23. Tang, S. C.; Koch, S.; Papaefthymiou, G. C.; Foner, S.; Frankel, R. B.; Ibers, J. A.; Holm, R. H., *J. Am. Chem. Soc.* **1976,** *98*, 2414-2434.

24. Bryn, M. P.; Strouse, C. E., *J. Am. Chem. Soc.* **1991,** *113*, 2501-2508.

25. Ueyama, N.; Nishikawa, N.; Yamada, Y.; Okamura, T.; Oka, S.; Sakurai, H.; Nakamura, A., *Inorg. Chem.* **1998,** *37*, 2415-2421.

26. Jentzen, W.; Ma, J.-G.; Shelnutt, J. A., *Biophysical Journal* **1998,** *74*, 753-763.

27. Jentzen, W.; Song, X.-Z.; Shelnutt, J. A., *J. Phys. Chem. B* **1997,** *101*, 1684-1699.

28. Walker, F. A., *J. Inorg. Biochem.* **2005,** *99*, 216-236.

29. Song, X. Z.; Jentzen, W.; Jaquinod, L.; Khoury, R. G.; Medforth, C. J.; Jia, S. L.; Ma, J. G.; Smith, K. M.; Shelnutt, J. A., *Inorg. Chem.* **1998,** *37*, 2117-2128.

30. Safo, M. K.; Walker, F. A.; Raitsimring, A. M.; Walters, W. P.; Dolata, D. P.; Debrunner, P. G.; Scheidt, W. R., *J. Am. Chem. Soc.* **1994,** *116*, 7760-7770.

31. Ueyama, N.; Nishikawa, N.; Yamada, Y.; Okamura, T.; Nakamura, A., *Inorg. Chim. Acta* **1998,** *283*, 91-97.

32. Ward, E. R.; Poesche, W. H.; Higgins, D.; Heard, D. D., *J. Chem. Soc.* **1962**, 2374-2379.

33. Ward, E. R.; Heard, D. D., *J. Chem. Soc.* **1963,** *1963*, 4794-4803.

34. Ward, E. R.; Heard, D. D., *J. Chem. Soc.* **1965**, 1023-1028.

35. Okamura, T.; Takamizawa, S.; Ueyama, N.; Nakamura, A., *Inorg. Chem.* **1998,** *37*, 18-28.

36. Chio, S.; Clements, D. J.; Pophristic, V.; Ivanov, I.; Vemparala, S.; Bennett, J. S.; Klein, M. L.; Winkler, J. D.; DeGrado, W. F., *Angew. Chem. Int. Ed.* **2005,** *44*, 6685-6689.

37. Reid, T. J.; Murthy, M. R. N.; Sicignano, A.; Tanaka, N.; Musick, W. D. L.; Rossmann, M. G., *Proc. Natl. Acad. Sci. USA* **1981,** *78*.

38. Murthy, M. R. N.; Reid, T. J.; Sicignano, A.; Tanaka, N.; Rossmann, M. G., *J. Mol. Biol.* **1981,** *152*, 465-499.

39. Holm, R. H.; Kennepohl, P.; Solomon, E. I., *Chem. Rev.* **1996,** *96*, 2239-2314.

40. Brown, G. C., *Eur. J. Biochem.* **1995,** *232*, 188-191.

41. Purwar, N.; McGarry, J. M.; Kostera, J.; Pacheco, A. A.; Schmidt, M., *Biochemistry* **2011,** *50*, 4491-4503.

42. Kanamori, D.; Yamada, Y.; Onoda, A.; Okamura, T.; Adachi, S.; Yamamoto, H.; Ueyama, N., *Inorg. Chim. Acta* **2005,** *358*, 331-338.

43. Lim, M. D.; Lorkovic, I. M.; Wedeking, K.; Zanella, A. W.; Works, C. F.; Massick, S. M.; Ford, P. C., *J. Am. Chem. Soc.* **2002,** *124*, 9737-9743.

44. Wade, R. S.; Castro, C. E., *Chem. Res. Toxicol.* **1990,** *3*, 289-291.

45. Paulat, F.; Lehnert, N., *Inorg. Chem.* **2007,** *46*, 1547-1549.

46. Xu, N.; Goodrich, L. E.; Lehnert, N.; Powell, D. R.; Richter-Addo, G. B., **2012**, submitted for publication.

47. Goodrich, L. E.; Paulat, F.; Praneeth, V. K. K.; Lehnert, N., *Inorg. Chem.* **2010,** *49*, 6293-6316.

48. Adler, A. D.; Longo, F. R.; Finarelli, J. D.; Goldmacher, J.; Assour, J.; Korsakoff, L., *J. Org. Chem.* **1967,** *32*, 476.

49. Ghiladi, R. A.; Kretzer, R. M.; Guzei, I.; Rheingold, A. L.; Neuhold, Y.-M.; Hatwell, K. R.; Zuberbuhler, A. D.; Karlin, K. D., *Inorg. Chem* **2001,** *40*, 5754-5767.

50. Huang, L.; Chen, Y.; Gao, G.-Y.; Zhang, X. P., *J. Org. Chem.* **2003,** *68*, 8179-8184.

51. Barkigia, K. M.; Berber, M. D.; Fajer, J.; Medforth, C. J.; Renner, M. W.; Smith, K. M., *J. Am. Chem. Soc.* **1990,** *112*, 8851-8857.

52. Peters, M. V.; Stoll, R. S.; Goddard, R.; Buth, G.; Hecht, S., *J. Org. Chem.* **2006,** *71*, 7840-7845.

53. Rose, E.; Kossanyi, A.; Quelquejeu, M.; Soleilhavoup, M.; Duwavran, F.; Bernard, N.; Lecas, A., *J. Am. Chem. Soc.* **1996,** *118*, 1567-1568.

54. Kanamori, D.; Yamada, Y.; Onoda, A.; Okamura, T.; Adachi, S.; Yamamoto, H.; Ueyama, N., *Inorganica Chimica Acta* **2005,** *358*, 331-338.

55. Nambu, H.; Hata, K.; Matsugi, M.; Kita, Y., *Chem. Eur. J.* **2005,** *11*, 719-727.

56. Honel, M.; Mosher, H. S., *J. Org. Chem.* **1985,** *50*, 4386-4388.

57. Merz, A.; Meyer, T., *Synthesis* **1999**, 94-99.

58. Merz, A.; Schropp, R.; Lex, J., *Angew. Chem. Int. Ed.* **1993,** *32*, 291-293.

59. Sheldrick, G. M. *Program for Empirical Absorption Correction of Area Detector Data*, v. 2008/1; University of Gottingen: Gottingen, Germany, 2008.

60. Sheldrick, G. M. v. 2008/3; Bruker Analytical X-ray: Madison, WI, 2008.

61. *Saint Plus*, v. 7.53a; Bruker Analytical X-Ray: Madison, WI, 2008.

62. Frisch, M. J.; Trucks, G. W.; Schlegel, H. B.; Scuseria, G. E.; Robb, M. A.; Cheeseman, J. R.; Montgomery, J., J. A.; Vreven, T.; Kudin, K. N.; Burant, J. C.; Millam, J. M.; Iyengar, S. S.; Tomasi, J.; Barone, V.; Mennucci, B.; Cossi, M.; Scalmani, G.; Rega, N.; Petersson, G. A.; Nakatsuji, H.; Hada, M.; Ehara, M.; Toyota, K.; Fukuda, R.; Hasegawa, J.; Ishida, M.; Nakajima, T.; Honda, Y.; Kitao, O.; Nakai, H.; Klene, M.; Li, X.; Knox, J. E.; Hratchian, H. P.; Cross, J. B.; Bakken, V.; Adamo, C.; Jaramillo, J.; Gomperts, R.; Stratmann, R. E.; Yazyev, O.; Ausin, A. J.; Cammi, R.; Pomelli, C.; Octerski, J. W.; Ayala, P. Y.; Morokuma, K.; Voth, G. A.; Salvador, P.; Dannenberg, J. J.; Zakrzewski, V. G.; Dapprich, S.; Daniels, A. D.; Strain, M. C.; Farkas, O.; Makick, D. K.; Rabuck, A. D.; Raghavachair, K.; Foresman, J. B.; Ortiz, J. V.; Cui, Q.; Baboul, A. G.; Clifford, S.; Cioslowski, J.; Stefanov, B. B.; Lui, G.; Laishenko, A.; Piskorz, R.; Komaromi, I.; Martin, R. L.; Fox, D. J.; Keith, T.; Al-Laham, M. A.; Peng, C. Y.; Nanayakkara, A.; Challacombe, M.; Gill, P. M. W.; Johnson, B.; Chen, W.; Wong, M. W.; Gonzalez, C.; Pople, J. A. *Gaussin 03*, Gaussian, Inc.: Pittsburgh, PA, 2003.

63. Perdew, J. P., *Phys. Rev. B* **1986,** *33*, 8822-8824.

64. Becke, A. D., *Phys. Rev. A* **1988,** *38*, 3098-3100.

65. Schaefer, A.; Horn, H.; Ahlrichs, R., *J. Chem. Phys.* **1992,** *97*, 2571-2577.

66. Schaefer, A.; Huber, C.; Ahlrichs, R., *J. Chem. Phys.* **1994,** *100*, 5829-5835.

67. Neese, F. *ORCA*, 2.2; Max-Planck Institut feur Bioanorganische Chemie: Meulheim/Ruhr, Germany, 2004.

68. Allouche, A.; Pourcin, J., *Spectrochim. Acta* **1993,** *49*, 571.

69. Praneeth, V. K. K.; Näther, C.; Peters, G.; Lehnert, N., *Inorg. Chem.* **2006,** *45*, 2795-2811.

Chapter 3

One-Electron Reduction of Five- and Six-Coordinate {FeNO}^{7} Porphyrin Complexes: Exploring the Reactivity of Low-Spin {FeNO}^{8} Complexes and the *trans* Effect of NO$^-$

Nitric oxide (NO) is toxic to cells at relatively low (μM) concentrations,[1] and it was therefore surprising when it was discovered in the 1980s that this diatomic is actually a signaling molecule in mammals at nM concentrations. In addition, macrophages produce NO at higher (local) concentration for the purpose of immune defense.[2-5] Due to its toxicity, both the biosynthesis of this molecule and its degradation are tightly regulated in mammalian organisms to prevent cellular damage. In denitrifying fungi that reduce nitrate to nitrous oxide (N_2O) for anaerobic respiration, the toxic metabolite NO is removed from the cell by the heme enzyme Cytochrome P450 nitric oxide reductase (P450nor) which catalyzes the following reaction:[6-7] 2 NO + NAD(P)H + 2 H^+ → N_2O + H_2O. Unlike most Cyt. P450s which perform oxidation chemistry, P450nor is one of the few enzymes in this class that reduces its substrate. P450nor, a heme enzyme with a proximal cysteinate ligand, reduces two equivalents of NO to N_2O through an initially formed ferric nitrosyl intermediate.[8-9] In a two-electron process, the ferric nitrosyl is reduced by NAD(P)H to form a ferrous nitroxyl (NO^- or HNO in aqueous environments) intermediate,[10] an {FeNO}^{8} or {FeNHO}^{8} complex in the Enemark-Feltham notation.[11] From stopped flow measurements on P450nor, a corresponding intermediate is observed upon

reaction of the initial Fe(III)-NO adduct with NAD(P)H. This “Intermediate I” was characterized by a Soret band absorbtion at 444 nm[10] and Fe-NO stretching frequency at 543 cm^{-1}.[12] Reaction with a second equivalent of NO then produces N_2O and closes the catalytic cycle.

DFT and QM/MM calculations[13-14] indicate that following a direct hydride transfer from NAD(P)H to the ferric nitrosyl complex, an Fe(II)-HNO complex is generated that could either react directly with NO, or that could undergo protonation to a formally Fe(IV)-NHOH/Fe(III)-NHOH(radical) structure prior to reaction with the second equivalent of NO—ultimately releasing N_2O and H_2O. Calculations predict that the Fe(II)-HNO species is basic due to the presence of the axial cysteinate ligand and, thus, will be easily protonated.[13-14] However, whether this step is mechanistically significant is not known. So despite all of these studies, the key question remains whether the nitroxyl intermediate of P450nor (Intermediate I) is singly or doubly protonated and what the significance of the protonation state is for the reactivity of this species with NO. In addition, little is known about the fundamental properties and reactivites of Fe(II)-nitroxyl complexes in general, making it difficult to evaluate the proposed mechanism based on the chemical properties of these species. Without ferrous heme-nitroxyl model complexes in hand, this is difficult to ascertain for the protein due to our inability to precisely control protons, and proton dependent reactions, in protein (aqueous) environments.

Ferrous nitroxyl intermediates have also been proposed in the catalytic cycle of bacterial nitric oxide reductases (NorBC). NorBC, like P450nor, reduces 2 equivalents of NO to N_2O, but instead of a single heme active site as found in P450nor, NorBC contains a bi-metallic heme/non-heme active site.[15] While the exact mechanism of NO reduction by NorBC is not known, one proposal (the “*cis*-heme b_3”

mechanism) suggests that all of the NO chemistry happens exclusively at the heme b_3 site.[16] The *cis*-heme b_3 mechanism proposes that NO first binds the heme b_3 to form a ferrous heme-nitrosyl. A recent DFT paper indicates that reduction of this species to generate an $\{FeNO\}^8$ complex is crucial for the following reaction with NO to form the N-N bond and create a hyponitrite-level intermediate.[17] As there is currently no experimental evidence to support the key N-N bond forming step of this hypothesis, elucidation of the reaction of free NO with Fe(II)-NO^- complexes is of key importance to further validate the chemical basis for this mechanism.

Two main approaches have been employed in the literature to generate ferrous heme-nitroxyl model complexes. First, free HNO can be reacted directly with a ferrous heme through the use of HNO donors such as Piloty's acid or methylsulfonylhydroxylamic acid.[18] This method has, to our knowledge, only been employed successfully in globin proteins by Farmer and co-workers.[19-20] These researchers first reported a long-lived six-coordinate ferrous Mb(II)-HNO complex with proximal histidine ligation, which has been characterized by resonance Raman, X-ray absorption,[21] and ^{1}H NMR spectroscopy.[22] An alternative route to generate Fe(II)-nitroxyl complexes is to start from a stable ferrous heme-nitrosyl adduct $\{FeNO\}^7$. The $\{FeNO\}^7$ species can then be reduced by one-electron to a $\{FeNO\}^8$ species or ferrous nitroxyl complex, which can subsequently be protonated. Initial studies by Kadish and co-workers demonstrated reversible one-electron reduction of five-coordinate ferrous heme-nitrosyls, utilizing TPP^{2-} and OEP^{2-} ligands, to generate Fe(II)-NO^- species as shown by UV-visible spectroelectrochemistry.[23-24] Ryan and co-workers provided further vibrational characterization of both [Fe(TPP)(NO)]$^-$ and [Fe(OEP)(NO)]$^-$.[25-26] Finally, using an extremely electron withdrawing porphyrin, $H_2TFPPBr_8$, Doctorovich and co-workers have isolated and characterized the

corresponding five-coordinate Fe(II)-NO⁻ complex, obtained by reduction of the Fe(II)-NO starting material by cobaltocene.[27] Unfortunately, all attempts at protonation of the formed Fe(II)-NO⁻ species to form a Fe(II)-HNO complex have resulted in generation of the corresponding Fe(II)-NO complex, presumably via disproportionation of an intermediately formed HNO adduct.[25, 27] Ryan and co-workers also reported H_2 generation during this process.[25] No other details about the reactivity of these species are known. Additionally, all $\{FeNO\}^8$ model complexes reported thus far are five-coordinate and hence, not ideal models for the coordination environment found in proteins. As such, the effect of a sixth ligand like histidine or cysteine on the properties of ferrous heme-nitroxyl complexes has yet to be explored experimentally.

In this study, we report the vibrational and electronic structural properties of four new $\{FeNO\}^8$ porphyrin complexes prepared through the one-electron reduction of the corresponding $\{FeNO\}^7$ precursors. The formed $\{FeNO\}^8$ species have been investigated for (1) reactivity towards weak acids and NO, and (2) the effect of an axially coordinated N-donor ligand. To prevent disproportionation of the putative HNO adduct and model the steric protection of a protein environment, we have employed the sterically encumbered bis-picket fence porphyrin 5,10,15,20-tetrakis(2,6-bis(2-methoxyphenoxy)phenyl)porphyrin, H_2[3,5-Me-BAFP]. Here, the large phenoxy pickets provide a binding pocket for NO⁻/HNO. In particular, we are exploring for the first time the reaction of $\{FeNO\}^8$ species with NO, and the effects of axial N-donor ligands on ferrous heme-nitroxyl complexes.

Results and Discussion

Preparation and Characterization of {FeNO}^{7} Complexes

[Fe(3,5-Me-BAFP)(NO)] (**1-NO**), a {FeNO}^{7} complex in the Enemark-Feltham notation,[11] was prepared by reductive nitrosylation of [Fe(3,5-Me-BAFP)(Cl)]. The identity of **1-NO** has been confirmed by X-ray crystallography at 95 K. The crystal structure has two equivalent molecules, **A** and **B**, in the unit cell that differ marginally in their structural parameters. Figure 3.1 shows a side view of one of the two molecules and crystallographic data is provided in Table 3.1. As listed in Table 3.2, the Fe-NO and N-O bond lengths (for molecule **A**) are 1.71 and 1.15 Å, respectively. The Fe-N-O angle is 146^o and the Fe-atom is displaced from the heme plane by 0.35 Å towards NO, typical of five-coordinate ferrous heme-nitrosyls.[28] Additionally, the crystal structure clearly demonstrates that the eight phenoxy-groups of the bis-picket fence porphyrin do, in fact, create a sterically hindered binding pocket for axial ligands, NO derivatives in our case.

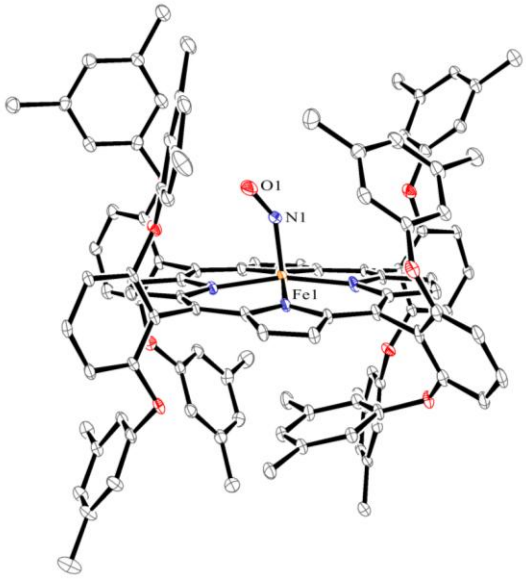

Figure 3.1. Crystal structure of [Fe(3,5-Me-BAFP)(NO)] (**1-NO**), hydrogen atoms are omitted for clarity. Selected bond lengths and angles are summarized in Table 3.2. Thermal ellipsoids are shown at 30% probability.

Table 3.1. Crystallographic data for compound [Fe(3,5-Me-BAFP)(NO)] (**1-NO**).

Formula Weight	1695.77
Empirical formula	$C_{110}H_{96}FeN_5O_{9.5}$
Temperature	-178.0°C
Crystal System	Triclinic
Space Group	P-1
Lattice Parameters	a = 12.8567(3) Å b = 23.8554(6) Å c = 29.412(2) Å α = 80.356(6)° β = 86.579(6)° γ = 84.793(6)° V = 8847.4(7) Å^3
Z value	2
calc. density	1.273 mg/m^3
Absorption coefficient	1.886 mm^{-1}
F(000)	3572
Crystal size	0.29 x 0.09 x 0.05 mm
μ(CuKα)	18.721 cm^{-1}
Exposure Rate	120.0 sec/°
$2\theta_{max}$	122.3°
No. of Reflections	Total: 67793 Unique: 7194
Data / restraints / parameters	25968 / 0 / 0.500
Goodness-of-fit on F^2	1.002
Final R indicies [I>2σ(I)]	R1 = 0.940 wR2 = 0.2190
R indicies (all data)	R1 = 0.1370 wR2 = 0.2582
Largest diff. peak & hole	0.819 & -0.968 e.A^{-3}
R_{int}	0.060

Table 3.2. Crystallographic parameters ([Å] and [°]) of selected five-coordinate ferrous porphyrin nitrosyls.

complex	T [K]	ΔFe-NO	ΔN-O	<Fe-N-O	ΔFe-$N_{pyrrole}$	ΔFe-$N_{pyrrole}$[a]	ΔFe[b]	ref.
[Fe(3,5-Me-BAFP)(NO)] (**1-NO**), **A**	95	1.712	1.150	146.27	1.969 1.997 1.992 2.005	1.991(8)	0.35	*t.w.*
[Fe(3,5-Me-BAFP)(NO)] (**1-NO**), **B**	95	1.714	1.142	146.52	1.975 1.989 2.002 2.008	1.993(5)	0.37	*t.w.*
[Fe(TPP)(NO)]	33	1.740	1.164	144.5	-	1.999	0.20	[29]5
[Fe(TPP)(NO)]	293	1.721	1.107	149.6	-	2.001	0.23	[29]
[Fe(OEP)(NO)], **A**	130	1.722	1.167	144.4	1.989 1.993 2.017 2.016	2.004	0.29	[30]
[Fe(OEP)(NO)], **B**	130	1.731	1.168	142.7	2.000 1.999 2.017 2.023	2.010	0.27	[30]

[a]Average of all four Fe-$N_{pyrrole}$ bond lengths
[b]Iron displacement from the 24 atom mean porphyrin plane

Interestingly, this is the first crystal structure of a five-coordinate ferrous heme-nitrosyl with a TPP^{2-} derivative as co-ligand that shows a *single conformation* of the Fe-NO unit. It has been shown previously by Scheidt and co-workers that at 293 K the NO unit in [Fe(TPP)(NO)] is disordered over eight possible positions (four on each side of the porphyrin plane).[31] Around 250 K, [Fe(TPP)(NO)] undergoes a phase transition from tetragonal to triclinic and NO is now limited to two unique positions, one on each face of the porphyrin plane.[29] Excitingly, the eight phenoxy groups of the porphyrin ligand in **1-NO** direct packing of the molecules in the crystal in a way that further limits the Fe-NO unit to a single orientation. The steric encumbrance of this bulky porphyrin also appears to direct the position of NO relative to the Fe-$N_{pyrrole}$ bonds: in the case of **1-NO**, the N-O unit is located *directly above* one of the Fe-$N_{pyrrole}$ bonds. This is in contrast to other five-coordinate ferrous

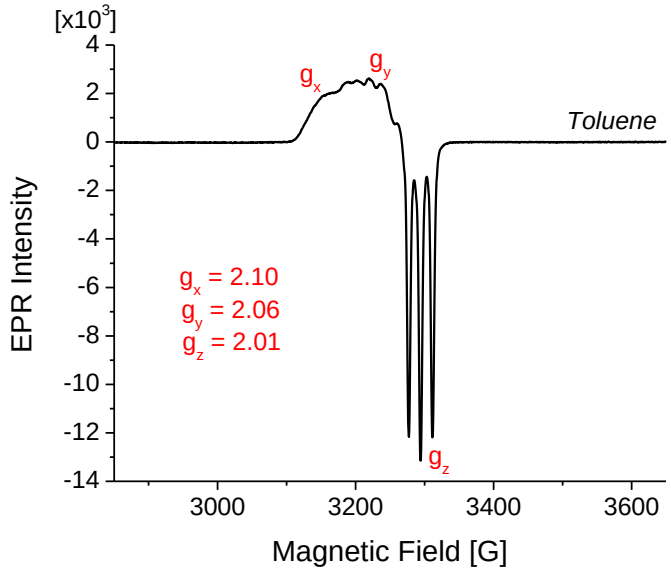

Figure 3.2. EPR spectrum of [Fe(3,5-Me-BAFP)(NO)] (**1-NO**) recorded at 77 K in frozen toluene. The spectrum shows typical g-values indicative of ferrous heme-nitrosyls with S = 1/2 ground state. The three-line hyperfine pattern on the smallest g-value, g_z, originates from the nuclear spin of the ^{14}N-atom (I = 1) of NO. The hyperfine coupling constant, A_z, is 50 MHz in toluene.

heme-nitrosyls where the O-atom is positioned towards a meso-carbon; for example, in [Fe(TPP)(NO)] the N-O unit is rotated 44^{o} from the closest Fe-$N_{pyrrole}$ bond.[29] This difference results in a unique core asymmetry in **1-NO**. In this complex, the Fe-$N_{pyrrole}$ bond which is aligned with the N-O unit (1.969 Å) is significantly shorter than the remaining three bonds (1.997, 1.992, and 2.005 Å). Typically, when the N-O unit points toward a meso-carbon of the porphyrin ligand two Fe-$N_{pyrrole}$ bonds are shorter (in the direction of NO) than the remaining two bonds.[32] In the case of [Fe(OEP)(NO)], the short Fe-$N_{pyrrole}$ bond lengths are 1.989 and 1.993 Å and the long bonds are 2.017 and 2.016 Å.[30]

The {FeNO}^{7} complex **1-NO** shows an EPR spectrum typical of a S = 1/2 five-coordinate ferrous heme-nitrosyl with g-values of 2.10, 2.06, and 2.01 in toluene (see Figure 3.2). A well defined 3-line hyperfine pattern is observed on the smallest g-value, g_z from the ^{14}N nuclear spin (I = 1) of bound NO. In THF, however, the

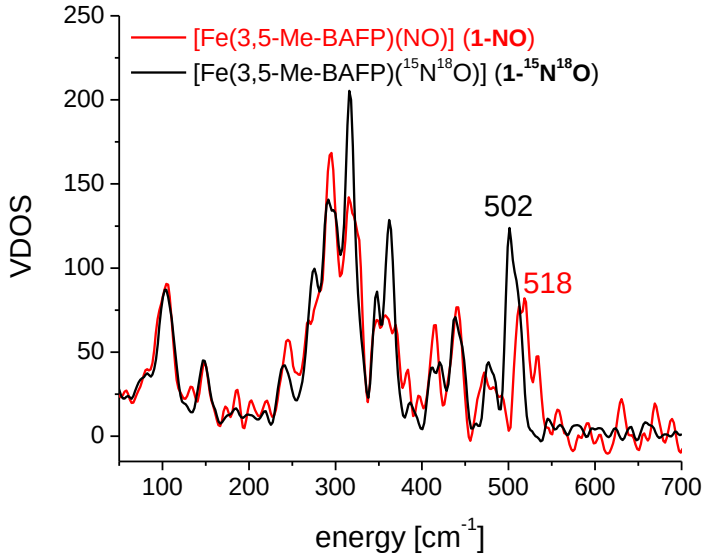

Figure 3.3. Vibrational density of states (VDOS) for [^{57}Fe(3,5-Me-BAFP)(NO)] (**1-NO**, red) and [^{57}Fe(3,5-Me-BAFP)(^{15}N^{18}O)] (**1-^{15}N^{18}O**, black) calculated from raw nuclear resonance vibrational spectroscopy (NRVS) data.

Table 3.3. Fe-NO and N-O stretching frequencies of selected five- and six-coordinate {FeNO}^{7} and {FeNO}^{8} porphyrin complexes.

Complex	v(N-O)	v(Fe-NO)	ref.
{FeNO}^{7}			
five-coordinate			
[Fe(OEP)(NO)]	1671	522	[33]
[Fe(3,5-Me-BAFP)(NO)] (**1-NO**)	1684	518	*t.w.*
[Fe(T*o*-F_2TPP)(NO)] (**2-NO**)	1687		*t.w.*
[Fe(T*o*-$(NO_2)_2$-*p*-tBuPP)(NO)] (**4-NO**)	1693		*t.w.*
[Fe(TPP)(NO)]	1697	532	[34]
[Fe(T*per*-F_5TPP)(NO)] (**3-NO**)	1699		*t.w.*
[Fe(TFPPBr$_8$)(NO)]	1727		[27]
six-coordinate			
[Fe(3,5-Me-BAFP)(THF)(NO)] (**1$_{THF}$-NO**)	1661		*t.w.*
[Fe(3,5-Me-BAFP)(MI)(NO)] (**1$_{MI}$-NO**)	1630		*t.w.*
[Fe(T*o*-F_2TPP)(MI)(NO)] (**2$_{MI}$-NO**)	1636		*t.w.*
[Fe(T*o*-$(NO_2)_2$-*p*-tBuPP)(MI)(NO)] (**4$_{MI}$-NO**)	1641		*t.w.*
[Fe(TPP)(MI)(NO)]	1630	437	[35-36]
[Fe(T*per*-F_5TPP)(MI)(NO)] (**3$_{MI}$-NO**)	1649		*t.w.*
{FeNO}^{8}			
[Fe(OEP)(NO)]$^-$	1441		[26]
[Fe(3,5-Me-BAFP)(NO)]$^-$ (**1-NO**$^-$)	1466		*t.w.*
[Fe(T*o*-F_2PP)(NO)]$^-$ (**2-NO**$^-$)	1473		*t.w.*
[Fe(T*o*-$(NO_2)_2$-*p*-tBuPP)(NO)]$^-$ (**4-NO**$^-$)	1482		*t.w.*
[Fe(TPP)(NO)]$^-$	1496	525	[25]
[Fe(T*per*-F_5TPP)(NO)]$^-$ (**3-NO**$^-$)	~1500		*t.w.*
[Fe(TFPPBr$_8$)(NO)]$^-$	1550		[27]

three-line hyperfine on g_z begins to migrate towards g_y—indicating possible binding of THF at 77 K to form a six-coordinate nitrosyl with bound THF in solution. IR spectra in KBr show a clear nitric oxide stretching frequency, *v*(N-O), of 1684 cm^{-1} which shifts to 1614 cm^{-1} upon $^{15}N^{18}O$ isotope labelling. Furthermore, utilizing nuclear resonance vibrational spectroscopy the Fe-NO stretching frequency, v(Fe-NO), of **1-NO** is found at 518 cm^{-1} which shifts by 16 cm^{-1} to lower energy in **1-^{15}N^{18}O** (Figure 3.3). The Fe-N-O bend is unable to be assigned due to noise in the **1-**

NO spectrum and overlap with other Fe-centered vibrations in the 380 cm^{-1} region.

Three additional "electron-poor" {FeNO}^{7} porphyrin complexes have been synthesized for the purpose of this study. [Fe(T*o*-F_2PP)(NO)] (**2-NO**), [Fe(T*per*-F_5PP)(NO)] (**3-NO**), and [Fe(T*o*-$(NO_2)_2$-*p*-*t*BuPP)(NO)] (**4-NO**) all show typical N-O stretching frequencies for five-coordinate ferrous heme-nitrosyls (Table 3.3). The ν(N-O) for **2-NO**, **3-NO**, and **4-NO** in a KBr matrix are 1687, 1699, and 1693 cm^{-1} respectively. EPR spectroscopy indicates that all three complexes are low-spin Fe(II)-NO species with S = ½ ground states, see Figure 3.4 and 3.5. For **3-NO** and **4-NO**, the EPR spectrum shows the usual case where a well defined three-line hyperfine pattern is observed on the smallest g-value, g_z, that stems from the ^{14}N nuclear spin (I = 1) of bound NO (Figure 3.5; A_z = 47 MHz in both spectra).

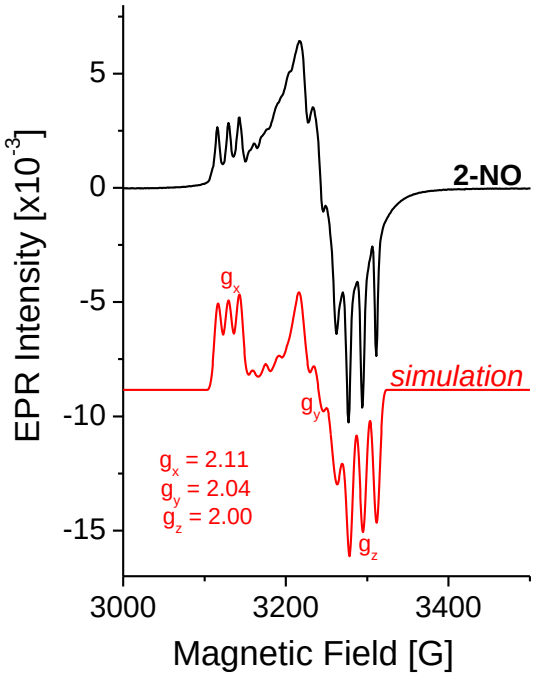

Figure 3.4. EPR spectrum of [Fe(T*o*-F_2PP)(NO)] (**2-NO**) at 77 K. The three-line hyperfine pattern on all g-values originates from the nuclear spin of the ^{14}N-atom (I = 1) of NO. The simulated spectrum was generated using the program SpinCount. Fit parameters are g_x = 2.109, g_y = 2.0375, g_z = 2.003, A_x = 39 MHz, A_y = 46 MHz, A_z = 47 MHz, sg_x (g-strain) = 0.0025, sg_y = 0.0035, and sg_z = 0.002.

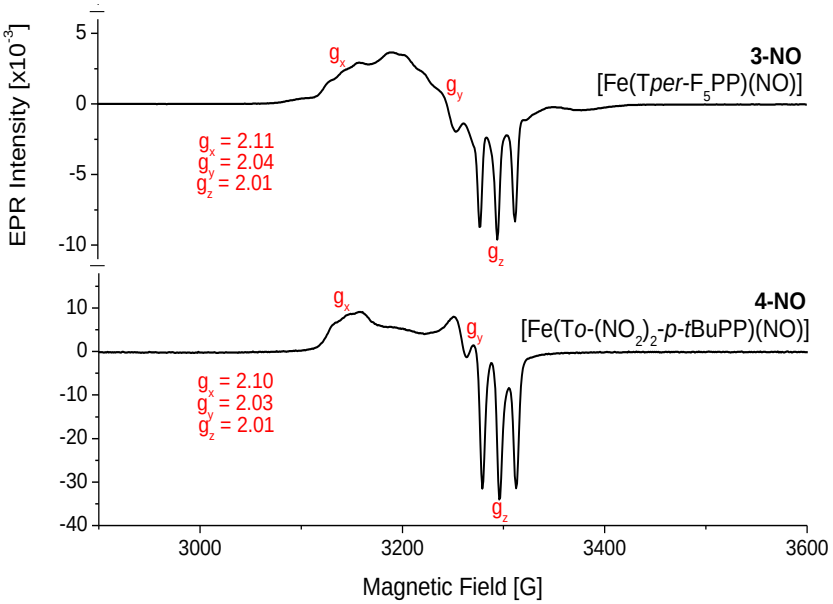

Figure 3.5. EPR spectra of [Fe(T*per*-F_5PP)(NO)] (**3-NO**) and [Fe(T*o*-$(NO_2)_2$-*p*-*t*BuP)(NO)] (**4-NO**) recorded at 77 K in frozen toluene. The spectra show typical g-values indicative of ferrous heme-nitrosyls with S = 1/2 ground state. The hyperfine coupling constant, A_z, for **3-NO** and **4-NO** is 47 MHz.

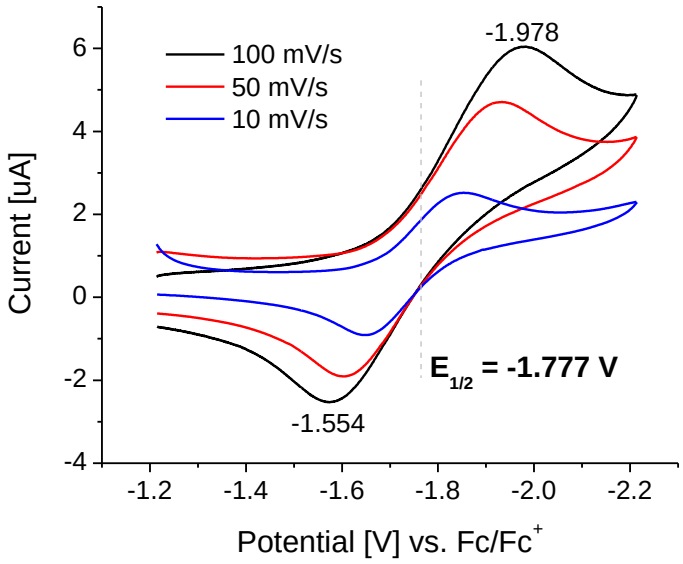

Figure 3.6. Cyclic voltammograms for [Fe(3,5-Me-BAFP)(NO)] (**1-NO**) in THF at various scan rates.

Table 3.4. Half wave potentials (in V vs. Fc/Fc^+) for the first reduction of ferrous porphyrin nitrosyls.

complex	solvent	[Fe(P)(NO)]/ [Fe(P)(NO)]⁻	ref.
[Fe(OEP)(NO)]	CH_2Cl_2	-1.59	[23]
[Fe(3,5-Me-BAFP)(NO)] (**1-NO**)	THF	-1.78	*t.w.*
[Fe(T*o*-F_2TPP)(NO)] (**2-NO**)	1,2-DCE	-1.18	*t.w.*
[Fe(T*o*-$(NO_2)_2$-*p*-tBuPP)(NO)] (**4-NO**)	1,2-DCE	-1.18	*t.w.*
[Fe(TPP)(NO)]	CH_2Cl_2 THF	-1.42 -1.47	[23] [23]
[Fe(T*per*-F_5TPP)(NO)] (**3-NO**)	1,2-DCE	-1.13	*t.w.*
[Fe(TFPPBr_8)(NO)]	CH_2Cl_2	-0.65	[27]

Interestingly, in the case of **2-NO**, this hyperfine interaction is now resolved on all three g-values. This is a unique case and correspondingly, the experimental spectrum and simulation generated using the program Spin Count are provided in Figure 3.4. The g-values are 2.11, 2.04, and 2.00—similar to both **3-NO**, **4-NO** and other five-coordinate ferrous heme systems.[16] The hyperfine coupling constants for A_x, A_y, and A_z are 39, 46, and 47 MHz, respectively.

Spectroelectrochemical Reduction of Five-Coordinate Ferrous Heme-Nitrosyls

The cyclic voltammogram of **1-NO** shows a quasi-reversible reduction at -1.78 V vs. Fc/Fc^+ in THF (Figure 3.6). This reduction potential is 310 and 190 mV more negative than those for the one-electron reduction of the previously characterized complexes [Fe(TPP)(NO)] and [Fe(OEP)(NO)], respectively (Table 3.4).[23-24] To characterize this reduction further, infrared spectroelectrochemical measurements were performed in thin layer cells. As shown in Figure 3.7, upon one-electron reduction of **1-NO** in 1,2-DCE-d_4 the ν(N-O) band at 1684 cm^{-1} of the $\{FeNO\}^7$ starting complex decreases in intensity as a new band at ~1466 cm^{-1} appears. While this N-O stretching vibration of the $\{FeNO\}^8$ complex (**1-NO**⁻) is

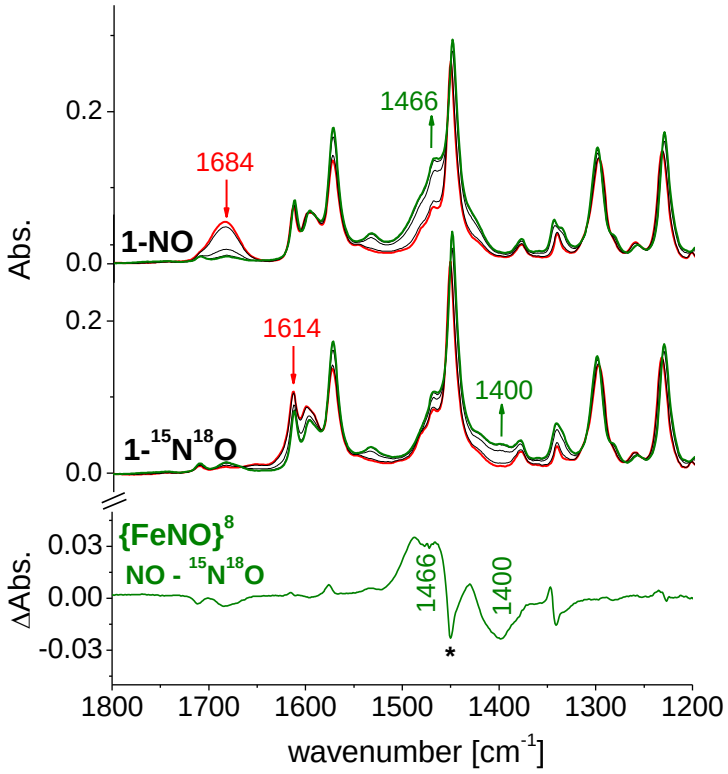

Figure 3.7. Infrared spectra from the spectroelectrochemical reduction of [Fe(3,5-Me-BAFP)(NO)] (top, **1-NO**) and [Fe(3,5-Me-BAFP)(^{15}N^{18}O)] (middle, **1-^{15}N^{18}O**) in 1,2-DCE-d_4. The asterisk (*) indicates poor subtraction of a porphyrin band at 1450 cm^{-1}. The estimated isotope shift (by DFT) of the N-O stretch in the NO$^-$ complex is 61 cm^{-1}, indicating that the 1450 cm^{-1} feature in the reduced compound is too high in energy to be the ν(^{15}N-^{18}O) stretch.

partially masked by a porphyrin ligand band, ^{15}N^{18}O labelling shifts this band into an open window of the IR spectrum at ~1400 cm^{-1}. Importantly, this reduction is completely reversible: upon re-oxidation, complex **1-NO** is regenerated. Natural abundance NO and ^{15}N^{18}O difference spectra for **1-NO**$^-$ is provided in Figure 3.7, to further confirm the assignment of the N-O stretching frequency of **1-NO**$^-$.

As listed in Table 3.3, the v(N-O) frequency of **1-NO**$^-$ is consistent with previously reported values for five-coordinate {FeNO}^{8} porphyrin systems, where v(N-O) is observed between 1440 – 1550 cm^{-1}. In contrast, low-spin *non-heme* iron

nitrosyls typically show significantly lower N-O stretching frequencies (~1300 cm^{-1}). This suggests a strongly NO ligand-centered reduction for the low-spin non-heme NO adducts and a more metal based reduction for the heme systems. Previous DFT calculations from our group have shown that for the heme complexes this corresponds to an electronic structure that is intermediate between low-spin Fe(II)-NO^- ↔ Fe(I)NO·.[13]

UV-visible spectroelectrochemical measurements in an OTTLE cell were used to further characterize the one electron reduced complex **1-NO**$^-$ as shown in Figure 3.8. As the potential is swept reductively from -0.4 V to -1.8 V vs. Ag wire at 10 mV/sec, there is essentially no change in the Soret band at 413 nm when 1,2-DCE is used as solvent, but dramatic changes are observed in the Q-band region (see Figure 3.8, top). The band at 478 nm decreases in intensity while a new band appears at 523 nm upon reduction. The clean isosbestic point at 504 nm is indicative of a clean conversion from **1-NO** to **1-NO**$^-$ without further intermediates. The spectral changes observed for the reduction of **1-NO** are in agreement with the reduction of [Fe(TPP)(NO)] reported previously.[25] Importantly, this does not correspond to a reduction of the porphyrin ligand, as this is accompanied by a dramatic loss of intensity of the Soret band not observed here. As an illustration of a porphyrin-centered reduction the spectroelectrochemical reduction of [Fe(3,5-Me-BAFP)] in THF is provided in Figure 3.9. For **1-NO**, this porphyrin reduction (corresponding to a two-electron reduction) is not accessible in 1,2-DCE.

Upon dissolving **1-NO** in THF, the Soret band shifts by 9 nm from 413 to 422 nm—indicating coordination of THF to the iron center in this system. Solution IR spectra support formation of [Fe(3,5-Me-BAFP)(NO)(THF)] with a new ν(N-O) band at 1661 cm^{-1}. Additionally, the EPR spectrum of **1-NO** in THF indicates weak binding

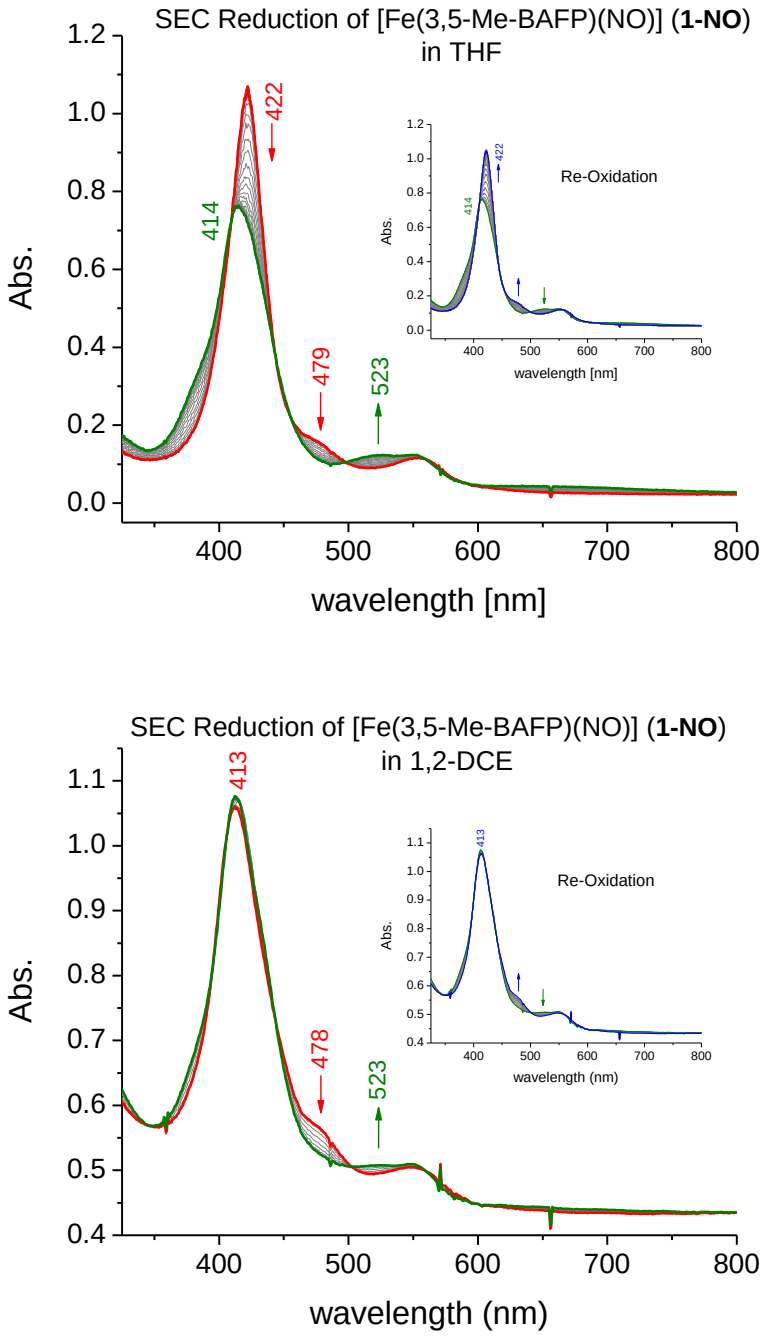

Figure 3.8. UV-visible absorption spectra from the spectroelectrochemical reduction of [Fe(3,5-Me-BAFP)(NO)] (**1-NO**, red to green), obtained by sweeping from -0.4 V to -1.8 V vs. Ag wire at a rate of 10 mV/s in a 0.1 M TBAP solution in dry (top) 1,2-DCE and (bottom) THF. The reaction is completely reversible upon sweeping from -1.8 V to -0.4 V vs. Ag wire (inset).

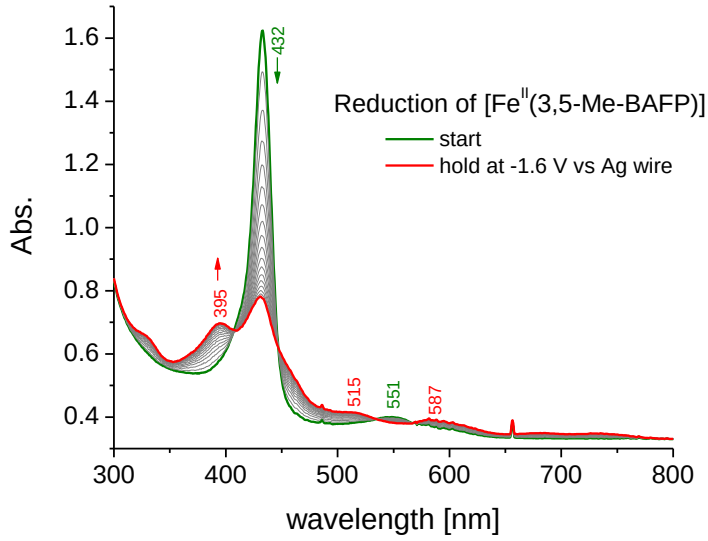

Figure 3.9. Reversible electrochemical reduction of [Fe(3,5-Me-BAFP)] to [Fe(3,5-Me-BAFP)]$^-$ in an OTTLE UV-vis cell, taken in 0.1 M TBAP solution in dry THF. The working electrode is Pt mesh.

of THF as discussed previously. However, upon one-electron reduction of this species (Figure 3.8, bottom), the resulting spectrum overlays perfectly with the data obtained for the reduction of five-coordinate **1-NO** in 1,2-DCE. This strongly suggests that the reduction product of six-coordinate [Fe(3,5-Me-BAFP)(NO)(THF)] is five-coordinate [Fe(3,5-Me-BAFP)(NO)] (**1-NO**$^-$). As such, this is the first indication that the thermodynamic σ-*trans* effect of NO$^-$ is actually *stronger* than that of NO$^\cdot$ (see below).[37] As in the IR spectroelectrochemical measurements, this reduction is fully reversible as shown in the insert of Figure 3.8. Finally, all attempts at chemical reduction (sodium anthracenide, KC_8) and isolation of **1-NO**$^-$ at room- and low-temperature were unsuccessful.

The spectroelectrochemical reductions of **2-NO**, **3-NO**, **4-NO** were also performed. The first half-wave reduction potentials of **2-NO** and **4-NO** are -1.18 V vs. Fc/Fc$^+$, and $E_{1/2}$ for the first reduction of **3-NO** is slightly more positive at -1.13 V vs. Fc/Fc$^+$ (Table 3.4). The UV-visible spectral changes upon reduction of **2-NO** are

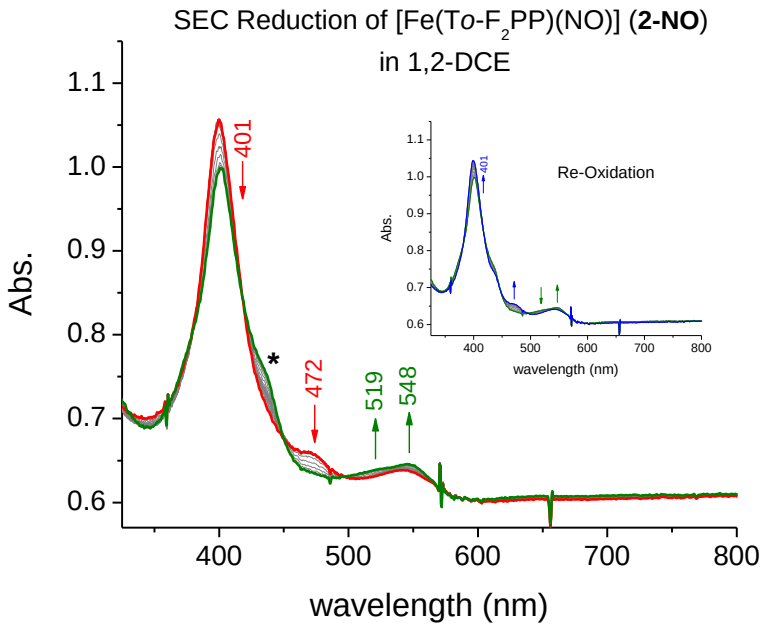

Figure 3.10. UV-visible absorption spectra from the spectroelectrochemical reduction of [Fe(T*o*-F_2PP)(NO)] (red to green), obtained by sweeping from 0 V to -1 V at a rate of 10 mV/s in a 0.1 M TBAP solution in dry 1,2-DCE. The reaction is completely reversible upon sweeping from -1 V to 0 V. Asterisk indicates a small amount of [Fe(T*o*-F_2PP)] impurity that reduces at ~ 200 mV vs. Ag wire.

quite similar to that of **1-NO**, see Figure 3.10. A decrease is observed in the band at 472 nm as two bands in the Q-region, at 519 and 548 nm, increase in absorbance. The reduction is completely reversible. The formation of **2-NO**$^-$ is also observed in IR experiments in 1,2-DCE-d_4, see Figure 3.11. Using spectroelectrochemical IR measurements, a new ν(N-O) band corresponding to **2-NO**$^-$ is observed at 1471 cm^{-1}, which shifts to 1405 cm^{-1} upon $^{15}N^{18}O$ isotope labelling. Similar experiments were also performed for **3-NO** and **4-NO**, and the corresponding ν(N-O) values for these species and corresponding one-electron reduced complexes are provided in Table 3.3. For **3-NO**$^-$ a ν(N-O) band of ~1500 cm^{-1} was observed and for **4-NO**$^-$ a N-O stretching frequency of 1482 cm^{-1} was identified. Importantly, the N-O stretching

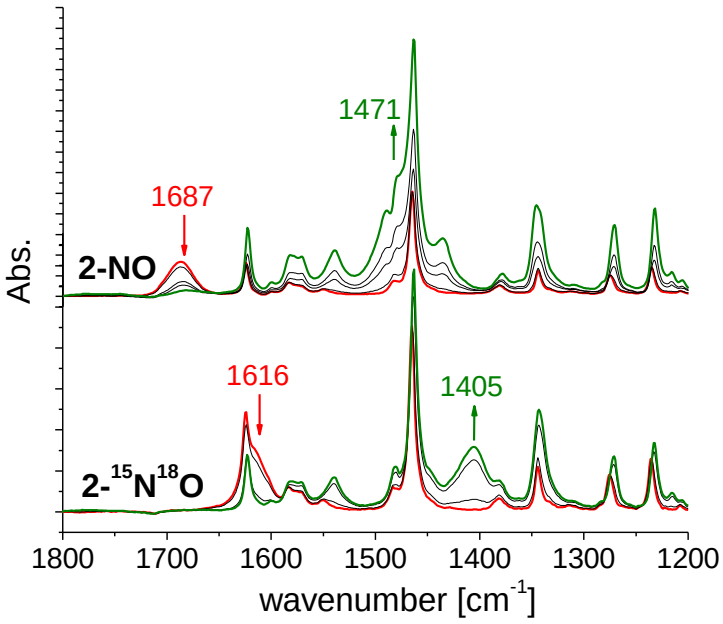

Figure 3.11. Infrared spectra from the spectroelectrochemical reduction of [Fe(T*o*-F_2PP)(NO)] (top, **2-NO**) and [Fe(T*o*-F_2PP)($^{15}N^{18}O$)] (bottom, **2-$^{15}N^{18}O$**) in 1,2-DCE-d_4. Difference spectra are provided in Figure 3.8.

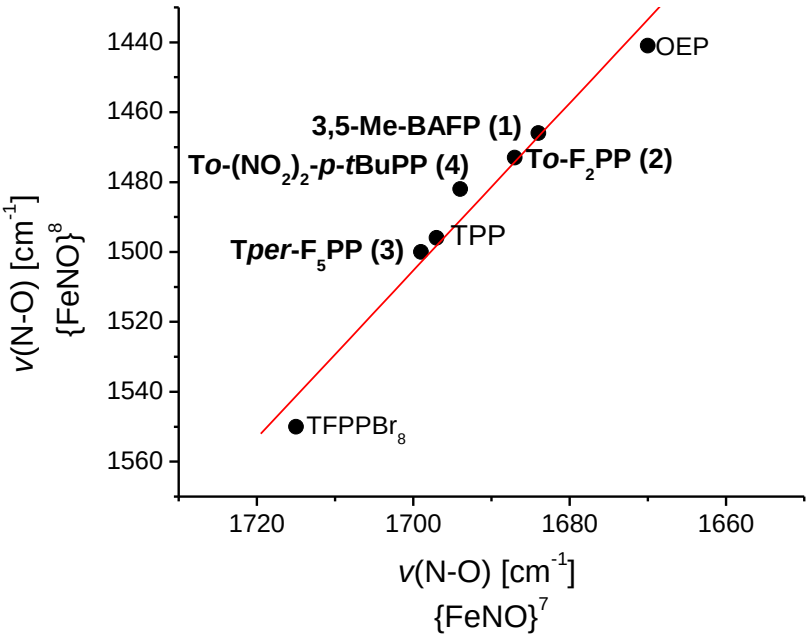

Figure 3.12. Comparison of N-O stretching frequencies in $\{FeNO\}^7$ and $\{FeNO\}^8$ porphyrin complexes.

frequency for **1-NO**$^-$ - **4-NO**$^-$ are in agreement with previous literature values as listed Table 3.3 and further illustrated in Figure 3.12. Importantly, the N-O stretching frequencies of the {FeNO}^{8} complexes shows a surprisingly strong, direct correlation with the ν(N-O) frequency in the corresponding {FeNO}^{7} precursors. This indicates strongly correlated electronic structures in corresponding {FeNO}^{7} and {FeNO}^{8} pairs, and this is discussed in detail below.

One-electron Reduction of a Six-Coordinate {FeNO}^{7} Porphyrin Complex: The trans Effect of NO$^-$

To explore the *trans* effect of NO$^-$ further and at the same time model the coordination environment of potential {FeNO}^{8} complexes in proteins we have investigated the reduction of six-coordinate ferrous heme-nitrosyls with the axial N-

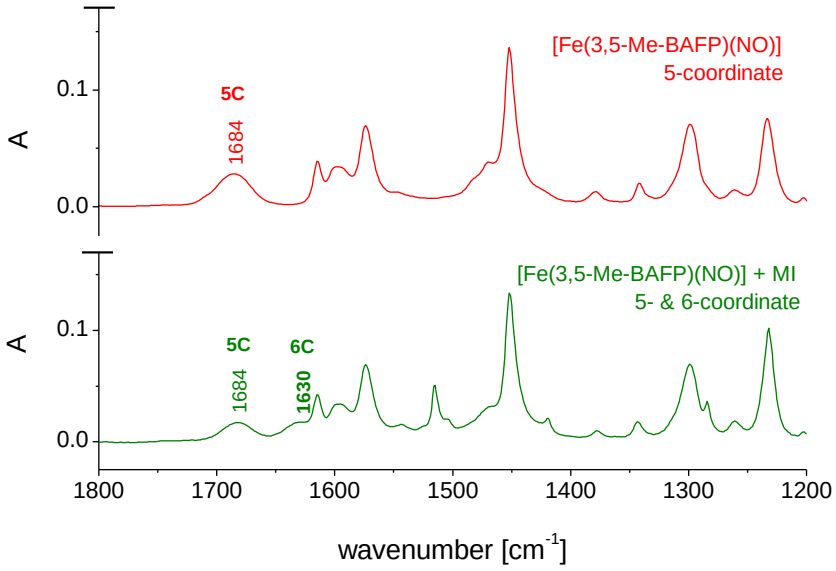

Figure 3.13. Solution IR spectra of [Fe(3,5-Me-BAFP)(NO)] (red, top) and [Fe(3,5-Me-BAFP)(NO)] with the addition of 15 μL MI (green, bottom). Incomplete conversion is observed from the five-coordinate species to the six-coordinate complex [Fe(3,5-Me-BAFP)(MI)(NO)] which has a N-O stretching frequency of 1630 cm^{-1}.

donor ligand 1-methylimidazole (MI) as a model for histidine in globins. We investigated the use of our ferrous picket fence porphyrin nitrosyl complex (**1-NO**) first. After addition of 50 eq. of MI to **1-NO** in a thin layer IR spectroelectrochemical cell, only ~40% of **1-NO** was converted to [Fe(3,5-MeBAFP)(MI)(NO)] (see Figure 3.13). As such, we needed to move to a system with a higher affinity for MI. Therefore, various porphyrins were screened as formation of six-coordinate ferrous nitrosyl complexes in solution requires excess N-donor as the σ-*trans* effect of NO is strong.[34, 38] Importantly, it has been shown previously that the use of electron withdrawing derivatives of TPP increases MI affinity for the ferrous nitrosyl form.[34]

To quantify MI binding to five-coordinate ferrous heme-nitrosyls, the binding constant can be calculated for the reaction below:

$$[Fe(TPP^*)(NO)] + MI \rightleftarrows [Fe(TPP^*)(MI)(NO)] \qquad (1)$$

where TPP^{*2-} is a tetraphenylporphyrin derivative. The titration of MI against the five-coordinate complex **1-NO** was followed by UV-visible spectroscopy and K_{eq} can then be calculated from the equation:

$$[MI] = c_T \Delta\varepsilon \frac{[MI]}{\Delta E} - K_{eq} \qquad (2)$$

which was originally developed by Drago and co-workers.[39-41] Here, c_T corresponds to the total concentration of porphyrin complexes, $c_T = c(6C) + c(5C)$, and Δε is the difference in extinction coefficients, $\Delta\varepsilon = \varepsilon(6C) - \varepsilon(5C)$. UV-vis absorption measurements are performed at different concentrations of MI ([MI]) and the change in absorbance (ΔE) is measured. A plot of [MI] versus [MI]/ΔE then gives K_{eq}^{-1}. Calculation of the binding constant of MI to **1-NO** supports the low conversion to the six-coordinate species under IR conditions as K_{eq} is only 76 M^{-1}, see Table 3.5. This is essentially equal to K_{eq} of MI binding to [Fe(TPP)(NO)], 26 M^{-1}, and significantly

Table 3.5. Equilibrium constants, K_{eq} [M^{-1}], and free reaction energies, ΔG (kcal/mol), for the reaction of [Fe(TPP*)(NO)] + MI ⇄ [Fe(TPP*)(MI)(NO).

complex	K_{eq}	ΔG	ref
[Fe(TPP)(NO)]	26	-1.9	[34]
[Fe(3,5-Me-BAFP)(NO)] (**1-NO**)	76	-2.6	*t.w.*
[Fe(T*o*-$(NO_2)_2$-*p*-tBuPP)(NO)] (**4-NO**)	714	-3.9	*t.w.*
[Fe(To-F_2PP)(NO)] (**2-NO**)	2055	-4.5	[34]
[Fe(To-F_2PP)(NO)]$^-$ (**2-NO**$^-$)	<< 0.2	>> +1	*t.w.*

lower than K_{eq} for MI binding to **2-NO**, 2055 M^{-1}.[34] Since the K_{eq} for **2-NO** is more favorable for our experimental conditions, **3-NO** was also considered. Surprisingly, K_{eq} for MI binding to **3-NO** is only 714 M^{-1}, lower than K_{eq} for **2-NO** by a factor of three. This is unexpected as the nitro-groups in the *ortho* position of **3-NO** were expected to act as stronger electron withdrawing groups than the fluorine atoms in **2-NO**. Based on this result, **2-NO** was used to investigate the *trans* effect of NO$^-$ in ferrous porphyrin systems with bound MI.

With the addition of 50 equivalents of MI the N-O stretching frequency for the six-coordinate {FeNO}^{7} complex, $\mathbf{2_{MI}}$**-NO**, is observed at 1636 cm^{-1}. This feature decreases upon one-electron reduction and a new band at 1473 cm^{-1} appears, corresponding to the {FeNO}^{8} complex. Surprisingly, this is the same ν(N-O) as observed for **2-NO**$^-$**—**suggesting a loss of MI upon formation of the reduced product. As shown in Figure 3.14, the spectra obtained by reduction of **2-NO** and $\mathbf{2_{MI}}$**-NO** are identical, demonstrating formation of five-coordinate **2-NO**$^-$ in both cases. According to BP86/TZVP calculated N-O stretching frequencies of five-coordinate [Fe(P)(NO)]$^-$ and six-coordinate [Fe(P)(MI)(NO)]$^-$, binding of MI to [Fe(P)(NO)]$^-$ should shift ν(N-O) to lower energy by at least 15 cm^{-1} as shown in Table 3.6. Thus, we have provided the first experimental evidence for the increased σ-*trans* effect of NO$^-$

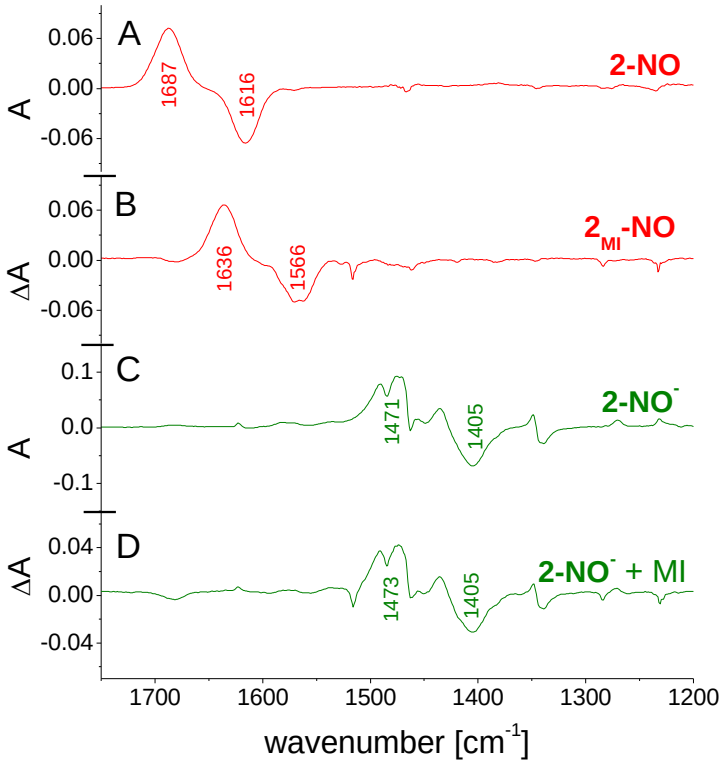

Figure 3.14. NO – $^{15}N^{18}O$ IR difference spectra from the spectroelectrochemical reduction of [Fe(T*o*-F_2PP)(NO)] in the absence (A: {FeNO} in , C: $\{FeNO\}^8$) and presence (B: $\{FeNO\}^7$, D: $\{FeNO\}^8$) of MI.

Table 3.6. BP86/TZVP calculated geometric and vibrational parameters of five- and six-coordinate $\{FeNO\}^7$ and $\{FeNO\}^8$ heme complexes.

	Geometric Parameters [Å] [°]					Vibrational Frequencies [cm^{-1}]	
Complex	ΔFe-N_{NO}	ΔN-O	ΔFe-N_{MI}	ΔFe-N_{porph}	< Fe-N-O	ν(Fe-NO)	ν(N-O)
five-coordinate							
[Fe(P)(NO)]	1.704	1.179	-	2.019	146	595	1703
$[Fe(P)(NO)]^-$	1.786	1.206	-	2.011	125	568/(428)	1533
six-coordinate							
[Fe(P)(MI)(NO)]	1.734	1.186	2.179	2.021	140	609	1662
$[Fe(P)(MI)(NO)]^-$	1.805	1.210	2.451	2.015	124	543/(434)	1518

relative to NO·. $^{15}N^{18}O$ isotope labelling further confirms this idea: the observed stretching frequency upon reduction of [Fe(T*o*-F_2PP)(MI)($^{15}N^{18}O$)] at 1405 cm^{-1} is exactly identical to **2-$^{15}N^{18}O^-$**, see Figure 3.14. The reduction is completely reversible and after re-oxidation the starting six-coordinate complexes, **2_{MI}-NO** and **2_{MI}-$^{15}N^{18}O$** are regenerated.

Increasing the amount of MI to 170 eq. still shows formation of N-O stretching frequencies at 1473 and 1405 cm^{-1} for the natural abundance isotopes and $^{15}N^{18}O$ complexes, respectively. Using this, we can *estimate* the upper limit of the MI binding constant to **2-NO**$^-$ to be 0.2 M^{-1}. Using the Van't Hoff equation at 298.15 K this corresponds to an unfavourable Gibbs free energy, ΔG, of +1 kcal/mol for MI binding as listed in Table 3.5. This K_{eq} is calculated assuming 10% conversion to **2_{MI}-NO**$^-$ at 170 equivalent of MI—which spectroscopically we do not observe. As a result, the actual K_{eq} for MI binding to **2-NO** is, in reality, significantly lower than 0.2 M^{-1}. DFT geometry optimizations and calculated N-O stretching frequencies of [Fe(P)(MI)(NO)] and [Fe(P)(MI)(NO)]$^-$ support the strengthened thermodynamic

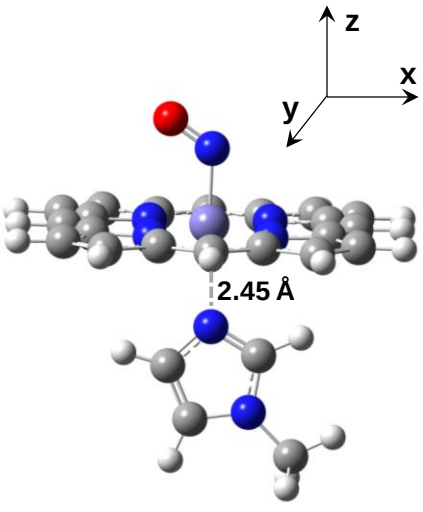

Figure 3.15. The model system [Fe(P)(MI)(NO)]$^-$, where P = porphine^{2-} and MI = 1=methylimidazole, and applied coordinate system. The structure shown is calculated using BP86/TZVP.

trans effect of NO^- in $\{FeNO\}^8$ porphyrin complexes compared to NO in the $\{FeNO\}^7$ analogues. The BP86/TZVP calculated Fe-N_{MI} bond length in $[Fe(P)(MI(NO)]^-$ is 2.45 Å (see Figure 3.15), essentially non-bonding compared to 2.18 Å for [Fe(P)(MI)(NO)] (see Table 3.6). Hence, NO^- has in fact the strongest *trans* effect of all diatomics in ferrous heme complexes!

The Electronic Structure of $\{FeNO\}^8$ Porphyrin Complexes and Comparison to the Analogous $\{FeNO\}^7$ Species

As shown in Figure 3.12, there is a surprisingly strong correlation between the N-O stretching frequencies in analogous $\{FeNO\}^7$ and $\{FeNO\}^8$ heme complexes. This implies that the nature of the singly occupied molecular orbital (SOMO) that is occupied with a second electron upon reduction of the complexes from $\{FeNO\}^7$ to $\{FeNO\}^8$ does not change to a significant degree in this process; i.e. whatever the composition of this MO is in the $\{FeNO\}^7$ complex is preserved in the $\{FeNO\}^8$ case. This implies that the properties of the $\{FeNO\}^8$ complexes investigated here in detail actually provide insight into the nature of the SOMO in the $\{FeNO\}^7$ precursors, and in this way, into the electronic structures of the $\{FeNO\}^7$ complexes.

Based on previous work,[37] detailed descriptions of the electronic structures of five- and six-coordinate ferrous heme-nitrosyls, $\{FeNO\}^7$, have been obtained. In these complexes, iron is in the +2 oxidation state and low-spin, leading to a $[t_2]^6[e]^0$ electron configuration of the metal. NO is a radical with one unpaired electron, which causes the resulting Fe(II)-NO adduct to have a total spin of S = 1/2. Hence, from a theoretical point of view, the spin-unrestricted scheme has to be applied to analyze bonding in the $\{FeNO\}^7$ complexes, which distinguishes between majority (α) and

Scheme 3.1. Molecular orbitals proposed to be involved in the σ-*trans* effect of NO in six-coordinate ferrous heme-nitrosyl complexes.

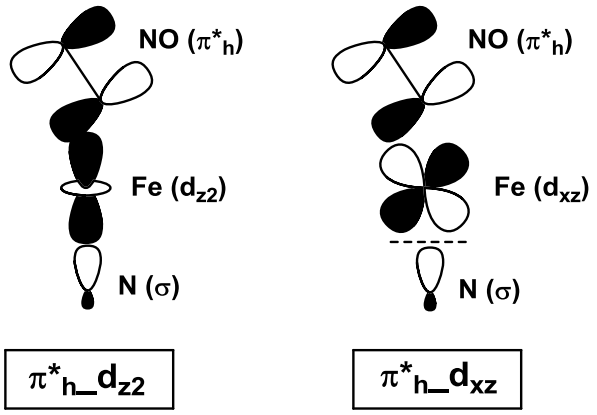

minority (β) MOs. In the five-coordinate case, strong donation from the singly-occupied π^* orbital of NO that is located in the Fe-N-O plane (α-π^*_h (h = horizontal) in the spin-unrestricted formalism) into the empty d_{z2} orbital of iron is observed, leading to the formation of a strong Fe-NO σ bond. The SOMO that results from this interaction is the bonding combination of α-π^*_h and α-d_{z2}, labelled π^*_h_d_{z2} in Scheme 3.1, left. Based on experimentally calibrated DFT (B3LYP) calculations,[34-35] this leads to a complete delocalization of the unpaired electron of NO, with resulting spin densities of about 50% on Fe and 50% on NO.[33] In addition, strong π-backbonding is observed between the unoccupied π^*_v orbital of NO (v = vertical, orthogonal the Fe-N-O plane) and the d_{yz} orbital of iron (in the applied coordinate system where the z axis is aligned with the heme-normal, and the Fe-N-O unit is in the xz plane). For a more detailed analysis see ref. [33, 37]. Additional contributions to the backbond are observed between the unoccupied β-π^*_h orbital of NO and β-d_{xz} of iron.

Upon coordination of an N-donor ligand (imidazole or His) in *trans* position to NO, a distinct weakening of the Fe-NO σ bond is observed. This induces a distinct

drop in the Fe-NO force constant and corresponding Fe-NO stretching frequency in the six-coordinate case as observed experimentally.[34, 42] In addition, the underlying σ-*trans* interaction between NO and imidazole leads to weak binding of imidazole in *trans* position to NO (K_{eq} is usually < 50 M^{-1}).[37] The presence of the axial imidazole ligand further induces a redistribution of the unpaired electron density of NO, which is mostly located on the NO ligand in the six-coordinate case. Based on B3LYP calculations,[34-35] the spin density distribution is estimated to be 80% on NO and 20% on Fe. This mechanism, the strong (thermodynamic) σ-*trans* effect of NO in low-spin $\{FeNO\}^7$ complexes, is responsible for the activation of the NO sensor soluble guanylate cyclase.[43-44]

Although basic agreement has been achieved in the literature on the overall electronic structure description of ferrous heme-nitrosyls as described above, the specific details are still highly controversial. The reason for this is that DFT methods are generally not very accurate in describing the properties of the Fe-N-O unit in these complexes.[37, 43, 45] In particular, the spin density distribution, i.e. the distribution of the unpaired electron of NO over the Fe-NO unit, and the shape of the SOMO are strongly affected by the chosen DFT method, as documented nicely by Pierloot and co-workers.[46-47] Where gradient-corrected functionals generally lead to metal-based spin (> 60% spin density on iron), hybrid functionals give a more unified distribution of the spin density over the whole Fe-N-O unit as described above.[37, 47] It has been recently suggested the metal-based spin description is more accurate due to high agreement of gradient-corrected functionals (for example, BP86, OLYP, PBE) with CASSCF/CASPT2 results.[47-48] However, CASSCF/CASPT2 calculations themselves can give highly varied spin density distributions based on the active space used in

these calculations and, as a result, may not provide the most accurate comparison.[45]

It is therefore most important to compare calculated properties to experiment to better assess the quality of the calculated results, in particular spectroscopic properties are a good way to gauge the quality of quantum-chemical calculations. In principal, EPR *g* values and hyperfine coupling constants (especially those of the coordinated ^{14}N atom of NO) should be a good experimental probe for the spin density distribution in ferrous heme-nitrosyls. In this case, it has been shown that gradient-corrected functionals[35, 49-50] perform slightly better than hybrid functionals[35] for the calculation of *g* tensors and hyperfine coupling constants. These types of calculations, however, generally show quite large deviations from experiment and are also strongly dependent on the geometry and the applied basis set.[51] Thus, it is difficult to judge the quality of the overall description solely based on comparisons of EPR parameters. On the other hand, calculated Fe-NO vibrational frequencies and force constants, which directly reflect the strength of the Fe-NO bond, show very clear trends when comparing the results from calculations using gradient-corrected and hybrid functional. Here, gradient-corrected functionals tend to overemphasize electron delocalization and, as demonstrated now for many cases,[37] lead to an overestimation of metal-ligand covalencies, and hence, bond strengths. In five- and six-coordinate ferrous heme-nitrosyls, the experimental Fe-NO stretching vibrations are located at 515 – 530 and ~440 cm^{-1}, respectively (see Table 3.3). Gradient-corrected functionals strongly overestimate the Fe-NO bond strength, predicting the Fe-NO stretching mode to occur at about 600 cm^{-1} in both the five- and six-coordinate complexes. In contrast, B3LYP predicts the Fe-NO stretch at 540 – 580 and ~420 cm^{-1} for the five- and six-coordinate $\{FeNO\}^7$ complexes, respectively, which is in much better agreement with experiment (see also ref. [37]). The

overestimation of the covalency of the Fe-NO bond with the gradient-corrected functionals goes along with a significant quenching of the spin density on the NO ligand. Because of this, the spin density distributions calculated with hybrid functionals (see above) can overall be expected to be more reliable, and hence, these should be in closer agreement with the electronic structures of the real complexes. Calculated Fe-NO binding energies further support these conclusions. Recently it has been shown that the inclusion of van der Waals interactions is of key importance to calculate accurate metal-ligand binding energies.[43, 52] When these contributions are included, hybrid functionals are able to predict quite accurate Fe-NO binding energies. In contrast, gradient-corrected functionals greatly overestimate NO binding energies[52] in agreement with overestimation of the Fe-NO bond strength.

Importantly, the experimental properties of the analogous {FeNO}^{8} comlexes investigated here provide further key insight into the properties of the SOMO in {FeNO}^{7} systems. Whereas previous DFT results characterize the SOMO of ferrous heme-nitrosyls as the *bonding* combination of α-π^*_h and α-d_{z^2}, π^*_h_d_{z^2}, as described above (see Scheme 3.1, left),[34, 53] it was recently proposed based on calculations performed with gradient-corrected functionals that for the corresponding six-coordinate complexes, this orbital should be considered the *antibonding* combination between α-π^*_h and α-d_{xz}, resulting in a SOMO that is strongly π-antibonding in nature as illustrated in Scheme 3.1, right.[48] This would *de facto* eliminate the Fe-NO σ bond in six-coordinate {FeNO}^{7} complexes. However, there are several experimental observations that argue against this notion. First, the strong thermodynamic σ *trans* effect of NO requires the presence of a distinct σ bond; in comparison, the strongly π backbonding ligand CO does not mediate much of a *trans* effect.[43, 54] Second, the

Table 3.7. Charge contributions of key σ bonding orbitals for $[Fe(P)(MI)(NO)]^{0/1-}$. Calculated with B3LTP/TZVP from BP86/TZVP optimized structures.

			Fe	NO	N_{MI}
Complex	**orbital**	**label**	**d**	**s+p**	**s+p**
[Fe(P)(MI)(NO)]	<120>	$\pi^*_h\_d_{z2}/d_{xz}$	27	58	2
$[Fe(P)(MI)(NO)]^-$	<122>	$\pi^*_h\_d_{z2}$	30	57	1

results of this study demonstrate that adding an electron to the SOMO of six-coordinate $\{FeNO\}^7$ complexes leads to a further increase of the *trans* effect as discussed above, which is evident from a further, dramatic decrease of the MI binding constant in the $\{FeNO\}^8$ case. As inferred from the strong correlation of ν(N-O) discussed above (see Figure 3.12), DFT calculations further confirm that this is not due to a change in the nature of the SOMO, but simply caused by the addition of one electron to this MO. As shown in Table 3.7 and Figure 3.16, the charge contributions of this MO are in fact invariant to the one-electron reduction. This is further illustrated in Scheme 3.2. Third, previous work by Ryan and co-workers on [Fe(TPP)(NO)] has shown that the Fe-NO stretching frequency is very similar in the

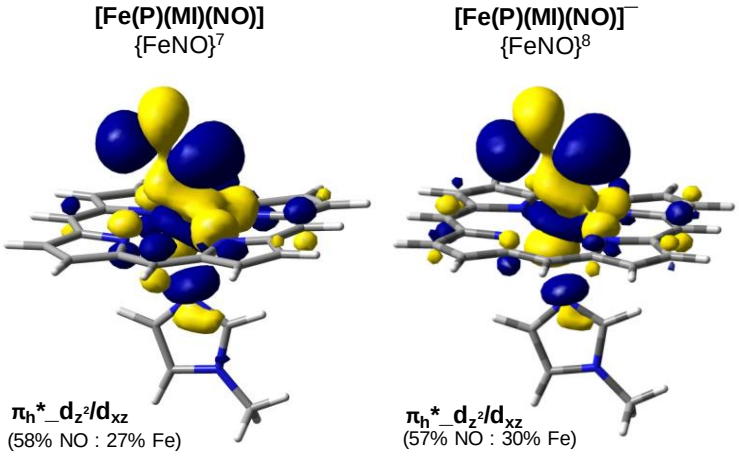

Figure 3.16. Key $\pi^*_h\_d_{z2}/d_{xz}$ molecular orbitals of (left) [Fe(P)(MI)(NO)] and (right) $[Fe(P)(MI)(NO)]^-$ which defines the thermodynamic σ-*trans* effect in ferrous porphyrin systems. Calculated with B3LYP/TZVP on BP86/TZVP optimized structures.

Scheme 3.2. Electronic structures of low-spin {FeNO}^{7} and {FeNO}^{8} complexes.

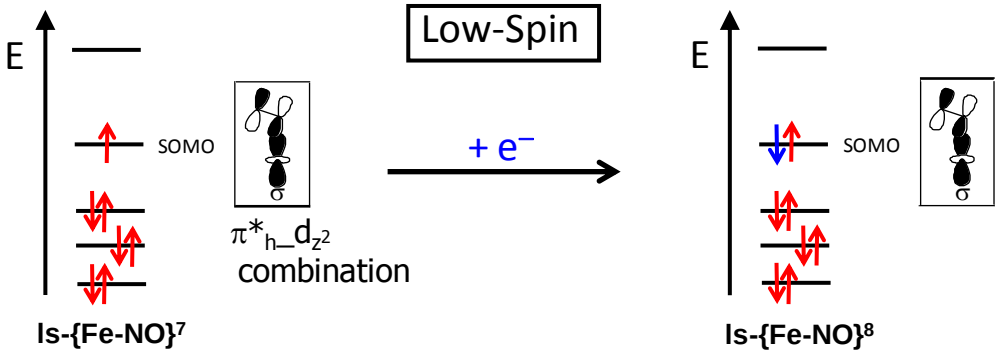

analogous {FeNO}^{7} and {FeNO}^{8} complexes (see Table 3.3).[25] This is due to the fact that the one-electron reduction leads to an increase in σ bonding and a reduction in π backbonding (between β-π^*_h and β-d_{xz}), leaving the Fe-NO bond essentially unchanged upon reduction. This finding disagrees with the idea that the SOMO is strongly π antibonding; in this case, occupation of this MO should lead to a distinct weakening of the Fe-NO bond, and a significant drop in the Fe-NO stretching frequency, which is not observed experimentally.

Reactivity of {FeNO}^{8} Complexes

Initial attempts at protonation of Fe(II)-NO⁻ heme complexes was focused on bulk electrolysis of the corresponding {FeNO}^{7} complex in the presence of acetic acid. For example, reduction of **2-NO** in THF at -0.9 V vs. Ag wire resulted in a ferrous product by UV-visible and EPR spectroscopy. The product does not show any isotope sensitive IR bands in the 1700-1200 cm^{-1} region as would be expected for a ferrous nitrosyl or nitroxyl product complex, and N_2O detection of the reaction head space did not show the presence of N_2O. Interestingly, coulometry indicated

that the reaction continued to progress well past one equivalent of electrons. In fact, the current did not stabilize until ~5 equivalents of electrons were passed. This implies that the formed Fe(II)-NHO complex is further reduced under our electrolysis conditions. As has been proposed previously in heme systems,[55-56] we expect our reaction to proceed as follows:

$$\text{Fe(II)-NO(radical)} + e^- \rightarrow \text{Fe(II)-NO}^- \quad (3)$$

$$\text{Fe(II)-NO}^- + H^+ \rightarrow \text{Fe(II)-NHO} \quad (4)$$

$$\text{Fe(II)-NHO} + 2\,e^- + 2\,H^+ \rightarrow \text{Fe(II)-NH}_2\text{OH} \quad (5)$$

$$\text{Fe(II)-NH}_2\text{OH} + 2\,e^- + 2\,H^+ \rightarrow \text{Fe(II)} + NH_3 + H_2O \quad (6)$$

where the reduction potentials of the intermittently formed Fe(II)-NHO and Fe(II)-NH_2OH complexes reported here are more positive than that of **2-NO**. Indeed, analysis of ammonia using Russell's hypochlorite-phenol[57-58] method yielded ~1 equivalent of NH_3 in the product mixture. As such, we propose our product to be a ferrous heme complex with bound ammonia or water. Similar reactivity was observed for the reduction of **1-NO** in the presence of acetic acid. Therefore, ferrous hemes can be considered catalysts for the electrochemical reduction of NO to NH_3 and water, similar to assimilatory nitrite reductases. However, due to the unfavourable reduction potential of the first step (equation 3), these catalysts are not very energy efficient.

As protonation of the formed $\{FeNO\}^8$ complexes in the presence of an applied potential results in further reduction of the generated Fe(II)-HNO species, it is essential to separate the reduction of the $\{FeNO\}^7$ complex from the protonation of the resulting $\{FeNO\}^8$ species. To accomplish this task, bulk electrolysis of **2-NO** was performed. Unfortunately, the reduction is unreliable and often leads to significant decomposition of **2-NO**$^-$.

Because of these difficulties, we devised an alternate route based on the observation that ferrous hemes can be reversibly reduced by bulk electrolysis (equation 7). The generated, formally iron(I), species (this actually corresponds to a reduction of the porphyrin ligand as discussed below) can then be reacted with NO, resulting in the desired {FeNO}^{8} complex:

$$[\text{Fe(porphyrin)}] + e^- \rightarrow [\text{Fe(porphyrin)}]^- \qquad (7)$$

$$[\text{Fe(porphyrin)}]^- + \text{NO} \rightarrow [\text{Fe(porphyrin)(NO)}]^- \qquad (8)$$

Here, the porphyrin ligand stores the electron necessary for reduction of the Fe-NO unit. This approach has been applied to [Fe(T*o*-F_2PP)] (**2**) and the resulting *in situ* UV-visible spectra are provided in Figure 3.17. Upon one-electron reduction in THF, the sharp Soret band at 422 nm decreases in intensity while new broad features at 364 and 386 nm appear (Figure 3.17, left). This drastic decrease in intensity is characteristic of a loss in porphyrin conjugation indicating that the product complex is formally a Fe(II)-porphyrin$^{\bullet-}$ (porphyrin radical) species.

Addition of low concentrations of NO gas generates a new 416 nm species,

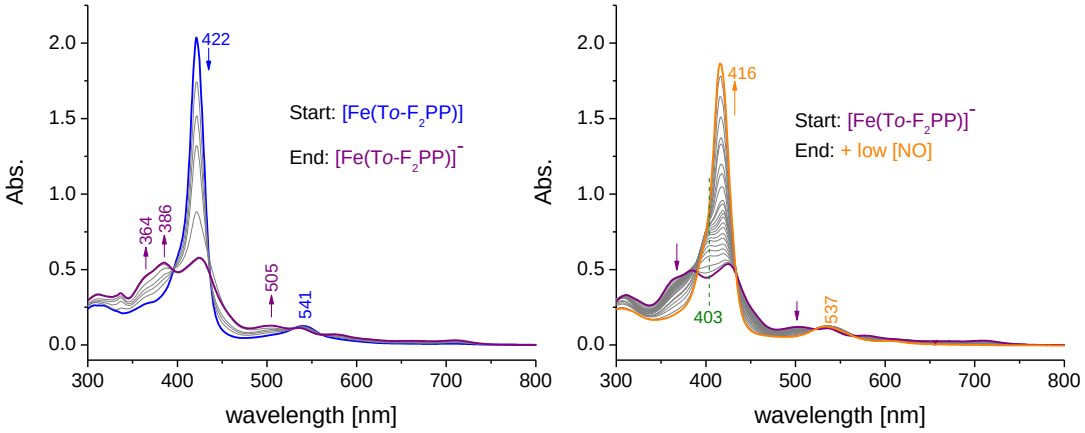

Figure 3.17. UV-vis spectra from the one-electron reduction of [Fe(T*o*-F_2PP)] (**2**, blue) to [Fe(T*o*-F_2PP)]$^-$ (**2**$^-$, purple), shown at left, and subsequent reaction with 10 µL NO (g) (right, orange) in THF at room temperature.

as shown in Figure 3.17 (right), of unknown nature. In contrast to this, if a high concentration of NO is added to **2**$^-$, see Figure 3.18, the desired **2-NO**$^-$ is generated without formation of the 416 nm complex. Our hypothesis is that the new 416 nm complex is a hyponitrite complex, or decomposition thereof. If correct, the formation of the 416 nm band would be dependent on the presence of **2-NO**$^-$, **2**$^-$ and free NO, as shown below:

$$\mathbf{2}^- + \mathrm{NO} + \mathbf{2\text{-}NO}^- \rightarrow \mathbf{2} + \mathbf{2\text{-}N_2O_2}^{2-} \qquad (9)$$

In order to test this we added NO gas to the pre-generated **2-NO**$^-$, resulting in formation of **2-NO** (the {FeNO}^{7} complex) with a Soret band at 408 nm instead of 416 nm (discussed below). This implies that only a mixture of **2**$^-$, NO, and **2-NO**$^-$ can generate this species, observed at 416 nm. Further work is needed to determine the exact identity of the 416 nm species.

Interestingly, **2-NO**$^-$ reacts with free NO in solution as mentioned above to form **2-NO**, as evident from UV-visible spectroscopy. This suggests that **2-NO**$^-$

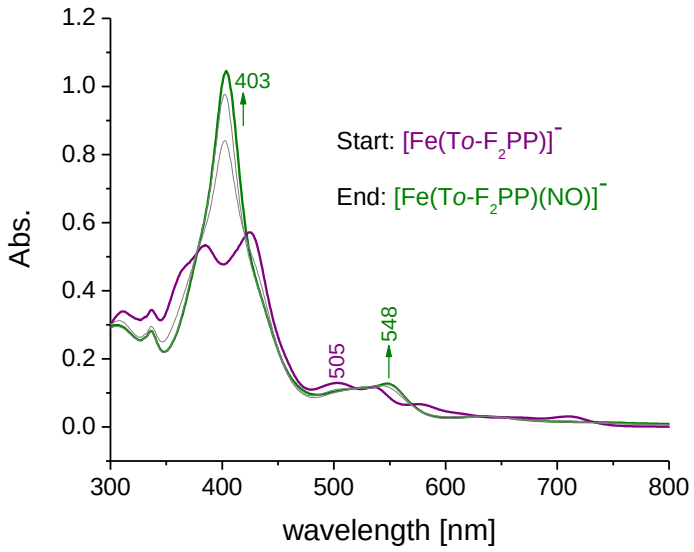

Figure 3.18. UV-visible spectra for the reaction of [Fe(T*o*-F_2PP)]$^-$ (**2**$^-$, purple) with NO to generate [Fe(T*o*-F_2PP)(NO)]$^-$ (**2-NO**$^-$, green) in THF at room temperature.

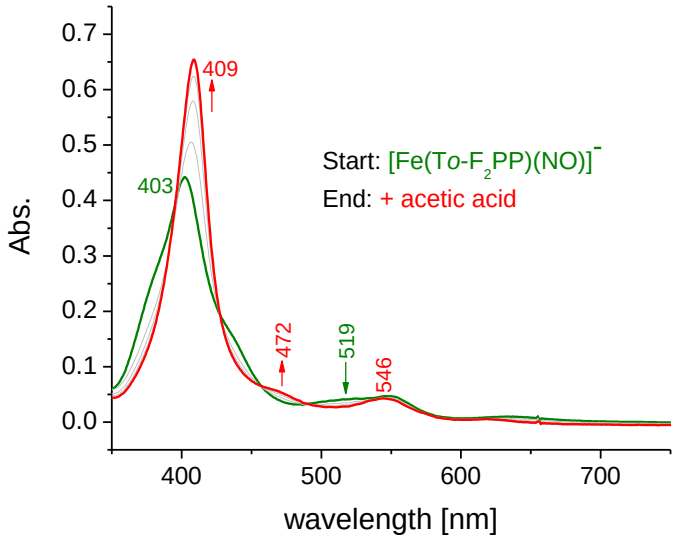

Figure 3.19. UV-visible spectra for the reaction of [Fe(T*o*-F_2PP)(NO)]$^-$ (**2-NO**$^-$, green) with 5 equivalents of acetic acid in THF at room temperature. The resulting spectrum (red) is in agreement with formation of [Fe(T*o*-F_2PP)(NO)] (**2-NO**).

actually reduces free NO, forming **2-NO** and NO$^-$, the latter then decomposes in an unknown fashion. In fact, the reduction potential of free NO is -0.8 V vs. SHE[59]—more positive than the resting potential of **2-NO**$^-$. Unfortunately, this reaction is not biologically relevant as biological deprotonated Fe(II)-NO$^-$ complexes do not likely exist, but become protonated quickly to the corresponding {FeNHO}^{8} species, due to their strong basicity.[13] Therefore, the protonation of **2-NO**$^-$ was explored.

Addition of acetic acid to **2-NO**$^-$ in THF resulted in the formation of **2-NO**, as shown in Figure 3.19. EPR spectroscopy of the reaction mixture shows the characteristic S = 1/2 signal, indicative of a low-spin ferrous heme-nitrosyl complex (data not shown). This is similar to the reactivity of [Fe(TPP)(NO)]$^-$ and [Fe(TFPPBr$_8$)(NO)]$^-$ with acid where the corresponding {FeNO}^{7} complex and 0.5 equivalents of H_2 are reported as products.[25, 27] This result is perhaps not surprising as T*o*-F_2PP^{2-}, similar to TPP^{2-} and TFPPBr$_8^{2-}$, lacks the steric protection needed to

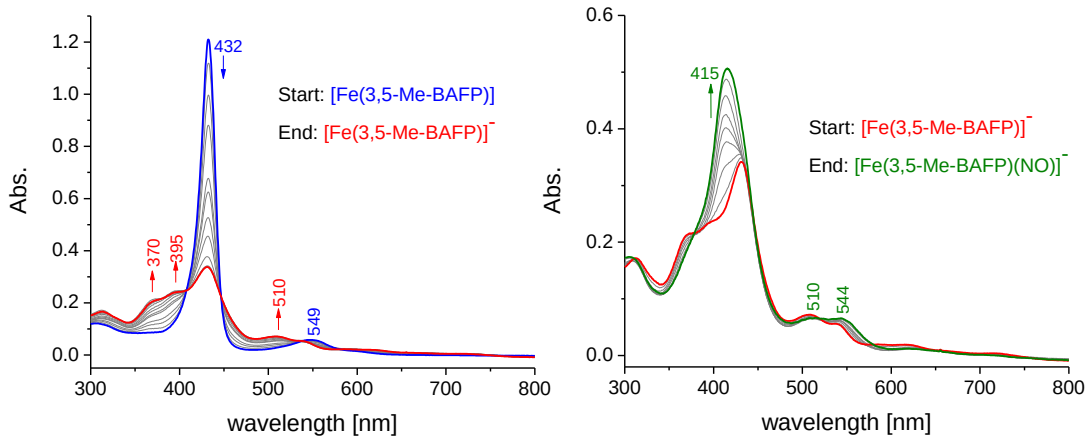

Figure 3.20. UV-vis spectra from the one-electron reduction of [Fe(3,5-Me-BAFP)] (**1**, blue) to [Fe(3,5-Me-BAFP)]– (**2**–, red), shown at left, and subsequent reaction with 100 µL NO (g) in THF at room temperature resulting in formation of [Fe(3,5-Me-BAFP)(NO)]– (right, green).

prevent this disproportionation of the Fe-NHO unit. In this sense, the reaction of the bis-picket fence porphyrin complex [Fe(3,5-Me-BAFP)(NO)]– (**1-NO**–) with acid is of extreme interest.

To this end, bulk electrolysis of [Fe(3,5-Me-BAFP)] (**1**) in THF was performed at room temperature. The *in situ* UV-visible spectra for the one-electron reduction to **1**– are reported in Figure 3.20 (left). Addition of 100 µL of NO to **1**– at room temperature results in formation of **1-NO**– with a Soret band at 415 nm (consistent with spectroelectrochemical measurements), as shown in Figure 3.20 (right). Subsequent reaction of **1-NO**– with ~ 5 equivalents of acetic acid indicates formation of a new complex with a Soret band at 426 nm, see Figure 3.21. Excitingly, this does not correspond to **1-NO**, which instead shows a Soret band of 422 nm in THF. This indicates that, through the use of a bis-picket fence porphyrin, we are able to block the disproportionation of bound HNO through the introduction of steric bulk around the HNO-adduct! Whether the generated species, observed at 426 nm, is the

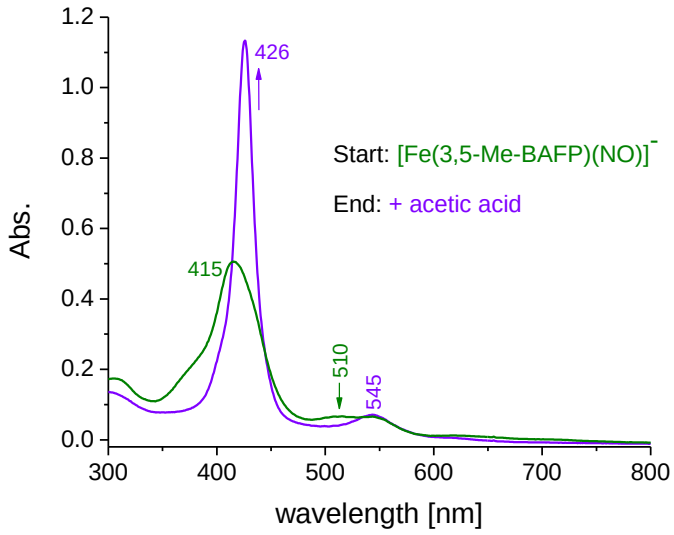

Figure 3.21. UV-visible spectra for the reaction of [Fe(3,5-Me-BAFP)(NO)]⁻ (**1-NO**⁻, green) with 5 equivalents of acetic acid in THF at room temperature. The resulting spectrum is shown in purple.

desired Fe(II)-NHO complex requires further investigation. It is also possible that the Fe(II)-NHO complex quickly looses HNO and, upon reaction of two free HNO molecules, generates an Fe(II)-H_2O complex and N_2O.

Conclusions

The properties and reactivity of a series of ferrous heme-nitroxyl complexes has been investigated. To this end, a new bis-picket fence porphyrin ferrous-nitrosyl complex, [Fe(3,5-Me-BAFP)(NO)], is prepared and one-electron reduction is performed. The N-O stretching frequency of the resulting reduced species ({FeNO}^{8}) is 1466 cm^{-1}. This is in agreement with other {FeNO}^{8} porphyrin complexes reported previously and the electron-poor heme complexes studied here. Importantly, we have demonstrated that the *trans* effect of bound NO⁻ is stronger than that of NO in ferrous heme systems. Upon one-electron reduction of the six-coordinate complex

[Fe(T*o*-F_2PP)(MI)(NO)], the resulting complex, [Fe(T*o*-F_2PP)(NO)]$^-$, is five-coordinate. This indicates loss of MI upon reduction to the {FeNO}^{8} complex, and an increased *trans* effect of NO$^-$ relative to NO. We estimate the binding constant, K_{eq}, of MI binding to [Fe(T*o*-F_2PP)(NO)] to be << 0.2 M^{-1}, at least four orders of magnitude smaller than that of MI binding to [Fe(T*o*-F_2PP)(NO)]. DFT results support this finding and indicate that the key molecular orbital, π^*_h_d_{z2}, responsible for the σ-*trans* effect in {FeNO}^{7} systems does not change upon one-electron reduction. Additionally, the reactivity of {FeNO}^{8} complexes with acid and free NO were explored. [Fe(T*o*-F_2PP)(NO)]$^-$ reacts with acetic acid to generate the corresponding {FeNO}^{7} complex and 0.5 equivalents H_2, whereas the corresponding sterically hindered 3,5-Me-BAFP^{2-} complex shows unique reactivity—effectively blocking the disproportionation of bound HNO. Finally, reaction of [Fe(T*o*-F_2PP)(NO)]$^-$ with NO results in reduction of free NO to NO$^-$ and oxidation of the ferrous nitroxyl complex to [Fe(T*o*-F_2PP)(NO)].

Experimental

All reactions were performed under an inert gas atmosphere using dried and distilled solvents. Handling of air-sensitive samples was carried out under an N_2 atmosphere in an MBraun glovebox equipped with a circulating purifier (O_2, H_2O < 0.1 ppm). Nitric oxide gas (Cryogenic Gases Inc., 99.5%) was passed through ascarite and then through a cold trap at –80°C prior to usage to remove higher nitrogen oxide impurities. Nitric oxide-$^{15}N^{18}O$ (Aldrich, 98% ^{15}N, 95% ^{18}O) was used without further purification. 1-methylimidazole (MI) was distilled and degassed prior to use. Ammonia analysis was carried out using the phenolate assay originally

developed by J. A. Russel.[57-58]

Tetrakis-5,10,15,20-(*per*-pentafluorophenyl)porphyrin, H_2[T*per*-F_5PP], and tetrakis-5,10,15,20-(*o*-difluorophenyl)porphyrin, H_2[T*o*-F_2PP], were synthesized and purified as previously reported.[60-61] Tetrakis-5,10,15,20-(2,6-dinitro-4-tert-butylphenyl)porphyrin, H_2[T*o*-$(NO_2)_2$-*p*-*t*BuPP], was prepared by BF_3-OEt catalyzed condensation of 2,6-dinitro-4-*tert*-butylbenzaldehyde[62] and pyrrole in CH_2Cl_2 as reported previously.[63] The porphyrin ligand H_2[3,5-Me-BAFP] was prepared according to modified literature procedures as described below.[64-65] Iron(III) chloride porphyrin complexes were prepared from the porphyrin ligand and excess $FeCl_2$ in refluxing DMF.[66] Five-coordinate ferrous porphyrin nitrosyls were prepared by reductive nitrosylation of the corresponding iron(III) chloride complexes.[31] A representative procedure for iron insertion and reductive nitrosylation is provided below. [^{57}Fe(3,5-Me-BAFP)(NO)] and [^{57}Fe(3,5-Me-BAFP)(^{15}N^{18}O)] for nuclear resonance vibrational spectroscopy (NRVS) measurements were prepared in the same manner as the n.a.i. complexes using $^{57}FeCl_2$ for the initial metallation.[67]

2,6-bis(3',5'-dimethylphenoxy)benzaldehyde. 3.4 g potassium methoxide, 12.5 mL dry benzene, and 6.1 g 3,5-dimethylphenol (50mmol) were added to a 100 mL Schlenk flask. The mixture was allowed to stir under Ar(g) for 1 hour. After 1 hour, benzene and methanol were removed via a Schlenk line. 12.5 mL dry pyridine was added and the mixture was brought to a reflux. Then, 3.2 g 2,6-dibromobenzaldehyde[64] and 0.19 g copper(I) chloride were added quickly to the mixture. The reaction was kept at reflux under Ar(g) for 17 hours. After 17 hrs, the mixture was added to 37 mL of ice water, and conc. hydrochloric acid was added until the solution became acidic. The reaction mixture was extracted with 20 mL

CH_2Cl_2 and the organic layer was washed with H_2O, saturated aqueous $NaHCO_3$, and H_2O. The mixture was concentrated to an oil using a rotary evaporator. The oil was chromatographed twice on silica with CH_2Cl_2 as the eluent. The fractions containing the desired product were rotary evaporated to a light yellow solid. Yield: 2.3 g (55%). ^{1}H-NMR (400 MHz, $CDCl_3$): 10.57 (s, 1H); 7.30 (t, 1H); 6.80 (s, 2H); 6.69 (s, 4H); 6.56 (d, 2H); 2.30 (s, 12H).

3,5-methyl-Bis(Aryloxy)-FencePorphyrin, H_2[3,5-Me-BAFP].[65] 1.135 g 2,6-bis(3,5-dimethylphenoxy)benzaldehyde, 325 mL CH_2Cl_2, and 2.5 mL absolute ethanol were placed in a 500 mL round bottom flask (RBF) and sparged with Ar (g). 0.25 mL pyrrole was then added via syringe and the solution was stirred for 5 min. Then, 0.16 mL boron trifluoride diethyletherate was added via syringe and the solution was stirred in the dark for one hour at room temperature. After one hour, 0.56 g

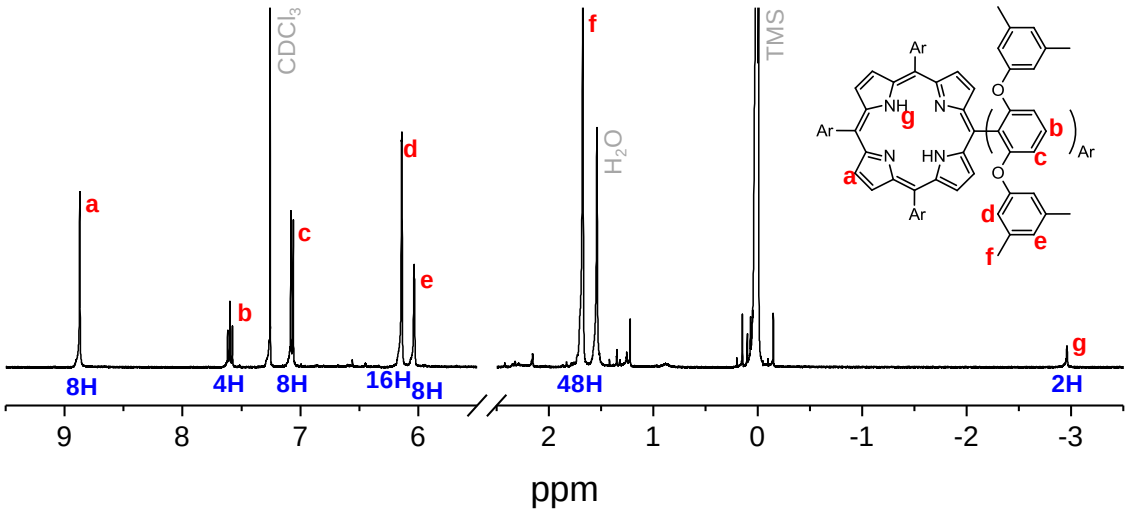

Figure 3.22. ^{1}H NMR of 3,5-methyl-Bis(Aryloxy)-FencePorphyrin, H_2[3,5-Me-BAFP] in $CDCl_3$.

dichlorodicyano-benzoquinone and 0.16 mL triethylamine were added, and the reaction was stirred for an additional hour. The reaction mixture was then evaporated to dryness, chromoatographed on silica with 100% CH_2Cl_2, and the obtained solid was recrystallized from CH_2Cl_2/MeOH. Yield: 349 mg (27%). ^{1}H-NMR (400MHz, $CDCl_3$): 8.86 (s, 8H); 7.59 (t, 4H); 7.06 (d, 8H); 6.13 (s, 16H); 6.02 (s, 8H); 1.66 (s, 48H); -2.98 (s, 2H); see Figure 3.22. LCT MS: m/z 1576.1 (M+1). UV-vis (CH_2Cl_2): 424, 517, 554, 593 nm.

[Fe(3,5-Me-BAFP)(Cl)]. 270 mg H_2[3,5-Me-BAFP] in 60 mL dry THF was brought to a reflux. Once refluxing, 0.22 g $FeCl_2$ was quickly added and the reaction was allowed to reflux for 3 hours. The solution was evaporated to dryness and the crude material chromatographed on silica with 100% CH_2Cl_2 (to remove free base porphyrin) and 98:2 CH_2Cl_2:MeOH to elute the ferric porphyrin. The product band was evaporated, the resulting solid was redissolved in CH_2Cl_2 and washed with ~1 M HCl. The organic layer was first dried with Na_2SO_4, and the solvent was then removed under reduced pressure to yield a dark purple powder. Yield: 186 mg (66%). LCT MS: m/z 1629.8 (M-Cl). UV-vis (CH_2Cl_2): 374, 424, 510, 584, 667 nm.

[Fe(3,5-Me-BAFP)(NO)] (**1-NO**). 325 mg of [Fe(3,5-Me-BAFP)(Cl)] was dissolved in 9 mL CH_2Cl_2 and 0.9 mL MeOH. The solution was exposed to excess NO (g) and stirred at room temperature for 30 min. The resulting nitrosyl complex was precipitated with the addition of 24 mL MeOH and stored at -30^{o}C overnight. The resulting solid was filtered under inert atmosphere and dried for 2 min under reduced pressure. Yield: 253 mg (78%). FT-IR: ν(N-O) 1686 cm^{-1}. [Fe(3,5-Me-BAFP)(^{15}N^{18}O)]

was prepared with $^{15}N^{18}O$ using the same procedure. FT-IR: $\nu(^{15}N\text{-}^{18}O)$ 1614 cm^{-1}. UV-vis (THF): 412, 483, 554 nm. UV-vis (1,2-DCE): 421, 480, 555 nm.

Crystallization of [Fe(3,5-Me-BAFP)(NO)]. In the glovebox, ~2 mg [Fe(3,5-Me-BAFP)(NO)] was dissolved in 1 mL THF and placed in a 7 mm glass tube. 5 mL MeOH was carefully layered on the THF solution and the setup was left under an inert atmosphere to crystallize. After 8 days, crystals suitable for X-ray analysis were collected.

Physical Measurements

Infrared spectra were obtained from KBr disks on a Perkin-Elmer BX spectrometer at room temperature. Resolution was set to 2 cm^{-1}. Proton magnetic resonance spectra were recorded on a Varian Inova 400 MHz instrument. Electronic absorption spectra were measured using an Analytical Jena Specord 600 instrument at room temperature. Electron paramagnetic resonance spectra were recorded on a Bruker X-band EMX spectrometer equipped with an Oxford Instruments liquid nitrogen cryostat. EPR spectra were typically obtained on frozen solutions using 20 mW microwave power and 100 kHz field modulation with the amplitude set to 1 G. Sample concentrations employed were ~1 mM. Nuclear resonance vibrational spectroscopy (NRVS) data were obtained as described previously[36] at beam line 3-ID-XOR of the Advanced Photon Source (APS) at Argonne National Laboratory. This beamline provides about 2.5 x 10^9 photons/sec in ~1 meV bandwidth (= 8 cm^{-1}) at 14.4125 keV in a 0.5 mm (vertical) x 0.5 mm (horizontal) spot. Samples were loaded into 4 x 7 x 1 mm copper NRVS cells. The final spectra represent averages of 6

scans. The program Phoenix was used to convert the NRVS raw data to the Vibrational Density of States (VDOS).[68-69]

Cyclic voltammograms (CVs) were recorded with a CH instruments CHI660C electrochemical workstation using a three component system consisting of a platinum or glassy carbon working electrode, a platinum auxiliary electrode, and an Ag wire pseudo-reference electrode. CVs were measured in 0.1 M tetrabutyl-ammonium perchlorate (TBAP) solutions in THF or 1,2-dichloroethane (1,2-DCE). Potentials are reported against the measured Fc/Fc^+ couple. IR spectroelectrochemistry was performed using a solution IR cell with CaF_2 windows as previously described.[26] Electrodes consist of an 8 x 10 mm Pt mesh (100 mesh, 99.9%, Aldrich) for the working, 3 x 10 mm Pt mesh for the counter, and Ag wire (0.1 mm diameter, 99.9%, Aldrich) as a pseudo-reference electrode. UV-vis spectroelectrochemistry was performed in a OTTLE cell.[70] Electrodes consist of an 8 x 10 mm Pt mesh (100 mesh, 99.9%, Aldrich) for the working, 3 x 20 mm Pt mesh for the counter, and Ag wire (1 mm diameter, 99.9%, Aldrich) as a pseudo-reference electrode. Bulk electrolysis was performed in a two compartment set-up where the carbon felt working electrode and Ag wire reference electrode are separated from the carbon felt counter electrode by a fine frit. The counter electrode compartment contains solvent in electrolyte. Electrolyte (TBAP of $TBAPF_6$) was 0.1 M. All bulk electrolysis experiments were performed in the glovebox (O_2 < 0.1 ppm).

X-ray crystallography measurements were performed on a Rigaku R-AXIS RAPID imaging plate diffractometer using graphite monochromated Cu-Kα radiation. A red prism crystal of $C_{108}H_{92}O_9N_5Fe$ having approximate dimensions of 0.20 x 0.20 x 0.20 mm was mounted on a glass fiber. See Table 3.1 for crystallographic

data and measurement parameters. The crystal-to-detector distance was 127.40 mm. Readout was performed in the 0.100 mm pixel mode. The data were processed with SADABS and corrected for absorption. The structure was solved and refined with the Bruker SHELXTL (vs. 2008/3) software package.

DFT Calculations

All geometry optimizations and frequency calculations were performed with the program package Gaussian 03[71] using the BP86[72-73] functional and TZVP[74-75] basis set. Molecular orbitals were obtained from B3LYP[73, 76-77]/TZVP single point calculations on the BP86/TZVP optimized structures using ORCA.[78] In all Gaussian calculations, convergence was reached when the relative change in the density matrix between subsequent iterations was less that 1×10^{-8}. Molecular orbitals were plotted with the program orca_plot included in the ORCA package and visualized using GaussView.

References

1. Burney, S.; Tamir, S.; Gal, A.; Tannenbaum, S. R., *Nitric Oxide* **1997,** *1*, 130-144.
2. Moncada, S.; Palmer, R. M.; Higgs, E. A., *Pharmacol. Rev.* **1991,** *43*, 109-142.
3. Snyder, S. H., *Science* **1992,** *257*, 494-496.
4. Bredt, D. S.; Snyder, S. H., *Annu. Rev. Biochem.* **1994,** *63*, 175-195.
5. Ignarro, L., *Nitric Oxide: Biology and Pathobiology*. Academic Press: San Diego, 2000.
6. Nakahara, K.; Tanimoto, T.; Hatano, K.; Usuda, K.; Shoun, H., *J. Biol. Chem.* **1993,** *268*, 8350-8355.
7. Dabier, A.; Shoun, H.; Ullrich, V., *J. Inorg. Biochem.* **2005,** *99*, 185-193.

8. Park, S.-Y.; Shimizu, H.; Adachi, S.; Nagagawa, A.; Tanaka, I.; Nakahara, K.; Shoun, H.; Obayashi, E.; Nakamura, H.; Iizuka, T.; Shiro, Y., *Nat. Struct. Biol.* **1997,** *4*, 827-832.

9. Shimizu, H.; Park, S.-Y.; Lee, D. S.; Shoun, H.; Shiro, Y., *J. Inorg. Biochem.* **2000,** *81*, 191-205.

10. Shiro, Y.; Fujii, M.; Iisuka, T.; Adachi, S.; Tsukamoto, K.; Nakahara, K.; Shoun, H., *J. Biol. Chem.* **1995,** *270*, 1617-1623.

11. Enemark, J. H.; Feltham, R. D., *Coord. Chem. Rev.* **1974,** *13*, 339-406.

12. Obayashi, E.; Takahashi, S.; Shiro, Y., *J. Am. Chem. Soc.* **1998,** *120*, 12964-12965.

13. Lehnert, N.; Praneeth, V. K. K.; Paulat, F., *J. Comp. Chem.* **2006,** *27*, 1338-1351.

14. Riplinger, C.; Neese, F., *Chem. Phys. Chem.* **2011,** *12*, 3192-3203.

15. Hino, T.; Matsumoto, Y.; Nagano, S.; Sugimoto, Y.; Fukumori, Y.; Murata, T.; Iwata, S.; Shiro, Y., *Science* **2010,** *330*, 1666-1670.

16. Lehnert, N.; Berto, T. C.; Galinato, M. G. I.; Goodrich, L. E., The Role of Heme-Nitrosyls in the Biosynthesis, Transport, Sensing, and Detoxification of Nitric Oxide (NO) in Biological Systems: Enzymes and Model Complexes. In *Handbook of Porphyrin Science*, Kadish, K. M.; Smith, K.; Guilard, R., Eds. World Scientific: 2012; Vol. 15, pp 1-247.

17. Yi, J.; Morrow, B. H.; Campbell, A. L. O. C.; Shen, J. K.; Richter-Addo, G. B., *Chem. Comm.* **2012,** *48*, 9041-9043.

18. King, S. B.; Nagasawa, H. T., *Methods Enzymol.* **1998,** *301*, 211-221.

19. Sulc, F.; Immoos, C. E.; Pervitsky, D.; Farmer, P. J., *J. Am. Chem. Soc.* **2004,** *126*, 1096-1101.

20. Kumar, M. R.; Pervitsky, D.; Chen, L.; Poulos, T.; Kundu, S.; Hargrove, M. S.; Rivera, E. J.; Diaz, A.; Colon, J. L.; Farmer, P. J., *Biochemistry* **2009,** *48*, 5018-5025.

21. Immoos, C. E.; Sulc, F.; Farmer, P. J.; Czarnecki, K.; Bocian, D. F.; Levina, A.; Aitken, J. B.; Armstrong, R. S.; Lay, P., *J. Am. Chem. Soc.* **2005,** *127*, 814-815.

22. Lin, R.; Farmer, P. J., *J. Am. Chem. Soc.* **2000,** *122*, 2393-2394.

23. Lancon, D.; Kadish, K. M., *J. Am. Chem. Soc.* **1983,** *105*, 5610-5617.

24. Olson, L. W.; Schaeper, D.; Lancon, D.; Kadish, K. M., *J. Am. Chem. Soc.* **1982,** *104*, 2042-2044.

25. Choi, I. K.; Liu, Y.; Feng, D. W.; Paeng, K. J.; Ryan, M. D., *Inorg. Chem.* **1991,** *30*, 1832-1839.

26. Wei, Z.; Ryan, M. D., *Inorg. Chem.* **2010,** *49*, 6948-6954.

27. Pellegrino, J.; Bari, S. E.; Bikiel, D. E.; Doctorovich, F., *J. Am. Chem. Soc.* **2010,** *132*, 989-995.

28. Wyllie, G. R. A.; Scheidt, W. R., *Chem. Rev.* **2002,** *102*, 1067-1090.

29. Silvernail, N. J.; Olmstead, M. M.; Noll, B. C.; Scheidt, W. R., *Inorg. Chem.* **2009,** *48*, 971-977.

30. Scheidt, W. R.; Duval, H. F.; Neal, T. J.; Ellison, M. K., *J. Am. Chem. Soc.* **2000,** *122*.

31. Scheidt, W. R.; Frisse, M. E., *J. Am. Chem. Soc.* **1975,** *97*, 17-21.

32. Scheidt, W. R.; Barabanschikov, A.; Pavlik, J. W.; Silvernail, N. J.; Sage, J. T., *Inorg. Chem.* **2010,** *49*, 6240-6252.

33. Lehnert, N.; Galinato, M. G. I.; Paulat, F.; Richter-Addo, G. B.; Sturhahn, W.; Xu, N.; Zhao, J., *Inorg. Chem.* **2010,** *49*, 4133-4148.

34. Praneeth, V. K. K.; Nather, C.; Peters, G.; Lehnert, N., *Inorg. Chem.* **2006,** *45*, 2795-2811.

35. Praneeth, V. K. K.; Neese, F.; Lehnert, N., *Inorg. Chem.* **2005,** *44*, 2570-2572.

36. Paulat, F.; Berto, T. C.; DeBeer George, S.; Goodrich, L.; Praneeth, V. K. K.; Sulok, C. D.; Lehnert, N., *Inorg. Chem.* **2008,** *47*, 11449-11451.

37. Goodrich, L. E.; Paulat, F.; Praneeth, V. K. K.; Lehnert, N., *Inorg. Chem.* **2010,** *49*, 6293-6316.

38. Berto, T. C.; Praneeth, V. K. K.; Goodrich, L. E.; Lehnert, N., *J. Am. Chem. Soc.* **2009,** *47*, 17116-17126.

39. Rose, N. J.; Drago, R. S., *J. Am. Chem. Soc.* **1959,** *81*, 6138-6141.

40. Beugelskijk, T. J.; Drago, R. S., *J. Am. Chem. Soc.* **1975,** *97*, 6466-6472.

41. Collman, J. P.; Brauman, J. I.; Doxsee, K. M.; Halbert, T. R.; Hayes, S. E.; Suslick, K. S., *J. Am. Chem. Soc.* **1978,** *100*, 2761-2766.

42. Lehnert, N.; Sage, J. T.; Silvernail, N. J.; Scheidt, W. R.; Alp, E. E.; Sturhahn, W.; Zhao, J., *Inorg. Chem.* **2010,** *49*, 7197-7215.

43. Goodrich, L. E.; Lehnert, N., *J. Inorg. Biochem.* **2012,** *in press*.

44. Traylor, T. G.; Sharma, V. S., *Biochemistry* **1992,** *31*, 2847-2849.

45. Boguslawski, K.; Jacob, C. R.; Reiher, M., *J. Chem. Theory Comput.* **2011,** *2011*, 2740-2752.

46. Radon, M.; Broclawik, E.; Pierloot, K., *J. Phys. Chem. B* **2010,** *114*, 1518-1528.

47. Radon, M.; Pierloot, K., *J. Phys. Chem. A* **2008,** *112*, 11824-11832.

48. Radoul, M.; Bykov, D.; Rinaldo, S.; Cutruzzola, F.; Neese, F.; Goldfarb, D., *J. Am. Chem. Soc.* **2011,** *133*, 3043-3055.

49. Radoul, M.; Sundararajan, M.; Potapov, A.; Riplinger, C.; Neese, F.; Goldfarb, D., *Phys. Chem. Chem. Phys.* **2010,** *12*, 7276-7289.

50. Zhang, Y.; Gossman, W.; Oldfield, E., *J. Am. Chem. Soc.* **2003,** *125*, 16387-16396.

51. Neese, F., *J. Chem. Phys.* **2001,** *115*, 11080-11096.

52. Siegbahn, P. E. M.; Bolmberg, M. R. A.; Chen, S. L., *J. Chem. Theory Comput.* **2010,** *6*, 2040-2044.

53. Patchkovskii, S.; Ziegler, T., *Inorg. Chem.* **2000,** *39*, 5354-5364.

54. Leu, B. M.; Silvernail, N. J.; Zgierski, M. Z.; Wyllie, G. R. A.; Ellison, M. K.; Scheidt, W. R.; Zhao, J.; Sturhahn, W.; Alp, E. E.; Sage, J. T., *Biophys. J.* **2007,** *92*, 3764-3783.

55. Barley, M. H.; Takeuchi, K. J.; Meyer, T. J., *J. Am. Chem. Soc.* **1986,** *108*, 5876-5885.

56. Barley, M. H.; Rhodes, M. R.; Meyer, T. J., *Inorg. Chem.* **1987,** *26*, 1746-1750.

57. Russell, J. A., *J. Biol. Chem.* **1944,** *156*, 457-462.

58. Choi, I. K.; Wei, Z.; Ryan, M. D., *Inorg. Chem.* **1997,** *36*, 3113-3118.

59. Bartberger, M. D.; Liu, W.; Ford, E.; Miranda, K. M.; Switzer, C.; Fukuto, J. M.; Farmer, P. J.; Wink, D. A.; Houk, K. N., *Proc. Nat. Acad. Sci. USA* **2002,** *99*, 10958-10963.

60. Quast, H.; Dietz, T.; Witzel, A., *Liebigs. Ann.* **1995**, 1495-1501.

61. Ghiladi, R. A.; Kretzer, R. M.; Guzei, I.; Rheingold, A. L.; Neuhold, Y.-M.; Hatwell, K. R.; Zuberbuhler, A. D.; Karlin, K. D., *Inorg. Chem.* **2001,** *40*, 5754-5767.

62. Peters, M. V.; Stoll, R. S.; Goddard, R.; Buth, G.; Hecht, S., *J. Org. Chem.* **2006,** *71*, 7840-7845.

63. Rose, E.; Kossanyi, A.; Quelquejeu, M.; Soleilhavoup, M.; Duwavran, F.; Bernard, N.; Lecas, A., *J. Am. Chem. Soc.* **1996,** *118*, 1567-1568.

64. Lulinski, S.; Servatowski, J., *J. Org. Chem.* **2003,** *68*, 5384-5387.

65. Tohara, A.; Sugawara, Y.; Sato, M., *J. Porphyrins Phthalocyanines* **2006,** *10*, 104-116.

66. Adler, A. D.; Longo, F. R.; Kampas, F.; Kim, J., *J. Inorg. Nucl. Chem.* **1970,** *32*, 2443-2445.

67. Berto, T. C.; Hoffman, M. B.; Murata, Y.; Landenberger, K. B.; Alp, E. E.; Zhao, J.; Lehnert, N., *J. Am. Chem. Soc.* **2011,** *133*, 16714-16717.

68. Sage, J. T.; Paxson, C.; Wyllie, G. R. A.; Sturhahn, W.; Durbin, S. M.; Champion, P. M.; Alp, E. E.; Scheidt, W. R., *J. Phys. Condens. Matter* **2001,** *13*, 7707-7722.

69. Sturhahn, W., *Hyperfine Interact.* **2000,** *125*, 149-172.

70. Lin, X. Q.; Kadish, K. M., *Anal. Chem.* **1985,** *57*, 1498-1501.

71. Frisch, M. J.; Trucks, G. W.; Schlegel, H. B.; Scuseria, G. E.; Robb, M. A.; Cheeseman, J. R.; Montgomery, J., J. A.; Vreven, T.; Kudin, K. N.; Burant, J. C.; Millam, J. M.; Iyengar, S. S.; Tomasi, J.; Barone, V.; Mennucci, B.; Cossi, M.; Scalmani, G.; Rega, N.; Petersson, G. A.; Nakatsuji, H.; Hada, M.; Ehara, M.; Toyota, K.; Fukuda, R.; Hasegawa, J.; Ishida, M.; Nakajima, T.; Honda, Y.; Kitao, O.; Nakai, H.; Klene, M.; Li, X.; Knox, J. E.; Hratchian, H. P.; Cross, J. B.; Bakken, V.; Adamo, C.; Jaramillo, J.; Gomperts, R.; Stratmann, R. E.; Yazyev, O.; Ausin, A. J.; Cammi, R.; Pomelli, C.; Octerski, J. W.; Ayala, P. Y.; Morokuma, K.; Voth, G. A.; Salvador, P.; Dannenberg, J. J.; Zakrzewski, V. G.; Dapprich, S.; Daniels, A. D.; Strain, M. C.; Farkas, O.; Makick, D. K.; Rabuck, A. D.; Raghavachair, K.; Foresman, J. B.; Ortiz, J. V.; Cui, Q.; Baboul, A. G.; Clifford, S.; Cioslowski, J.; Stefanov, B. B.; Lui, G.; Laishenko, A.; Piskorz, R.; Komaromi, I.; Martin, R. L.; Fox, D. J.; Keith, T.; Al-Laham, M. A.; Peng, C. Y.; Nanayakkara, A.; Challacombe, M.; Gill, P. M. W.; Johnson, B.; Chen, W.; Wong, M. W.; Gonzalez, C.; Pople, J. A. *Gaussin 03*, Gaussian, Inc.: Pittsburgh, PA, 2003.

72. Perdew, J. P., *Phys. Rev. B* **1986,** *33*, 8822-8824.

73. Becke, A. D., *Phys. Rev. A* **1988,** *38*, 3098-3100.

74. Schaefer, A.; Horn, H.; Ahlrichs, R., *J. Chem. Phys.* **1992,** *97*, 2571-2577.

75. Schaefer, A.; Huber, C.; Ahlrichs, R., *J. Chem. Phys.* **1994,** *100*, 5829-5835.

76. Becke, A. D., *J. Chem. Phys.* **1993,** *98*, 1372-1377.

77. Becke, A. D., *J. Chem. Phys.* **1993,** *98*, 5648-5652.

78. Neese, F. *ORCA*, 2.2; Max-Planck Institut feur Bioanorganische Chemie: Meulheim/Ruhr, Germany, 2004.

Chapter 4

Investigations into the Active Species of P450nor:

Towards High-Valent Iron Porphyrin Complexes with N-Based Ligands

From enzyme studies on P450nor, it is known that NO reacts with the ferric state of the enzyme to form a ferric heme-nitrosyl. This species is reduced by NADH in the next step, resulting in a ferrous heme-nitroxyl (HNO) intermediate.[1-2] DFT predicts that this species (basic due to the presence of the cysteinate ligand) will be easily protonated to form a formally Fe(IV)-NHOH complex.[3] At this point, two mechanistic pathways exist as illustrated in Scheme 4.1, either the ferryl species reacts with a second equivalent of NO *or* this complex loses H_2O to form a (formally) Fe(VI)-nitride complex which in turn reacts with NO. The latter species is the nitrogen analog of the highly oxidizing Fe(IV)=O complexes found in monooxygenase cytochrome P450s. This leads to an important mechanistic question: which complex is the actual catalyst—is it the Fe(IV)-NHOH or Fe(VI)-

Scheme 4.1. Two possible mechanistic pathways for N_2O production by P450nor.

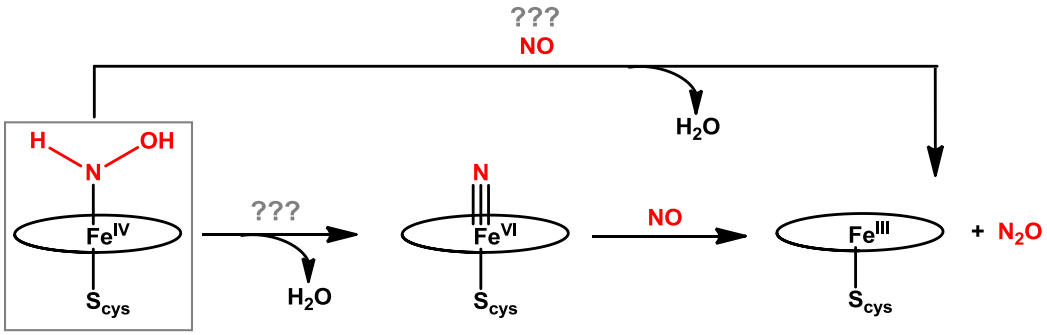

nitride species—that performs the crucial N-N bond coupling reaction required to form N_2O? Unfortunately, P450nor protein studies are unable to identify the exact nature of this key intermediate ('Intermediate I').

In this chapter, we work towards answering this question. Section 4.1 will address the synthesis and characterization of ferric porphyrin hydroxylamine complexes, with the eventual goal of one-electron electrochemical oxidation to form the desired ferryl intermediate. Section 4.2 discusses whether formation of an Fe(VI)-nitride is energetically favorable in solution followed by attempts at synthesis of Fe(V)-nitride complexes through the irradiation of high- and low-spin ferric porphyrin azide complexes.

4.1. Ferric Porphyrin O-Benzylhydroxylamide Complexes

Since iron(IV) porphyrin complexes are highly reactive and, in general, quite unstable, we propose the synthesis of the desired Fe(IV)-NHOH intermediate through one-electron oxidation of the corresponding ferric species. Here, hydroxylamine (NH_2OH) can be deprotonated (hydroxylamide, $NHOH^-$) and bound to a ferric heme prior to one-electron oxidation to the desired ferryl complex. Surprisingly, however, a stable ferric heme NHOH-type complex has not been reported. This is likely due to dispropotionation of the bound $NHOH^-$ unit by iron(III), as reported previously,[4-5] and the temperature instability of hydroxylamine. To combat these decomposition pathways we decided to employ the model complex [Fe(3,5-Me-BAFP)(NHOBn)], as illustrated in Scheme 4.2. Here, the bulky bis-picket fence porphyrin, 3,5-Me-$BAFP^{2-}$, should effectively block disproportionation of bound hydroxylamine ligands by sterically preventing intermolecular interactions between

Scheme 4.2. Target complex, [Fe(3,5-Me-BAFP)(NHOBn)], for modeling the proposed Fe(IV)-NHOH intermediate in the catalytic cycle of P450nor.

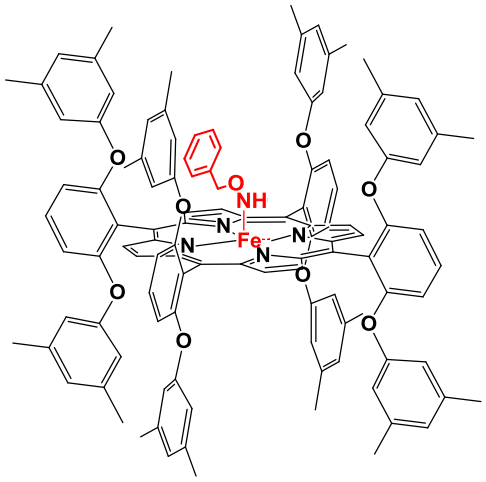

two Fe-NHOH units. Additionally, employing O-benzylhydroxylamide ($NHOBn^-$) will impart temperature stability to the hydroxylamine ligand while promoting nitrogen coordination to the iron center. This work was completed together with summer undergraduate student Claire Goodrich (University of Minnesota, Morris).

Reduction of a Ferric Bis-Picket Fence Porphyrin by O-Benzylhydroxylamine

In an initial attempt to synthesize a ferric-NHOBn porphyrin complex, [Fe(3,5-Me-BAFP)(ClO_4)] was mixed with excess O-benzylhydroxylamine (NH_2OBn) in toluene. In theory, after reaction with the ferric heme species, the bound NH_2OBn could be deprotonated to produce the desired Fe(III)-NHOBn complex. The resulting UV-visible spectrum is shown in Figure 4.1. The UV-visible spectrum of the starting [Fe(3,5-Me-BAFP)(ClO_4)] complex has a Soret band at 416 nm in toluene and a prominent Q band at 518 nm. Upon addition of NH_2OBn, the Soret band shifts to 433 nm and the highest energy Q band is observed at 537 nm. The changes are accompanied by a dramatic sharpening of the Soret band.

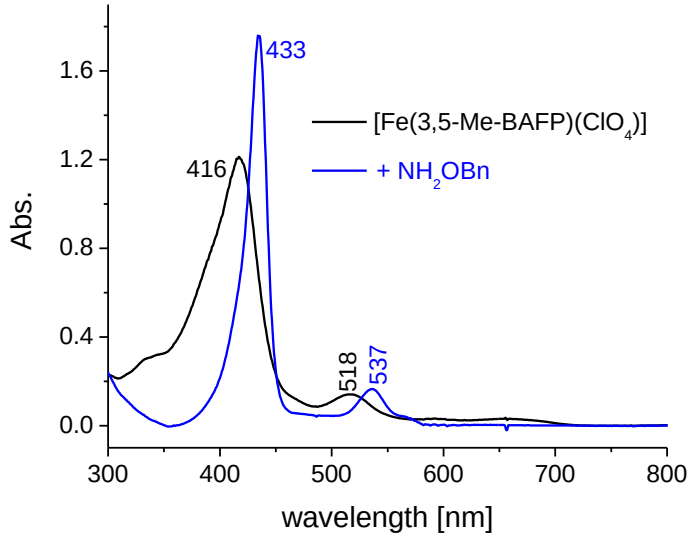

Figure 4.1. UV-visible spectra of [Fe(3,5-Me-BAFP)(ClO_4)] (black) and of the product of the reaction of this complex with excess NH_2OBn (blue) in toluene at room temperature.

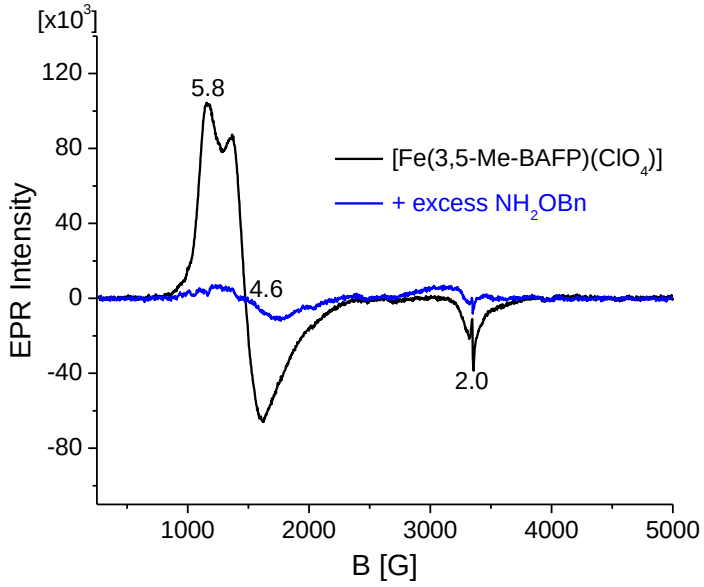

Figure 4.2. EPR spectra of [Fe(3,5-Me-BAFP)(ClO_4)] (black) and of the product of the reaction of this complex with excess NH_2OBn (blue) in toluene. Spectra measure at 10 K.

EPR spectroscopy was employed to determine the oxidation state of the product complex. The EPR of [Fe(3,5-Me-BAFP)(ClO_4)] in toluene at 10 K, shown in Figure 4.2, is indicative of a S = 5/2, 3/2 spin-admixture commonly observed for ferric heme perchlorate complexes.[6] Reaction with NH_2OBn results in a completely silent EPR spectrum, indicative of a ferrous heme product, rather than the desired Fe(III)-NH2OBn complex. Feng and Ryan have observed this reduction previously in the reaction of [Fe(TPP)(Cl)] with NH_2OH, generating the final ferrous product [Fe(TPP)($NH_2OH)_2$].[4] As such, we hypothesized our product was [Fe(3,5-Me-BAFP)($NH_2OBn)_2$]; although NH_3, N_2O, and water (benzyl alcohol in our case) are also commonly observed products in hydroxylamine disproportionation reactions.[4-5] Interestingly, crystallization of [Fe(3,5-Me-BAFP)(ClO_4)] in the presence of excess NH_2OBn resulted in the ferrous bis-ammonia complex [Fe(3,5-Me-BAFP)($NH_3)_2$], as shown in Figure 4.3 (crystallization and NH_3 detection were performed by Ashley McQuarters). Although crystal structure analysis fails to distinguish between H_2O

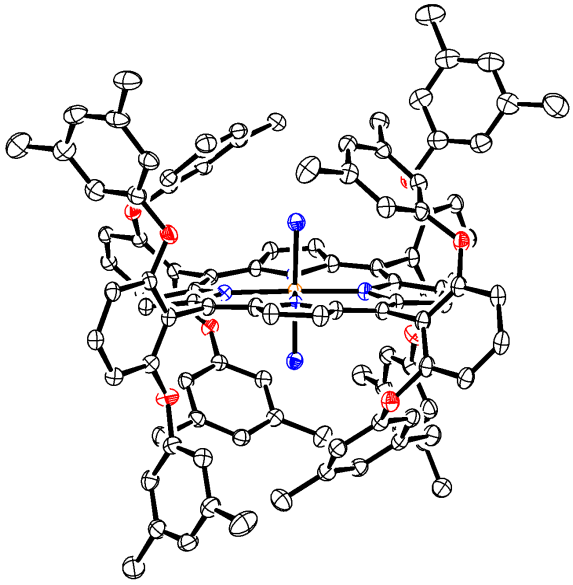

Figure 4.3. Crystal structure of [Fe(3,5-Me-BAFP)($NH_3)_2$]. Hydrogen atoms and a solvent molecule (toluene) are omitted for clarity. Thermal ellipsoids are shown at 30%. The structure was obtained by Ashley McQuarters.

and NH_3 as axial ligands, using Russell's phenolate-hypochlorite assay, two equivalents of NH_3 are detected in the crystalline material, confirming the product as [Fe(3,5-Me-BAFP)$(NH_3)_2$]. To the best of our knowledge, this is the first crystal structure of an ammonia bound ferrous heme model complex. The two Fe-NH_3 bond lengths are 2.016 and 1.990 Å. While the slight difference in Fe-NH_3 bond lengths was unexpected, the packing of the phenolate pickets of 3,5-Me-$BAFP^{2-}$ (~3 Å away from the N-atom of NH_3) around the NH_3 molecule and minor saddling of the heme could modulate this difference.

Reaction of a Ferric Bis-Picket Fence Porphyrin with O-Benzylhydroxylamide

As the reaction of ferric [Fe(3,5-Me-BAFP)(ClO_4)] with O-benzylhydroxylamine resulted in the ferrous product [Fe(3,5-Me-BAFP)$(NH_3)_2$] through the disproportionation of O-benzylhydroxylamine (NH_2OBn), we hypothesized that deprotonation of NH_2OBn to O-benzylhydroxylamide ($NHOBn^-$) prior to reaction with ferric heme will prevent this unfavorable reduction reaction. To this end, NH_2OBn was deptrotonated with sodium hydride or potassium methoxide to generate Na[NHOBn] or K[NHOBn], respectively, and stirred with [Fe(3,5-Me-BAFP)(ClO_4)] in toluene at room temperature. The reaction was monitored by UV-visible and EPR spectroscopy. While the Soret band only shifts 5 nm to 421 nm for the product complex as shown in Figure 4.4, the first Q band shifts from 518 nm for [Fe(3,5-Me-BAFP)(ClO_4)] to 583 nm for the product. The UV-visible spectrum of this complex is different from that of [Fe(3,5-Me-BAFP)$(NH_3)_2$] (see Figure 4.1).

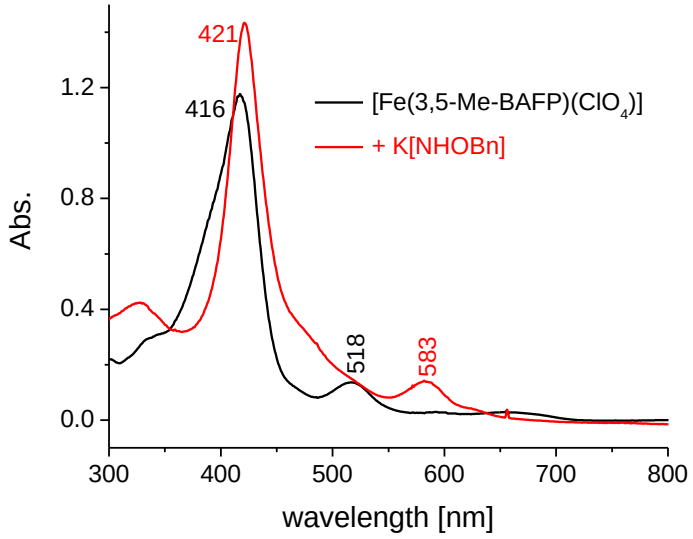

Figure 4.4. UV-visible spectra of [Fe(3,5-Me-BAFP)(ClO_4)] (black) and of the product of the reaction of this complex with excess K[NHOBn] (red) in toluene at room temperature.

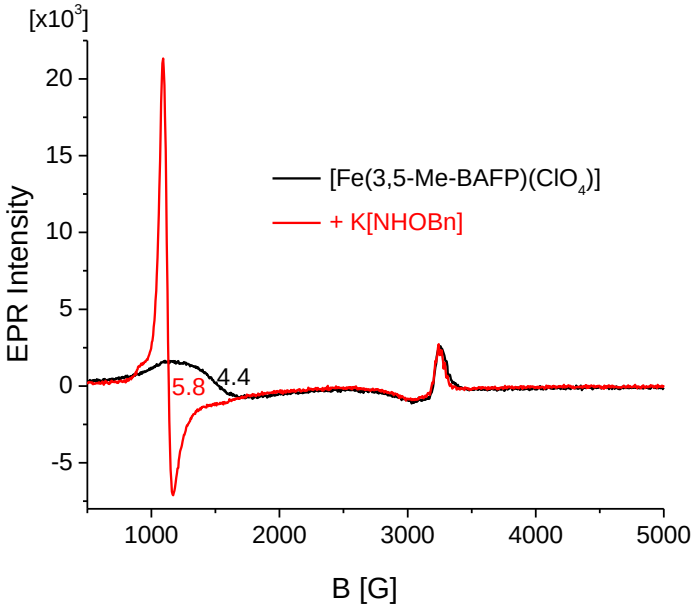

Figure 4.5. EPR spectra of [Fe(3,5-Me-BAFP)(ClO_4)] (black) and of the product of the reaction of this complex with excess K[NHOBn] (red) in toluene. Measure at 77 K.

Table 4.1. Potentials [V vs. Fc/Fc^+] of various ferric bis-picket fence porphyrin complexes. Measured in THF with 0.1 M TBAP at 100 mV/sec.

	Fe^{IV}/Fe^{III}			Fe^{III}/Fe^{II}
Complex	E_{ox}	E_{red}	$E_{1/2}$	$E_{1/2}$
[Fe(3,5-Me-BAFP)(ClO_4)]	0.58	-0.28	0.15	-0.69
[Fe(3,5-Me-BAFP)(ClO_4)] + K[NHOBn]	0.43	-0.19	0.12	-0.67
[Fe(3,5-Me-BAFP)(OH)]	0.45	-	irrev	-1.10

EPR spectroscopy at 77 K shows g-values indicative of a high-spin (S = 5/2) ferric heme: $g_x = g_y = 5.8$, $g_z = 2.0$ (Figure 4.5). From these results we propose the ferric product complex to be [Fe(3,5-Me-BAFP)(NHOBn)]. Unfortunately, K[NHOBn] is only slightly soluble in toluene. This means an excess of O-benxylhydroxylamide is required to push the reaction to completion. With excess insoluble K[NHOBn] in solution, growth of single crystals for X-ray analysis was difficult. Crown ethers were employed in an attempt to solublize K[NHOBn] and Na[NHOBn] into toluene, but both 18-crown-6 and 15-crown-5 were unsuccessful at increasing the solubility of sodium or potassium O-benzylhydroxylamide.

Electrochemistry of a Ferric Porphyrin Hydroxylamide Complex

With the desired ferric heme O-benzylhydroxylamide complex in hand, we are now prepared to perform one electron oxidation to the corresponding ferryl species. The cyclic voltammogram of [Fe(3,5-Me-BAFP)(NHOBn)] in THF is reported in Figure 4.6 with oxidation and reduction potentials vs. Fc/Fc^+ listed in Table 4.1. The cyclic voltammogram shows Fe^{IV}/Fe^{III} and Fe^{III}/Fe^{II} redox events at +120 and -670 mV, respectively. Importantly, oxidation to the desired ferryl product [Fe^{IV}(3,5-Me-BAFP)(NHOBn)]$^+$ is quasi-reversible—indicating a reasonably stable ferryl complex, potentially allowing for isolation of this important model complex. Comparison to

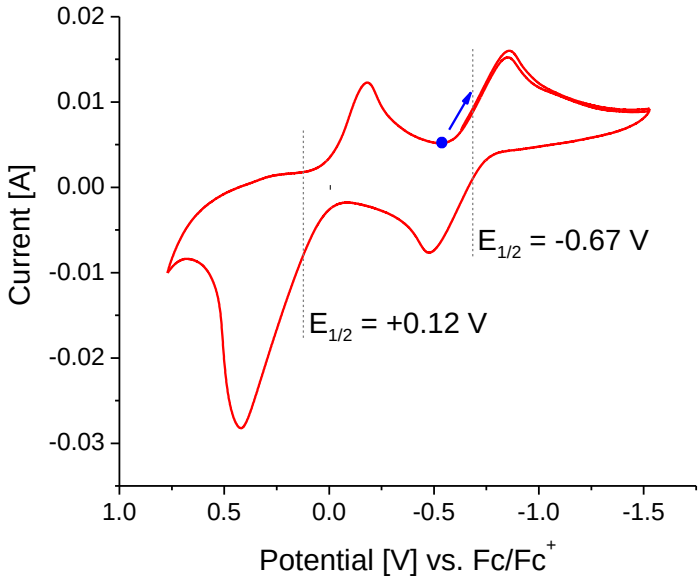

Figure 4.6. Cyclic volatmmogram of a solution of [Fe(3,5-Me-BAFP)(ClO_4)] and K[NHOBn]. Measured at 100 mV/sec in THF with 0.1 M TBAP.

other ferric bis-picket fence porphyrin complexes is provided in Table 4.1. Encouragingly, the electrochemistry of [Fe(3,5-Me-BAFP)(NHOBn)] is unique from that of the corresponding ferric hydroxide and perchlorate complexes.

Future work will focus on bulk electrochemical oxidation of [Fe(3,5-Me-BAFP)(NHOBn)] to the corresponding ferryl complex. Reactivity with NO will be tested to determine if Fe(IV)-NHOH complexes are, in fact, catalytically competent intermediates in the catalytic cycle of P450nor.

4.2. Towards High-Valent Iron Porphyrin Nitride Complexes

4.2.a. Is Formation of a Fe(VI) Porphyrin Nitride Complex Energetically Feasible? A DFT Analysis

Although mononuclear heme-nitride complexes have not been isolated previously, DFT calculations predict that, if formed, reaction with NO to generate

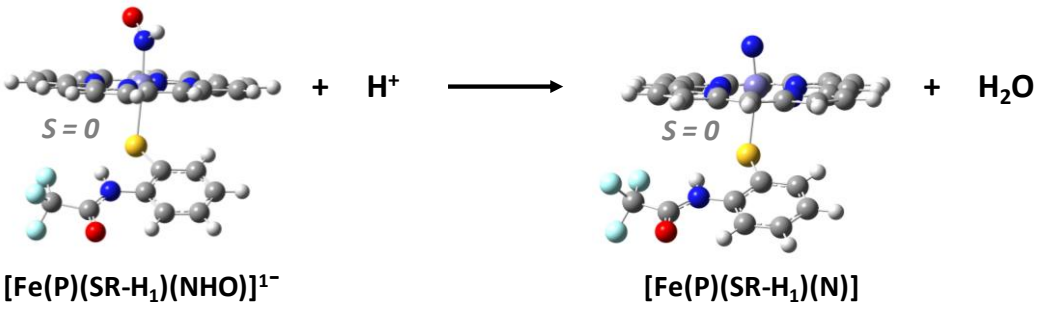

Figure 4.7. BP86/TZVP optimized structures of $[Fe(P)(SR\text{-}H_1)(NHO)]^-$ (S = 0) and $[Fe(P)(SR\text{-}H_1)(N)]$ (S = 0) used to calculate ΔG for the reaction above.

N_2O will be very favorable.[7] While it is perhaps not surprising that the formed iron(VI) complex will be highly reactive, the interesting question is if formation of an iron(VI) nitride complex is energetically favorable from a ferrous heme-nitroxyl complex, as would be required in the catalytic cycle of P450nor. In other words, is N-O bond cleavage to form a terminal nitride complex and release of water feasible in heme systems? The reaction of interest is shown in Figure 4.7. Porphine, P^{2-} is employed as the porphyrin ligand and the thiolate ligand, $SR\text{-}H_1^-$, is used as a model for the axial cysteinate in P450nor. It has been shown previously through sulfur K-edge X-ray absorption spectroscopy that the Fe-S bond covalency in P450-type enzymes is most closely modeled by the single hydrogen-bond stabilized thiolate ligand $SR\text{-}H_1^-$.[8-9]

Five- and six-coordinate Fe(II)-NHO and Fe(VI)-N complexes were optimized with BP86/TZVP and the geometric parameters are collected in Table 4.2. In all cases, the Fe-N and Fe-S bonds are longer in the high-spin complex relative to the corresponding S = 0 species. For example, for $[Fe(P)(SR\text{-}H_1)(N)]$ the optimized S = 0 Fe-N bond length is 1.550 Å whereas the S = 1 optimized Fe-N bond length for the same complex is 1.589 Å. Likewise, the Fe-S bond length for the S = 0 and S = 2 states of $[Fe(P)(SR\text{-}H_1)(NHO)]^-$ are 2.458 and 2.638 Å, respectively. Additionally, the

Table 4.2. BP86/TZVP calculated geometric parameters of various Fe(II)-NHO and Fe(VI)-nitride porphyrin complexes. Energies calculated with B3LYP/TZVP.

	Rel. Energy [kcal/mol]	Calculated Geometric Parameters [Å] [°]				
		ΔFe-N(HO)	ΔN-O	<Fe-N-O	ΔFe-S	ΔFe-$N_{pyrrole}$[a]
$[Fe(P)(N)]^+$						
S = 0	0	1.512	-	-	-	2.000
S = 1	10	1.582	-	-	-	1.999
$[Fe(P)(SR\text{-}H_1)(N)]$						
S = 0	-	1.550	-	-	2.582	2.023
S = 1	-	1.589	-	-	3.060	2.015
[Fe(P)(NHO)]						
S = 0	0	1.741	1.235	131.5	-	2.004
S = 2	2	1.953	1.246	130.6	-	2.097
$[Fe(P)(SR\text{-}H_1)(NHO)]^-$						
S = 0	0	1.803	1.243	133.0	2.458	2.016
S = 2	21	2.249	1.268	127.2	2.638	2.022

[a]Average of four individucal Fe-$N_{pyrrole}$ bonds

Fe-N bond length in both [Fe(P)(NHO)] and [Fe(P)(N)] increases dramatically in the optimized structures of the six-coordinate $SR\text{-}H_1^-$ complexes. Here, the Fe-N bond length of $[Fe(P)(N)]^+$ (S = 0) is 1.512 Å, which increases to 1.550 Å upon addition of $SR\text{-}H_1^-$ to generate $[Fe(P)(SR\text{-}H_1)(N)]$. B3LYP/TZVP single point energy calculations were then performed to determine the lowest energy spin state of each complex studied here. For all complexes, B3LYP/TZVP predicts S = 0 to be the lowest energy spin state. For example, B3LYP/TZVP predicts the S = 0 states for [Fe(P)(NHO)] and $[Fe(P)(SR\text{-}H_1)(NHO)]^-$ to be 2 and 21 kcal/mol lower in energy, respectively, than the S = 2 state. For $[Fe(P)(SR\text{-}H_1)(N)]$, S = 0 is 10 kcal/mol lower in energy than the S = 1 spin state. As a result, all free energy calculations were performed on the S = 0 spin-states for all iron complexes.

To determine if it is energetically favorable to lose water from a ferrous heme-nitroxyl (HNO) complex, ΔG was calculated for the following reaction:

$$[Fe(P)(NHO)] + H^+ \rightarrow [Fe(P)(N)]^+ + H_2O$$

Table 4.3. B3LYP/TZVP calculated free energies (ΔG) for reaction of five- (without SR-H_1^-) and six-coordinate [Fe(P)(SR-H_1)(NHO)]$^-$ + H^+ → [Fe(P)(SR-H_1)(N)] + H_2O at 298.15 K in toluene.

H^+ Source (pKa)	coordination number	ΔG [kcal/mol]
Phenol (10)	5	79.7
	6	49.8
2,6-lutidinium (5)	5	24.4
	6	**-5.6**

However, calculation of the energy of a free proton, H^+, is problematic. For this reason, the weak acids phenol and 2,6-lutitidium were used in these DFT calculations. Then, to balance the equation, phenolate or 2,6-lutidine is also included as a product. The free energy was calculated in toluene using a polarizable continuum model (PCM) available in Gaussian 03. ΔG for this reaction was also calculated for the corresponding six-coordinate thiolate complexes, [Fe(P)(SR-H_1)(NHO)]$^-$ and [Fe(P)(SR-H_1)(N)], as illustrated in Figure 4.7. Calculated free energies are reported in Table 4.3. Interestingly, if phenol is used as the proton source, ΔG for the reaction of the five-coordinate (without SR-H_1^-) and six-coordinate (with SR-H_1^-) complexes is highly unfavorable at 79.7 and 49.8 kcal/mol, respectively. Interestingly, addition of the thiolate ligand SR-H_1^- decreases ΔG for the reaction by 30 kcal/mol. As this reaction should be driven by acid strength, ΔG was recalculated using the moderately stronger acid 2,6-lutidinium. In this case, ΔG for the reaction of [Fe(P)(NHO)] with 2,6-lutidinium to form $[Fe(P)(N)]^+$ and water is 24.4 kcal/mol—still highly unfavorable, but 25 kcal/mol less endothermic than with phenol. When 2,6-lutidium is used as a the proton source and the thiolate ligand SR-H_1^- is applied, the calculated ΔG is now -5.6 kcal/mol as listed in Table 4.3. This indicates that with thiolate coordination, as is present in P450nor, it could be energetically feasible to generate a iron(VI) porphyrin nitride complex via release of

water. Additionally, in the presence of an even stronger acid, this reaction may be favorable for both five- or six-coordinate ferrous nitroxyl (HNO) complexes. It is important to note, however, that there is no experimental evidence to support the formation of an Fe(VI)-nitride complex in the catalytic cycle of cytochrome P450nor. In particular, the Fe-N stretching frequency of intermediate I has been observed at 596 cm^{-1}, which is incompatible with an Fe(VI)-nitride intermediate.[10]

4.2.b. Photochemistry of Ferric Bis-Picket Fence Porphyrin Azide Complexes

High-valent *non-heme* iron nitride complexes are commonly prepared through one of two methods (1) N-atom transfer from an organic donor[11-12] or (2) through photolysis of azide (N_3) complexes.[13-15] In the latter method, irradiation of azide causes cleavage of a N-N bond, driving off N_2 yielding a terminal nitride at the iron center. Mononuclear heme-nitride complexes, however, have not been reported in the literature. The main reason is that they dimerize upon formation. For example, upon irradiation (or thermal decomposition) of [Fe(TPP)(N_3)], the resulting product is a Fe(III)-Fe(IV) μ-nitride complex, [(Fe(TPP))$_2$N].[16]

We propose synthesis of an iron(V) porphyrin nitride species through irradiation of the high-spin ferric bis-picket fence porphyrin azide complex, [Fe(3,5-Me-BAFP)(N_3)], as illustrated in Scheme 4.3 (left). The steric bulk provided by 3,5-Me-BAFP^{2-} should prevent formation of a bridging nitride complex. Additionally, Neese and co-workers have proposed that formation of iron nitride complexes is possible only in corresponding low-spin iron complexes.[17] To this end, the porphyrin Im-BAFP^{2-} ligand and the corresponding low-spin ferric azide complex, [Fe(Im-BAFP)(N_3)] (Scheme 4.3, right) have been prepared.

Scheme 4.3. [Fe(3,5-Me-BAFP)(N_3)] (left) and [Fe(Im-BAFP)(N_3)] (right).

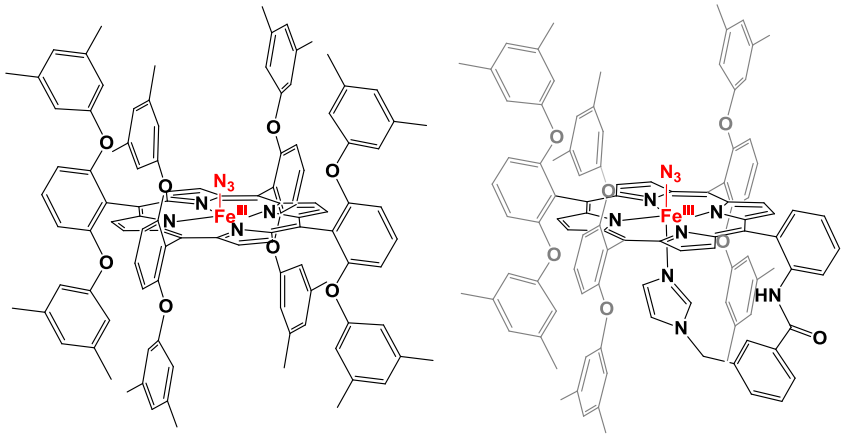

Characterization of Five- and Six-Coordinate Ferric Heme Azide Complexes

The five-coordinate ferric heme azide complex, [Fe(3,5-Me-BAFP)(N_3)] is prepared by stirring [Fe(3,5-Me-BAFP)(Cl)] in toluene with aqueous sodium azide. Interestingly, the UV-visible spectrum of [Fe(3,5-Me-BAFP)(N_3)] is similar to that of [Fe(3,5-Me-BAFP)(Cl)] in CH_2Cl_2 (Figure 4.8) with the exception of the highest energy feature at ~370 nm. In [Fe(3,5-Me-BAFP)(Cl)], the highest energy absorption

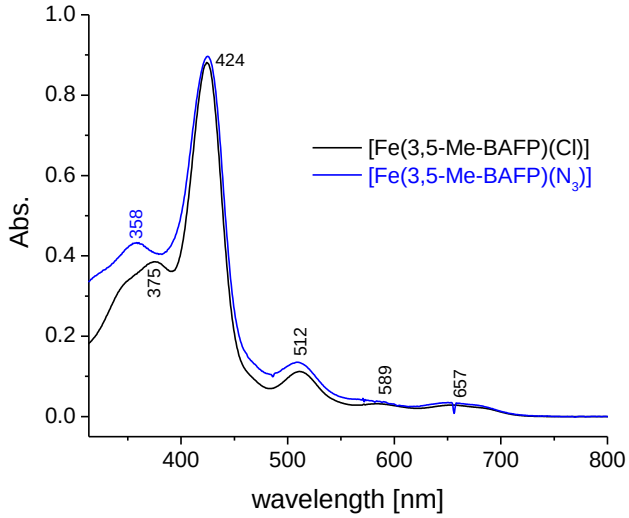

Figure 4.8. UV-visible spectra of [Fe(3,5-Me-BAFP)(Cl)] and [Fe(3,5-Me-BAFP)(N_3)] in CH_2Cl_2.

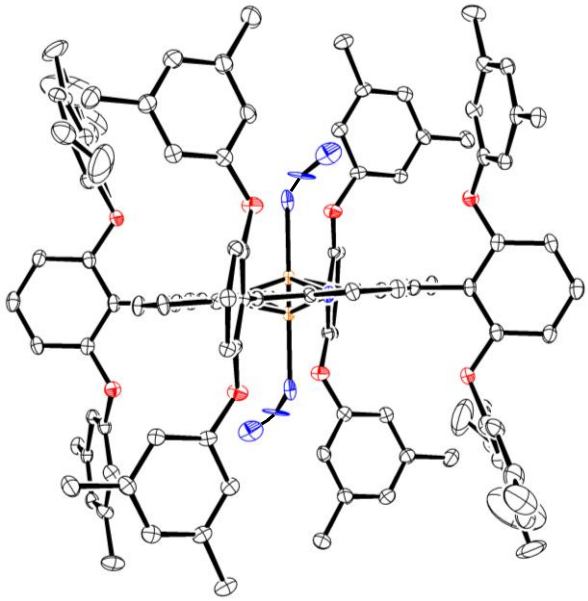

Figure 4.9. Preliminary crystal structure of [Fe(3,5-ME-BAFP)(N_3)]. Thermal ellipsoids are shown at 30% probability and hydrogen atoms are omitted for clarity.

feature is at 375 nm which shifts to 358 nm in [Fe(3,5-Me-BAFP)(N_3)]. To further confirm the identity of [Fe(3,5-Me-BAFP)(N_3)], the complex was crystallized for X-ray structural analysis. The preliminary crystal structure is shown in Figure 4.9 (X-ray crystallography performed by Dr. Saikat Roy, Matzger laboratory). The azide unit shows 1:1 disorder above and below the heme plane with the Fe center displaced 0.48 Å toward the bound N_3. The Fe-N_3 bond length, in the preliminary structure, is 2.064 Å and the Fe-N-N angle is 133.3^o. The porphyrin plane in this structure is remarkably flat. This is in contrast to [Fe(3,5-Me-BAFP)(NH_3)$_2$], shown in Figure 4.3, where the heme shows slight saddling distortions. The EPR spectrum indicates that the ferric azide complex is high-spin (S = 5/2) with $g_x = g_y = 5.7$ and $g_z = 2.0$. Finally, [Fe(3,5-Me-BAFP)(N_3)] has a strong asymmetric N-N stretching band of azide in the IR spectrum at 2055 cm^{-1}, similar to that of [Fe(TPP)(N_3)] as listed in Table 4.4. The

Table 4.4. Asymmetric azide N-N stretch in five-coordinate [Fe(porphyrin)(N_3)] and six-coordinate [Fe(porphyrin)(MI)(N_3)] complexes measured in a KBr matrix.

	$\nu(N_3)$		
porphyrin	5C	6C	ref
TPP	2040	2000[a]	[18]
T*o*-$(OBn)_2$PP	2055	-	t.w.
3,5-Me-BAFP	2055	1999	t.w.
Im-BAFP	-	1997	t.w.

[a][Fe(TPP)(pyridine)(N_3)]

ferric azide complex [Fe(T*o*-$(OBn)_2$PP)(N_3)] (T*o*-$(OBn)_2PP^{2-}$ is shown in Scheme 2.1) was also prepared and shows an identical asymmetric *ν*(N-N) band of 2055 cm^{-1}.

Six-coordinate ferric heme azide complexes have also been prepared. Upon addition of 1-methylimidazole (MI) to [Fe(3,5-Me-BAFP)(N_3)], the asymmetric N-N stretching frequency of azide shifts to 1999 cm^{-1}. Binding an axial N-donor ligand generates a low-spin (S = ½) complex, although excess MI is able to displace anionic ligands in ferric porphyrin complexes, generating a bis-MI species.[19] In order to synthesize a more stable six-coordinate complex, the porphyrin Im-$BAFP^{2-}$ (Scheme 4.3) was employed. Here, the axial N-donor ligand is tethered to the porphyrin providing exactly one equivalent of imidazole while phenolate "pickets" provide the steric bulk necessary to prevent formation of a μ-N compound upon irradiation. The resulting six-coordinate ferric azide complex, [Fe(Im-BAFP)(N_3)], is low-spin as determined by EPR spectroscopy in 2-MeTHF at 77 K. The spectrum is anisotropic with three unique g-values: g_x = 2.69, g_y = 2.17, g_z = 1.80. As expected, the asymmetric N-N stretching frequency of azide is observed at 1997 cm^{-1}, characteristic of a six-coordinate azide complex as listed in Table 4.4.

Irradiation of Five- and Six-Coordinate Ferric Heme Azide Complexes

With high- and low-spin ferric bis-picket fence porphyrin azide complexes in hand, UV irradiation of the complexes was performed. First, the five-coordinate complex [Fe(3,5-Me-BAFP)(N_3)] was irradiated with UV light at room temperature in 2-MeTHF. Reaction progress was first monitored by IR spectroscopy. The asymmetric N-N stretch of azide (Figure 4.10) decreases upon UV irradiation. By UV-visible spectroscopy, as shown in Figure 4.11, clean conversion to a species with a Soret band at 432 nm is observed. This is accompanied by a new Q band at 540 nm. EPR spectroscopy, however, indicates formation of an EPR silent product (see Figure 4.12). As the desired iron(V) nitride species is EPR active, with S = 1/2 or 3/2 total spin, the product corresponds to a ferrous heme complex. As such, upon irradiation of [Fe(3,5-Me-BAFP)(N_3)], we propose formation of ferrous [Fe(3,5-Me-BAFP)] through homolytic Fe-N_3 bond cleavage:

$$[Fe(3,5\text{-Me-BAFP})(N_3)] + h\nu \rightarrow [Fe(3,5\text{-Me-BAFP})] + \cdot N_3$$

The formed $\cdot N_3$ then decomposes to dinitrogen. [Fe(3,5-Me-BAFP)] was synthesized independently and UV-visible features are identical to the reaction product with absorbance features at 432 and 539 nm, see Figure 4.13. This homolytic Fe-N_3 bond cleavage reaction has been proposed previously for the photolysis of the non-heme iron complex $[Fe(cyclam)(N_3)_2]^+$ at low temperature.[13] Similar reactivity was observed upon UV irradiation of [Fe(T*o*-(OBn)$_2$PP)(N_3)] (data not shown).

Since irradiation of high-spin ferric bis-picket fence porphyrin azide complexes resulted in homolytic cleavage of the Fe-N_3 bond, the analgous photochemistry was investigated with the low-spin ferric complex [Fe(Im-BAFP)(N_3)] (see Scheme 4.3, right). Disappointingly, UV-visible and EPR spectroscopy indicate

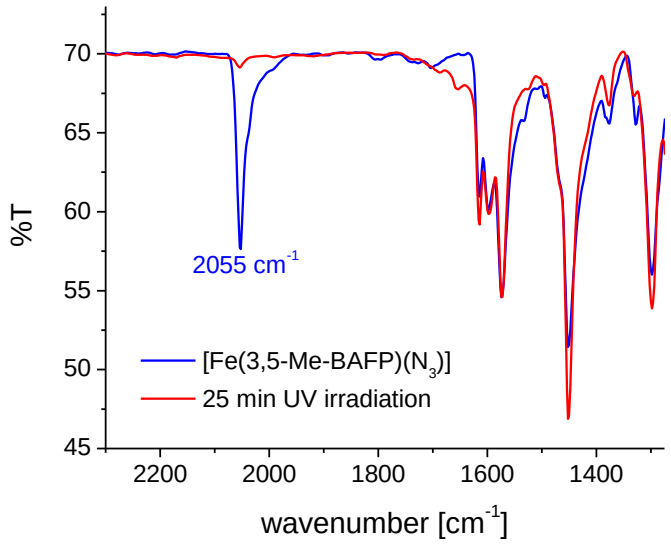

Figure 4.10. IR spectra (KBr pellets) of [Fe(3,5-Me-BAFP)(N_3)] before (blue) and after (red) UV irradiation for 25 minutes.

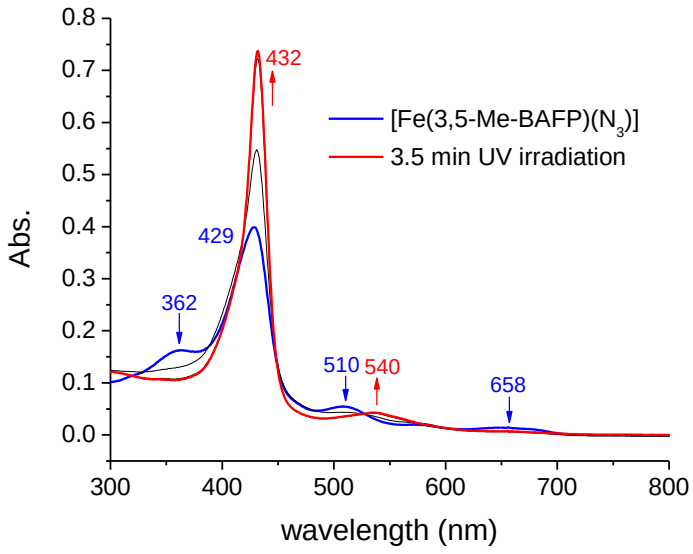

Figure 4.11. UV-visible spectral changes after UV irradiation of [Fe(3,5-Me-BAFP)(N_3)] in 2-MeTHF for 3.5 minutes at room temperature.

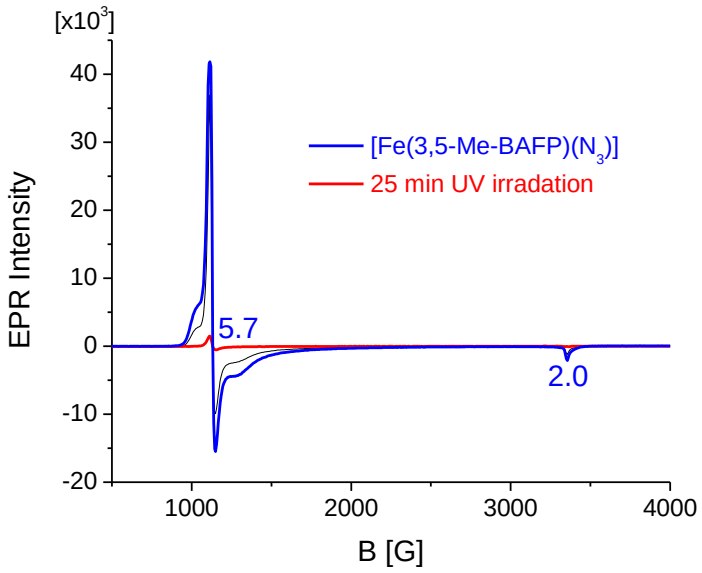

Figure 4.12. EPR spectra of 2 mM [Fe(Im-BAFP)(N_3)] (blue), indicative of a high-spin ferric complex (S = 5/2), and of the EPR silent photolysis product (red) after 25 minutes of UV irradiation in 2-MeTHF at room temperature. EPR spectra were recorded at 10 K.

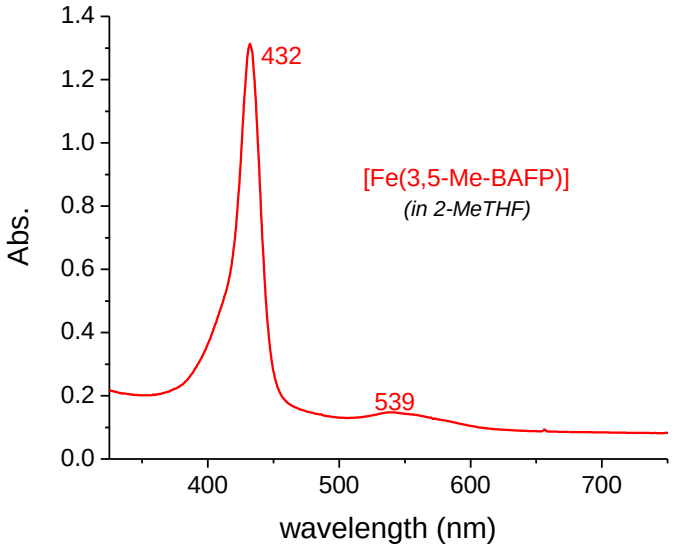

Figure 4.13. UV-visible spectrum of [Fe(3,5-Me-BAFP)] in 2-MeTHF prepared through the reduction of [Fe(3,5-Me-BAFP)(ClO_4)] with 1 equivalent of KC_8.

formation of a ferrous product rather than the desired iron(V) complex. UV-visible spectra of [Fe(Im-BAFP)(N_3)] and of the irradiation product are provided in Figure 4.14. The Q band at 535 nm is characteristic of the ferrous complex [Fe(Im-BAFP)]. Finally, as shown in Figure 4.15, the EPR spectrum of the irradiation product is EPR silent. These spectra are all consistent with a ferrous product and, thus, photo-induced homolytic Fe-N_3 bond cleavage.

In our hands, UV irradiation of high- and low-spin ferric heme azide complexes at room temperature induces homolytic Fe-N_3 bond cleavage resulting in formation of the corresponding ferrous porphyrin complexes. Although our bis-picket fence porphyrin complexes show a unique reactivity compared to TPP^{2-}, this result is dissatisfactory in that we do not generate the desired high-valent heme-nitride species. Future work will focus on generation of iron(V) bis-picket fence porphyrin nitride complexes through the use of N-atom transfer agents.[20-21]

Experimental

All reactions were performed under inert conditions with dried and freeze pump thawed solvents unless stated otherwise. O-benxylhydroxylamine (NH_2OBn)[22] and α-imidazolyl-*m*-toluic acid hydrochloride[23] were prepared as reported previously. 1-methylimidazole (MI) was distilled prior to use. H_2[3,5-Me-BAFP] and H_2[T*o*-(O-Bn)$_2$PP] and their ferric chloride analogues were synthesized according to procedures reported in Chapter 3. 2,6-bis(3',5'-dimethylphenoxy)benzaldehyde was also prepared as described in Chapter 3. Ammonia analysis was carried out using the phenolate assay originally developed by J. A. Russel.[24-25]

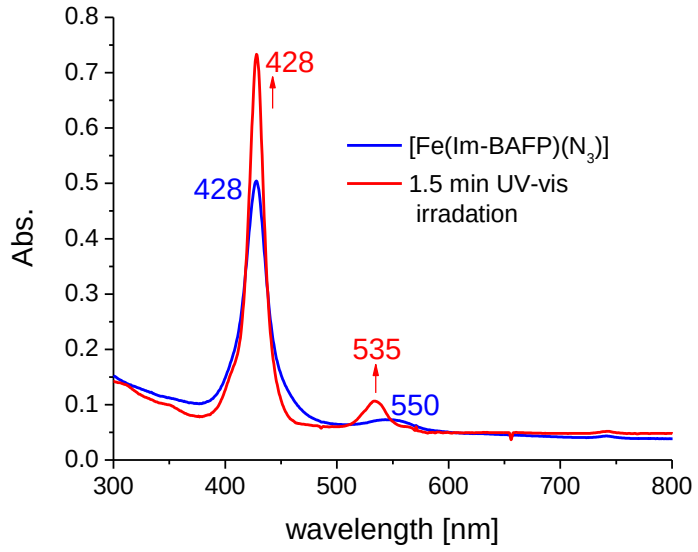

Figure 4.14. UV-visible spectra of [Fe(Im-BAFP)(N_3)] (blue) and of the photolysis product (red) after 1.5 minutes of UV irradiation in 2-MeTHF at room temperature.

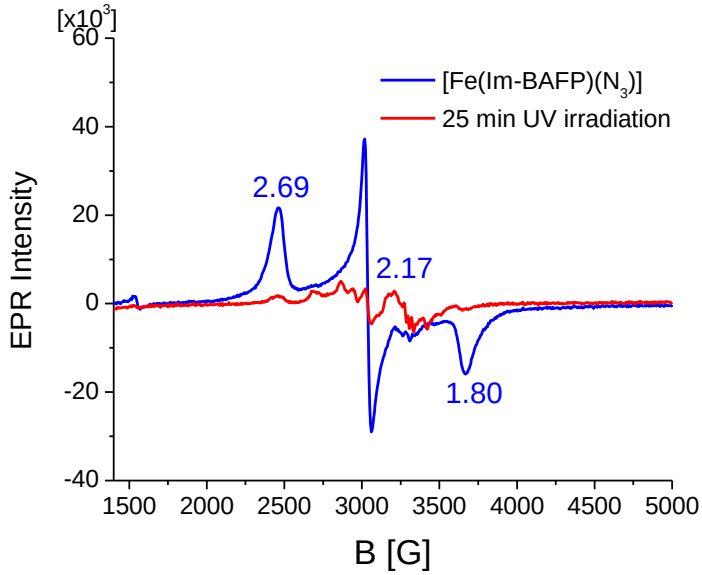

Figure 4.15. EPR spectra of 2 mM [Fe(Im-BAFP)(N_3)] (blue), indicative of a low-spin ferric complex (S = 1/2), and of the EPR silent photolysis product (red) after 25 minutes of UV irradiation in 2-MeTHF at room temperature. EPR spectra were recorded at 77 K.

Synthetic Procedures

Na[NHOBn]. 100 mg O-benzylhydroxylamine (0.81 mmol) and 19 mg sodium hydroxide (0.81 mmol) were stirred for 1 hour in 1.5 mL methanol. Then, the solvent was removed via a Schlenk line to yield a white solid. The product was used without further purification. Yield: quantative.

K[NHOBn]. 226 mg O-benzylhydroxylamine (1.84 mmol) and 129 mg potassium methoxide (1.84 mmol) were stirred for 1 hour in 3.3 mL methanol. Then, the solvent was removed via a Schlenk line to yield a white solid. The product was used without further purification. Yield: quantative.

[Fe(3,5-Me-BAFP)(ClO_4)]. 286 mg [Fe(3,5-Me-BAFP)(Cl)] (0.172 mmol) and 36 mg silver perchlorate (0.172 mmol) were dissolved in 17 mL 2-methyltetrahydrofuran. The reaction mixture was refluxed for 1 hour and filtered hot through a fine frit. The filtrate was layered with 30 mL hexanes and allowed to precipitate at -30^{o}C. After 20 hours, the resulting purple crystalline material was filtered and vacuum dried for 4 hours. Yield: 185 mg (62%). UV-vis (CH_2Cl_2): 405, 524, 593, 623 nm. UV-vis (toluene): 416, 515, 597, 661 nm.

Reaction of [Fe(3,5-Me-BAFP)(ClO_4)] with NH_2OBn. In 5 mL of toluene, 18 mg of [Fe(3,5-Me-BAFP)(ClO_4)] (0.01 mmol) and 10 equivalents O-benzylhydroxylamine (12.5 mg, 0.1 mmol) were stirred for 20 min. The resulting solution is EPR silent. UV-vis (toluene): 435, 537, 569 nm.

Crystallization of [Fe(3,5-Me-BAFP)(NH_3)$_2$]. In a 5 mm diameter glass tube, 5 mg of [Fe(3,5-Me-BAFP)(ClO_4)] and ~5 equivalents O-benzylhydroxylamine were dissolved in 0.2 mL toluene. The mixture was layered carefully with 1.5 mL hexanes and closed with a rubber septum. After 5 days, crystals suitable for X-ray analysis were harvested.

Reaction of [Fe(3,5-Me-BAFP)(ClO_4)] with K[NHOBn]. Under inert atomosphere, 100 mg [Fe(3,5-Me-BAFP)(ClO_4)] (0.058 mmol) and 47 mg K[NHOBn] (0.29 mmol) were stirred in 3 mL toluene 12 hours. The product was precipitated with 9 mL hexanes. The brown solid was filtered via fine frit. Yield: 75 mg (74%). UV-vis (toluene): 423, 583, 631 nm.

[Fe(To-(OBn)$_2$PP)(N_3)]. 170 mg [Fe(To-(O-Bn)$_2$PP)(Cl)] (0.11 mmol) was dissolved in 10 mL CH_2Cl_2 from the solvent system and stirred with 3.25 g sodium azide in 10 mL water (5 M) overnight. The organic layer was then separated, dried with sodium sulfate, and rotovaped to dryness. Yield: quantative. UV-vis (CH_2Cl_2): 376, 422, 511, 584, 650, 688 nm. IR (KBr,): 2054 cm^{-1} ($\nu(N_3)$).

[Fe(3,5-Me-BAFP)(N_3)]. 232 mg [Fe(3,5-Me-BAFP)(Cl)] (0.14 mmol) was dissolved in 25 mL toluene and stirred with 4.04 g sodium azide in 13 mL water (5 M) overnight. The organic layer was then separated, dried with sodium sulfate, and rotovaped to dryness. Yield: quantative. UV-vis (2-MeTHF): 361, 428, 507, 579, 650, 676 nm. IR (KBr): 2055 cm^{-1} ($\nu(N_3)$).

Cyrstallization of [Fe(3,5-Me-BAFP)(N_3)]. ~2 mg of [Fe(3,5-Me-BAFP)(N3)] was dissolved in 0.1 mL toluene in a 5 mm diameter tube. The mixture was layered with 2 mL hexanes and closed with a rubber septum. X-ray quality crystals were observed after 8 days.

NO_2-BAFP. Under inert atmosphere, 2.0 g 2,6-bis(3',5'-dimethylphenoxy)benzaldehyde (5.8 mmol), 290 mg 2-nitrobenzaldehyde (1.9 mmol), and 0.53 mL freshly distilled pyrrole (7.7 mmol) were dissolved in a mixture of 690 mL CH_2Cl_2 and 5.3 mL absolute ethanol. The mixture was allowed to stir for 20 minutes before addition of 0.34 mL boron trifluoride diethyletherate via syringe. The reaction stirred at room temperature for 1.5 hours. After 1.5 hours, 1.2 g 2,3-dichloro-5,6-dicyano-1,4-benzoquinone was added and the reaction stirred at room temperature for 12 hours. The reaction mixture was rotovaped to dryness and purified through a series of silica columns: (1) 100% CH_2Cl_2, (2) 1:1 hexanes:CH_2Cl_2, and (3) 100% CH_2Cl_2. Yield: 202 mg (11%). ^{1}H-NMR ($CDCl_3$): 8.95 (s, 4H); 8.87 (d, 2H); 8.48 (d, 2H); 8.39 (dd, 1H); 8.16 (dd, 1H); 7.86 (m, 2H); 7.62 (m, 3H); 7.09 (m 4H); 7.02 (dd, 2H); 6.25 (s, 2H); 6.22 (s, 4H); 6.20 (s, 2H); 6.16 (s, 1H); 6.14 (s, 4H); 6.08 (s, 4H); 5.98 (s, 1H); 1.80 (s, 12H); 1.78 (s, 6H); 1.67 (s, 12H); 1.62 (s, 6H); -2.86 (s, 2H); see Figure 4.16. UV-vis (CH_2Cl_2): 423, 518, 551, 594, 649 nm. LCT-MS: m/z 1380.8.

NH_2-BAFP. 140 mg NO_2-BAFP and 260 mg tin(II) chloride were dissolved in a mixture of 3.5 mL concentrated HCl and 2 mL CH_2Cl_2. The reaction mixture was stirred overnight at room temperature. An additional 300 mg tin(II) chloride was added and the reaction stirred for another 3 hours. The mixture was neutralized with

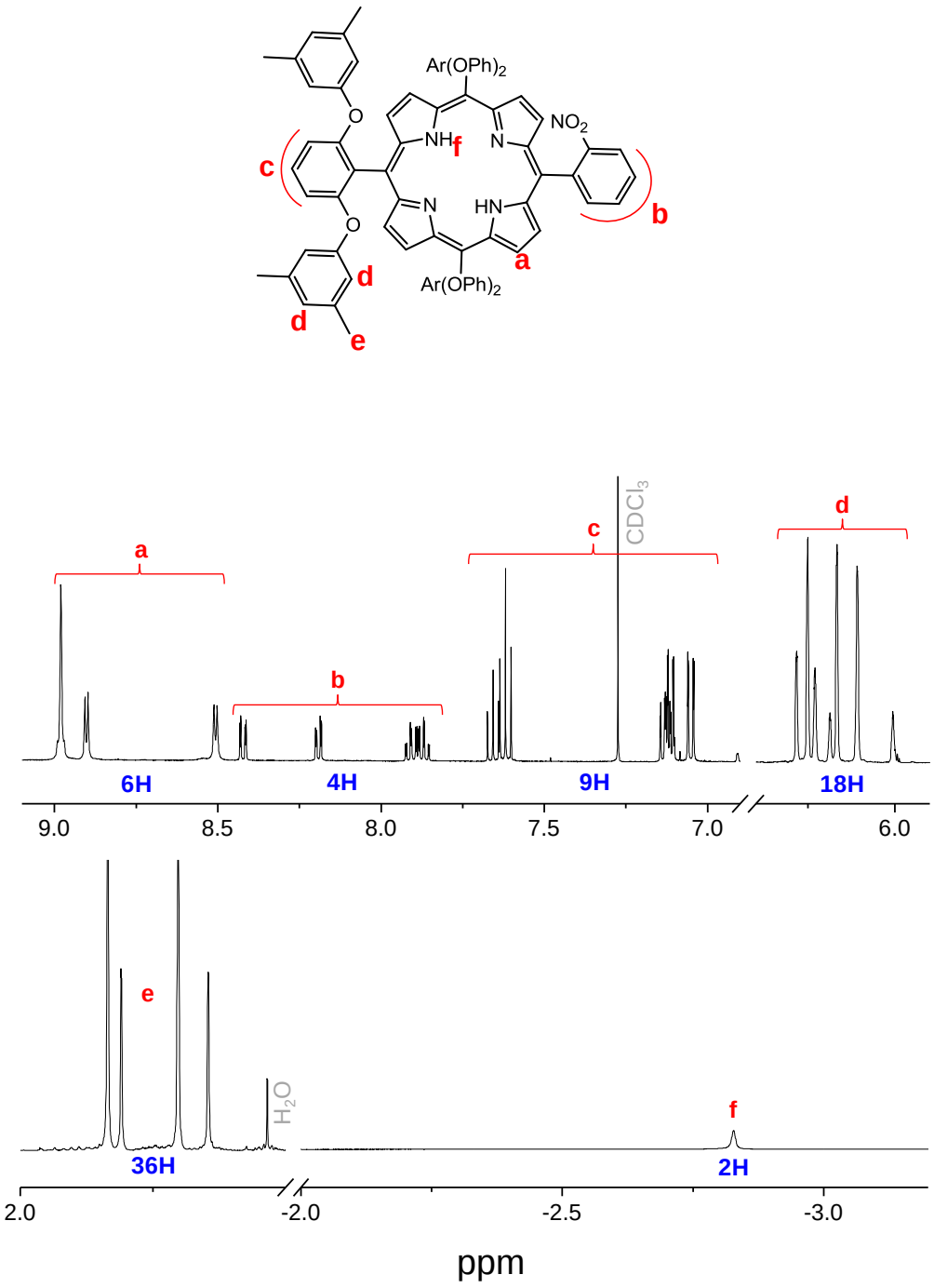

Figure 4.16. ^{1}H NMR spectrum of NO_2-BAFP in $CDCl_3$. Top portion of spectrum is intensified x 3.

sodium carbonate and then portioned between CH_2Cl_2 and water. The organic layer was dried with sodium sulfate and evaporated to dryness. The resulting purple residue was column chromatographed on silica with 1:2 hexanes:CH_2Cl_2. Yield: 67 mg (49%). ^{1}H-NMR ($CDCl_3$): 8.97 (q, 4H); 8.91 (d, 2H); 8.74 (d, 2H); 7.88 (dd, 1H); 7.59 (m, 4H); 7.10 (m, 4H); 7.02 (d, 4H); 6.28 (s, 4H); 6.25 (s, 2H); 6.22 (s, 8H); 6.20 (s, 2H); 6.15 (s, 1H); 6.10 (s, 1H); 3.48 (s, 2H); 1.85 (s, 12H); 1.78 (s+s, 16H); 1.73 (s, 8H); -2.84 (s, 2H). UV-vis (CH_2Cl_2): 422, 517, 549, 591, 646 nm. LCT-MS: m/z 1350.8.

Im-BAFP. 350 mg α-imidazolyl-*m*-toluic acid hydrochloride was brought to reflux in 4 mL CH2Cl2. Once at reflux, 0.6 mL thionyl chloride (freshly distilled) was added and the reaction refluxed for 1.5 hours. The solvent and unreacted thionyl chloride were removed via vacuum. The resulting solid was redissolved in 4 mL CH2Cl2 and added dropwise to a solution of 97 mg NH_2-BAFP (0.072 mmol) in 6 mL CH_2Cl_2 at 0^{o}C. The reaction then stirred at room temperature for 19 hours. After 19 hours, the reaction mixture was diluted with 100 mL CH_2Cl_2 and neutralized with 60 mL concentrated sodium bicarbonate. The organic layer was separated, washed with water twice, dried with sodium sulfate, and evaporated to dryness. The resulting purple solid was column chromatographed on silica with (1) CH_2Cl_2 followed by (2) 19:1 CH_2Cl_2:methanol. The product is not eluted until methanol is introduced to the column. Yield: 102 mg (92%). ^{1}H-NMR ($CDCl_3$): 9.00 (dd, 4H); 8.97 (d, 2H); 8.88 (d, 1H); 8.74 (d, 2H); 8.17 (d, 1H); 7.85 (t, 1H); 7.56 (m, 6H); 7.06 (d, 1H); 7.01 (d, 1H); 6.97 (d 2H); 6.90 (d, 2H); 6.62 (s, 1H); 6.34 (s, 3H); 6.29 (s, 5H); 6.26 (s, 2H); 6.21 (s, 2H); 6.15 (s, 6H); 6.11 (s, 1H); 6.02 (s, 1H); 5.94 (d, 1H); 5.75 (t, 1H); 5.39 (s,

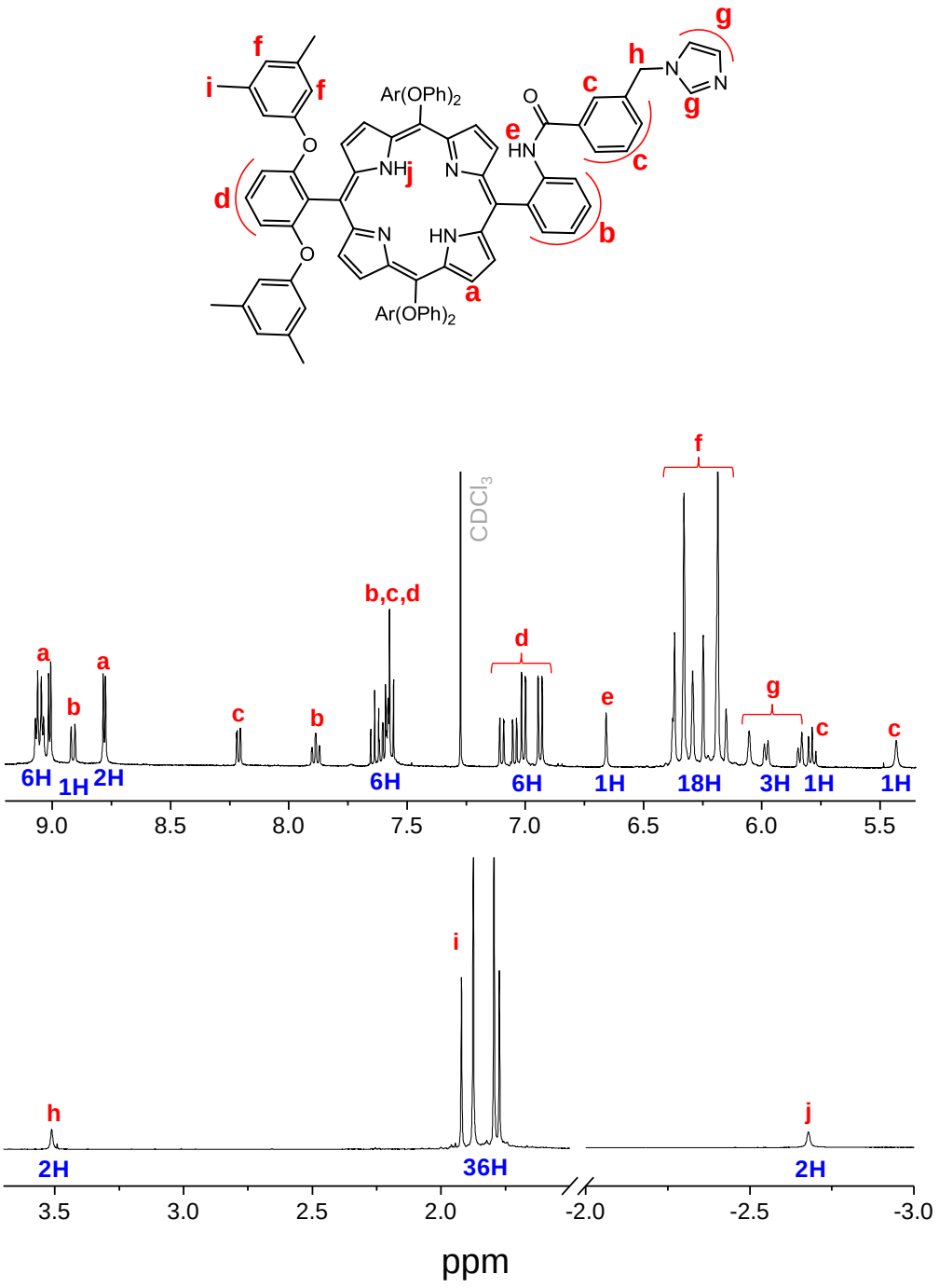

Figure 4.17. ^{1}H NMR spectrum of Im-BAFP in $CDCl_3$. Top portion of spectrum is intensified x 3.

1H); 3.48 (s, 1H); 1.88 (s, 6H); 1.84 (s, 12H); 1.76 (s, 12H); 1.74 (s, 6H); -2.72 (s, 2H); see Figure 4.17. UV-vis (CH_2Cl_2): 424, 518, 553, 590, 645 nm. LCT-MS: m/z 1535.3.

[Fe(Im-BAFP)(Cl)]. 102 mg Im-BAFP (0.07 mmol) was brought to reflux in 8 mL dry, degassed THF. Then 42 mg anhydrous iron(II) chloride (0.33 mmol) was added and the reaction refluxed for 4 hours. The solvent was removed via evaporation and the resulting brown solid was column chromatographed on silica with 97:3 CH_2Cl_2:methanol. Yield: 97 mg (91%). UV-vis (CH_2Cl_2): 421, 514, 546, 653 nm. LCT-MS: m/z 1588.3 (M – Cl).

[Fe(Im-BAFP)(N_3)]. 20 mg [Fe(3,5-Me-BAFP)(Cl)] (0.012 mmol) was dissolved in 20 mL CH_2Cl_2 and stirred with 200 mg sodium azide in 40 mL for 5 hours. The organic layer was then separated, dried with sodium sulfate, and rotovaped to dryness. Yield: quantative. UV-vis (CH_2Cl_2): 425, 550 nm. UV-vis (2-MeTHF): 429, 550 nm. IR (KBr): 1998 cm^{-1} ($\nu(N_3)$).

Physical Methods

Infrared spectra were obtained from KBr disks on a Perkin-Elmer BX spectrometer at room temperature. Resolution was set to 2 cm^{-1}. Proton magnetic resonance spectra were recorded on a Varian Inova 400 MHz instrument. Electronic absorption spectra were measured using an Analytical Jena Specord 600 instrument at room temperature. *In situ* UV-visible measurements were taken with a Hellma quartz immersion probe with 10 mm pathlength. Electron paramagnetic resonance

spectra were recorded on a Bruker X-band EMX spectrometer equipped with an Oxford Instruments liquid nitrogen or helium cryostat. EPR spectra were typically obtained on frozen solutions using 20 mW microwave power and 100 kHz field modulation with the amplitude set to 1 G. Sample concentrations employed were ~2 mM.

DFT Calculations

All geometry optimizations and frequency calculations were performed with the program package Gaussian 03[26] using the BP68[27-28] functional and TZVP[29-30] basis set. Single point energy calculations were performed using B3LYP[28, 31-32]/TZVP with toluene as the solvent using the polarizable continuum model (PCM). Free energies, ΔG, were calculated by applying BP86/TZVP thermal corrections to B3LYP/TZVP calculated energies. In all calculations, convergence was reached when the relative change in the density matrix between subsequent iterations was less that 1×10^{-8}.

References

1. Nakahara, K.; Tanimoto, T.; Hatano, K.; Usuda, K.; Shoun, H., *J. Biol. Chem.* **1993,** *268*, 8350-8355.

2. Shiro, Y.; Fujii, M.; Iizuka, T.; Adachi, S.; Tsukamoto, K.; Nakahara, K.; Shoun, H., *J. Biol. Chem.* **1995,** *270*, 1617-1623.

3. Lehnert, N.; Praneeth, V. K. K.; Paulat, F., *J. Comp. Chem.* **2006,** *27*, 1338-1351.

4. Feng, D.; Ryan, M. D., *Inorg. Chem.* **1987,** *26*, 2480-2483.

5. Bari, S. E.; Amorebieta, V. T.; Gutierrez, M. M.; Olabe, J. A.; Doctorovich, F., *J. Inorg. Biochem.* **2010,** *104*, 30-36.

6. Kintner, E. T.; Dawson, J. H., *Inorg. Chem.* **1991,** *30*, 4892-4897.

7. Harris, D. L., *Int. J. Quantum Chem.* **2002,** *88*, 183-200.

8. Dey, A.; Okamura, T.; Ueyama, N.; Hedman, B.; Hodgson, K. O.; Solomon, E. I., *J. Am. Chem. Soc.* **2005,** *127*, 12046-12053.

9. Dey, A.; Jiang, Y.; Ortiz de Montellano, P. R.; Hodgson, K. O.; Hedman, B.; Solomon, E. I., *J. Am. Chem. Soc.* **2009,** *131*, 7869-7878.

10. Petrenko, T.; DeBeer George, S.; Aliaga-Alcalde, N.; Bill, E.; Mienert, B.; Xiao, Y.; Guo, Y.; Sturhahn, W.; Cramer, S. P.; Wieghardt, K.; Neese, F., *J. Am. Chem. Soc.* **2007,** *129*, 11053–11060.

11. Smith, J. M.; Subedi, D., *Dalton Trans.* **2012,** *41*, 1423-1429.

12. Betley, T. A.; Peters, J. C., *J. Am. Chem. Soc.* **2004,** *126*, 6252-6254.

13. Meyer, K.; Bill, E.; Mienert, B.; Weyhermuller, T.; Wieghardt, K., *J. Am. Chem. Soc.* **1999,** *121*, 4859-4876.

14. Scepaniak, J. J.; Young, J. A.; Bontchev, R. P.; Smith, J. M., *Angew. Chem. Int. Ed.* **2009,** *48*, 3158-3160.

15. Scepaniak, J. J.; Vogel, C. S.; Khusniyarov, M. M.; Heinemann, F. W.; Meyer, K.; Smith, J. M., *Science* **2011,** *331*, 1049-1052.

16. Summerville, D. A.; Cohen, I. A., *J. Am. Chem. Soc.* **1976,** *98*, 1747-1752.

17. Aliaga-Alcalde, N.; DeBeer George, S.; Mienert, B.; Bill, E.; Wieghardt, K.; Neese, F., *Angew. Chem. Int. Ed.* **2005,** *44*, 2908-2912.

18. Adams, K. M.; Rasmussen, P. G.; Scheidt, W. R.; Hatano, K., *Inorg. Chem.* **1979,** *18*, 1892-1899.

19. Byers, W.; Cossham, J. A.; Edwards, J. O.; Gordon, A. T.; Jones, J. G.; Kenny, E. T. P.; Mahmood, A.; McKnight, J.; Sweigart, D. A.; Tondreau, G. A.; Wright, T., *Inorg. Chem.* **1986,** *25*, 4767-4774.

20. Carpino, L. A.; Padykula, R. E.; Barr, D. E.; Hall, F. H.; Krause, J. G.; Dufresne, R. F.; Thoman, C. J., *J. Org. Chem.* **1988,** *53*, 2565-2572.

21. Mindiola, D. J.; Cummins, C. C., *Angew. Chem. Int. Ed.* **1998,** *37*, 945-947.

22. Falborg, L.; Jorgensen, K. A., *J. Chem. Soc. Perkin Trans. 1* **1996**, 2823-2826.

23. Berto, T. C.; Praneeth, V. K. K.; Goodrich, L. E.; Lehnert, N., *J. Am. Chem. Soc.* **2009,** *131*, 17116-17126.

24. Choi, I.-K.; Liu, Y.; Wei, Z.; Ryan, M. D., *Inorg. Chem.* **1997,** *36*, 3113-3118.

25. Russell, J. A., *J. Biol. Chem.* **1944,** *156*, 457-462.

26. Frisch, M. J.; Trucks, G. W.; Schlegel, H. B.; Scuseria, G. E.; Robb, M. A.; Cheeseman, J. R.; Montgomery, J., J. A.; Vreven, T.; Kudin, K. N.; Burant, J. C.; Millam, J. M.; Iyengar, S. S.; Tomasi, J.; Barone, V.; Mennucci, B.; Cossi, M.; Scalmani, G.; Rega, N.; Petersson, G. A.; Nakatsuji, H.; Hada, M.; Ehara, M.; Toyota, K.; Fukuda, R.; Hasegawa, J.; Ishida, M.; Nakajima, T.; Honda, Y.; Kitao, O.; Nakai, H.; Klene, M.; Li, X.; Knox, J. E.; Hratchian, H. P.; Cross, J. B.; Bakken, V.; Adamo, C.; Jaramillo, J.; Gomperts, R.; Stratmann, R. E.; Yazyev, O.; Ausin, A. J.; Cammi, R.; Pomelli, C.; Octerski, J. W.; Ayala, P. Y.; Morokuma, K.; Voth, G. A.; Salvador, P.; Dannenberg, J. J.; Zakrzewski, V. G.; Dapprich, S.; Daniels, A. D.; Strain, M. C.; Farkas, O.; Makick, D. K.; Rabuck, A. D.; Raghavachair, K.; Foresman, J. B.; Ortiz, J. V.; Cui, Q.; Baboul, A. G.; Clifford, S.; Cioslowski, J.; Stefanov, B. B.; Lui, G.; Laishenko, A.; Piskorz, R.; Komaromi, I.; Martin, R. L.; Fox, D. J.; Keith, T.; Al-Laham, M. A.; Peng, C. Y.; Nanayakkara, A.; Challacombe, M.; Gill, P. M. W.; Johnson, B.; Chen, W.; Wong, M. W.; Gonzalez, C.; Pople, J. A. *Gaussin 03*, Gaussian, Inc.: Pittsburgh, PA, 2003.

27. Perdew, J. P., *Phys. Rev. B* **1986,** *33*, 8822-8824.

28. Becke, A. D., *Phys. Rev. A* **1988,** *38*, 3098-3100.

29. Schaefer, A.; Horn, H.; Ahlrichs, R., *J. Chem. Phys.* **1992,** *97*, 2571-2577.

30. Schaefer, A.; Huber, C.; Ahlrichs, R., *J. Chem. Phys.* **1994,** *100*, 5829-5835.

31. Becke, A. D., *J. Chem. Phys.* **1993,** *98*, 1372-1377.

32. Becke, A. D., *J. Chem. Phys.* **1993,** *98*, 5648-5652.

Chapter 5

The *trans* Effect of Nitroxyl (HNO) in Ferrous Heme Systems: Implications for Soluble Guanylate Cyclase Activation by HNO

Nitroxyl, HNO, is the protonated and one electron reduced form of the signaling diatomic molecule nitric oxide, NO. While the physiological role of NO is well established,[1-5] the role of HNO in biological systems is very controversial. HNO has been proposed to be an intermediate in the catalytic cycle of assimilatory nitrite reductase[6-7] and P450 nitric oxide reductase,[8-9] to be an irreversible inhibitor of mitochondrial aldehyde dehydrogenase[10] and glyceraldehyde-3-phosphate dehydrogenase[11] through cysteine modification, and to be an oxidant of thiols to the corresponding disulfides with formation of hydroxylamine.[12] Interestingly, it is still unknown whether HNO is produced *in vivo*. Proposals for endogenous HNO generation include reduction of NO by cyctochrome *c* oxidase and hemoglobin,[12] reaction of S-nitrosothiols with excess thiol,[13] or perhaps most prominently through nitric oxide synthase mediated oxidation of L-arginine in the absence of tetrahydrobiopterin.[14]

Although HNO has chemical properties, and thus physiological effects, distinct from that of NO,[15-16] both nitrogen oxides have been reported to activate soluble guanylate cyclase (sGC), a ferrous heme enzyme primarily responsible for vasodilation in mammalian organisms.[17] sGC is a ~150 kDa heterodimer consisting of three domains: a N-terminal sensing domain that contains a ferrous heme, the

dimerization domain, and a C-terminal catalytic domain. In the presence of NO, a conformational change takes place in the heme domain of sGC, activating the catalytic domain of the enzyme that mediates the conversion of GTP to the biochemical messenger cyclic guanosine monophosphate, cGMP.[18] It has been proposed that two distinct binding sites exist for NO in the sensing domain of sGC. The primary, high-affinity site consists of a ferrous heme *b* ligated by a proximal histidine ligand, His105 in human and bovine sGC.[19] Upon binding of NO, an intermediate six-coordinate complex is formed before the strong thermodynamic σ-*trans* effect (also called *trans* "interaction") of NO induces cleavage of the Fe-N_{His105} bond to form the activated five-coordinate heme-nitrosyl complex.[20-23] This movement of His105 induces a conformational change in the sensing domain which activates the catalytic domain of the enzyme. The second, low affinity binding site is proposed to be the thiol of a cysteine residue.[24-25]

While NO has been established as the endogenous activator of sGC,[26] several reports have shown increased sGC dependent vasodilation in the presence of HNO donors.[27-30] In the presence of SOD, HNO is readily oxidized to NO which can then activate sGC through the previously discussed pathway.[31-32] Hence, one important question is whether HNO could ***directly*** activate sGC. In an initial report, Dierks and Burstyn determined that HNO is unable to activate sGC.[33] However, the possibility remains that HNO was scavenged by the 10 mM DTT in the buffer prior to reaction with sGC in these experiments. In a second study, Mayer and co-workers confirmed that HNO does not activate sGC in the absence of SOD.[34] However, Miller et al. demonstrated sGC activity in thiol and O_2-free buffer in the presence of the HNO donors 1-nitrosocyclohexyl trifluoroacetate and Angeli's salt.[17] The activity was 1.9 and 3.4 fold lower than NO induced activity at 10 μM, respectively, but

Scheme 5.1. The key Fe-NO σ-bonding orbital of six-coordinate ferrous heme-nitrosyls [23, 35].

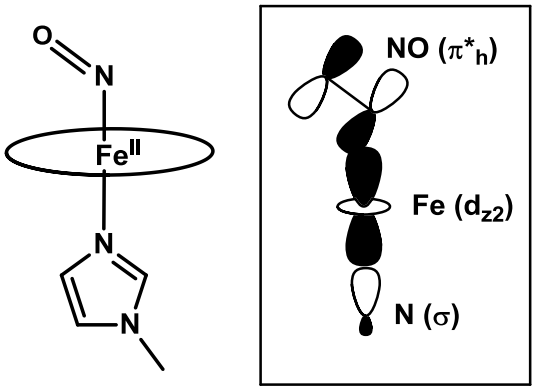

importantly, removal of the heme led to decreased HNO induced sGC activity suggesting activation occurs predominately at the heme center. Interestingly, HNO-mediated cysteine thiol modification led to inhibition of enzyme activity.[17]

With conflicting reports, the key question remains if it is chemically feasible for HNO to induce a thermodynamic σ-*trans* effect strong enough to cleave the Fe-N_{His105} bond and in this way, activate the catalytic domain of sGC in a manner similar to NO. As shown in Scheme 5.1, the σ-*trans* effect of NO manifests itself in the competition of the σ-donor orbitals, π^*_h of NO and His105(σ), for the d_{z2} orbital of iron as reported previously.[23, 35-37] Considerable donation of the π^*_h orbital of NO into the d_{z2} orbital of Fe weakens the bond to the *trans* ligand of NO significantly. Interestingly, the weak σ-donor carbon monoxide (CO) is also able to bind to the Fe center of sGC, but fails to induce cleavage the Fe-N_{His105} bond, instead forming a stable six-coordinate complex,[38-39] which causes only a low-level activation of sGC (see below). This indicates a weaker *trans* effect of CO relative to NO. Further evidence for this weaker *trans* effect of CO comes from spectroscopic and crystallographic data on tetraphenylporphyrin (TPP) model complexes. For example, Fe-N_{MI} stretching frequencies, ν(Fe-N_{MI}), in [Fe(TPP)(MI)(NO)][37] and

[Fe(TPP)(CO)(MI)][40] complexes (MI = 1-methylimidazole) directly reflect this difference between CO and NO. In the six-coordinate NO complex, ν(Fe-N_{MI}) is observed at 149 cm^{-1} whereas this mode is found at 172/225 cm^{-1} for the analogous CO complex and at 210-220 cm^{-1} in deoxy-Mb. Additionally, crystal structures of [Fe(TPP)(MI)(NO)][41] and [Fe(TPP)(MI)(CO)][42] show Fe-N_{MI} bond lengths of 2.173 Å and 2.071 Å, respectively. By comparison, the Fe-N_{MI} bond length of [Fe(TPP)$(MI)_2$],[43] where no *trans* interaction exists, is 1.997 Å. These observations can be explained by the fact that CO binds to ferrous heme systems predominantly via strong π-backbonds, which do not give rise to a large thermodynamic *trans* effect. It should be noted, though, that CO is able to activate sGC, although the effect is quite weak relative to NO—100% CO and 0.5% NO atmosphere result in 4.4- and 128-fold activation, respectively.[38] It has been suggested that this low-level activation by CO may be due to changes in heme conformation.[44-46]

Thus, it seems that a moderate lengthening of the Fe-N_{His105} bond, as in the case of CO coordination, does not induce the conformational change necessary for high (as in the case of NO) catalytic production of cGMP and instead a stronger *trans* effect, as in the case of NO, is required. To understand this effect better, we have employed DFT calculations to investigate the thermodynamic *trans* effect (referred to as the *trans* effect in this paper) induced by NO, HNO, and CO on 1-methylimidazole (MI) in ferrous heme model complexes. Here we use DFT total energy calculations to evaluate the binding of MI to five-coordinate ferrous porphyrins in *trans* position to NO, HNO, CO, and MI as a way to (a) systematically assess the relative strength of the *trans* effect induced by each of these small molecules and (b) to calibrate DFT methods for the accurate calculation of weak binding constants in ferrous heme complexes.

Results and Discussion

Geometric Parameters and Spin States of Model Complexes

In order to determine the extent to which HNO is able to induce a σ-*trans* effect in sGC, density functional theory calculations were performed on the five- and six-coordinate model systems [Fe(P)(X)] and [Fe(P)(MI)(X)] (P^{2-} = porphine ligand), where X = NO, HNO, CO, and MI, as shown for X = HNO in Figure 5.1. To decrease computational cost, the porphine approximation was applied and MI was used as a model for histidine ligation to the ferrous heme center. To determine which DFT method predicts the most accurate optimized structures in our system, [Fe(P)(MI)(X)] where X = NO and MI were optimized using a variety of functional/basis set combinations, listed in Table 5.1. Calculated structures with BP86/TZVP, B3LYP/LanL2DZ*, and B3LYP/6-31G* reproduce experimental bond lengths and angles with reasonable accuracy, as shown in Table 5.1. Interestingly, BP86/TZVP

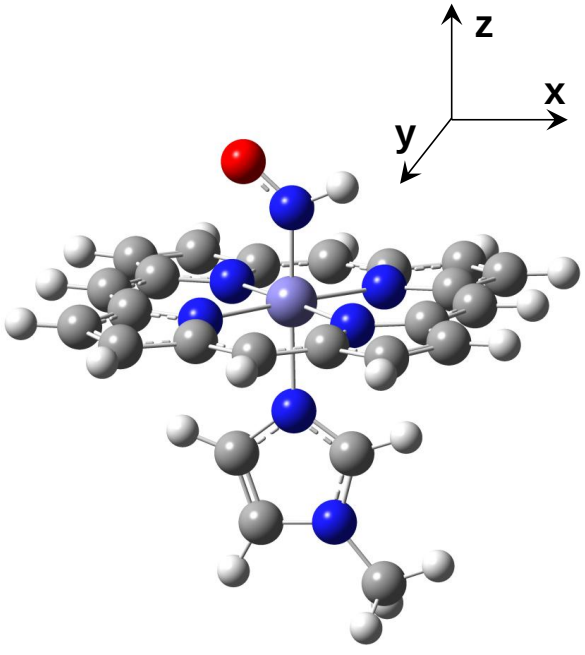

Figure 5.1. The model system [Fe(P)(MI)(X)], where P = porphine2-, MI = 1=methylimidazole, and X = NHO, and applied coordinate system. The structure shown is calculated with BP86/TZVP.

Table 5.1. Experimental and calculated geometric parameters of [Fe(P)(X)] and [Fe(P)(MI)(X)], where X = NO, HNO, CO, and MI.

			Geometric Parameters [Å] [°]					
Complex		**method**	**ΔFe-X**	**ΔX-O**	**ΔFe-N_{MI}**	**ΔFe-N_{porph}**	**< Fe-X-O**	**ref.**
[Fe(P)(NO)]	*S = ½*	*exp. [Fe(TPP)(NO)]*	1.739	1.163	-	2.000	144	47
		BP86/TZVP	1.704	1.179	-	2.019	146	
[Fe(P)(MI)(NO)]	*S = 1/2*	*exp. [Fe(TPP)(MI)(NO)]*	1.750	1.182	2.173	2.008	138	48
		BP86/TZVP	1.734	1.186	2.179	2.021	140	
		B3LYP/6-31G*	1.759	1.177	2.105	2.019	140	
		B3LYP/LanL2DZ*	1.787	1.172	2.105	2.030	140	
		mPWVWN/6-311++G**	1.745	1.188	2.518	2.045	141	
		OLYP/TZVP	*Fe-N_{MI} bond broken during optimization*					
[Fe(P)(NHO)]	*S = 0*	*exp.*	-	-	-	-	-	
		BP86/TZVP	1.741	1.235	-	2.004	131	
		B3LYP/6-31G*	1.732	1.226	-	2.002	131	
	S = 2	*exp.*	-	-	-	-	-	
		BP86/TZVP	1.953	1.246	-	2.097	131	
		B3LYP/6-31G*	1.953	1.246	-	2.097	131	
[Fe(P)(MI)(NHO)]	*S = 0*	*exp. Mb-NHO* (EXAFS)	1.82	1.24	2.09	2	131	49
		BP86/TZVP	1.789	1.236	2.082	2.016	132	
		B3LYP/6-31G*	1.789	1.226	2.060	2.017	132	
[Fe(P)(CO)]	*S = 0*	*exp.*	-	-	-	-	-	
		BP86/TZVP	1.705	1.166	-	2.001	180	
		B3LYP/6-31G*	1.716	1.154	-	2.001	180	
	S = 2	*exp.*	-	-	-	-	-	
		BP86/TZVP	1.999	1.149	-	2.093	180	
		B3LYP/6-31G*	2.371	1.133	-	2.070	180	
[Fe(P)(MI)(CO)]	*S = 0*	*exp. [Fe(TPP)(MI)(CO)]*	1.793	1.061	2.071	2.003	179	42
		BP86/TZVP	1.756	1.162	2.068	2.018	180	
		B3LYP/6-31G*	1.774	1.151	2.063	2.019	180	
[Fe(P)(MI)]	*S = 0*	*exp.*	-	-	-	-	-	
		BP86/TZVP	1.900	-	-	1.995	-	
		B3LYP/6-31G*	1.924	-	-	2.002	-	
	S = 2	*exp. [Fe(TPP)(2-MeHIm)]*	2.127	-	-	2.073	-	50
		BP86/TZVP	2.146	-	-	2.086	-	
		B3LYP/6-31G*	2.158	-	-	2.086	-	
[Fe(P)$(MI)_2$]	*S = 0*	*exp. [Fe(TPP)$(MI)_2$]*	2.014	-	2.014	1.997	-	43
		BP86/TZVP	1.994	-	1.994	2.071	-	
		B3LYP/LanL2DZ*	2.036	-	2.036	2.028	-	
		B3LYP/6-31G*	2.011	-	2.011	2.013	-	
		mPWVWN/6-311++G**	2.067	-	2.067	2.033	-	
		OLYP/TZVP	2.047	-	2.047	2.010	-	

predicts slightly shorter Fe-X bond lengths in both [Fe(P)(MI)(NO)] and [Fe(P)$(MI)_2$] than B3LYP/6-31G* and B3LYP/LanL2DZ*. This is not surprising as pure density functionals generally overestimate metal-ligand covalencies. We also tested the functional OLYP, which has been recently suggested to work well for ferrous heme systems.[51] However, OLYP/TZVP geometry optimizations let to the breaking of the Fe-N_{MI} bond in [Fe(P)(MI)(NO)], preventing formation of the six-coordinate complex in this case. Zhang and co-workers further recommended using the mPWVWN/"6-311++G**" method for calculating HNO and NO adducts of heme complexes.[52] In this method the 6-311++G** basis set is applied to the first coordination sphere elements of Fe, LanL2DZ to Fe, and 6-31G* to all other atoms. The choice of the inferior basis set LanL2DZ for iron is surprising as it generates a poorly balanced description of the system, which reduces the quality of this approach. Interestingly, when we instead use mPWVWN/6-311++G**, where 6-311++G** is now applied to all atoms, the Fe-N_{MI} bond lengths in [Fe(P)(MI)(X)], where X = NO and MI, are dramatically elongated relative to experimental values (see Table 5.1), showing that this method is not useful for the investigation of the heme complexes considered here.

Based on these findings, initial geometry optimizations of all five- and six-coordinate complexes were performed with BP86/TZVP. This basis set and functional combination, in general, provides reliable geometries and, as expected, the obtained structures for all model systems compare well to experimental parameters (see Table 5.1). Prior to calculation of binding energies, the ground states of all reactants were determined for each functional/basis set combination utilized here. The five- and six-coordinate ferrous heme-nitrosyl complexes were computed as S = 1/2, in accordance with experimental data.[53] For X = HNO, CO,

and MI the ferrous six-coordinate complexes were computed as low-spin (S = 0), but for the corresponding five-coordinate complexes both the S = 0 and 2 spin states were included to determine the lowest energy spin state in each case. Whereas DFT predicts quite clearly that [Fe(P)(X)] with X = CO, HNO to be low-spin (experimentally not known), the spin state of [Fe(P)(MI)] is very ambiguous.[54] Experimentally, the latter complex is high-spin.

Method Calibration: Calculation of Binding Constants for 1-Methylimidazole Ligation to [Fe(P)(NO)] and [Fe(P)(MI)]

As a measure of the σ-*trans* interaction exerted by each of the four small molecules HNO, CO, NO, and MI in ferrous heme complexes, we have evaluated the binding constants (K_{eq}) of MI to the five-coordinate species [Fe(P)(X)], which are obtained from the calculated ΔG values at 298.15 K for the reaction:

$$[Fe(P)(X)] + MI \rightleftarrows [Fe(P)(MI)(X)]$$

Due the lack of experimental binding constants for both X = HNO and CO, the NO and MI complexes were utilized to assess the accuracy of DFT to calculate these binding energies (Table 5.2) and K_{eq} values (Table 5.3). Since gradient-corrected functionals generally overestimate metal-ligand covalencies, and also show strong preference for low-spin states, accurate metal-ligand binding energies are often times only available from hybrid functionals.[23] Given that BP86/TZVP generates good structures at low computational cost, we used these structures and then calculated binding energies, ΔE, with a large number of methods as listed in Table 5.2. Calculated basis set superposition errors (BSSE), usually around 2

Table 5.2. Reaction Energies (kcal/mol) for [Fe(P)(X)] +MI ⇄ [Fe(P)(X)(MI)] at 298.15K.

		X = NO	X = NHO[b]		X = CO[b]		X = MI[b]	
	sp method	S = 1/2	S= 0	S = 2	S = 0	S = 2	S = 0	S = 2
ΔE	***experimental***[a]	**(-16)**						**(-26)**
ΔG		**-1.9**						**-6.7**
	BP86/TZVP optimized geometries							
ΔE	BP86/TZVP	-2.4	**-11.7**	-41.0	**-12.5**	-49.3	**-17.7**	-31.0
	B3LYP/TZVP	-3.5	**-11.9**	-13.7	**-12.2**	-34.8	-13.7	**-5.1**
	B3LYP*/TZVP	-3.8	**-12.3**	-20.5	**-12.6**	-29.0	-15.2	**-14.8**
	B3LYP-D/TZVP	-16.8	**-26.2**	-29.2	**-26.2**	-37.1	-28.6	**-26.7**
	B3LYP*-D/TZVP	-17.3	**-26.7**	-36.9	**-26.8**	-44.9	**-30.2**	-34.5
	OLYP/TZVP	-17.3	**0.3**	-11.6	**-0.7**	-23.1	-5.2	**0.6**
	O3LYP/TZVP	-2.2	**-12.7**	-20.9	**-13.3**	-31.8	-17.0	**-11.3**
	O3LYP*/TZVP	-0.9	**-13.2**	-15.6	**-13.8**	-27.1	-16.8	**-6.5**
	O3LYP-D/TZVP	-17.6	**-29.1**	-39.6	**-29.5**	-50.0	-34.2	**-33.9**
	O3LYP*-D/TZVP	-16.3	**-29.6**	-34.4	**-30.1**	-45.2	-34.0	**-29.0**
thermal correction		*14.0*	*13.8*	*19.6*	*13.7*	*19.9*	*14.8*	*18.9*
ΔG	BP86/TZVP	11.6	2.1	-21.4	1.2	-29.4	-2.9	-12.1
	B3LYP/TZVP	10.5	1.9	5.9	1.5	-14.9	1.1	13.8
	B3LYP*/TZVP	10.2	1.5	-0.9	1.1	-9.1	-0.4	4.1
	B3LYP-D/TZVP	-2.8	-12.4	-9.6	-12.5	-17.2	-13.8	-7.8
	B3LYP*-D/TZVP	-3.3	-12.9	-17.3	-13.1	-25.0	-15.4	-15.6
	OLYP/TZVP	-3.3	14.1	8.0	13.0	-3.2	9.6	19.5
	O3LYP/TZVP	11.8	1.1	-1.3	0.4	-11.9	-2.2	7.6
	O3LYP*/TZVP	13.1	0.6	4.0	-0.1	-7.2	-2.0	12.4
	O3LYP-D/TZVP	-3.6	-15.3	-20.0	-15.8	-30.1	-19.4	-15.0
	O3LYP*-D/TZVP	-2.3	-15.8	-14.8	-16.4	-25.3	-19.2	-10.1
	B3LYP/6-31G optimized geometries*							
ΔE	B3LYP/6-31G*							-12.5
	B3LYP-D/TZVP							-26.9
	O3LYP*-D/TZVP							-28.5

[a]Determined for the corresponding TPP complexes [Fe(TPP)(MI)(NO)] and [Fe(TPP)$(MI)_2$)]. ΔE is predicted using experimental ΔG values and BP86/TZVP predicted thermal and entropic corrections (see text).

[b]For [Fe(P)(CO)] and [Fe(P)(NHO)] the spin state of the complex is not known and could either be high-spin (S = 2) or low-spin (S = 0). Hence, both spin states were considered here. For completion, we also included the low-spin state of [Fe(P)(MI)]. In all of these cases, ΔE values printed in bold represent the one for which the spin state is predicted by DFT to have the lowest energy.

kcal/mol, are corrected for in the reported binding energies. Finally, a thermal and entropic correction (taken from BP86/TZVP calculations) is applied to the calculated ΔE values, resulting in the free energies, ΔG at 298.15 K, listed in Table 5.2. Importantly, this thermal correction is essentially method independent (with typical errors of less than 5%) and, as a result, we can apply a BP86/TZVP thermal correction to energies calculated with an alternate method. For example, calculated thermal corrections for the reaction: [Fe(P)(MI)] (S = 2) + MI ⇄ [Fe(P)$(MI)_2$], are 18.9 and 19.7 kcal/mol when applying BP86/TZVP and B3LYP/6-31G* respectively. If X = NO, thermal corrections for BP86/TZVP and B3LYP/LanL2DZ* are 14.0 and 13.4 kcal/mol, again, a deviation of less than 5%.

The experimental ΔG values for binding MI to [Fe(TPP)(NO)][35] is -1.9 kcal/mol and, using a calculated thermal correction of about 14.0 kcal/mol, the binding energy can be estimated around -16 kcal/mol. The B3LYP/TZVP calculated binding energy for MI ligation to [Fe(P)(NO)] (Table 5.2) is, however, only -3.5 kcal/mol; underestimated by >10 kcal/mol. Similarly, ΔG for binding MI to [Fe(TPP)(MI)] is -6.7 kcal/mol experimentally. After applying a 18.9 kcal/mol thermal correction, ΔE can be predicted around -26 kcal/mol. B3LYP/TZVP significantly underestimates this value by >20 kcal/mol, calculating a ΔE value of -5.1 kcal/mol. Accordingly, the B3LYP/TZVP K_{eq} values (calculated from ΔG) for MI ligation to [Fe(P)(NO)] and [Fe(P)(MI)] show significant errors compared to reported experimental values. For [Fe(TPP)(NO)] and [Fe(TPP)(MI)],[55] MI binding constants of 26 and 7.8 x 10^4 M^{-1} are reported, whereas the calculations yield 1.1 x 10^{-6} and 4.2 x 10^{-9} M^{-1}, respectively (Table 5.3).

Table 5.3. Binding constants (M^{-1}) for [Fe(P)(X)] + MI ⇄ [Fe(P)(X)(MI)] at 298.15 K. K_{eq} is calculated using the listed method on BP86/TZVP geometries.

	X = NO	X = NHO		X = CO		X = MI	
sp method	S = 1/2	S= 0	S = 2	S = 0	S = 2	S = 0	S = 2
experimental	**26**						**7.8×10^{4}**
BP86	3.1×10^{-9}	2.9×10^{-2}	5.0×10^{15}	1.3×10^{-1}	3.5×10^{21}	1.4×10^{2}	7.2×10^{8}
B3LYP	1.9×10^{-8}	4.0×10^{-2}	5.0×10^{-5}	7.6×10^{-2}	7.9×10^{10}	1.7×10^{-1}	7.4×10^{-11}
B3LYP*	3.2×10^{-8}	7.8×10^{-2}	4.2	1.7×10^{-1}	4.5×10^{6}	1.8	9.2×10^{-4}
B3LYP-D	1.1×10^{2}	1.1×10^{9}	1.2×10^{7}	1.5×10^{9}	4.1×10^{12}	1.3×10^{10}	5.6×10^{5}
B3LYP*-D	2.7×10^{2}	2.7×10^{9}	4.5×10^{12}	4.3×10^{9}	2.0×10^{18}	1.9×10^{11}	2.7×10^{11}
OLYP	2.7×10^{2}	4.7×10^{-11}	1.3×10^{-6}	2.9×10^{-10}	2.1×10^{2}	8.5×10^{-8}	5.2×10^{-15}
O3LYP	2.2×10^{-9}	1.5×10^{-1}	8.7	5.2×10^{-1}	5.3×10^{8}	39	2.7×10^{-6}
O3LYP*	2.4×10^{-10}	3.7×10^{-1}	1.2×10^{-3}	1.2	1.9×10^{8}	30	7.5×10^{-10}
O3LYP-D	4.7×10^{2}	1.7×10^{11}	4.9×10^{14}	4.1×10^{11}	1.1×10^{22}	1.5×10^{14}	9.4×10^{10}
O3LYP*-D	53	4.1×10^{11}	6.9×10^{10}	9.7×10^{11}	3.5×10^{18}	1.2×10^{14}	2.6×10^{7}

Since the calculated binding constants are seven (or more) orders of magnitude underestimated using B3LYP/TZVP, ΔE was recalculated for X = NO and MI using a modified B3LYP functional where HF exact exchange is reduced to 15% (B3LYP*), in combination with the TZVP basis set. It has been noted previously by Hess and co-workers that decreasing the 20% HF exact exchange in the original B3LYP functional to 15% greatly improves computational results for transition metal complexes without compromising the quality of the hybrid functional.[56] While using the B3LYP* functional favorably increased the binding energy of MI to [Fe(P)(MI)] to -14.8 kcal/mol, ΔE for [Fe(P)(NO)] is essentially unaffected at -3.8 kcal/mol. This translates to a free energy for MI binding to [Fe(P)(MI)] of 4.1 kcal/mol, 10 kcal/mol higher than the experimental ΔG of -6.7 kcal/mol for [Fe(TPP)(MI)]. Correspondingly, the predicted K_{eq} value for [Fe(P)(MI)] of 9.2×10^{-4} M^{-1} is eight orders of magnitude too low. The calculated free energy, ΔG, for MI binding to [Fe(P)(NO)] is still predicted ~10 kcal/mol too high compared to the experimental value of -1.9 kcal/mol for [Fe(TPP)(NO)]; translating to a calculated K_{eq} value of 3.2×10^{-8} M^{-1} (nine orders of magnitude too low, see Table 5.3).

Finally, recent computational work by Siegbahn and co-workers has shown that inclusion of van der Waals interactions is important for the accurate determination of metal-ligand binding constants.[57] If van der Waals interactions are included in the B3LYP functional (B3LYP-D/TZVP), ΔE is now predicted for [Fe(P)(NO)] to be -16.8 kcal/mol, only 0.8 kcal/mol from the "experimental" MI binding energy of -16 kcal/mol as shown in Table 5.2. K_{eq} of the NO complex increases to 1.1 x 10^2 M^{-1}, now only overestimating MI affinity for [Fe(P)(NO)] by one order of magnitude, or 0.9 kcal/mol in terms of ΔG. Additionally, with B3LYP-D we predict ΔE of -26.7 kcal/mol for [Fe(P)(MI)] which is also within 1 kcal/mol of the experimental value for the tetraphenylporphyrin complex. The B3LYP-D/TZVP calculated MI binding constant for [Fe(P)(MI)] is 5.6 x 10^5 M^{-1}, again only one order of magnitude from the experimental value of 7.8 x 10^4 M^{-1} (1.1 kcal/mol in terms of ΔG). Excitingly, the ΔG values obtained with B3LYP-D/TZVP, and hence, binding constants are well within the error of DFT (~2 kcal/mol). Finally, we explored whether a combination of the two previously introduced corrections, i.e. both van der Waals interactions and a 15% HF exact exchange (B3LYP*-D), would further improve the computational results. With B3LYP*-D, the MI binding constant for X = NO remains essentially unchanged, but the MI binding affinity for X = MI is now overestimated by seven orders of magnitude (2.7 x 10^{11} M^{-1}) compared to the experimental K_{eq} value. Therefore, inclusion of van der Waals interactions (with the original 20% HF exact exchange present in B3LYP) in the calculation of K_{eq} values (B3LYP-D) affords the most accurate MI binding constants for [Fe(P)(NO)] and [Fe(P)(MI)]; see Figure 5.2.

Interestingly, the success of the B3LYP-D functional lies largely in the fact that the van der Waals interactions essentially compensate for the thermal and

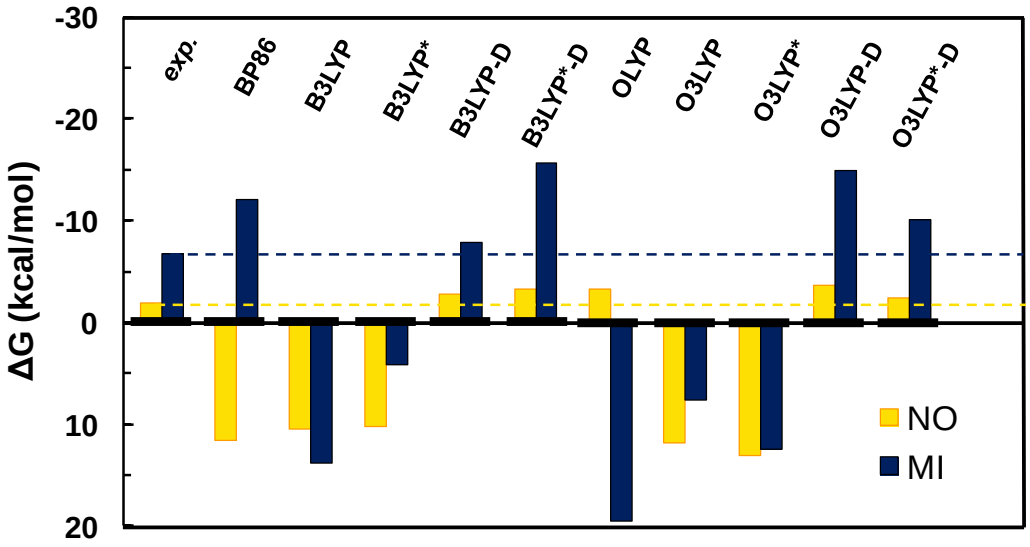

Figure 5.2. Experimental and DFT free energies (kcal/mol) for the reaction: [Fe(P)(X)] + MI ⇄ [Fe(P)(MI)(X)] where X = NO and MI at 298.15 K. All calculations were performed on BP86/TZVP structures.

entropic corrections. Hence, using the B3LYP/TZVP binding energies, ΔE, instead of the ΔG values, for the calculation of binding constants actually provides a good estimate of K_{eq} values. This observation has been previously reported in the literature,[58] although the exact reasons for this coincidental finding were not clear.

In addition, the newer functional OLYP was recommended by Radon and Pierloot[51] and others in recent studies for the calculation of binding constants in heme systems, so we also investigated how this method performs for the scientific problem investigated here. OLYP/TZVP energies (calculated from BP86/TZVP structures) predict ΔE for ligation of MI to [Fe(P)(NO)] quite well at -17.3 kcal/mol, which is within 2 kcal/mol of the estimated experimental MI binding energy for [Fe(TPP)(NO)] of ΔE ~ -16 kcal/mol. However, OLYP actually predicts stronger MI binding to the five-coordinate NO complex than to the corresponding five-coordinate

MI complex, as shown in Table 5.3, with a predicted binding energy of only 0.6 kcal/mol for [Fe(P)(MI)]. This is in stark contrast to experimental findings. Combined with the problems of OLYP/TZVP to determine an accurate structure for [Fe(P)(MI)(NO)] (see above), this clearly renders this method unusable for the system under study here. If instead the corresponding hybrid functional O3LYP is employed, the absolute ΔE values for X = NO and MI, -2.2 and -11.3 kcal/mol, are still significantly in error but the trend is now correctly described. After applying the thermal and entropic correction, though, ΔG is found to be incorrectly predicted to be positive with this method, 11.8 and 7.6 kcal/mol for the NO and MI complexes, respectively. These values are highly inconsistent with the experimental free energies of -1.9 (NO) and -6.7 (MI) kcal/mol, and hence, this result is still highly unsatisfactory. In the end, K_{eq} values predicted by O3LYP are nearly 10 orders of magnitude underestimated (Table 5.3).

Applying van der Waals interactions (O3LYP-D) and setting the HF exact exchange to 15% (O3LYP*) again improves the quality of the overall predictions as shown in Table 5.3. In contrast to B3LYP, the O3LYP functional with both modifications included (O3LYP*-D) actually predicts the best binding energies, ΔE, for X = NO and MI, -16.3 and -29.0 kcal/mol, respectively. As a result, the calculated ΔG value for X = NO is -2.3 kcal/mol with O3LYP*-D, only overestimating the experimental value by 0.4 kcal/mol. The free energy for X = MI is -10.1 kcal/mol, overestimated compared to experiment by 3.4 kcal/mol. Therefore, the O3LYP*-D binding constants are the most accurate for any modified O3LYP functional investigated here (see Figure 5.2) with K_{eq} values for MI binding of 53 and 2.6×10^7 M^{-1} for X = NO and MI, respectively. This now provides an accurate prediction of MI

binding constants to ferrous heme-nitrosyl systems, although binding of MI to [Fe(P)(MI)] is overestimated by 3 orders of magnitude.

In comparison to experimental values for the corresponding ferrous tetraphenylporphyrin complexes, B3LYP-D/TZVP predicts the most accurate MI binding constants to [Fe(P)(X)] (where X = NO and MI) of all the methods tested here. Excitingly, the K_{eq} values predicted by this method are well within the error of density functional theory calculations. B3LYP-D/TZVP is followed closely in accuracy by binding constants for O3LYP*-D/TZVP as shown in Tables 5.2 and 5.3.

To examine the effect of alternate geometries on the predicted ΔE values, B3LYP-D/TZVP and O3LYP*-D/TZVP energies (most accurate for the BP86/TZVP structures) were recalculated using B3LYP/6-31G* fully optimized structures. B3LYP/6-31G* was determined to predict the most accurate Fe-N_{MI} bond lengths for [Fe(P)$(MI)_2$] in comparison to experimental data for [Fe(TPP)$(MI)_2$] (see above). Importantly, calculated binding energies (ΔE) vary by less than 0.5 kcal/mol when using the BP86/TZVP and B3LYP/6-31G* structures, see Table 5.3. This is found for both the B3LYP-D and the O3LYP*-D functional used in combination with the TZVP basis set. While this may be expected as geometries are, in general, relatively similar between the BP86/TZVP and B3LYP/6-31G* optimizations, it does indicate that the most important parameter in determining accurate *absolute* binding energies and K_{eq} values is the method by which the single-point energies are calculated, as long as the structures are reasonable. In addition, as mentioned above, the thermal and entropy corrections to obtain ΔG from ΔE values are essentially constant, emphasizing that the accurate calculation of ΔE values on good geometries is key to success in K_{eq} calculations.

In summary, prediction of accurate MI binding constants, K_{eq}, in ferrous heme systems poses a serious challenge due to the fact that computational errors in ligand binding energies are of the same magnitude as the actual binding energies that we are trying to calculate. Several previous computational studies[51, 57] have discussed the difficulties in obtaining accurate binding energies for heme systems and our work suggests similar conclusions. Therefore, it is crucial that all theoretical binding constants are reported using experimental values as a calibration for method accuracy.

Examination of the Thermodynamic σ-trans Effect of HNO in sGC Model Systems: Calculation of Binding Constants for 1-Methylimidazole Ligation to Five-Coordinate Heme Complexes

Based on our method calibration, inclusion of van der Waals interactions is crucial to calculation of MI binding constants to [Fe(P)(X)] where X = NO and MI, *vide supra*. Specifically the B3LYP-D and O3LYP*-D functionals gave particularly accurate K_{eq} values (Table 5.3) for our system. Upon applying the B3LYP-D functional with the TZVP basis set we are able to calculate free energies, ΔG, for MI binding to both [Fe(P)(NO)] and [Fe(P)(MI)] that are within ~1 kcal/mol of experimental values—well within the error of DFT. Due to the exponential relationship between ΔG and K_{eq}, this translates to K_{eq} values predicted within one order of magnitude of experimental values for [Fe(TPP)(NO)] and [Fe(TPP)(MI)].

While the absolute values of the calculated binding constants for many of the tested methods (Table 5.3) are significantly in error compared to experimental data, the binding constants of MI to [Fe(P)(NHO)] and [Fe(P)(CO)] are generally predicted to be within the same order of magnitude, indicating that HNO and CO exhibit a

Table 5.4. Relative binding constants (M^{-1}) for [Fe(P)(X)] + MI ⇄ [Fe(P)(X)(MI)] at 298.15 K. K_{eq} values are taken from Table 5.3.

	X = NO	X = NHO		X = CO		X = MI
sp method	S = 1/2	S= 0	S = 2	S = 0	S = 2	S = 2
experimental	**1**					**3.0×10^3**
B3LYP-D	1	1.0×10^7	1.0×10^5	1.4×10^7	3.6×10^{10}	5.0×10^3
B3LYP*-D	1	1.0×10^7	1.7×10^{10}	1.6×10^7	7.2×10^{15}	1.0×10^9
O3LYP*-D	1	7.8×10^9	1.3×10^9	1.8×10^{10}	6.7×10^{16}	4.9×10^5

comparable *trans* effect. This does not appear to depend much on the applied computational method. In addition, the best method from our method calibration study, B3LYP-D/TZVP, predicts *relative* MI binding constants of 1.0×10^7 and 1.4×10^7 M^{-1} for HNO (five-coordinate, S = 0) and CO (five-coordinate, S = 0) complexes, respectively, as shown in Table 5.4. K_{eq} values for the five-coordinate HNO and CO complexes are approximately seven orders of magnitude larger than that of the corresponding NO complex. Oddly, however, B3LYP-D/TZVP predicts the *relative* binding constant of MI to [Fe(P)(MI)] (S = 2) to be only 5.0×10^3 M^{-1}—three orders of magnitude lower than for the CO complex (Table 5.4). While CO should have a relatively small *trans* effect, it is still thought to have a larger *trans* effect than MI, based on crystallographic Fe-N_{MI} bond lengths and Fe-N_{MI} stretching frequencies, see above. A similar situation is observed for O3LYP*-D/TZVP binding constants where X = HNO and CO are predicted to have larger binding constants than X = MI. Conversely, as shown in Table 5.4, utilization of B3LYP*-D/TZVP, where the HF exact exchange is lowered to 15%, yields *relative* MI binding constants of 1.0×10^7 and 1.6×10^7 M^{-1} for the five-coordinate HNO and CO complexes (S = 0), and 1.0×10^9 M^{-1} for X = MI (S = 2); i.e. B3LYP*-D predicts that both CO and HNO exert a stronger *trans* interaction in ferrous heme systems than MI (see Table 5.4). In accordance with the strong σ-*trans* effect of NO, the binding constant of MI to

[Fe(P)(NO)] obtained with B3LYP*-D/TZVP is much lower than that for X = CO, HNO, and MI and is predicted to be 2.7 x 10^2 M^{-1} (see Table 5.3). Therefore, although the absolute MI binding constant to [Fe(P)(MI)] is significantly in error with B3LYP*-D, lowering the HF exact exchange in B3LYP to 15% appears to aid in the prediction of good relative binding constants for all complexes considered here. While DFT's ability to accurately predict binding constants is in question (*vide supra*), it appears to consistently predict similar binding constants for both HNO and CO which are at least 6 orders of magnitude larger than that of NO. This indicates that the thermodynamic *trans* effect of NO is much stronger than that of CO and HNO, suggesting that HNO cannot *directly* activate sGC through cleavage of the Fe-N_{His105} bond, as observed for CO.

Examination of the Thermodynamic σ-trans Effect of HNO in sGC Model Systems: Fe-N_{MI} Bond Lengths and Orbital Analysis

Further support for the weakened *trans* effect of HNO relative to NO is obtained by the BP86/TZVP optimized Fe-N_{MI} bond lengths for the six-coordinate structures with X = HNO or NO, where values of 2.082 Å and 2.179 Å are obtained, respectively. These values are in fact in very good agreement with the experimental data (Table 5.1). This comparison indicates that HNO does not induce a *trans* effect of the same magnitude as NO. HNO does, however, induce slightly longer Fe-N_{MI} bond lengths than both CO, 2.068 Å, and MI, 1.994 Å in the BP86/TZVP optimizations.

The difference in *trans* interaction is further illustrated by the B3LYP/TZVP calculated molecular orbitals for the six-coordinate complexes, as shown in the contour plots in Figure 5.3. Here, the competition of the π^*_h orbital of HNO and the

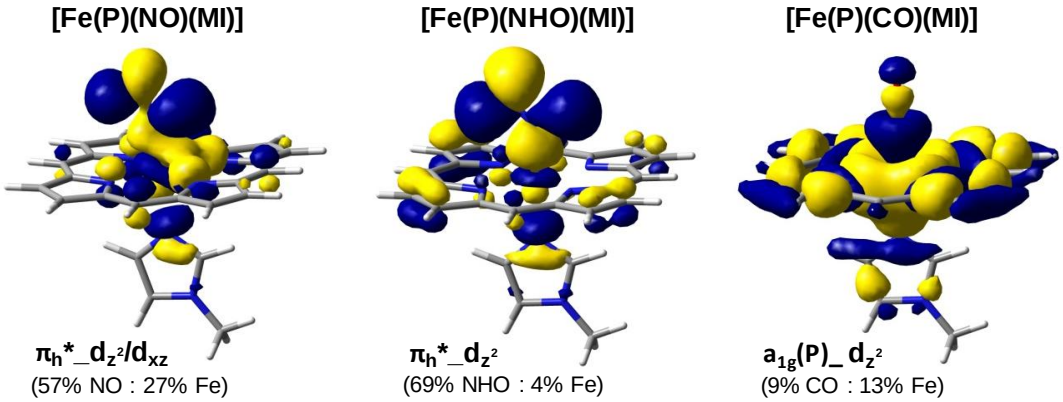

Figure 5.3. Relevant molecular orbitals of (a) [Fe^{II}(P)(NO)(MI)], (b) [Fe^{II}(P)(NHO)(MI)], and (c) [Fe^{II}(P)(CO)(MI)] which define the thermodynamic σ-*trans* effect in these ferrous porphyrin systems. Calculated with B3LYP/TZVP on the BP86/TZVP optimized structures.

σ(N) orbital of MI for the d_{z2} orbital of Fe defines the σ-*trans* interaction induced by HNO.[23] For [Fe(P)(MI)(NO)], the important Fe-NO σ bonding orbital shows 57% π^*_h and 27% Fe d_{z2}/d_{xz} contributions, corresponding to a strong σ-bond, inducing a large *trans* interaction. Here, the weakening of the Fe-N_{MI} bond is due to the antibonding Fe-N_{MI} interaction in this molecular orbital (cf. Scheme 5.1). In contrast, in the HNO bound model system, the important Fe-NO σ bonding orbital shows 69% π^*_h character and only 4% Fe d_{z2} contribution, see Table 5.5. The decrease in the Fe d_{z2} percentage in the orbital of the HNO complex relative to the corresponding orbital of the NO complex indicates a much smaller σ-*trans* effect for HNO, i.e. a weaker Fe-N_{MI} antibonding interaction, thus making it unlikely that this molecule could induce the cleavage of the Fe-histidine bond in sGC in agreement with the calculated binding constants discussed above. This also indicates that HNO is mostly a π-backbonding ligand (with the main π-backbonding (occupied) MO containing 48% d_{yz} and 15% π^*_v character), similar to CO.

Table 5.5. Charge contributions of the key Fe-X σ-bonding orbitals for [Fe(P)(MI)(X)] calculated with B3LYP/TZVP.

			Fe	X		O		N_{MI}
X	orbital	label	d	s	p	s	p	s+p
NO	<120>	$\pi^*_h\_d_{z2}/d_{xz}$	27	2	30	0	26	2
NHO	<116>	$\pi^*_h\_d_{z2}$	4	1	10	0	58	3
CO	<102>	$a_{1g}(P)\_ d_{z2}$	13	3	4	0	1	4

Comparison to the ferrous CO complex, [Fe(P)(CO)(MI)], further supports this conclusion. Experimentally, it is known that CO binds to ferrous sGC, but forms a stable six-coordinate complex.[39] The BP86/TZVP calculated Fe-N_{MI} distance with either CO or HNO in the *trans* position is quite similar (2.082 Å for HNO and 2.068 Å for CO), indicating that HNO will behave more similarly to CO as compared to NO. The contour plot of the corresponding Fe-CO bonding orbital does not show significant CO contributions, in agreement with a weak σ-*trans* effect of this diatom. Interestingly, this orbital contains 13% d_{z2} which is higher than that of HNO. The stronger d_{z2} contribution (with respect to HNO), however, is counteracted by the fact that the overall CO contribution to this orbital is quite small, only 9%. In fact, most of the contributions to this molecular orbital originate from the porphyrin(a_{1g})_d_{z2} bonding interaction (this molecular orbital has 67% porphyrin character). Overall, we would predict HNO and CO to exert similar thermodynamic σ-*trans* effects in six-coordinate ferrous porphyrin systems, suggesting HNO cannot chemically induce cleavage of the Fe-N_{His105} bond in sGC.

Alternate Methods of sGC Activation by HNO

Although HNO does not induce a significant thermodynamic σ-*trans* effect it is predicted from previous work that NO^-, the deprotonated form of HNO, actually has

Scheme 5.2. Possible route for sGC activation by HNO through strong hydrogen bonding from HNO to an amino acid side chain.

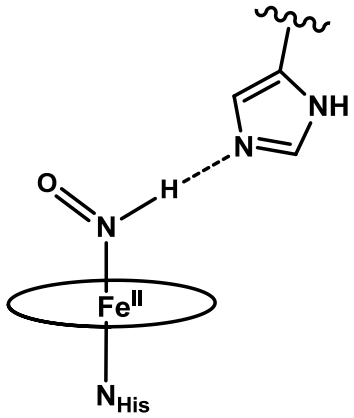

an even stronger σ-*trans* effect than NO (Goodrich and Lehnert, manuscript in preparation). DFT optimized structures predict an Fe-N_{MI} bond length of 2.44 Å for [Fe(P)(MI)(NO)]⁻—essentially MI is non-bonding.[9] This is significantly longer than the calculated Fe-N_{MI} bond length of 2.18 Å in [Fe(P)(MI)(NO)]. Therefore, it may be feasible for HNO to activate sGC if the distal pocket contains a strong hydrogen bond accepting amino acid, for example histidine as shown in Scheme 5.2. Since the pKa of bound HNO is unknown, it is not known if this partial "deprotonation" to give the ligand more NO^- character is biologically relevant. DFT calculations suggest that bound NO^- is very basic (in ferrous heme thiolate complexes), suggesting that biological hydrogen bonds are not strong enough to cause a significant deprotonation, and hence, increase in *trans* effect. Interestingly, however, a recent study by Montenegrao et al. reports the pKa for the non-heme $[Fe(CN)_5(HNO)]^{3-}$ complex to be 7.7,[59] significantly lower than that of free HNO (pKa of 11.6). At such a low pKa, HNO is potentially prone to significant hydrogen bonding to distal pocket residues.

Conclusions

In summary, weak metal-ligand binding constants are inherently difficult to calculate by DFT methods. The prediction of accurate MI binding constants to [Fe(P)(X)] for X = NO and MI is dependent on the inclusion of van der Waals interactions. In this study, the best K_{eq} values were obtained with B3LYP-D/TZVP energies on BP86/TZVP geometries. The calculated MI binding constants for X = NO and MI are 110 and 5.6 x 10^5 M^{-1}, predicted only one order of magnitude higher than experimentally determined values of 26 and 7.8 x 10^4 M^{-1} for ferrous tetraphenylporphyrin complexes. Interestingly, the addition of van der Waals interactions in the calculation of binding energies, ΔE, essentially compensates for the thermal and entropic corrections to ΔG. As a result, calculated ΔE values from simple B3LYP/TZVP calculations are actually good estimates for corresponding ΔG values and can be used to roughly estimate K_{eq} values in a fast and straightforward way. Although calculated K_{eq} values are prone to errors, calculated MI binding constants indicate that the thermodynamic σ-*trans* effect exerted by HNO and CO in these six-coordinate heme complexes is essentially equal, independent of the computational method employed. Additionally, the binding constants for MI to [Fe(P)(NHO)] are consistently predicted six orders of magnitude higher than those for MI ligation to [Fe(P)(NO)]. This indicates that the thermodynamic σ-*trans* effect induced by HNO is significantly weaker than that induced by NO, and is instead comparable to that of CO. This conclusion is supported by (a) Fe-N_{MI} bond lengths in both model complexes and DFT-calculated geometries and (b) molecular orbital analysis of the key σ-bonding orbitals in these complexes, as described in this paper. The optimized Fe-N_{MI} bond length of [Fe(P)(MI)(NHO)] is ~0.1 Å shorter than that in [Fe(P)(MI)(NO)], essentially equal to [Fe(P)(MI)(CO)], and ~0.09 Å longer

than that in [Fe(P)(MI)$_2$]. Molecular orbital analysis indicates 23% less Fe-d_{z2} character in the relevant π^*_h_d_{z2} orbital of HNO relative to that of the strong σ-*trans* ligand NO. Hence, HNO is predominantly a π-backbonding ligand, similar to CO. As such, we predict that HNO cannot *directly* activate sGC through binding to the heme and cleavage of the Fe-N_{His105} bond.

Experimental

To determine the accuracy of density functional theory (DFT) methods for the prediction of structures and binding constants in ferrous heme complexes, an investigation into various computational methods was performed. Functionals utilized include BP86,[60-61] B3LYP,[61-63] O3LYP,[64-65] OLYP,[66-67] and mPWVWN[68-69] in combination with the basis sets TZVP,[70-71] LanL2DZ*,[72-73] 6-31G*,[74] and 6-311++G**.[75] Modified versions of the hybrid functionals were also utilized. This includes addition of van der Waals interactions (for example, B3LYP-D) or decrease of the HF exact exchange contribution to 15% (for example, B3LYP*).[56-57] The most accurate computational results were obtained using the BP86 functional and TZVP basis set for geometry optimizations and the B3LYP-D functional and TZVP basis set for total energy calculations (unless stated otherwise). The calculated lowest energy spin state was utilized for all five-coordinate complexes unless the spin state is known experimentally. Counterpoise calculations to estimate the basis set superposition error (BSSE) are also included in all calculated ΔE values. Frequency calculations were performed using the same basis set/functional combination as the optimizations to determine the thermal and entropic corrections to ΔE to obtain the Gibbs free energies, ΔG, for all reactions.

All geometry optimizations and single point energy calculations were performed with the program package Gaussian 03.[76] Molecular orbitals were obtained from single point calculations using ORCA.[77] In all calculations, convergence was reached when the relative change in the density matrix between subsequent iterations was less that 1×10^{-8}. Molecular orbitals were plotted with the program orca_plot included in the ORCA package and visualized using GaussView.

References

1. Culottta, E.; Koshland, D. E., Jr., *Science* **1992,** *258*, 1862-1865.
2. Bredt, D. S.; Snyder, S. H., *Annu. Rev. Biochem.* **1994,** *63*, 175-195.
3. Moncada, S.; Palmer, R. M.; Higgs, E. A., *Pharmacol. Rev.* **1991,** *43*, 109-142.
4. Butler, A. R.; Williams, D. L. H., *Chem. Soc. Rev.* **1993**, 223-241.
5. Ignarro, L., *Nitric Oxide: Biology and Pathobiology*. Academic Press: San Diego, 2000.
6. Lui, S. M.; Soriano, A.; Cowan, J. A., *J. Am. Chem. Soc.* **1993,** *115*, 10483-10486.
7. Crane, B. R.; Seigel, L. M.; Getzoff, E. D., *Biochemistry* **1997,** *36*, 12120-12137.
8. Shiro, Y.; Fujii, M.; Iisuka, T.; Adachi, S.; Tsukamoto, K.; Nakahara, K.; Shoun, H., *J. Biol. Chem.* **1995,** *270*, 1617-1623.
9. Lehnert, N.; Praneeth, V. K. K.; Paulat, F., *J. Comput. Chem.* **2006,** *27*, 1338-1351.
10. Nagasawa, H. T.; DeMaster, E. G.; Redfern, B.; Shirota, F. N.; Goon, D. J. W., *J. Med. Chem.* **1990,** *33*, 3120-3122.
11. Lopez, B. E.; Wink, D. A.; Fukuto, J. M., *Arch. Biochem. Biophys.* **2007,** *465*, 430-436.
12. Paolocci, N.; Jackson, M. I.; Lopez, B. E.; Miranda, K.; Tocchetti, C. G.; Wink, D. A.; Hobbs, A. J.; Fukuto, J. M., *Pharmacol. Ther.* **2007,** *113*, 442-458.
13. Arnelle, D. R.; Stamler, J. S., *Arch. Biochem. Biophys.* **1995,** *318*, 279-285.
14. Schmidt, H. H. H. W.; Hofmann, H.; Schindler, U.; Shutenko, Z. S.; Cunningham, D. D.; Feelish, M., *Proc. Natl. Acad. Sci. USA* **1996,** *93*, 14492-14497.

15. Miranda, K. M., *Coord. Chem. Rev.* **2005,** *249*, 433-455.

16. Doctorovich, F.; Bikiel, D.; Pellegrino, J.; Suarez, S. A.; Larsen, A.; Marti, M. A., *Coord. Chem. Rev.* **2011,** *255*, 2764-2784.

17. Miller, T. W.; Cherney, M. M.; Lee, A. J.; Francoleon, N. E.; Farmer, P. J.; King, S. B.; Hobbs, A. J.; Miranda, K. M.; Burstyn, J. N.; Fukuto, J. M., *J. Biol. Chem.* **2009,** *284*, 21788-21796.

18. Ignarro, L. J., *J. Biochem. Soc. Trans.* **1992,** *20*, 465-469.

19. Zhao, Y.; Marletta, M. A., *Biochemistry* **1997,** *36*, 15959-15964.

20. Traylor, T. G.; Sharma, V. S., *Biochemistry* **1992,** *31*, 2847-2849.

21. Yu, A. E.; Hu, S. S. T. G.; Burstyn, J. N., *J. Am. Chem. Soc.* **1994,** *116*, 4117-4118.

22. Zhao, Y.; Brandish, P. E.; Ballou, D. P.; Marletta, M. A., *Proc. Natl. Acad. Sci. USA* **1999,** *96*, 14753-14758.

23. Goodrich, L. E.; Paulat, F.; Praneeth, V. K. K.; Lehnert, N., *Inorg. Chem.* **2010,** *49*, 6293-6316.

24. Cary, S. P.; Winger, J. A.; Marletta, M. A., *Proc. Natl. Acad. Sci. USA* **2005,** *102*, 13064-13069.

25. Fernoff, N. B.; Derbyshire, E. R.; Marletta, M. A., *Proc. Natl. Acad. Sci. USA* **2009,** *106*, 21602-21607.

26. Kimura, H.; Mittal, C. K.; Murad, F., *J. Biol. Chem.* **1975,** *250*, 8016-8022.

27. Paolocci, N.; Saavedra, W. F.; Miranda, K. M.; Martignani, C.; Isoda, T.; Hare, J. M.; Espey, M. G.; Fukuto, J. M.; Feelisch, M.; Wink, D. A.; Kass, D. A., *Proc. Natl. Acad. Sci. USA* **2001,** *98*, 10463-10468.

28. Ellis, A.; Li, C. G.; Rand, M. J., *Br. J. Pharmacol.* **2000,** *129*, 315-322.

29. Favaloro, J. L.; Kemp-Harper, B. K., *Cardiovas. Res.* **2007,** *73*, 587-596.

30. Fukuto, J. M.; Chiang, K.; Hszieh, R.; Wong, P.; Chaudhuri, G., *J. Pharmacol. Exp. Ther.* **1992,** *263*, 546-551.

31. Fukuto, J. M.; Hobbs, A. J.; Ignarro, L. J., *Biochem. Biophys. Res. Commun.* **1993,** *196*, 707-713.

32. Murphy, M. E.; Sies, H., *Proc. Natl. Acad. Sci. USA* **1991,** *88*, 10860-10864.

33. Dierks, E. A.; Burstyn, J. N., *Biochem. Pharmacol.* **1996,** *51*, 1593-1600.

34. Zeller, A.; Wenzl, M. V.; Beretta, M.; Stessel, H.; Russwurm, M.; Koesling, D.; Schmidt, K.; Mayer, B., *Mol. Pharmacol.* **2009,** *76*, 1115-1122.

35. Praneeth, V. K. K.; Näther, C.; Peters, G.; Lehnert, N., *Inorg. Chem.* **2006,** *45*, 2795-2811.

36. Berto, T. C.; Praneeth, V. K. K.; Goodrich, L. E.; Lehnert, N., *J. Am. Chem. Soc.* **2009,** *131*, 17116-17126.

37. Lehnert, N.; Sage, J. T.; Silvernail, N.; Scheidt, W. R.; Alp, E. E.; Sturhahn, W.; Zhao, J., *Inorg. Chem.* **2010,** *49*, 7197-7215.

38. Stone, J. R.; Marletta, M. A., *Biochemistry* **1994,** *33*, 5636-5640.

39. Burstyn, J. N.; Yu, A. E.; Dierks, E. A.; Hawkins, B. K.; Dawson, J. H., *Biochemistry* **1995,** *34*, 5896-5903.

40. Leu, B. M.; Silvernail, N. J.; Zgierski, M. Z.; Wyllie, G. R. A.; Ellison, M. K.; Scheidt, W. R.; Zhao, J.; Sturhahn, W.; Alp, E. E.; Sage, J. T., *Biophys. J.* **2007,** *92*, 3764-3783.

41. Wyllie, G. R. A.; Schulz, C. E.; Scheidt, W. R., *Inorg. Chem.* **2003,** *42*, 5722-5734.

42. Salzmann, R.; Ziegler, C. J.; Godbout, N.; McMahon, M. T.; Suslick, K. S.; Oldfield, E., *J. Am. Chem. Soc.* **1998,** *120*, 11323-11334.

43. Li, J.; Nair, S. M.; Noll, B. C.; Schulz, C. E.; Scheidt, W. R., *Inorg. Chem.* **2008,** *47*, 3841-3850.

44. Erbil, W. K.; Price, M. S.; Wemmer, D. E.; Marletta, M. A., *Proc. Natl. Acad. Sci. USA* **2009,** *106*, 19753-19760.

45. Ma, X.; Sayed, N.; Bbeuve, A.; van den Akker, F., *EMBO J.* **2007,** *26*, 578-588.

46. Muralidharan, S.; Boon, E. M., *J. Am. Chem. Soc.* **2012,** *134*, 2044-2046.

47. Silvernail, N. J.; Olmstead, M. M.; Noll, B. C.; Scheidt, W. R., *Inorg. Chem.* **2009,** *48*, 971-977.

48. Graeme, R. A.; Schulz, C. E.; Scheidt, W. R., *Inorg. Chem.* **2003,** *42*, 5722-5734.

49. Immoos, C. E.; Sulc, F.; Farmer, P. J.; Czarnecki, K.; Bocian, D. F.; Levina, A.; Aitken, J. B.; Armstrong, R. S.; Lay, P. A., *J. Am. Chem. Soc.* **2005,** *127*, 814-815.

50. Ellison, M. K.; Schulz, C. E.; Scheidt, W. R., *Inorg. Chem.* **2002,** *41*, 2173-2181.

51. Radon, M.; Pierloot, K., *J. Phys. Chem. A* **2008,** *112*, 11824-11832.

52. Ling, Y.; Mills, C.; Weber, R.; Yang, L.; Zhang, Y., *J. Am. Chem. Soc.* **2010,** *132*, 1583-1591.

53. Lehnert, N.; Berto, T. C.; Galinato, M. G. I.; Goodrich, L. E., The Role of Heme-Nitrosyls in the Biosynthesis, Transport, Sensing, and Detoxification of Nitric

Oxide (NO) in Biological Systems: Enzymes and Model Complexes. In *The Handbook of Porphyrin Science*, Kadish, K.; Smith, K.; Guilard, R., Eds. World Scientific: 2011; Vol. 15, pp 1-247.

54. Jensen, K. P.; Ryde, U., *Mol. Phys.* **2003,** *101*, 2003-2018.

55. Portela, C. F.; Magde, D.; Traylor, T. G., *Inorg. Chem.* **1993,** *32*, 1313-1320.

56. Reiher, M.; Salomon, O.; Hess, B. A., *Theor. Chem. Acc.* **2001,** *107*, 48-55.

57. Siegbahn, P. E. M.; Blomberg, M. R. A.; Chen, S.-L., *J. Chem. Theory Comput.* **2010,** *6*, 2040-2044.

58. Praneeth, V. K. K.; Paulat, F.; Berto, T. C.; DeBeer George, S.; Näther, C.; Sulok, C. D.; Lehnert, N., *J. Am. Chem. Soc.* **2008,** *130*, 15288-15303.

59. Montenegro, A. C.; Amorebieta, V. T.; Slep, L. D.; Martin, D. F.; Roncaroli, F.; Murgida, D. H.; Bari, S. E.; Olabe, J. A., *Angew. Chem. Int. Ed.* **2009,** *48*, 4213-4216.

60. Perdew, J. P., *Phys. Rev. B* **1986,** *33*, 8822-8824.

61. Becke, A. D., *Phys. Rev. A* **1988,** *38*, 3098-3100.

62. Becke, A. D., *J. Chem. Phys.* **1993,** *98*, 1372-1377.

63. Becke, A. D., *J. Chem. Phys.* **1993,** *98*, 5648-5652.

64. Handy, N. C.; Cohen, A. J., *Mol. Phys.* **2001,** *99*, 403-412.

65. Hoe, W.-M.; Cohen, A.; Handy, N. C., *Chem. Phys. Lett.* **2001,** *341*, 319-328.

66. Lee, C.; Yang, W.; Parr, R. G., *Phys. Rev. B.* **1988,** *37*, 785-789.

67. Miehlich, B.; Savin, A.; Stoll, H.; Preuss, H., *Chem. Phys. Lett.* **1989,** *157*, 200-206.

68. Adamo, C.; Barone, V., *J. Chem. Phys.* **1998,** *108*, 664-675.

69. Vosko, S. H.; Wilk, L.; Nusair, M., *Can. J. Phys.* **1980,** *58*, 1200-1211.

70. Schaefer, A.; Horn, H.; Ahlrichs, R., *J. Chem. Phys.* **1992,** *97*, 2571-2577.

71. Schaefer, A.; Huber, C.; Ahlrichs, R., *J. Chem. Phys.* **1994,** *100*, 5829-5835.

72. Praneeth, V. K. K.; Neese, F.; Lehnert, N., *Inorg. Chem.* **2005,** *44*, 2570-2572.

73. Lehnert, N.; Galinato, M. G. I.; Paulat, F.; Richter-Addo, G. B.; Sturhahn, W.; Zhao, J., *Inorg. Chem.* **2010,** *49*, 4133-4148.

74. Rassolov, V.; Pople, J. A.; Ratner, M.; Redfern, P. C.; Curtiss, L. A., *J. Comp. Chem.* **2001,** *22*, 976-984.

75. Raghavachari, K.; Binkley, J. S.; Seeger, R.; Pople, J. A., *J. Chem. Phys.* **1980,** *72*, 650-654.

76. Frisch, M. J.; Trucks, G. W.; Schlegel, H. B.; Scuseria, G. E.; Robb, M. A.; Cheeseman, J. R.; Montgomery, J., J. A.; Vreven, T.; Kudin, K. N.; Burant, J. C.; Millam, J. M.; Iyengar, S. S.; Tomasi, J.; Barone, V.; Mennucci, B.; Cossi, M.; Scalmani, G.; Rega, N.; Petersson, G. A.; Nakatsuji, H.; Hada, M.; Ehara, M.; Toyota, K.; Fukuda, R.; Hasegawa, J.; Ishida, M.; Nakajima, T.; Honda, Y.; Kitao, O.; Nakai, H.; Klene, M.; Li, X.; Knox, J. E.; Hratchian, H. P.; Cross, J. B.; Bakken, V.; Adamo, C.; Jaramillo, J.; Gomperts, R.; Stratmann, R. E.; Yazyev, O.; Ausin, A. J.; Cammi, R.; Pomelli, C.; Octerski, J. W.; Ayala, P. Y.; Morokuma, K.; Voth, G. A.; Salvador, P.; Dannenberg, J. J.; Zakrzewski, V. G.; Dapprich, S.; Daniels, A. D.; Strain, M. C.; Farkas, O.; Makick, D. K.; Rabuck, A. D.; Raghavachair, K.; Foresman, J. B.; Ortiz, J. V.; Cui, Q.; Baboul, A. G.; Clifford, S.; Cioslowski, J.; Stefanov, B. B.; Lui, G.; Laishenko, A.; Piskorz, R.; Komaromi, I.; Martin, R. L.; Fox, D. J.; Keith, T.; Al-Laham, M. A.; Peng, C. Y.; Nanayakkara, A.; Challacombe, M.; Gill, P. M. W.; Johnson, B.; Chen, W.; Wong, M. W.; Gonzalez, C.; Pople, J. A. *Gaussin 03*, Gaussian, Inc.: Pittsburgh, PA, 2003.

77. Neese, F. *ORCA*, 2.2; Max-Planck Institut feur Bioanorganische Chemie: Meulheim/Ruhr, Germany, 2004.

Chapter 6

Conclusions

The critical degradation of toxic nitric oxide (NO) in biological systems is performed either through the oxidation of NO to nitrate by globins[1] or through reduction to nitrous oxide (N_2O) by a class of enzymes called nitric oxide reductases (NORs). Bacterial and fungal NORs reduce NO to N_2O as a part of the denitrification process where nitrate is reduced in a step-wise fashion to N_2 (bacteria) or N_2O (fungi).[2] The fungal NOR, cytochrome P450 nitric oxide reductase (P450nor), is a ferric heme thiolate enzyme.[3-4] This dissertation is focused on the generation of small molecule models of intermediates in the catalytic cycle of P450nor.

The first step in reduction of NO to N_2O by P450nor is coordination of NO to the active site ferric heme to generate a ferric heme-nitrosyl complex with cysteinate ligation.[5] Chapter 2 is focused on synthesis of model complexes of this important intermediate. In the first section, we screen both porphyrin and thiolate ligands in an attempt to prepare stable ferric heme-nitrosyl complexes with thiolate ligation. While the porphyrin ligand appears to contribute to fine tuning the stability of ferric nitrosyls with thiolate coordination, the key factor to successful preparation of ferric heme-nitrosyls is the presence of SR-H_2^-, a *two* hydrogen-bond stabilized thiolate ligand.[6] Unfortunately, the synthesis of SR-H_2^- is time consuming and results in low yields. For this reason, we have developed a new synthetic procedure for large scale preparation of this important ligand. In the second section, the reactivity of NO with

ferric heme phenolate complexes was tested. Surprisingly, upon addition of NO, decomposition of the complex was observed rather than formation of the desired six-coordinate ferric nitrosyl. Finally, the effect of axial ligand donor strength on ferric heme-nitrosyls was explored. DFT calculations predict that as electron donation from the axial ligand increases, the Fe-NO and N-O bonds become weaker. This is accompanied by a distinct bending of the Fe-N-O unit.[7] Excitingly, this trend is also observed experimentally.

Chapter 3 is focused on modeling the second intermediate in the catalytic cycle of P450nor, a ferrous heme-nitroxyl complex.[8] Here, a new bis-picket fence porphyrin ferrous nitrosyl complex is prepared and one-electron reduction is performed. The N-O stretching frequency of the resulting reduced species ({FeNO}^{8}) is 1466 cm^{-1}. This is in agreement with other {FeNO}^{8} porphyrin complexes reported previously. Importantly, we have demonstrated that the *trans* effect of bound NO$^-$ is stronger than that of NO in ferrous heme systems. Upon one-electron reduction of the six-coordinate complex [Fe(T*o*-F_2PP)(MI)(NO)], the resulting complex, [Fe(T*o*-F_2PP)(NO)]$^-$, is five-coordinate. This indicates loss of MI upon reduction to the {FeNO}^{8} complex, and an increased *trans* effect of NO$^-$ relative to NO. DFT results support this finding and indicate that the key molecular orbital, π^*_h_d_{z2}, responsible for the σ-*trans* effect in {FeNO}^{7} systems does not change upon one-electron reduction. Additionally, the reactivity of {FeNO}^{8} complexes with acid and free NO was explored. [Fe(T*o*-F_2PP)(NO)]$^-$ reacts with acetic acid to generate the corresponding {FeNO}^{7} complex and 0.5 equivalents H_2. Finally, reaction of [Fe(T*o*-F_2PP)(NO)]$^-$ with NO results in reduction of free NO to NO$^-$ and oxidation of the ferrous nitroxyl complex to [Fe(T*o*-F_2PP)(NO)].

Chapter 4 addresses the key intermediate in the catalytic cycle of P450nor responsible for the crucial N-N bond formation. This intermediate is proposed to be a Fe(IV)-NHOH complex[9] or, upon loss of water, a Fe(VI)-N heme complex. In the first part of Chapter 4, we prepare a bis-picket fence porphyrin ferric O-benzylhydroxylamide complex, [Fe(3,5-Me-BAFP)(NHOBn)]. This complex is now ready for one-electron oxidation to the corresponding Fe(IV) complex and reaction with NO. In the second half of Chapter 4, we work towards preparing high-valent heme-nitride complexes. DFT calculations suggest that in the presence of an axial thiolate ligand, as is found in P450nor, loss of water from a doubly protonated ferrous nitroxyl complex is energetically feasible. Additionally, irradiation of heme azide complexes was tested in an attempt to generate a Fe(V)-nitride complex through release of N_2. Unfortunately, irradiation of both five- and six-coordinate ferric bis-picket fence porphyrin azide complexes resulted in photoinduced cleavage of the Fe-N_3 bond, generating the corresponding ferrous complexes rather than the desired Fe(V)-N complex.

Finally, in Chapter 5, activation of the primary mammalian nitric oxide (NO) sensor, soluble guanylate cyclase (sGC), is discussed. Through the strong thermodynamic σ-*trans* effect of NO, binding of NO at the distal side of the ferrous heme induces cleavage of the proximal Fe-N_{His} bond, activating the catalytic domain of the enzyme.[10] It has been proposed that nitroxyl (HNO) is also capable of activating sGC, but the key question remains as to whether HNO can induce cleavage of the Fe-N_{His} bond. Here, we report calculated binding constants for 1-methylimidazole (MI) to [Fe(P)(X)] (P = porphine^{2-}) where X = NO, HNO, CO, and MI to evaluate the *trans* interaction of these molecules, X, with the proximal imidazole (histidine) in sGC. A systematic assessment of DFT methods suggests that the

prediction of accurate MI binding constants is critically dependent on the inclusion of van der Waals interactions (-D functionals). Calculated (B3LYP-D/TZVP) MI binding constants for X = NO and MI are 110 and 5.6 x 10^5 M^{-1}, respectively, predicted only one order of magnitude higher than the corresponding experimentally determined values. MI binding constants where X = HNO and CO are consistently predicted to be essentially equal and around six orders of magnitude larger than those of NO, indicating that CO and HNO mediate a weak thermodynamic *trans* effect in this system. Orbital analysis of the key σ-bonding orbital, $\pi^*_h\_d_{z2}$, and comparison of Fe-N_{MI} bond lengths support this prediction. This suggests that HNO does not induce a σ-*trans* effect strong enough to promote cleavage of the Fe-N_{His} bond—a key step in activation of sGC.[11]

References

1. Gardner, P. R.; Gardner, A. M.; Martin, L. A.; Salzman, A. L., *Proc. Natl. Acad. Sci. USA* **1998,** *95*, 10378-10383.

2. Zumft, W. G., *J. Inorg. Biochem.* **2005,** *99*, 194-215.

3. Nakahara, K.; Tanimoto, T.; Hatano, K.; Usuda, K.; Shoun, H., *J. Biol. Chem.* **1993,** *268*, 8350-8355.

4. Lehnert, N.; Berto, T. C.; Galinato, M. G. I.; Goodrich, L. E., The Role of Heme-Nitrosyls in the Biosynthesis, Transport, Sensing, and Detoxification of Nitric Oxide (NO) in Biological Systems. In *Handbook of Porphyrin Science*, Kadish, K.; Smith, K.; Guilard, R., Eds. World Scientific: 2011; Vol. 15, pp 1-247.

5. Shiro, Y.; Fujii, M.; Iizuka, T.; Adachi, S.; Tsukamoto, K.; Nakahara, K.; Shoun, H., *J. Biol. Chem.* **1995,** *270*, 1617-1623.

6. Goodrich, L. E.; Paulat, F.; Praneeth, V. K. K.; Lehnert, N., *Inorg. Chem.* **2010,** *49*, 6293-6316.

7. Xu, N.; Goodrich, L. E.; Lehnert, N.; Powell, D. R.; Richter-Addo, G. B., **2012**, submitted for publication.

8. Goodrich, L. E.; Roy, S.; Matzger, A. J.; Lehnert, N., **2012**, manuscript in preparation.

9. Lehnert, N.; Praneeth, V. K. K.; Paulat, F., *J. Comp. Chem.* **2006,** *27*, 1338-1351.

10. Traylor, T. G.; Sharma, V. S., *Biochemistry* **1992,** *31*, 2847-2849.

11. Goodrich, L. E.; Lehnert, N., *J. Inorg. Biochem.* **2012**, accepted.